UNIVERSITY OF LEEDS

Molecular Outflows in Massive Star Forming Regions

Nichol Cunningham

School of Physics and Astronomy

University of Leeds

Submitted in accordance with
the requirements for the degree of

Doctor of Philosophy

August 2015

The candidate confirms that the work submitted is her own, except where work which has formed part of jointly authored publications has been included. The contribution of the candidate and the other authors of this work has been explicitly indicated. The candidate confirms that appropriate credit has been given within this thesis where reference has been made to the work of others.

Preface

Within this thesis, some chapters have been based on work presented in the following jointly authored publications:

I. "Submillimeter Array Observations of NGC 2264-C: Molecular Outflows and Driving Sources ", **N.Cunningham**, S. L. Lumsden, C. J. Cyganowski, L. T. Maud, C. Purcell, 2015, submitted to MNRAS .

Paper I forms the basis of Chapter 2. The paper describes the SMA 1.3 mm continuum and molecular line observations towards the intermediate/massive star forming region NGC 2264-C. The data reduction, and analysis of these observations were carried out by the primary author, N. Cunningham, and the text in the submitted manuscript was also written by the primary author. The co-authors provided comments on various drafts of the manuscript which were incorporated in final submission.

The data reduction of the observations presented in Chapter 5 were completed by Cormac Purcell.

Acknowledgements

First and foremost I would like to thank my supervisor Stuart Lumsden for his guidance, encouragement and continued support throughout my PhD. Your door was always open, particularly during those most stressful times. You have helped me shape and focus this PhD. Thank you for giving me the opportunity to pursue this dream. I would also like to thank Claudia Cyganowski for her continued help, support and time, initially with the data reduction and then with the reading of countless paper drafts. I would like to thank Cormac Purcell for the many useful suggestions and discussions.

I would like to thank everyone who made my time at Leeds such a special time, there are too many to mention but Leeds will always hold a special place in my heart. The last four years have been an amazing journey.

I would like to thank my office mates, John Fairlamb, Tom Douglas, and Karim Ababakr thank you for listening to me vent when things got stressful, and sharing so many fun memories. A massive, huge thanks go to Jonny Henshaw, Luke Maud and John Ilee thank you for letting me your pick your brains, keeping me positive, feeding me chocolate and the many beers and rums we shared. I will treasure

those memories and I look forward sharing many more beers in the future. Thanks to everyone, both the staff and students at Leeds who made it such an awesome department to spend the last 4 years. Friday nights without the Fenton are not the same.

Thanks to Jill, Tasha, Paula, Nikki and Linda who even though I have not been able to spend much time you all this last year you have always been there in spirit and kept me laughing. Yes Linda I have finally finished. Ignacio, thank you for always believing in me even when I had stopped believing in myself. You always found a way to make me smile, and gave me a new way of looking at things. I know am a better person for knowing you.

Finally, the biggest thanks of all go to my family, my brother Paul, my grandmother Hazel and especially my parents Jan and Paul, I would not be who or where I am today without your constant love and unquestioned support. I am eternally grateful for everything you have done for me.

Abstract

This thesis presents millimetre continuum and molecular line observations exploring the properties of molecular outflows towards massive star forming regions. Massive stars produce some of the most energetic phenomena in the Galaxy, yet we still do not have a comprehensive understanding of how they actually form. Outflows are known to play a key role in this formation process and their properties, particularly how they change depending on the mass, luminosity and evolution of the driving source can shed light on how massive stars actually form. This thesis presents observations at both high (SMA 3″) and low (JCMT 15″) spatial resolution of the known jet/outflow tracers, SiO and ^{12}CO, towards a sample massive star forming region drawn from the RMS survey. Furthermore, the presence of infall signatures is explored through observations of HCO^+ and $H^{13}CO^+$, and the hot core nature of the regions is probed using tracers such as CH_3CN, HC_3N and CH_3OH.

SiO is detected towards ∼50% of the massive young stellar objects and HII regions in the JCMT sample. The detection of SiO appears to be linked to the age of the RMS source, with the younger sources showing a stronger dependence with SiO. The presence of SiO also

appears to be linked to the CO velocity, with SiO more efficiently tracing sources with higher velocity dispersions. In the MOPRA observations towards a sample of 33 RMS sources, CH_3CN is detected towards 66% of the sources, with the redder likely younger sources having the largest rotational temperatures.

This thesis presents the first interferometric SiO (5-4) and ^{12}CO (2-1) observations, taken with the SMA, towards the massive star forming region G203.3166/NGC 2264-C. In this intermediate/massive star forming cluster, SiO is again tracing the youngest sources. Both the SiO and ^{12}CO emission trace two bipolar, high velocity outflows towards the mm brightest, IR-dark, likely youngest sources in this region. In contrast the IR-bright RMS source, AFGL 989-IRS1, in NGC 2264-C displays no associated molecular outflow emission. Furthermore, the high resolution follow-up SMA observations towards G192.6005/S255IR and the first interferometric ^{12}CO and SiO observations towards G194.9349 show a high velocity outflow traced by ^{12}CO in each region. In both regions the outflow appears to be driven by the IR-bright RMS source. However, no high velocity SiO counterpart is observed in either region. Thus, the lack of associated SiO emission may be a sign of age in these regions.

Abbreviations

ACSIS	Auto Correlation Spectral Imaging System
ALMA	Atacama Large Millimeter Array
ATCA	Australia Telescope Compact Array
AU	Astronomical Unit
arcsec/arcsecond	Second of Arc
COM	Complex Organic Molecule
CASA	Common Astronomy Software Package
EHV	Extremely High Velocity
FIR	Far-Infrared
FWHP	Full Width at Half Power
FWHM	Full Width at Half Maximum
FOV	Field of View
GMC	Giant Molecular Cloud
HARP	Heterodyne Array Receiver Program
HMC	Hot Molecular Core
HMPO	High Mass Protostellar Object
IHV	Intermediate High Velocity
IR	Infrared
IRAC	Infrared Array Camera
IRAS	Infrared Astronomical Satellite
IRDC	Infrared Dark Cloud
ISM	Interstellar Medium
JCMT	James Clerk Maxwell Telescope
KAPPA	Kernel Application Package
KH	Kelvin-Helmholtz

LSB	Lower Side Band
LSR	Local Standard of Rest
LTE	Local Thermal Equilibrium
MIR	Mid-Infrared
MIRIAD	Multichannel Image Reconstruction Image Analysis Display
MIPS	Multiband Imaging Photometer
MP	Molecular Peak
MSX	Midcourse Space Experiment
MYSO	Massive Young Stellar Object
NIR	Near-Infrared
PA	Position Angle
PACS	Photodetector Array Camera and Spectrometer
PdBI	Plateau de Bure Interferometer
RMS	Red MSX Source
SCUBA	Sub-Millimetre Common-User Bolometer Array
SED	Spectral Energy Distribution
SHV	Standard High Velocity
SMA	Sub-Millimetre Array
SMURF	Sub-Millimetre User Reduction Facility
SPIRE	Spectral and Photometric Imaging Receiver
YSO	Young Stellar Object
UCHII	Ultra Compact HII
USB	Upper Side Band
UV	Ultraviolet
VLA	Very Large Array
WISE	Wide-field Infrared Survey Explorer

Contents

List of Figures

LIST OF FIGURES

LIST OF FIGURES

List of Tables

LIST OF TABLES

Chapter 1

Introduction

Stars are the building blocks of galaxies. In particular, massive stars (stars with a mass $M_* > 8\,M_\odot$) are responsible for many of the most energetic phenomena, injecting considerable amounts of energy and radiation into their surrounding environment through their winds, outflows, and ultimately their energetic deaths. These energetic phenomena completely characterise and regulate the evolution of galaxies, both initiating and inhibiting new generations of star birth. Furthermore, massive stars are the nuclear powerhouses that drive the chemical evolution within galaxies, without which the complex molecules and elements we need to live would not exist. In spite of this, we still do not have a comprehensive understanding of how these progenitors of our existence actually form.

Massive stars are rarer and so on average more distant than their low mass counterparts. They evolve more rapidly with most of their early formation occurring in dense, deeply embedded, complex environments making it difficult to dissect the emission from a single massive protostellar object. Our understand-

ing of the early stages in the formation of massive stars is thus limited by the lack of an observationally based evolutionary sequence.

The aim of this thesis is to contribute to our knowledge of the jets/outflows driven by massive stars, and how we can use their properties to further understand how massive stars form. This thesis presents both low and high spatial resolution observations, combining a number of probes to explore and compare the environments of young high mass stars. The remainder of this chapter will review the current status of our understanding of the star formation processes relevant to the focus of this thesis.

1.1 Overview of Star Formation

1.1.1 Large Scales - Molecular Clouds

Stars form in dense, cold molecular cloud complexes within the interstellar medium (ISM). The largest of which, giant molecular clouds (GMCs), represent some of the largest structures in the Galaxy with sizes of the the order 50-200 pc, and masses in the range 10^4-$10^6 M_\odot$, and are home to the majority of the star formation in the Galaxy (Blitz 1993). GMCs are composed primarily of molecular hydrogen (H_2), however, the symmetric nature of this molecule renders it observationally elusive at the temperatures typical of GMCs (10-20 K). Instead, the low J transitions of CO (e.g. J=1-0, and J=2-1), which are readily excited at the temperatures of these clouds, have been used to characterise them. The first observations of these large structures were carried out in the 1970's (e.g. Scoville *et al.* 1975), but they were limited to small sections of

the Galaxy. It was not until composites of several larger scale Galactic surveys were combined by Dame *et al.* (1987, 2001) that the full extent of the large scale molecular gas distribution in the Galaxy was revealed. The inspection of the Galactic longitude-velocity plots from the CO observations further revealed the clumpy and inhomogeneous nature of GMCs (Bronfman *et al.* 1989). High resolution follow-up observations of several opaque regions in nearby clouds, using molecular species with higher critical densities than CO, such as NH_3 (e.g. Myers & Benson 1983), again revealed the inhomogeneity of molecular clouds, showing denser substructures associated with sites of active star formation. In comparison to the mean molecular hydrogen densities of GMCs, found to be around $100\,\mathrm{cm}^{-3}$ (Blitz 1993), these denser substructures were identified to have densities of the order 10^3-$10^4\mathrm{cm}^{-3}$. This observed inhomogeneity in molecular clouds was categorised by Williams *et al.* (2000) into a hierarchical structured system using the nomenclature of clouds, clumps and cores. The term "clump" is used to describe coherent structures within the cloud, where clusters of stars will form. Finally, "cores" describe dense regions where a single star or binary will form. A summary of the physical properties over the range of size scales within molecular clouds is given in Table 1.1. However, there is still debate regarding the physical properties and assigned nomenclature, particularly in the high mass regime where higher resolution observations of massive "cores" have revealed further fragmentation at scales of a few 1000 AU. An example of this fragmentation towards the massive star forming region IRAS 19410+2336 is presented in Figure 1.1. The image, taken from Beuther & Schilke (2004), displays the mm dust continuum emission at increasing spatial resolution of $11''$, $\sim 5''$, and $\sim 1''$ from left to right. At the lowest resolution (single dish IRAM

Table 1.1: Typical Physical Properties for Structures within Molecular Clouds.

	Size (pc)	Mass ($M_\odot$)	Density (cm^{-3})	Temperature (K)
GMC	50-200	10^4-10^6	100-300	10-15
Cloud	3-20	10^3-10^4	10^3-10^4	15-30
Clump	0.5-3	10^3-10^4	10^4-10^6	15-40
Cold core	0.1-0.5	10^2-10^3	10^5-10^7	30-100
Hot core	$\leq$0.1	10^2	10^6-10^8	100-200

Assembled from values from Cesaroni *et al.* (1992); Blitz (1993); Kurtz *et al.* (2000); Williams *et al.* (2000); Pillai *et al.* (2006); and Beuther *et al.* (2007)

30m observations at $\sim$11″) the emission is observed as two clumps on scales of $\sim$0.3-0.5 pc. However, the increased resolution of the interferometric observations (PdBI $\sim$5″) reveals further fragmentation within both clumps at scales of a few 1000 AU.

More recently, the advent of the Herschel Space Observatory (Pilbratt *et al.* 2010) has led to the large scale structure of the Galaxy being probed in the far-IR regimes. The Herschel observations have improved our understanding of the filamentary nature of GMCs (e.g. Molinari *et al.* 2010). These filaments are intricately linked on a variety of scales, and at the densest points harbour young proto/prestellar cores (e.g. André *et al.* 2010; André 2013). An example of the ubiquitous filamentary nature of GMCs is shown in Figure 1.2. This Figure shows a 3-colour composite mosaic of the W3 GMC, where red=250μm, green=160μm, and blue=70μm emission taken with the Photodetector Array Camera and Spectrometer (PACS), and the Spectral and Photometric Imaging Receiver (SPIRE) instruments of Herschel. The corresponding column density map is also shown in the right hand panel of that Figure. The blue emission

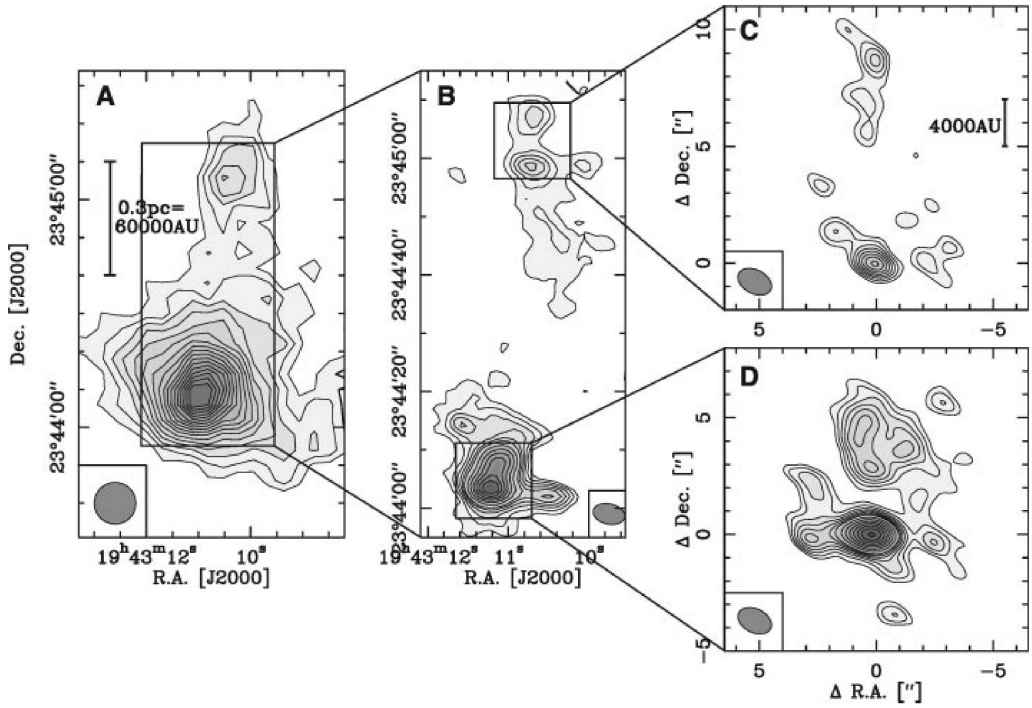

Figure 1.1: Dust continuum images taken from Beuther & Schilke (2004), showing increasing levels of fragmentation within molecular clouds. The left panel displays the 1.2 mm single dish continuum emission observed with the IRAM 30 m telescope at $\sim 11''$ resolution. The middle and right hand panel show interferometric data at 1.3 mm taken with the PdBI at resolutions of $\sim 5''$ and $\sim 1''$ respectively. The image highlights the propensity of fragmentation in molecular clouds down to size scales of a few 1000 AU.

shows the warmer components, likely sites of active star formation, whereas the colder gas (seen in red) traces multiple filaments which are threaded throughout the region. At several positions along these dense filaments, increased column densities are observed, which likely harbour young proto/prestellar cores.

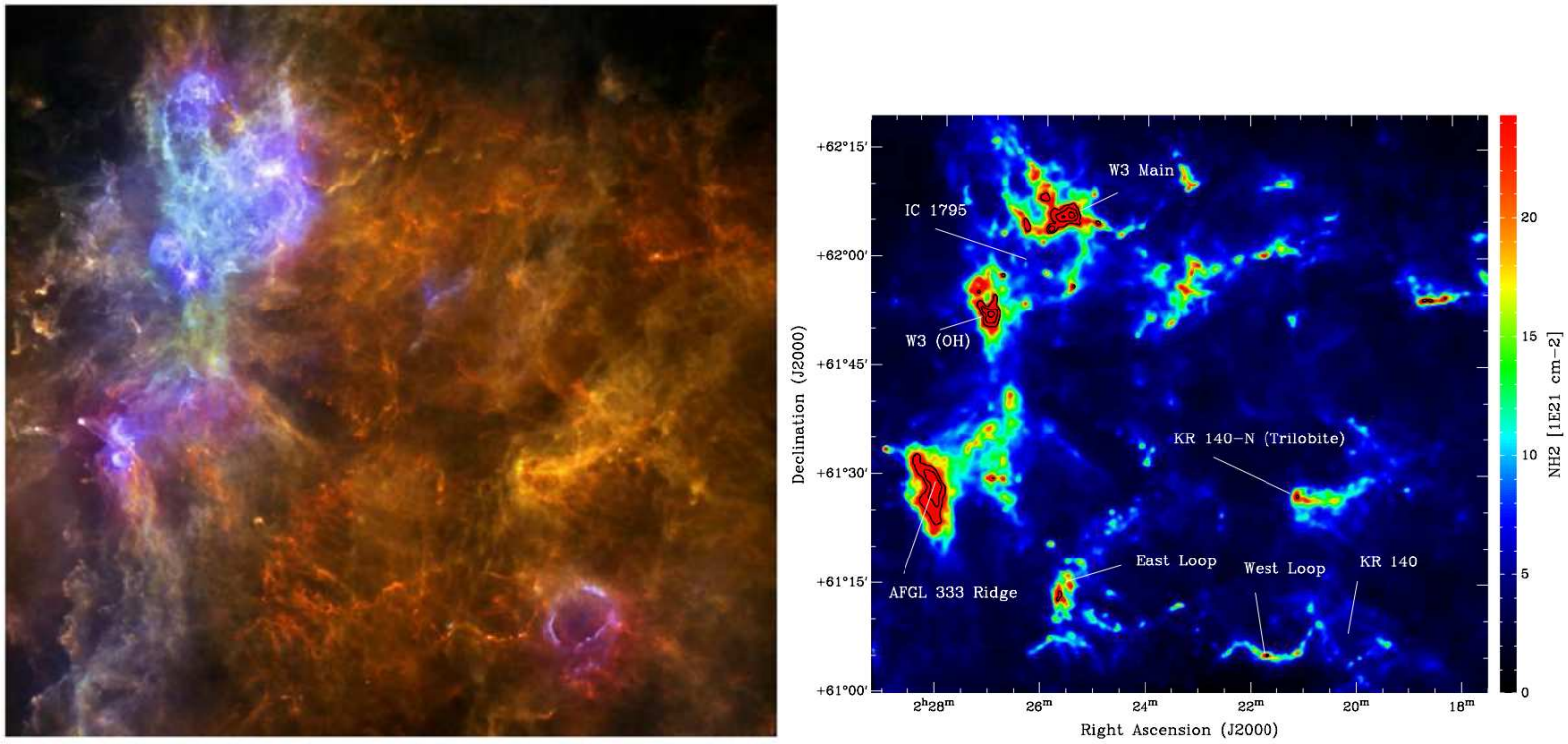

Figure 1.2: The left panel shows a 3-colour composite mosaic of the W3 GMC complex, where the red, green and blue emission are at 250μm, 160μm, and 70μm respectively. The warmer gas is seen in blue, whereas the red emission shows the cooler gas, which show filamentary structures threaded throughout the cloud. The right hand panel shows the derived column density. The data is part of the Herschel HOBYS key program (see text) and the images are directly taken from Figures 1 and 2 of Rivera-Ingraham *et al.* (2013), highlighting the ubiquitous filamentary and inhomogeneous nature of molecular clouds.

1.1.2 Small Scales - Star Forming Cores

Cores represent the smallest scales in the hierarchical fragmentation of molecular clouds, and are the birth sites of a single star or binary system. In the "standard model" of star formation presented by Shu *et al.* (1987), a star forms through the gravitational collapse of a dense isothermal sphere. It is widely accepted that low mass stars $M_* = 0.8\text{-}2M_\odot$ can form in this manner (Shu *et al.* 1987). In the simplest case, considering only thermal support of an isothermal sphere, the mass at which a system will undergo gravitational collapse is given by the Jeans mass,

$$M_J = \left(\frac{5k_bT}{\mu m_H G}\right)^{3/2}\left(\frac{3}{4\pi\rho}\right)^{1/2} \tag{1.1}$$

where ρ and T are the local density and temperature of the system, m_H is the mass of a hydrogen atom, μ is the mean molecular weight and G is the gravitational constant. Once gravity dominates the internal support, spherical collapse occurs on a timescale given by the free-fall timescale (Shu *et al.* 1987),

$$t_{ff} = \left(\frac{3\pi}{32G\rho}\right)^{1/2} = 3.4\times10^7\, n^{-1/2} \quad \text{years} \tag{1.2}$$

where ρ is the average mass density in $kg\,cm^{-3}$ and n is the number density in cm^{-3}. For molecular clouds the mean density is $\sim 100\,cm^{-3}$, giving a free-fall timescale of the order of a few Myrs.

In the standard model of star formation, the result of angular momentum conservation during the collapse of a rotating core under gravity leads to the formation of a flattened disc structure. As material infalls during collapse and

moves closer to the central core (decreasing radius) the velocity of the matter will increase to conserve momentum. Given the centrifugal force is strongest perpendicular to the axis of rotation and weakest along the rotation axis the net result is the formation of a disc. The central core increases in mass as material is transported through the accretion disc onto the central protostar (Shu *et al.* 1987). Another fundamental feature of the low mass star formation process is the ubiquity of jets and outflows during the early evolution (e.g. Arce & Sargent 2006 and references therein). However, there are at least two fundamental differences in the formation of high mass stars with respect to low mass stars; the timescales over which they form and the larger size scales involved in their formation. These two main differences have led to several competing theories to explain the formation of massive stars. If the formation of massive stars can be described as a scaled-up version of the low mass paradigm is still debated.

1.2 High Mass Star Formation

As previously mentioned, one of the fundamental differences between the formation of low and high mass stars is their respective formation timescales. For massive stars the Kelvin Helmholtz (KH) timescale is of the order t_{KH} =10^{4-5} yrs, which is considerably shorter than the free-fall timescale. Whereas in the low mass regime, the KH timescale is considerably longer ($\sim$1$\times$$10^7$ yrs for a 1 $M_\odot$ star) than the free fall timescale. The KH timescale is given by,

$$t_{KH} \approx \frac{GM_*^2}{R_* L_*} \tag{1.3}$$

(where M_*, R_*, and L_* are the mass, radius, and luminosity of a given star respectively), which describes the approximate timescale a protostar of a given mass could sustain a given luminosity without requiring the onset of H_2 burning in the core. In the low mass case, where $t_{KH} > t_{ff}$, accretion has ended before the onset of hydrogen burning. Whereas for high mass stars, $t_{KH} < t_{ff}$, and the resulting effect is that a massive star will reach the main sequence whilst still heavily embedded and accreting (Kahn 1974). A massive star therefore has no optically visable pre-main sequence evolution. A further consequence of the short formation of a massive star is the generation of feedback produced after the onset of hydrogen burning, which can suppress further accretion, dissipating the infalling envelope, and potentially limiting the mass of the final star (e.g. Larson & Starrfield (1971) suggest a mass limit $<60M_{\odot}$).

A second major difference between the formation of low and high mass stars is the larger size scales involved in the formation of a massive star. As gravitational collapse will tend to produce objects with masses comparable to the Jeans mass (given by Equation 1.1), additional support is required in the high mass regime to prevent further fragmentation of the single massive core into multiple components.

The two main competing theories of massive star formation are; Core Accretion (McKee & Tan 2003), and Competitive Accretion (Bonnell *et al.* 1997), and are discussed in more detail below. A third possible formation mechanism, involving the coalescence of smaller mass protostars to form a larger star, was initially suggested by Bonnell *et al.* (1998). However, the high densities required for this mechanism to prevail ($> 10^8\,\mathrm{pc}^{-3}$) are not typically observed in star forming clusters. Furthermore, simulations by Baumgardt & Klessen

(2011) have shown that collisions would play only a minor role (if any) in the formation of a massive star. Thus, this mechanism cannot be a viable scenario for the majority of the massive star formation occurring in the Galaxy.

1.2.1 Core Accretion

Core Accretion favours a scenario in which massive star formation can be seen as a "scaled-up" version of the standard model of low mass star formation (e.g. Shu *et al.* (1987) see Section 1.1.2). Towards cores associated with massive stars, the internal motions are found to be primarily nonthermal, increasing with radius (e.g. Myers & Fuller 1992; Caselli & Myers 1995). Through the inclusion of nonthermal motions, Myers & Fuller (1992) found the formation of star of $10M_{\odot}$ occurs more quickly compared with only a thermally supported isothermal core. Further development of this work by McKee & Tan (2003) led to the formation of the "Turbulent Core" model. The turbulent core model is seen as an extension of the low mass case and is supported by nonthermal pressure in the form of turbulence and/or magnetic fields during collapse. In this model, the material that ends up on the star is accreted almost exclusively from the single massive core that collapses to form a protostar. The higher accretion rates predicted in this model, $10^{-3}\,M_{\odot}yr^{-1}$, are suggested to be sufficient to overcome the radiation pressure, producing a $100M_{\odot}$ star in $\sim 10^5$yrs. Moreover, recent work by Krumholz *et al.* (2009), indicate that radiation pressure does not halt accretion in their simulations. Material is accreted via a rotating disc which can self shield against the radiation pressure from the central star. However, simulations of core collapse performed by Dobbs *et al.* (2005), sug-

gest fragmentation is prevalent in turbulent cores and will dominate over the formation of a singular massive core, producing further substructure. Therefore, additional support is required to prevent further fragmentation. Magnetic fields of the order of ∼mG (Tan *et al.* 2013) have been suggested to provide such support against fragmentation.

1.2.2 Competitive Accretion

Competitive Accretion has been suggested as an alternative formation scenario for massive stars. The model favours a high degree of fragmentation, resulting in the initial formation of several low mass protostars. The fragments then grow in a highly non-uniform manner dependent upon their location within the cluster (e.g. Bonnell *et al.* 1998). Stars preferentially located at the centre of the gravitational potential well (i.e. at the centre of the cluster), will have more material available for accretion. Thus, these stars will grow more massive compared with those stars less favourably positioned in the gravitational potential well. As the low mass protostars accrete from material bound to the shared cluster potential and not from an individual massive starless core, this model does not predict any gravitationally bound, massive starless cores forming in isolation.

1.2.3 Exploring the Formation Process through Observations

To confront the predicted models for massive star formation on a global scale, observations of a large sample of massive stars are required. The RMS survey

(Lumsden *et al.* 2013) currently provides one of the largest samples, ∼700 YSOs and HII regions complete out to a distance of 7 kpc, with confirmed luminosities down to typical B1 stars. The RMS survey provides an excellent base from which to explore the properties of massive stars.

The presence of both outflows and discs around high mass stars is a possible indication that the massive star formation process may be an extension of the standard low mass formation scenario. Outflows are also found to be a prevalent feature during the early formation of high mass stars (e.g. Zhang *et al.* 2005; Beuther *et al.* 2002). Maud *et al.* (2015b) have drawn on a sample of 99 massive young stellar objects (MYSOs) and compact HII regions from the RMS survey, providing one of the largest surveys to date of outflow properties in the high mass regime, finding a scaling of the outflow parameters in the high mass regime consistent with the observed properties in the low mass regime. Ilee *et al.* (2013) observed CO bandhead emission towards a sample of 20 MYSOs from the RMS survey, finding the spectra to be well fit by a model of a keplerian rotation disc. Yet, only a few examples of imaged discs around high mass stars are currently known, and only around B-type stars (e.g. IRAS 13481-6124: Kraus *et al.* 2010; IRAS 20126+4104: Cesaroni *et al.* 2014). This is likely to change in the coming years with the advent of high sensitivity and high resolution observations provided by Atacama Large Millimeter Array (ALMA).

1.3 Jets and Outflows

Outflows affect their natal cloud on a variety of size scales from 10's of AU to several pc (e.g. Frank *et al.* 2014). In the early stages they are likely responsible

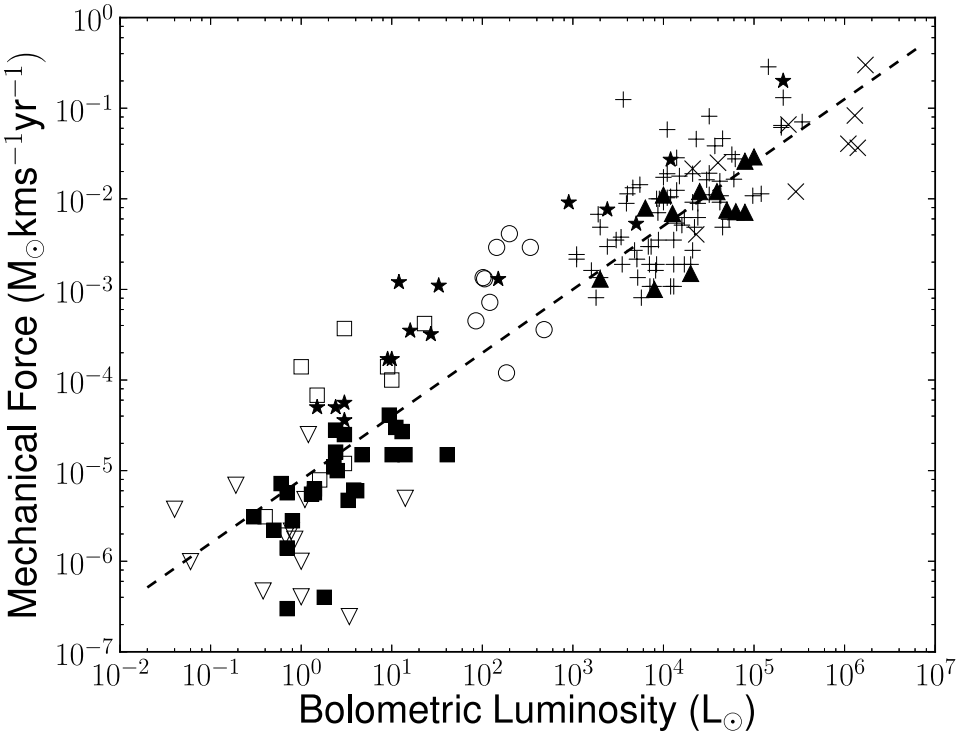

Figure 1.3: Outflow force vs bolometric luminosity (which I compiled from several previous single dish outflow surveys). The bolometric luminosity range extends over 6 orders of magnitude, showing a tight correlation with outflow force. The black triangles are outflow sources from Beuther *et al.* (2002), the black stars are values taken from Cabrit & Bertout (1992), the black crosses (x) represent sources from López-Sepulcre *et al.* (2009), the upside down open triangles are values from van der Marel *et al.* (2013), and the black pluses (+) are values taken from Maud *et al.* (2015b) from a sample of RMS sources. The open and filled squares are Class 0 and Class I low mass outflow sources from Bontemps *et al.* (1996), and the open circles are intermediate-mass class 0 analogues from Duarte-Cabral *et al.* (2013). The black dashed line is the result of a linear regression fit including all of the previous literature values presented.

for setting the final mass of the star. While on larger scales their interaction with the surrounding ambient medium may disrupt or initiate star formation. They are also a prevalent feature in the star formation process over the whole mass range, from brown dwarfs (e.g. Whelan *et al.* 2014), to low mass (e.g. Arce & Sargent 2006) and high mass (e.g. Zhang *et al.* 2013), as shown in Figure 1.3.

1.3.1 Jet and Outflow Properties

An observed tight correlation, was initially observed over five orders of magnitude, between the bolometric luminosity and outflow force, power and mass flow rate by Cabrit & Bertout (1992). Since then, many subsequent, independent, observational studies have expanded this relationship to over six orders of magnitude (e.g. Shepherd & Churchwell 1996; Bontemps *et al.* 1996; Beuther *et al.* 2002; Duarte-Cabral *et al.* 2013; Maud *et al.* 2015b) of which Figure 1.3 shows the resultant correlation between bolometric luminosity (L_{bol} =0.1-10^6 $L_\odot$) and outflow force. Outflows observed towards MYSOs can contain momentum, mass and energy up to a few orders of magnitude larger (e.g. Beuther *et al.* 2002; Wu *et al.* 2004; Zhang *et al.* 2005) than outflows observed toward lower mass YSOs (e.g. Kim & Kurtz 2006a). This is indicative that massive stars are driven in a similar manner to low mass stars, and a single outflow mechanism would imply that all stars acquire mass by a similar disc-accretion process that scales with source luminosity. However, there are large uncertainties associated when estimating the outflow properties; these include the difficulties in identifying the inclination angle of the outflow, the optical depth correction and the dif-

ficulty in separating outflow emission from the envelope material, particularly in the typically more complex regions home to massive stars. Furthermore, the results are derived from single dish observations, which probe different physical scales in the low and high mass regimes. In the high mass regime the increased mass and luminosities involved would also undoubtedly lead to increased flow properties, likely independent of the mechanism involved (Richer *et al.* 2000). It is therefore not clear if the observed correlations are truly representative of a common driving mechanism between the two regimes, or are the result of potential observational biases.

Outflows observed towards MYSOs were initially found to be less collimated than those observed towards low mass YSOs (e.g. Wu *et al.* 2004). In contrast, both Beuther *et al.* (2004) and Zhang *et al.* (2005) identified similar degrees of collimation towards the jets/outflows driven by young MYSOs as found in jets/outflows from low mass YSOs. To account for both low and high degrees of collimation observed in massive outflows, Beuther & Shepherd (2005a) proposed a scenario in which an initially well collimated jet/outflow driven by a high mass protostellar object (HMPO), would gradually de-collimate with time, eventually forming a wide angle wind (see Figure 1.4). In the early stages, outflows driven by HMPOs/MYSOs are potentially magnetically dominated and therefore highly collimated (e.g. HH80/81, Carrasco-González *et al.* 2010). For more evolved MYSOs, a radiatively driven stellar wind naturally gives rise to a less collimated outflow (e.g. Vaidya *et al.* 2011). However, collimated outflows have also been identified towards more evolved MYSOs, thus using outflow/jet collimation as an indication of the evolutionary stage of the central driving star may not be a viable approach.

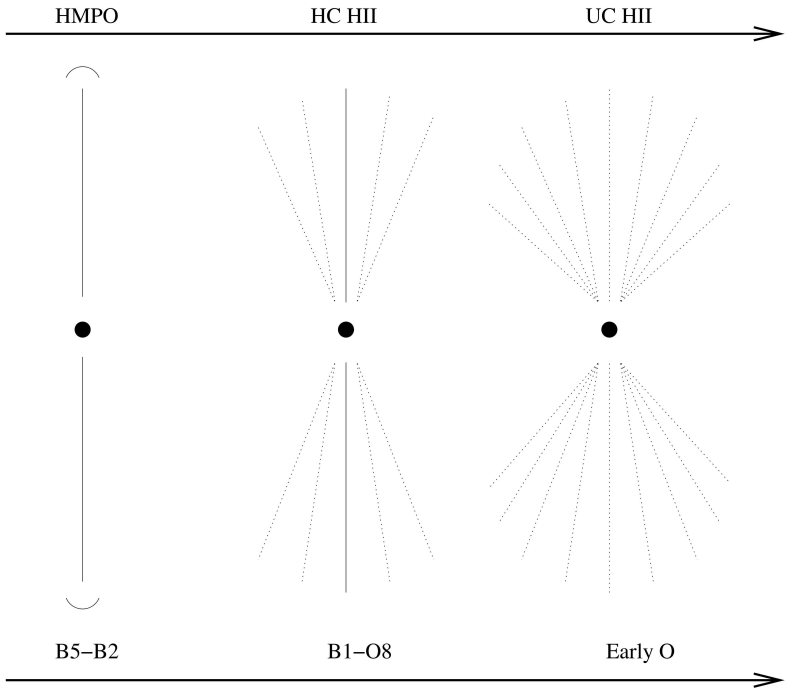

Figure 1.4: A schematic representation of the proposed outflow evolutionary sequence for massive stars. The image is taken from Figure 4 of Beuther & Shepherd (2005b). The star is seen to evolve from an initial early B-type star (e.g. a HMPO) on the left, to a late B-type star finally entering the UHCHII region phase and emerging as an early O-type star on the right. As the central star evolves, the emerging wind from the central star is suggested to produce an additional less collimated outflow component (Beuther & Shepherd 2005b).

1.3.2 Observable Tracers of Outflows

Jets and outflows are observed across a number of wavelengths regimes, from radio, sub(mm), IR, through to optical and X-ray. In the early stages, the outflow will still be heavily embedded in the natal core. Thus, the molecular transitions of H_2v=1-0 S(1) in the near-IR, and the rotational transitions of molecular species, such as CO, in the mm regimes, provide the best means to

observe the young jets and outflows. H_2 emission is a powerful tracer of shock excited gas at temperatures of few 1000 K (Scoville *et al.* 1986).

In the mm regime, CO was the first molecule observed to trace bipolar molecular outflows (Snell *et al.* 1980), and still remains the primarily used species to trace them. This molecule, owing to its easy excitation, is an effective tracer of the cool, massive reservoir of swept up ambient material. However, its easy excitation may also lead to CO emission tracing a cavity which is no longer being "actively" driven. These "fossil" or "coasting" flows may represent an older stage that is no longer being accelerated by a jet or wind. This can obscure the underlying effects, since it is possible for weak outflows to effectively be "fossil" momentum driven remnants even after the central driving engine declines (e.g. Klaassen *et al.* 2006). Moreover, CO can also readily trace the envelope and cloud. This can lead to problems distinguishing CO emission that is directly tracing outflow emission from emission tracing the ambient envelope, particularly at lower spatial resolution. Alternatively, silicon monoxide (SiO) has revealed itself as an effective tracer of jets/outflows from both low mass YSOs (e.g. Codella *et al.* 2014; Tafalla *et al.* 2010; López-Sepulcre *et al.* 2011; Gibb *et al.* 2004; Sakai *et al.* 2010) and MYSOs (e.g. Gibb *et al.* 2007; Codella *et al.* 2013; Sanchez-Monge *et al.* 2013; Leurini *et al.* 2013).

Figure 1.5 shows the different components traced by H_2v=1-0 S(1), ^{12}CO (2-1), and SiO (5-4) towards the young jet HH 211 (Hirano *et al.* 2006; Gueth & Guilloteau 1999; McCaughrean *et al.* 1994). The H_2 emission can be seen tracing the shocked emission. The low velocity CO emission is tracing a wider area compared with the higher velocity CO component, which displays more collimated emission. Whereas the SiO emission traces the jet-like narrow cavity

more obviously than the high velocity CO emission.

1.3.3 SiO as a Tracer of Outflows

Silicon (Si) is typically locked into the dust grains in the ISM, and as such the fractional abundance of SiO (relative to H_2) is low ($\sim 10^{-12}$ in dark clouds Ziurys *et al.* 1989). The passage of fast shocks (e.g. C-type shocks $\nu_s \sim 20-50\,\mathrm{kms}^{-1}$) are required to release Si into the gas phase through sputtering (Gusdorf *et al.* 2008a) and/or grain destruction resulting from grain-grain collisions inside J-shocks (Guillet *et al.* 2009). Once in the gas phase, Si undergoes oxidation with O_2 or OH resulting in the production of SiO (Schilke *et al.* 1997). Thus, the abundance of SiO is significantly enhanced along the outflow/jet axis, increasing by several orders of magnitude (e.g. López-Sepulcre *et al.* 2011; Sanchez-Monge *et al.* 2013) compared with ISM abundances. SiO emission, unlike CO, does not suffer from confusion with easily excited ambient material. Furthermore, SiO has a relatively short gas phase lifetime of $<10^4$ years under typical cloud conditions, after which it will be potentially depleted back onto dust grains (e.g. Bergin *et al.* 1998) or go on to form SiO_2 (Martin-Pintado *et al.* 1992; Mikami *et al.* 1992; Pineau des Forêts & Flower 1997). SiO is an excellent tracer of the fast shocks associated with outflows (e.g. Schilke *et al.* 1997, i.e. of an active flow near the stellar driving source), since only shocks passing through the dense surrounding gas and dust can destroy the dust grains in which the Si is otherwise locked. The presence of SiO is therefore a good indication of relatively recent or current jet activity. Previous single dish observations towards massive star forming regions have indicated a decrease in SiO luminosity and abundance

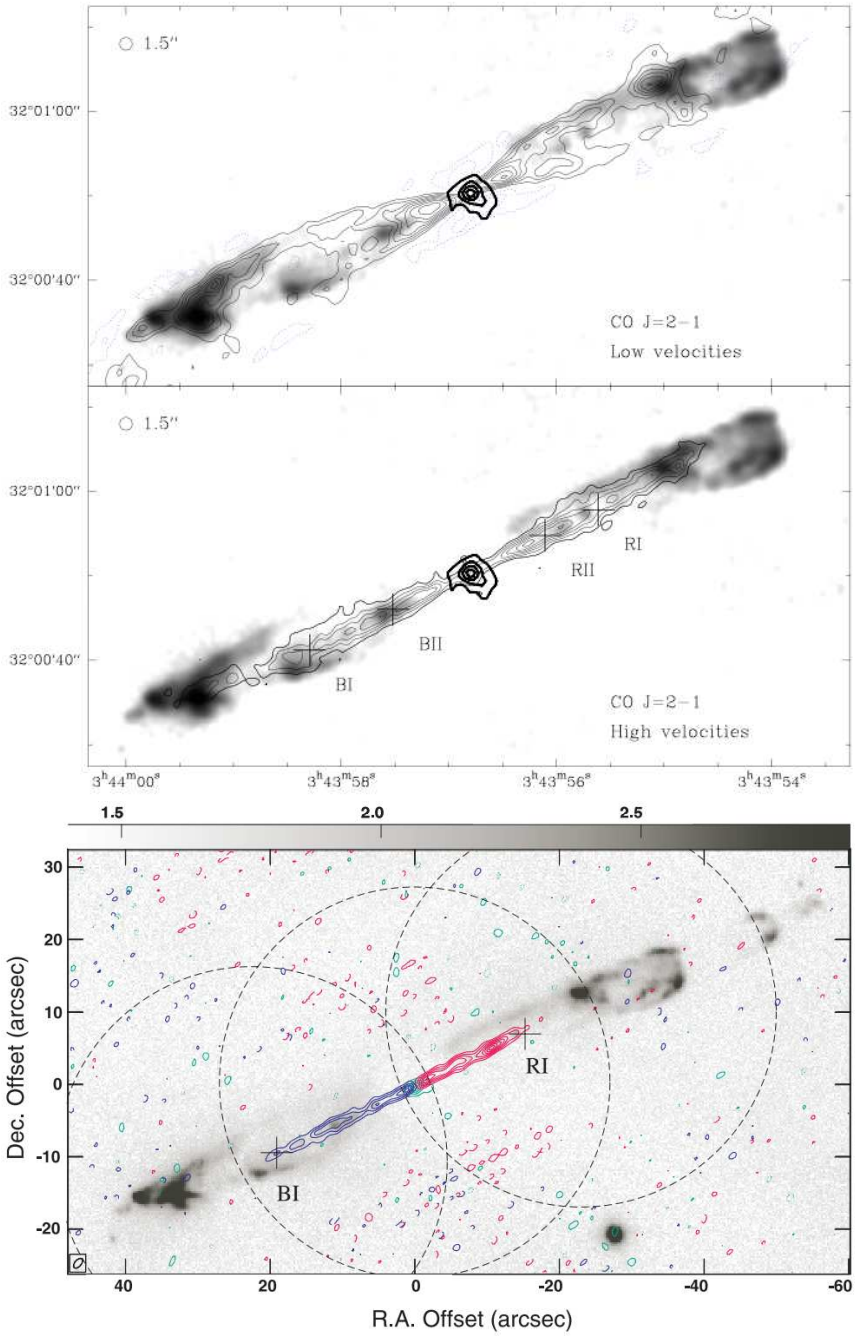

Figure 1.5: The HH 211 jet as traced by H_2, CO, and SiO emission. The first image shows both the low ($<$10 kms^{-1} with respect to the v_{LSR}), and high velocity ($>$10 kms^{-1} with respect to the v_{LSR}) ^{12}CO (2-1) emission as thin solid contours superimposed on the H_2 v=1-0 S(1) emission in greyscale. The thick black solid contours are the 1.3 mm continuum emission. The image is directly taken from Gueth & Guilloteau (1999), whilst the H_2 emission was originally presented in McCaughrean *et al.* (1994). The second image, in the lower panel, shows the red and blueshifted SiO (5-4) emission taken with the SMA ($\sim$1″ resolution, Hirano *et al.* 2006), overlaid again on the H_2 emission (greyscale).

with the age of the central driving source (e.g. López-Sepulcre *et al.* 2011; Sakai *et al.* 2010; Sanchez-Monge *et al.* 2013; Gibb *et al.* 2007). This suggests that the abundance of SiO, initially enhanced by the early protostellar jet, decreases as the central core evolves and the jet weakens. Unlike the lower energy SiO transitions (e.g. J=1-0, 2-1), which have also been observed to trace lower velocity shocks (10-20 kms^{-1}) (Schilke *et al.* 2001) and colliding flows in IRDCs (Jiménez-Serra *et al.* 2010), the higher energy SiO transitions from J=8-7, and J=5-4 are thought to be directly associated with jet/outflows in star forming regions. Recent high resolution ALMA observations of HH 212 (Codella *et al.* 2014) have shown that the SiO (8-7) traces a narrow bipolar jet launched from the protostar on scales <1000 AU.

1.3.4 Jet Formation Process

In the low mass regime jets are thought to be launched and accelerated through the interplay of the magnetic field and the accretion flow, through either disc or X-winds. While the exact formation and launching mechanisms are still debated, the magnetic field is believed to be a key component. The collimated jet is then responsible for entraining and accelerating the molecular material in the surrounding envelope, producing a molecular outflow. However, in the high mass regime, owing to their radiative outer layers and high surface temperatures, they are not expected to have strong magnetic fields. The current observations of magnetic fields towards massive stars, while still few, find strengths of a few mG (e.g. DR 21(OH): Girart *et al.* 2013). These are weak compared with the typical magnetic fields observed towards low mass young stars

($\sim$KG, e.g. Johns-Krull 2007). Thus, the production of collimated jets through magnetospheric accretion becomes problematic in the high mass regime. Several alternative mechanisms have been invoked to explain the production of outflows in the high mass regime, including radiation pressure (Kuiper *et al.* 2015), ionisation feedback and the possibility that in these highly clustered environments the contribution from several members could collectively power a perceived larger scale outflow (Peters *et al.* 2014). However, theoretical work by Hosokawa & Omukai (2009), suggest that in massive stars with a high accretion rate of $10^{-3}\mathrm{M}_{\odot}\mathrm{yr}^{-1}$, the protostellar radius would swell to $100\,\mathrm{R}_{\odot}$ or larger. The increase in radius and decrease in temperature of the system, may result in the presence of stronger magnetic fields in high mass stars, and the ability to power jets in a similar manner to the low mass case. However, as of yet it is not clear what mechanism drives outflows in the high mass regime, though it has been suggested that magnetic fields are responsible in at least one example (e.g. HH80/81, Carrasco-González *et al.* 2010).

Massive stars formed via Competitive Accretion or Core Accretion are expected to form through an accretion disc. Therefore, in both models jets and outflows will be produced during the formation process. However, if the process is a continuation of the low mass case, then the outflow properties should scale with those found in the low mass case. In comparison, if the formation occurs through a different mechanism (i.e. Competitive Accretion), then a break in the outflow properties between the two regimes is more likely.

1.4 Evolutionary Sequence in Massive Stars

In the low mass regime, the evolutionary progression from protostellar (class 0) to class I, and class II is based on differences in their respective spectral energy distributions (SEDs). However, as discussed previously, massive stars are formed in embedded, dense cores located in large, complex, clustered molecular clouds. The evolutionary stages are therefore considerably more difficult to distinguish for a massive star than in the low mass regime. The key observable features associated with each of these stages is discussed below. However, it is noted that the distinction of one evolutionary stage from another is tenuous, and the process is likely continuous with an overlap between stages. Furthermore, observations reveal cores at different evolutionary stages are present in the same parent structure, making the separation of observable features even more difficult than in the low mass regime, especially when observed at low spatial resolution.

The general evolutionary progression of a massive star is believed to follow the path from infrared dark clouds (IRDCs) to hot molecular core (HMC)/MYSO, followed by hyper-compact HII regions (HCHII region), which then grows into a ultra-compact HII region (UCHII region). Figure 1.6 provides a schematic representation of these expected evolutionary stages, with the proposed evolution progressing from left to right in the image. In the initial stages, the cold, dense core undergoes gravitational collapse, during which the gravitational energy is transferred into radiation and can heat up the envelope releasing molecules into the gas phase, and initiating the HMC/MYSO phase. Additionally, the formation of an accretion disc and a jet/outflow during gravitational collapse further

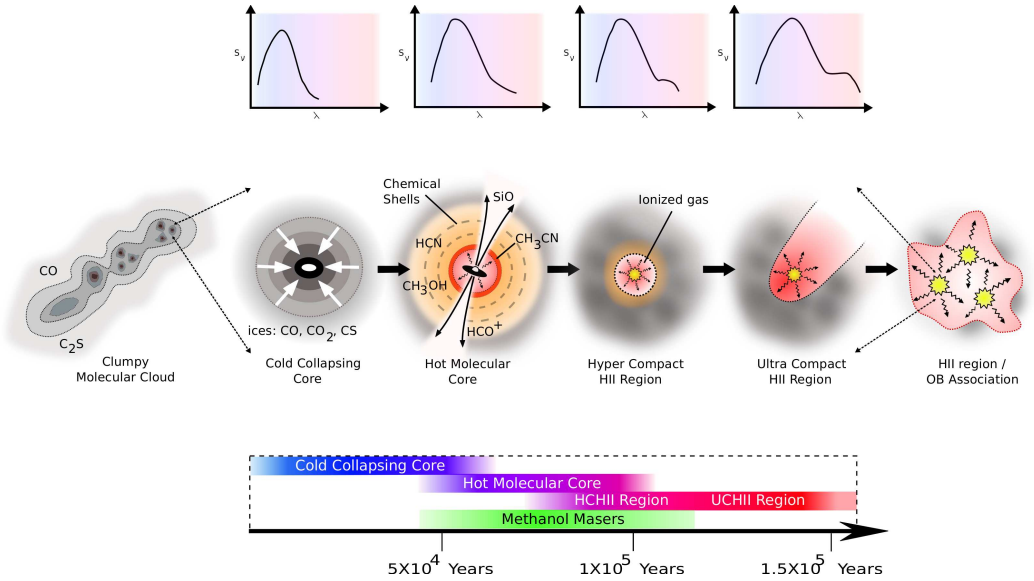

Figure 1.6: A schematic view of the early evolutionary stages in the formation of high mass star(s). It shows the proposed evolutionary sequence evolving from left to right (see text for a discussion). This image was provided courtesy of C. Purcell.

aid in heating of the surrounding environment through winds and shocks, producing further chemistry. Eventually, as the central star accretes, hydrogen burning will be initiated in the core producing surplus Lyman continuum radiation that can ionise the surrounding envelope. This will initially produce a HCHII region, which then gradually expands into the surrounding envelope forming an UCHII region, and finally an HII region.

1.4.1 Cold Clumps, Cores and IRDCs

IRDCs are believed to be the natal sites of all massive stars and stellar clusters (e.g. Rathborne *et al.* 2006; Rathborne *et al.* 2010). They are cold (10-20 K) (Pillai *et al.* 2006), dense ($>10^5\,\mathrm{cm}^{-3}$) and likely host the earliest stages of high mass star formation; the prestellar and starless core phases (e.g. Chambers

et al. 2009, Pillai *et al.* 2011, Rygl *et al.* 2010, Rathborne *et al.* 2010). As CO is more prone to depletion, they are typically traced by dense gas tracers such as N_2H^+, and NH_3 (e.g. Henshaw *et al.* 2013; Pillai *et al.* 2006). They are observed as dark structures in the mid-IR, appearing bright in the far IR and mm regimes. As seen in Figure 1.2 their filamentary nature is ubiquitous at wavelengths of 250μm. Within these clouds the presence of 70 μm emission has been used to distinguish between the protostellar and starless cores (e.g. Dunham *et al.* 2008; Dunham *et al.* 2014). Ragan *et al.* (2012) suggest from their population of massive star forming region in IRDCs that cores lacking a 70μm detection are potentially less evolved than those with a 70μm counterpart.

1.4.2 Hot Molecular Cores

Characterised by their rich molecular chemistry, HMCs are home to a multitude of complex organic molecules (COMs) (Herbst & van Dishoeck 2009). They are dense ($>10^7\,\mathrm{cm}^{-3}$), compact (diameters typically $<0.1\,\mathrm{pc}$) and warm (Kurtz *et al.* 2000) (temperatures in excess of 100 K), with average kinetic temperatures of the gas ranging from $100-250\,\mathrm{K}$ (Cesaroni *et al.* 1992). HMCs represent an intermediate stage in the early evolution of a massive star (Churchwell 2002). However, it is suggested that many classified HMCs may have already reached the UCHII phase. There is possibly an overlap period between the HMCs and UCHII's heated by the same star. As radiation from the central star begins to sufficiently heat up the surrounding envelope, molecules that were frozen out onto dust grains in the cold dense environment during collapse are released from the ice mantles on grain surfaces back into the gas phase.

HMCs are observationally very interesting as they produce a plethora of thermal and non thermal molecular line emission in the mm/submm regimes (e.g. Beuther *et al.* 2007; Beltrán *et al.* 2014). This rich chemistry is produced by the evaporation of ices from dust grains. At temperatures >90 K, species such as CH_3OH and H_2CO are evaporated from grain mantles and are present in the gas phase. Gas phase reactions of these molecules can produce more complex molecular species such as HC_3N and CH_3CN. The symmetric top nature of CH_3CN renders it a particularly useful probe of the physical conditions of the gas, providing estimates of both the temperature and the density of the gas (e.g. Araya *et al.* 2005). Furthermore, emission from CH_3CN has been associated with velocity gradients purporting to possible disc rotation in massive star forming regions (e.g. Beltrán *et al.* 2014; Cesaroni *et al.* 2014 and references therein). Detections of these complex organic species, which are rare in the cold interstellar medium, are a signpost of a HMC. However, the production of COMs in the HMC phase is likely not an instantaneous process, and is probably proceeded by a warm up phase (e.g.Viti *et al.* 2004). In addition, HMCs likely possess a time-dependent chemical differentiation, dependent on both the temperature and mass of the star (e.g. Calcutt *et al.* 2014 Choudhury *et al.* 2015 and references therein). Furthermore, HMCs are typically observed to be bright in both the IR and the mm/submm regime.

1.4.3 HCHII/UCHII/HII Regions

An UCHII region forms as the Lyman continuum from the central MYSO becomes sufficient to ionise the surrounding natal envelope. In these highly em-

bedded regions, this first manifests itself as an HCHII region (sizes <0.01 pc), expanding to form an UCHII region (sizes <0.1 pc) (e.g. Churchwell 2002) and eventually forming an HII region. These objects are extremely bright in the mid-IR, as well as being strong radio continuum emitters. Furthermore, given their hot temperatures (of the order 10^4 K) they will dissociate molecular species, becoming less chemically rich close to the central stars. Whether accretion (and therefore jets) is still occurring in UCHII regions is still debated (e.g. Cesaroni *et al.* 2015; Keto 2007).

1.5 Motivation

It is still not clear if the formation of high-mass stars can be described as a scaled-up version of low-mass star formation or if they form in some other way (e.g. Competitive Accretion). As protostellar jets and outflows are a prevalent feature of the star formation process, their study provides an important means of addressing this fundamental question. Moreover, a comprehensive understanding of how the properties of jets/outflows change with the evolution of the central massive driving source is still lacking.

As SiO emission is an effective tracer of young active outflows, its presence is an indication of current or recent jet activity. In comparison, emission from CO, while tracing an active jet, may also trace a "fossil" cavity no longer being accelerated by a jet or wind component. Therefore, a comparison of SiO and CO emission towards outflows may provide a means of distinguishing between active and fossil outflows, and could provide an indication of the age of the central driving source. Furthermore, as CH_3CN emission is associated with

HMCs, the detection or non-detection of this species towards a massive star forming region may provide a further indication of its evolutionary nature.

Through a combination of single dish and interferometric observations towards a sample of regions selected from the RMS survey, this thesis aims to explore how the properties of jets/outflows, along with the molecular environment, change depending on the age and mass of the central driving source.

1.6 Outline of Thesis

This thesis is structured as follows:

- Chapter 2 presents James Clerk Maxwell Telescope (JCMT) single dish molecular line data of the established outflow tracer, SiO (8-7), and infall tracers $H^{13}CO^+$ (4-3), and HCO^+ (4-3) towards a sample of 33 high mass star forming drawn from the RMS survey. The sample is selected to probe regions in various stages of evolution, with all sources having previous single dish ^{12}CO (3-2) observations.

- Chapter 3 presents 1.3 mm Submillimeter Array (SMA) observations at $\sim 3''$ resolution towards the intermediate/massive star forming cluster NGC 2264-C. The primary molecules targeted in this study are the known molecular jet/outflows tracer SiO (5-4) and ^{12}CO (2-1), and provide the first high resolution observations of these tracers towards this region.

- Chapter 4 presents interferometric follow-up observations performed with the SMA towards two massive star forming regions observed as part of

the JCMT SiO survey. The two regions; G192.6005 and G194.9349, were selected to probe potentially "active" and "fossil" outflows.

- Chapter 5 presents CH_3CN (J=5-4) emission observed towards a sample of 33 high mass star forming regions drawn from the RMS survey.

- Chapter 6 provides a summary of the main conclusions found in this thesis. A section on future work, following on from the work presented in this thesis is also given.

Chapter 2

Outflow and Infall Properties Towards a Sample of Massive Star Forming Regions

2.1 Introduction

There is still considerable debate regarding the formation process of massive stars. In the low mass scenario, the star is fed through an accretion disk, which is initiated from an inside out collapse. Jets, molecular outflows and infall play a key role in this formation process. Their properties are found to observably change through the early evolution, with the jet force and energy decreasing with evolution (e.g. Bontemps *et al.* 1996). Thus, observing similar outflow and infall properties towards high mass stars would indirectly imply that they acquire mass by a similar disc-accretion process that scales with source luminosity. The key evidence in favour of this was an observed correlation, over five

orders of magnitude, between the force, power and mass flow rate and bolometric luminosity of the source (e.g. Cabrit & Bertout (1992), see Section 1.3). In comparison to observations targeting low mass star forming regions, the observational evidence of the presence of infall towards massive star forming regions is still scarce. Long standing difficulties remain in the observational interpretation of the presence of infall. This is mainly due to the complexity of star forming regions. Infall occurs simultaneously with turbulence, jets/outflows and rotation, making it difficult to separate the infall signature from the additional turbulent components. Understanding how the properties and characteristics of infall, along with jets and outflows driven by high mass stars change with evolution is a major goal to understanding high mass star formation in comparison to low mass star formation. This chapter presents molecular line data, taken with the JCMT, of the established outflow tracer, SiO (8-7), and infall tracers; $H^{13}CO^+$ (4-3) and HCO^+ (4-3), towards a sample of 33 high mass star forming regions. Further details of the line parameters for each molecule are given in Table 2.1, and a brief discussion is presented below.

2.1.1 SiO Emission

The primary outflow tracer in this survey is the SiO J=8-7 transition. As previously discussed (see Section 1.3.3), the higher J transitions of SiO are effective tracers of jets/outflows towards both low and high mass star forming regions. A particularly useful aspect of using SiO to observe outflows, is that unlike the more commonly used outflow tracer CO, it does not suffer from confusion with easily excited ambient material. In particular, the higher energy

SiO (8-7) line is likely tracing emission closely related to the jet (e.g. Codella *et al.* 2014). Furthermore, given the fast shocks required to release SiO into the gas-phase, in addition to the expected lifetime of SiO in the gas-phase $<10^4$ yrs, this molecule is likely tracing recent shock activity associated with "active" jets/outflows. The detection or non-detection of SiO (8-7) emission, towards previously observed CO outflows may highlight "active" outflows compared with potentially "fossil" momentum driven remnants traced by CO only (e.g. Klaassen *et al.* 2006). In the low mass regime Gibb *et al.* (2004) found SiO, when detected, to be preferentially associated with the youngest, class 0 sources. However, observations of SiO towards high mass regions (e.g. Klaassen *et al.* 2012, Gibb *et al.* 2007, López-Sepulcre *et al.* 2011, Leurini *et al.* 2014, Sanchez-Monge *et al.* 2013) find differences in the SiO emission with source evolution. Gibb *et al.* (2007), López-Sepulcre *et al.* (2011), and Sanchez-Monge *et al.* (2013) found the properties of SiO to decrease with time consistent with the low mass scenario, whereas Klaassen *et al.* (2012) and found an opposite trend, they observed an increase of the SiO (8-7) luminosity with evolution. Thus, it is still unclear in the high mass regimes how the SiO emission in outflows evolves with time.

2.1.2 HCO^+ and $H^{13}CO^+$ Emission

Both HCO^+ and its isotopologue $H^{13}CO^+$ are good tracers of dense gas in star forming clouds due to their relatively high critical densities (see Table 2.1). The emission from the optically thick HCO^+ transition, in comparison to the optically thin isotopologue $H^{13}CO^+$, can provide information on the bulk gas

Table 2.1: Molecules observed in this survey, the transition is given in (Column 2). The rest frequencies (Column 3), energies of the upper level above the ground state (Column 4), and the Einstein-A coefficients (Column 6) are all taken from LAMBDA (http://home.strw.leidenuniv.nl/moldata/). The critical densities given in Column 5 are calculated using the Einstein-A coefficients in Column 6 and the collision rate coefficients, again obtained from LAMBDA, for a temperature of 20 K.

Species	Transition	Frequency (GHz)	E_{upper}/k (K)	N_{crit} (cm^{-3})	A_{ul} (s^{-1})
SiO	(8 - 7)	347.330	75.02	2.0×10^{7}	2.2×10^{-3}
$H^{13}CO^{+}$	(4 - 3)	346.998	41.63	8.2×10^{6}	3.3×10^{-3}
HCO^{+}	(4 - 3)	356.735	42.80	9.0×10^{6}	3.6×10^{-3}

motions in star forming clouds such as large scale infall. In the low mass case infall signatures have been well established using this molecule (e.g. Gregersen *et al.* 1997). However, in the high mass regime the presence of infall signatures is less established in these transitions (e.g. Fuller *et al.* 2005; Rygl *et al.* 2013). Additionally, previous studies (e.g. Rawlings *et al.* 2000; Rawlings *et al.* 2004) have suggested HCO^{+} is also enhanced by outflows.

2.1.3 Sample Selection

The sample consists of 33 massive star forming regions drawn from the RMS survey (Lumsden *et al.* 2013). The sources were selected to represent a reasonable range of evolutionary stages and luminosities and includes; 20 YSOs, 11 HII and 2 HII/YSO RMS classified regions. Furthermore, the sources were selected to have a distance within 4.5 kpc. In addition, all sources were part of a previous ^{12}CO (3-2) outflow survey by Maud *et al.* (2015b). The sample was chosen to explore differences between the outflow driving sources with and

without SiO emission (i.e. active and potentially fossil driven outflows). The majority of the sources, 27, have a confirmed ^{12}CO (3-2) outflow detection in Maud *et al.* (2015b). Table 2.2 presents the properties of each source taken from the RMS survey, the sources are labelled by their Galactic name (Column 1), and properties such as RMS survey classification (e.g. YSO and HII), source v_{LSR}, distance and bolometric luminosity are given. Where possible the IRAS name and/or more commonly used name(s) for each source are provided.

2.2 Observations and Data Reduction

2.2.1 JCMT Observations

SiO, $H^{13}CO^+$ and HCO^+ were observed using the Heterodyne Array Receiver program (HARP) (Buckle *et al.* 2009) at the 15 m James Clerk Maxwell Telescope (JCMT) as part of the projects M09AU18 (SiO (8-7), and $H^{13}CO^+$ (4-3)) and M10AU04 (HCO^+ (4-3)). Due to time limitations, only 25 sources were observed as part of the project M10AU04 (HCO^+ (4-3)). Project M09AU18 was observed between 12/04/2009 - 05/04/2010, and project M10AU04 between 16/04/2010 and 01/09/2010. The HARP array consists of 16 receiver elements, during both projects receiver H14 was not operational and is subsequently missing from the data. The observations were taken in position switched jiggle chop mode, creating $\sim$ 2 arcminute by 2 arcminute maps. The observations were taken with between 30-60 minutes on source, and the pointing was checked every hour on a known bright molecular source and is accurate to within $\sim 5''$. $H^{13}CO^+$ and SiO were observed simultaneously in the same fre-

quency set-up, where the Auto-Correlation Spectral Imaging System (ACSIS) was configured with an operational bandwidth of 1000 MHz×2048 channels, providing a velocity resolution of 0.42 kms^{-1}. For HCO^+ the bandwidth was set-up at 250 MHz×4096 channels giving a velocity resolution of 0.05 kms^{-1}. At the wavelength range observed ∼345 GHz the JCMT has a beam size of ∼15″. The average value of $\tau_{(225GHz)}$ given by CSO during both sets of observations was 0.07.

2.2.2 Reduction Process

Data reduction was undertaken using the packages SMURF, KAPPA, and GAIA which form part of the Starlink software[1]. The data were initially converted to spectral (RA-DEC-velocity) cubes using the SMURF command MAKECUBE. The data were gridded on to cubes with a pixel size of 7.5″ by 7.5″ using the function sincsinc. The channels at the edges of the bandwidth were also removed, and a linear baseline was subtracted. The data were converted from the antenna temperature scale T_A^* (Kutner & Ulich 1981) to main-beam brightness temperatures T_{mb} using $T_{mb} = T_A^*/\eta_{mb}$, where the main beam efficiency η_{mb} has a value of 0.61 (Buckle *et al.* 2009). To increase the signal to noise of the SiO (8-7) line the velocity resolution of this line was re-sampled to 1.68 kms^{-1} using the KAPPA command SQORST. The 1σ rms $T_{mb(rms)}$ per channel was determined excluding any noisy pixels towards the edges of the map and from line free channels; the typical values are 0.08 K, 0.04 K, and 0.6 K for $H^{13}CO^+$ (0.42 kms^{-1}), SiO (1.68 kms^{-1}) and HCO^+ (0.05 kms^{-1}) respectively. Table A.1 in Appendix A gives the rms values for individual sources. As men-

[1]http://starlink.eao.hawaii.edu/starlink

tioned in the previous section, towards 8 sources HCO^+ was not observed, these sources are noted in Table 2.3.

2.2.3 Herschel PACS 70μm data

Far-IR 70μm observations performed with the ESA Herschel space observatory (Pilbratt *et al.* 2010) using the PACS instrument (Poglitsch *et al.* 2010) were obtained from the Herschel archive. The standard product generation data was downloaded from the archive[1] with the majority of the data taken from the HOBYS (Motte *et al.* 2010) and HiGal (Molinari *et al.* 2010) surveys. Only two regions, G018.3412 and G078.1224, were not observed as part of these two surveys, and were observed under the PIs; Krauss (observation ID:1342191813) and Cesaroni (observation ID:1342211514) respectively. In total 28 of the 33 sources observed are covered by the Herschel maps.

[1]http://www.cosmos.esa.int/web/herschel/science-archive

Table 2.2: Properties of the sources observed in this JCMT survey. The sources are labelled by their Galactic name (Column 1), with the given RMS survey classification (Column 2). The RA and DEC are given in (Column 3 and Column 4) respectively. The source v_{LSR}, distance, and bolometric luminosity are presented in Column 5, Column 6, and Column 7 respectively. All properties are taken from the RMS survey. In Column 8, the IRAS name and/or more commonly used names for each source are provided where possible.

Source Name	Type	RA (J2000)	Dec (J2000)	v_{LSR} (kms^{-1})	D (kpc)	Bol Lum ($L_\odot$)	IRAS/Common Name
CO Outflow [b]							
G010.8411-02.5919	YSO	18:19:12.09	-20:47:30.9	12.3	1.9	2.4e+04	18162-2048
G012.9090-00.2607	YSO	18:14:39.56	-17:52:02.3	36.7	2.4	3.2e+04	18117-1753/ W33A
G013.6562-00.5997	YSO	18:17:24.38	-17:22:14.8	47.4	4.1	1.4e+04	18144-1723
G017.6380+00.1566	YSO	18:22:26.37	-13:30:12.0	22.1	2.2	1.0e+05	18196-1331
G018.3412+01.7681	YSO	18:17:58.11	-12:07:24.8	33.1	2.8	2.2e+04	18151-1208
G020.7617-00.0638	HII/YSO	18:29:12.36	-10:50:38.4	56.9	11.8[a]	1.3/3.6e+04	
G043.3061-00.2106	HII	19:11:16.97	+09:07:28.9	59.6	4.4	1.1e+04	19088+0902
G045.0711+00.1325	HII	19:13:22.10	+10:50:53.4	59.2	4.4[a]	2.0e+05	19110+1045
G050.2213-00.6063	YSO	19:25:57.77	+15:02:59.6	40.6	3.3	1.3e+04	19236+1456
G078.1224+03.6320	YSO	20:14:25.86	+41:13:36.3	-3.9	1.4	4.0e+03	20126+4104
G079.1272+02.2782	YSO	20:23:23.83	+41:17:39.3	-2.0	1.4	1.6e+03	20216+4107
G079.8749+01.1821	HII	20:30:27.45	+41:15:58.5	-4.3	1.4	1.1e+03	20286+4105
G081.7133+00.5589	HII	20:39:02.36	+42:21:58.7	-3.8	1.4	1.9e+03	
G081.7220+00.5699	HII	20:39:01.01	+42:22:50.2	-4.7	1.4	1.2e+04	DR21 OH
G081.7522+00.5906	YSO	20:39:01.98	+42:24:59.1	-4.0	1.4	9.0e+03	

Continued on next page

Table 2.2 – continued from previous page

Source Name	Type	RA (J2000)	Dec (J2000)	v_{LSR} (kms^{-1})	D (Kpc)	Bol Lum ($L_\odot$)	IRAS Name
G081.7624+00.5916	YSO	20:39:03.72	+42:25:29.6	-4.4	1.4	2.6e+03	
G081.8652+00.7800	YSO	20:38:35.36	+42:37:13.7	9.4	1.4	3.6e+03	
G081.8789+00.7822	HII	20:38:37.71	+42:37:58.6	8.1	1.4	1.1e+04	
G083.0936+03.2724	HII	20:31:35.44	+45:05:45.8	-3.1	1.4	1.2e+04	
G083.7071+03.2817	YSO	20:33:36.51	+45:35:44.0	-3.6	1.4	3.9e+03	
G083.7962+03.3058	HII	20:33:48.02	+45:40:54.5	-4.3	1.4	4.8e+03	
G103.8744+01.8558	YSO	22:15:09.08	+58:49:07.8	-18.3	1.6	6.8e+03	22134+5834
G109.8715+02.1156	YSO	22:56:17.98	+62:01:49.7	-11.1	0.7	1.5e+04	22543+6145/Cep A
G192.6005-00.0479	YSO	06:12:54.01	+17:59:23.1	7.4	2.0	4.5e+04	06099+1800/ S255 IR
G194.9349-01.2224	YSO	06:13:16.14	+15:22:43.3	15.9	2.0	3.0e+03	06103+1523
G203.3166+02.0564	YSO	06:41:10.15	+09:29:33.6	7.4	0.7	1.8e+03	06384+0932/NGC2264-C
G207.2654-01.8080	HII/YSO	06:34:37.74	+04:12:44.2	12.6	1.0	1.3/9.1e+03	06319+0415
No CO Outflow [b]							
G080.8645+00.4197	HII	20:36:52.16	+41:36:24.0	-3.1	1.4	9.1e+03	
G080.9383-00.1268	HII	20:39:25.91	+41:20:01.6	-2.0	1.4	3.2e+04	
G081.7131+00.5792	YSO	20:38:57.19	+42:22:40.9	-3.6	1.4	4.9e+03	
G196.4542-01.6777	YSO	06:14:37.06	+13:49:36.4	18.0	5.3	9.4e+04	06117+1350
G217.3771-00.0828	HII	06:59:15.73	-03:59:37.1	25.1	1.3	8.0e+03	06567-0355
G233.8306-00.1803	YSO	07:30:16.72	-18:35:49.1	44.6	3.3	1.3e+04	07280-1829

(a) The distance to G020.7617 has been updated to the far distance after observations were undertaken. A distance of 7.75±0.4 kpc to G045.0711 has recently been identified through measurements of parallax and proper motions by Wu *et al.* (2014). The corrected distances for both of these sources are used in the remainder of the analysis. **(b)** The CO outflow sources all have a confirmed ^{12}CO(3-2) outflow in Maud *et al.* (2015b), whereas the No CO outflow sources had no observed emission consistent with an outflow in Maud *et al.* (2015b).

2.3 Results

2.3.1 Defining and Extracting the $H^{13}CO^+$ and HCO^+ Emission

$H^{13}CO^+$ zero moment or integrated intensity maps were created using the KAPPA command COLLAPSE. The $H^{13}CO^+$ emission is integrated over the full velocity range, determined from the velocities of the lowest and highest channels in the cube containing at least 3σ emission (the individual 1σ rms noise values per channel for each source are presented in Table A.1 of Appendix A).

To define the limits of the integrated $H^{13}CO^+$ emission, and identify any potential multiple components in the emission, the integrated intensity maps were fitted using a combination of the clump finding algorithms FELLWALKER (part of the CUPID package within Starlink), and the python based structure tree finding algorithm ASTRODENDRO (Astropy Collaboration *et al.* 2013). An $H^{13}CO^+$ detection is determined, for both clump finding algorithms, from a minimum 5σ detection per pixel over a minimum of 4 contiguous pixels (equivalent to the beam area of 4.45 pixels). The rms noise per pixel in the integrated intensity maps was determined using $\Delta I = T_{mb(rms)}\,\Delta v\sqrt{N_{chan}}$, where $T_{mb(rms)}$ is the rms noise level in K per channel (see Table A.1 in Appendix A for individual sources), Δv is the velocity resolution in kms^{-1} ($0.42\ \mathrm{kms}^{-1}$ for $H^{13}CO^+$) and N_{chan} is the number of channels used to integrate the emission over. For the majority of sources, the $H^{13}CO^+$ emission identified using FELLWALKER and ASTRODENDRO was in agreement. However, for several sources, where multiple RMS sources were observed in the same field of view (e.g. G081.7131,

G081.7133, and G081.7220 were observed in a single map) and/or multiple components were present towards a single RMS source (e.g. G203.3166 displays two separated $H^{13}CO^+$ components) FELLWALKER could not separate the multiple components. In these sources, both the FELLWALKER and ASTRODENDRO fits were used to determine the $H^{13}CO^+$ masks with which to extract the spectra. Towards two regions, G081.7522 and G203.3166, two $H^{13}CO^+$ components were identified in the DENDROGRAM fit. In both sources one component is associated with the RMS source position, and the second component is found to be in an offset position ($>14.5''$ from the RMS coordinates). The offset components are discussed in more detail below. Towards three sources, G233.8306, G081.7131, and G083.9383, no $H^{13}CO^+$ emission is detected in a single pixel above 5σ. Further inspection of these three sources revealed no $H^{13}CO^+$ emission detected at the 3σ limit. For the remaining sources, a single $H^{13}CO^+$ component is detected. However for four sources, G079.8749, G081.8789, G081.8652, and G083.7071 the single $H^{13}CO^+$ component is not coincident with the RMS source position and is located in an offset position.

2.3.1.1 $H^{13}CO^+$ Offset Components

An offset component is identified if the pixel containing the peak of the $H^{13}CO^+$ integrated intensity emission -within the masked limits of the DENDROGRAM fit- is found to be offset by more than a beam size ($14.5''$) from the RMS source position. In total six $H^{13}CO^+$ offset components are identified and are discussed below.

1. Towards G079.8749, only one $H^{13}CO^+$ component is identified in either of the fits, and the peak emission is offset ($\sim 24''$) from the RMS source,

however, there is a clear enhancement in the $H^{13}CO^+$ emission towards the RMS source position. Interferometric ammonia observations by Lu *et al.* (2014) clearly show two separate molecular components in this region; one component peaking at the RMS position, and a second component peaking at the $H^{13}CO^+$ integrated intensity peak at the offset position. Thus, the single identified component in the DENDROGRAM fit is split into two components, a smaller component peaking at the RMS position, and the main component in the offset position now labelled G079.8749-OFFSET (see Figure 2.1).

2. Towards G081.7522, an additional $H^{13}CO^+$ component is identified $\sim 30''$ to the south of this source and is labelled G081.7522-OFFSET.

3. Towards G081.7624, one $H^{13}CO^+$ component is identified and is offset from the RMS position by $\sim 22''$ to the north of the RMS source position. This source is now labelled G081.7624-OFFSET.

4. The RMS sources; G081.8789, and G081.8652 were observed in the same map, and the offset $H^{13}CO^+$ component is located between the two positions, $\sim 40''$ from G081.8789, and $\sim 20''$ from G081.8652. As $H^{13}CO^+$ emission does extend over the whole region, but there appears to be no obvious extension or enhancement towards either RMS source, this $H^{13}CO^+$ component is listed as an OFFSET source from the closest RMS source G081.8652 and labelled as G081.8652-OFFSET.

5. Towards G083.7071, only one $H^{13}CO^+$ component is identified in the field and it is offset from the RMS position by $\sim 16''$. This offset source is

labelled G083.7071-OFFSET.

6. Towards G203.3166, two $H^{13}CO^+$ components are identified in the DENDROGRAM fit. One component which coincides with the RMS source and a second component offset by $\sim 37''$ to the south-east of the RMS source position. The position of this offset $H^{13}CO^+$ component, G203.3166-OFFSET, is coincident with the position of C-MM3 (see Peretto *et al.* 2007, and Chapter 3).

The $H^{13}CO^+$ spectra, for all identified $H^{13}CO^+$ components (i.e. RMS source positions and OFFSET sources), were then extracted from the summation of the pixels defined within the respective DENDROGRAM and FELLWALKER fits. The HCO^+ spectra were extracted using only pixels within the $H^{13}CO^+$ defined masks. The results of Gaussian fits to the extracted $H^{13}CO^+$ spectra can be found in Table A.2 of Appendix A. Figure 2.1 presents an example of the $H^{13}CO^+$ and HCO^+ integrated intensity maps towards a region with two $H^{13}CO^+$ components (G079.8749, and G079.8749-OFFSET), along with the $H^{13}CO^+$ and HCO^+ spectra extracted from the masked region. The $H^{13}CO^+$ and HCO^+ integrated intensity maps and spectra for the whole sample are presented in Figure A.1. As mentioned previously, towards 8 sources HCO^+ observations were not performed, thus the HCO^+ emission and respective spectra are therefore missing for these sources in this Figure.

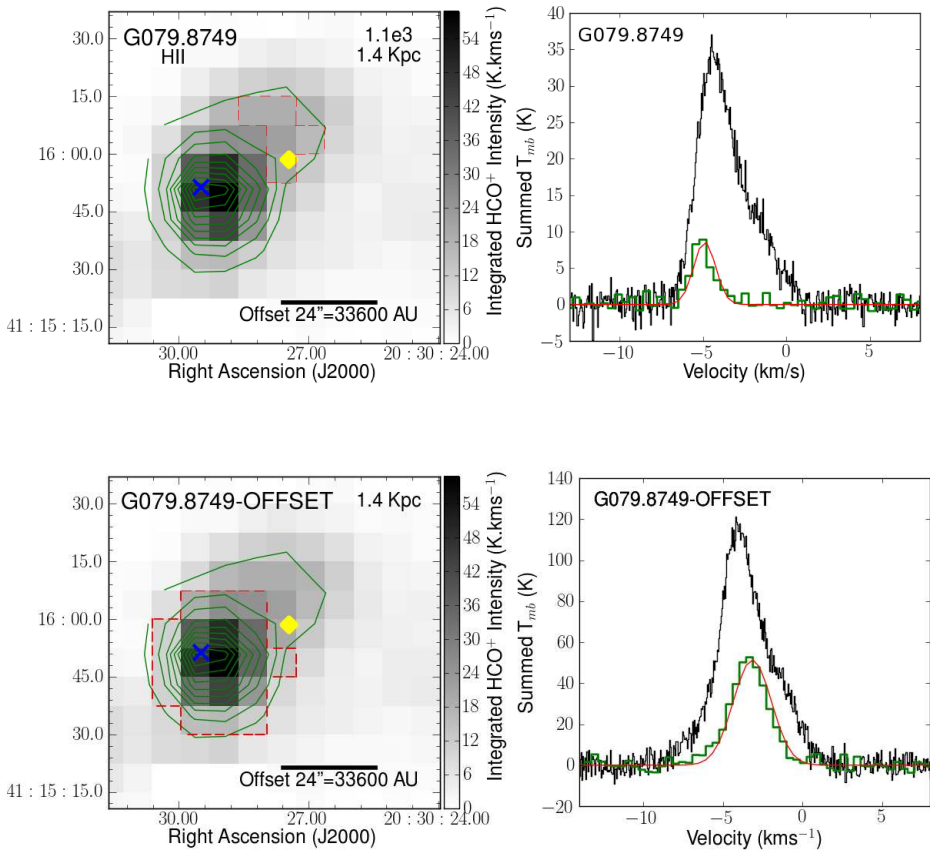

Figure 2.1: The left panels show the HCO^+ (greyscale), and $H^{13}CO^+$ (solid green contours) integrated intensity maps. The HCO^+ and $H^{13}CO^+$ integrated intensity maps are the same for both plots, and the green contours levels are given by $\sigma = 0.11\,\mathrm{K.kms^{-1}}$ ×5,10,15,20,25,30,35,40,45,50. The yellow diamond and blue cross mark the positions of the RMS source and the peak of the $H^{13}CO^+$ emission in the offset component respectively. The red dashed contours define the boundary of the $H^{13}CO^+$ mask used for each source. The scale bar gives the offset in arcseconds, and the equivalent distance in AU between the peak of the $H^{13}CO^+$ emission in the offset position and the RMS source position ($\sim 24''$), assuming a distance to the region of 1.4 kpc. The right panels, show the $H^{13}CO^+$ (green contours) and HCO^+ (black contours) spectra extracted from the pixels within the respective masked region. The $H^{13}CO^+$ emission has been multiplied by a factor of 4. The red solid line displays the Gaussian fit increased by a factor of 4 (see Table A.2 for the Gaussian fit parameters).

Table 2.3: Summary of the molecular line detections towards the sources surveyed, along with correspondence of asymmetry profiles in the $H^{13}CO^+$ and HCO^+ emission, and Herschel detections towards the observed sources. Column 1, gives the Galactic name, sources where a $H^{13}CO^+$ component was detected more than 14.5″ offset from the RMS source position are labelled Galactic name-OFFSET. Column 2 gives the RMS classification of the source. Columns 3, 4, and 5 give the corresponding detection (Y), non-detection (N) or were not observed (–) of SiO, $H^{13}CO^+$ and HCO^+ respectively. Column 6 is the asymmetry between the $H^{13}CO^+$ and HCO^+ emission, as described in Section 2.3.7, where N represents no asymmetry, and R, B is red and blue identified asymmetry respectively. Column 7 is the detection (Y), and non-detection (N) of Herschel 70μm emission, for sources not covered by Herschel they are noted by (–).

Source Name	RMS Type	SiO (8-7)	$H^{13}CO^+$ (4-3)	HCO^+ (4-3)	Asymmetry	Herschel 70μm data
CO Outflow						
G010.8411	YSO	N	Y	Y	N	–
G012.9090	YSO	Y	Y	Y	N	Y
G013.6562	YSO	Y	Y	Y	R	Y
G017.6380	YSO	N	Y	Y	N	Y
G018.3412	YSO	Y	Y	Y	N	Y
G020.7617	HII/YSO	N	Y	Y	N	Y
G043.3061	HII	Y	Y	Y	B	Y
G045.0711	HII	Y	Y	Y	N	Y
G050.2213	YSO	Y	Y	Y	N	Y
G078.1224	YSO	Y	Y	Y	N	Y
G079.1272	YSO	Y	Y	Y	N	Y
G079.8749	HII	N	Y	Y	R	Y
G079.8749-OFFSET	HII	N	Y	Y	N	Y
G081.7133	HII	Y	Y	–	–	Y
G081.7220	HII	Y	Y	Y	B	Y
G081.7522	YSO	Y	Y	–	–	Y
G081.7522-OFFSET	YSO	N	Y	–	–	Y
G081.7624	YSO	N	N	–	–	Y
G081.7624-OFFSET	YSO	Y	Y	–	–	Y
G081.8652*	YSO	N	N	Y	–	N
G081.8652-OFFSET*	YSO	Y	Y	Y	R	Y

Continued on next page

Table 2.3 – continued from previous page

Source Name	RMS Type	SiO (8-7)	$H^{13}CO^+$	HCO^+	Asymmetry	Herschel 70μm data
G081.8789*	HII	N	N	Y	–	N†
G083.0936	HII	N	Y	Y	N	–
G083.7071	YSO	N	N	Y	N	–
G083.7071-OFFSET	YSO	N	Y	Y	N	–
G083.7962	HII	N	Y	Y	R	–
G103.8744	YSO	N	Y	Y	N	Y
G109.8715	YSO	Y	Y	Y	N	Y
G192.6005	YSO	Y	Y	Y	N	Y
G194.9349	YSO	N	Y	Y	N	Y
G203.3166	YSO	Y	Y	Y	R	Y
G203.3166-OFFSET	YSO	Y	Y	Y	B	N
G207.2654	HII/YSO	Y	Y	Y	N	Y
No CO Outflow						
G080.8645	HII	N	Y	–	–	Y
G080.9383	HII	N	N	–	–	Y
G081.7131	YSO	N	N	–	–	Y
G196.4542	YSO	N	Y	Y	N	–
G217.3771	HII	N	Y	–	–	Y
G233.8306	YSO	N	N	–	–	Y

(*) These three sources are all spatially located within ∼1 arcminute. The $H^{13}CO^+$ emission peaks between the two RMS sources, $\sim 40''$ from G081.8789, and $\sim 20''$ from G081.8652. While $H^{13}CO^+$ emission does extend over the whole region, there appears to be no obvious extension or enhancement towards either RMS source, therefore this $H^{13}CO^+$ component is listed as an OFFSET source from the closest RMS source G081.8652 (i.e. as G081.8652-OFFSET).(†) There is a slight enhancement in the Herschel emission towards this source, however the DENDROGRAM fit cannot separate the emission from the dominant 70μm component in the field.

2.3.2 SiO Detection

SiO integrated intensity maps were created for each source using three velocity ranges; the CO velocity intervals determined in Maud *et al.* (2015b), along with velocity ranges of 10 kms^{-1}, and 20 kms^{-1}. An SiO detection, in any of the three velocity ranges, is based on a minimum 3σ detection in at least one pixel within the respective $\mathrm{H}^{13}\mathrm{CO}^{+}$ integrated intensity mask. In total SiO is detected towards 15 of the 33 RMS sources observed (i.e. $\sim$45% see Table 2.3 for reference to individual sources). Only one SiO detected source, G081.7522, was not detected above 3σ in all three velocity ranges, as it is not detected in the CO velocity range. However, the CO velocity range for this source is the largest of the sample at $\sim$72 kms^{-1}, therefore the estimated 1σ limits are higher in this velocity range and the emission falls under the threshold. SiO was detected towards three of the six defined OFFSET sources, G203.3166-OFFSET, G081.7624-OFFSET, and G081.8652-OFFSET. For those sources with an SiO detection, the channel maps were further inspected and an additional integrated intensity map was created using the velocity of the upper and lower channels with emission above 3σ. However, for a number of the weaker SiO sources it is difficult to estimate a velocity range from the channel maps. Where the SiO velocity range could be estimated, the total integrated intensity was within 8% of the total integrated intensity estimated using the CO velocity limits. When possible the SiO velocity limits are used to estimate the integrated intensity, otherwise the SiO integrated intensity is estimated using the CO velocity limits. In addition, the total integrated SiO intensity is extracted using only pixels that have at least a 3σ detection and are within

Table 2.4: Outflow and Infall Detections

Source Type	Total Observed	SiO 3σ Detection	Total HCO^+ Observed	Blue Asymmetry Profile	Of those with HCO^+ Infall and Outflow
YSO	20	10	16	0	–
HII	11	4	7	2	2
HII/YSO	2	1	2	0	–
Offset	6	3	4	1	1

the respective $H^{13}CO^+$ mask. The SiO luminosity (in units of $K.\,kms^{-1}\,kpc^2$) is then calculated using, $L_{SiO} = \int T_{mb(SiO)}dv \times 4\pi d^2$, where $T_{mb(SiO)}dv$ is the SiO integrated intensity, and d is the distance to the respective source. The 3σ upper limits are estimated for sources without an SiO detected, from the rms in a single pixel of the integrated intensity maps (using a velocity range of $20\,kms^{-1}$ centred on the v_{LSR} estimated from the $H^{13}CO^+$ Gaussian fit).

Approximately half of the observed RMS sources (15) have an SiO detection. Of these, none are part of the sample of six sources without an associated CO outflow in Maud *et al.* (2015b) (see Table 2.3). If only sources with a previously confirmed CO outflow are considered, then SiO is detected towards ∼56% of the RMS sources. Table 2.4, presents a summary of the detection of SiO towards the four classifications; YSO, HII, HII/YSO and OFFSET. SiO is detected towards 50%, 36%, 50% and 50% of the YSO, HII, and HII/YSO samples respectively. When considering only previously confirmed CO outflow sources, SiO is now detected towards 59% (10 of 17), 50% (4 of 8), 50% (1 of 2), and 50% (3 of 6) YSO, HII, HII/YSO and OFFSET sources respectively.

2.3.3 Distance or Sensitivity Limited Sample

It is possible that the lack of detected SiO emission towards ∼50% of the sample may be due to either sensitivity and/or distance limitations. In Figure 2.2, the average $H^{13}CO^+$ (4-3) main beam brightness temperatures are compared to the average $C^{18}O$ (3-2) main beam temperatures from Maud *et al.* (2015a). The five weakest $C^{18}O$ (3-2) sources are also SiO non-detections. Furthermore, of these five weakest $C^{18}O$ (3-2) sources, two are also $H^{13}CO^+$ non-detections (shown as upper limits in Figure 2.2). Moreover, of the eight weakest $H^{13}CO^+$ sources (those with brightness temperatures $\leq$0.4 K) only one source has an SiO detection. Therefore, for the weakest $H^{13}CO^+$ sources, a corresponding non-detection of SiO may be due to sensitivity. However, approximately half of the SiO non-detections show no obvious reason for sensitivity limits to be a factor in the lack of an SiO detection. Thus, for at least half of the SiO non-detected sources there appears to be no link to the sensitivity for their resulting non-detection.

In addition to the sensitivity limitations, the distance to sources without an SiO detection may be responsible for a non-detection. As the SiO emission is likely tracing the jet close to the central source, it is possible that more distant sources may be more affected by beam dilution within the 14.5″ JCMT beam. In Figure 2.3 the average SiO integrated intensity per pixel is plotted as a function of distance. For sources without an SiO detection the 3σ upper limits are presented. For sources within the original distance limits of the survey ($\leq$4.5 kpc) there appears to be no tendency for those sources without an SiO detection to be further away. Since the observations were undertaken, two sources; G020.7617, and G045.0711, have had their distances corrected. G020.7621 to the far dis-

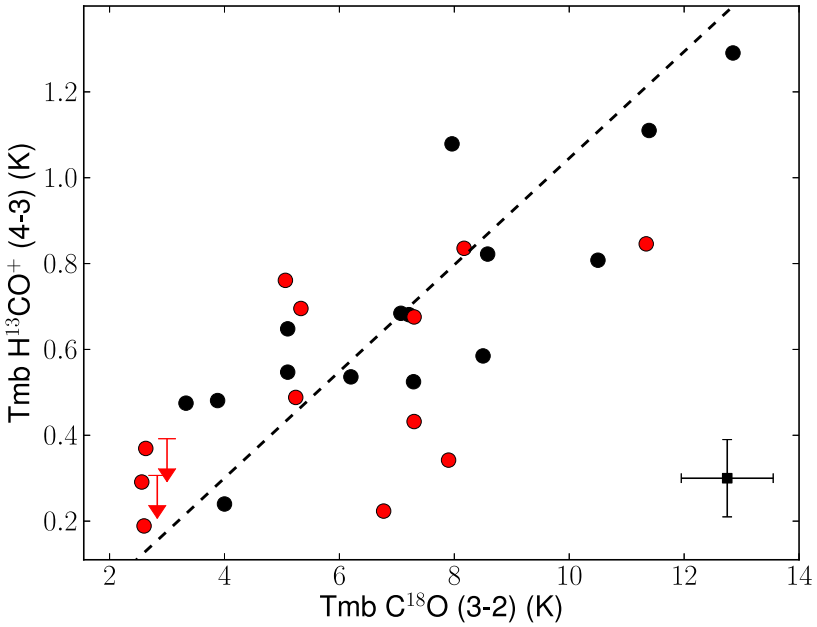

Figure 2.2: The main beam brightness temperature of $H^{13}CO^+$ (4-3) plotted against the main beam brightness temperature of $C^{18}O$ (3-2) from Maud *et al.* (2015a). The black, and red circles represent the SiO detected and non-detected sources respectively. The red arrows represent 3σ upper limits for sources with no detected $H^{13}CO^+$ or SiO emission. The typical errors are shown in the bottom right, and represent the average $1\,\sigma$ rms noise per channel, 0.09 K for the $H^{13}CO^+$ (4-3) for a velocity resolution of 0.42 kms^{-1}, and 0.8 K for a velocity resolution of 0.4 kms^{-1} taken from Maud *et al.* (2015a). The black dashed line displays the result of a linear regression fit to the data.

tance of 11.8 kpc, and G045.0711 to a distance of 7.75±0.4 kpc obtained from parallax and proper motion measurements (Wu *et al.* 2014). G045.0711 has an SiO detection, whereas G020.7617 does not. G020.7617 is also one of the five weakest $C^{18}O$ (3-2) sources, and one of the weakest $H^{13}CO^+$ sources shown in Figure 2.2. Thus, the distance of this object may be the cause of its non-detection. For the remainder of the analysis G020.7617 will be omitted from the analysis. The average distance, excluding G020.7617 and G045.0511, is

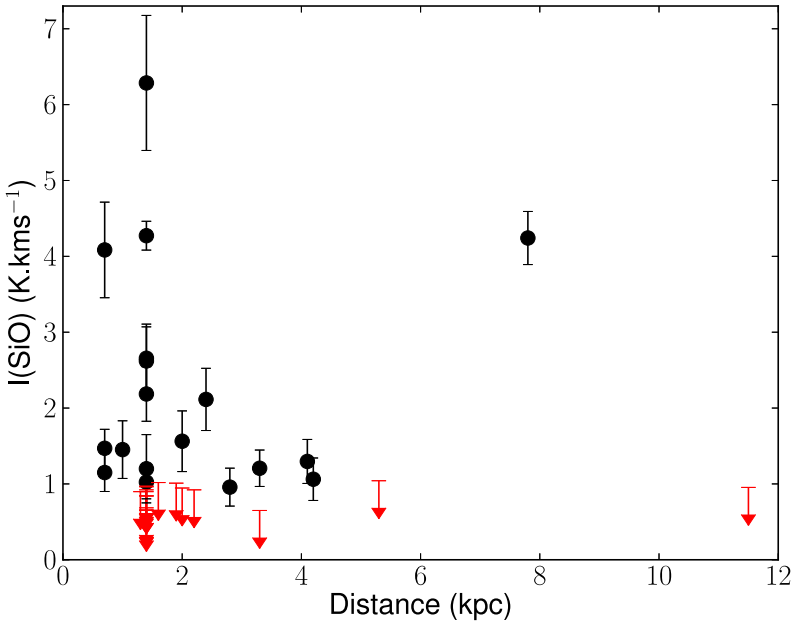

Figure 2.3: Distance vs the average SiO integrated intensity. The SiO detections are given by a black circles, the 3σ upper limits of the non-detected sources are shown in red.

1.9±1.1 kpc for sources with and without an SiO detection. Moreover, a KS test gives a likelihood of 0.7 that the distances of the SiO detected and non-detected sources are drawn from the same population. While a small number of SiO non-detections may be due to sensitivity limits, there appears to be no obvious distance effects in the non-detection of SiO, with the exception of G020.7617. Thus, the source distance or sensitivity of the observations does not appear to be responsible for the lack of an SiO detection in at least half of the SiO non-detections.

2.3.4 Column Density, Abundance and Mass Estimates

If the detection or non-detection of SiO is not limited by the observations for the majority of sources, then are there measurable differences between the two samples. As discussed previously, the $H^{13}CO^+$ and HCO^+ emission can provide information on the large scale kinematics, and physical properties of the regions. The excitation temperature is calculated assuming the HCO^+ (4-3) line emission is optically thick following,

$$T_{ex} = \frac{h\nu_u}{k}[ln(1 + \frac{(h\nu + u/k)}{T_{HCO^+} + J_\nu(T_{bg})})]^{-1} \tag{2.1}$$

where T_{HCO^+} is the peak beam corrected brightness temperature, and T_{bg} is the background temperature assumed to be 2.73 K. Using this excitation temperature, the optical depth of the $H^{13}CO^+$ line can be estimated from,

$$\tau_{H^{13}CO^+} = -ln[1 - \frac{T_{H^{13}CO^+}}{T_{ex} - J_\nu(T_{bg})}] \tag{2.2}$$

where $T_{H^{13}CO^+}$ is the beam corrected brightness temperature of the $H^{13}CO^+$ line emission taken from the respective Gaussian fits (see Table A.2 of Appendix A). For $H^{13}CO^+$ the line emission is generally well represented by a single Gaussian fit and the emission is found to be optically thin τ <0.08. However, the HCO^+ emission displays a double peaked profile (in many cases) or contains a line wing and is not represented well by a single Gaussian fit. The average excitation temperature using the peak of the HCO^+ emission is found to be ∼12 K. Given the upper energy of the HCO^+ (4-3) transition is 44 K, the derived excitation temperatures are likely underestimated. To obtain a more

accurate estimate of the excitation temperature, the method presented in Purcell *et al.* (2006) was employed. This involves masking the self absorption dip and the line wings in the HCO^+ line profile, and fitting a Gaussian considering only the sides of the emission profile. The absorption dip was masked considering the FWHM of the $H^{13}CO^+$ line profiles. The excitation temperatures were then re-calculated using the corrected brightness temperatures from the updated HCO^+ Gaussian fits, and an average value of $\sim$19 K is now found (see Table 2.5 for the excitation temperatures of individual sources). For the 8 sources without HCO^+ observations, the average excitation temperature of 19 K is used. Assuming these excitation temperatures and that the $H^{13}CO^+$ emission is optically thin the column density is estimated using,

$$N_{H^{13}CO^+} = \frac{8\pi\kappa\nu^2}{hc^3}\frac{1}{g_u A_{ul}} Q(T_{ex}) e^{\frac{E_u}{k,T_{ex}}} \int T_{mb} dv \tag{2.3}$$

where $\int T_{mb} dv$ is the beam averaged integrated intensity of the $H^{13}CO^+$ emission, and $N_{H^{13}CO^+}$ is then the beam averaged column density. $Q(T_{ex})$ is the partition function, and is estimated for linear rotator using $Q(T_{ex})=(kT_{ex})/(hB)$, where B is the rotational constant. HCO^+ column densities are also estimated assuming an abundance ratio between $H^{13}CO^+$ and HCO^+ to be 65 (Rygl *et al.* 2013). The gas mass can then be estimated from the derived HCO^+ column densities following,

$$M_{HCO^+} = (D)^2 \mu\, A\, M_H N_{HCO^+} X^{-1}_{HCO^+} \tag{2.4}$$

where A is the total area of the emitting region, D is the distance to a given source, X_{HCO^+} is the abundance of HCO^+ with respect to H_2, and M_H is the mass of hydrogen and μ is taken to be 2.35. The abundance of HCO^+ is typically

assumed to be in the range 1×10^{-9}-1×10^{-10}. However, the HCO^+ abundance can be estimated for individual sources from the HCO^+ column density if the N_{H_2} column density is known, where,

$$X_{HCO^+} = \frac{N_{HCO^+}}{N_{H_2}}. \tag{2.5}$$

Using SCUBA 850μm flux densities extracted from Di Francesco *et al.* (2008), the N_{H_2} column densities are calculated following,

$$N_{H_2} = \frac{R_{gd} S_\nu}{B_\nu(T_{dust})\kappa_\nu m_{H_2}\Omega} \tag{2.6}$$

where B_ν is the Plank function for a given dust temperature (T_{dust}), S_ν is the peak flux at 850μm taken from the SCUBA data (Di Francesco *et al.* 2008), and κ_ν is the dust mass absorption coefficient taken to be $1.4\,cm^2g^{-1}$ at 850μm and R_{gd} is the gas to dust ratio and is assumed to be 100. The solid angle, Ω, is estimated from the area subtended by a single SCUBA beam. The dust temperature is taken from the excitation temperatures estimated from the HCO^+ emission. For sources that were not observed in the HCO^+ observations, an average excitation temperature of 19 K is used. The position of the SCUBA sources was checked to ensure that the peak fluxes were attributed to the given source. Given the SCUBA beam size at 850μm is equivalent to the beam size obtained in these observations, the values were extracted with no re-sampling. The HCO^+ abundances were then estimated using Equation 2.6. The derived abundances are in the range 1.8×10^{-9} to 4.8×10^{-10} with average and median values of $1.3\pm2\times10^{-9}$, 7.2×10^{-10}, respectively for the whole sample. This is in agreement with previous HCO^+ abundance in massive star forming regions.

The average HCO^+ abundance is 1.7×10^{-9} for sources with an SiO detection and 9.8×10^{-10} for sources without an SiO detection. The HCO^+ column densities and HCO^+ abundance estimates are presented in Table 2.5. The HCO^+ mass is estimated using the derived abundances where possible, for sources not covered in Di Francesco *et al.* (2008) the median HCO^+ abundance of 7.2×10^{-10} is used for the mass estimate. The mass estimates are presented in Table 2.5. The deconvolved radius for each source is also given in this table, it is estimated using the total number of pixels in the $H^{13}CO^+$ masks assuming a circular aperture. From the radius and mass estimates, the density is calculated (see Column 10 of Table 2.5), with the average density in the sample estimated to be $\sim2\times10^6\,cm^{-3}$.

Table 2.5: Physical properties estimated for the sources. Where (-) is given an estimate of this parameter was not possible. The 3σ upper limts are given by <.

Source Name	T_{ex} (K)	$N_{H^{13}CO^+}$ (cm^{-2}) ($\times10^{12}$)	N_{HCO^+} (cm^{-2}) ($\times10^{14}$)	N_{SiO} (cm^{-2}) ($\times10^{13}$)	N_{H_2} (cm^{-2}) ($\times10^{24}$)	A_{HCO^+} ($\times10^{-10}$)	A_{SiO} ($\times10^{-9}$)	Mass $M_\odot$	n_{H_2} (cm^{-3}) ($\times10^{6}$)	D_{Radius} (pc)
CO Outflow										
G010.8411	17.7	4.9±0.5	3.2±0.3	<0.6	1.5	2.2±0.2	<10.3	501±46	0.66	0.15
G012.9090	11.9	13.1±1.2	8.6±0.8	1.5±0.3	4.0	2.1±0.2	5.2±1.0	4878±457	0.81	0.29
G013.6562	19.5	4.5±0.5	2.9±0.4	0.9±0.2	0.5	6.1±0.7	2.0±0.5	176±20	1.12	0.09
G017.6380	14.2	8.8±0.5	5.7±0.4	<0.6	1.4	4.2±0.3	<5.0	1209±35	0.33	0.25
G018.3412	14.9	6.4±0.5	4.2±0.3	0.7±0.2	1.2	3.4±0.2	4.5±1.1	1137±81	0.32	0.24
G043.3061	7.5	41.8±14.5	27.2±9.4	0.8±0.2	4.5	6.1±2.0	–	2626±911	3.16	0.16
G045.0711	9.8	43.4±6.7	28.2±4.4	3.0±0.3	1.9	14.9±2.3	6.1±0.5	8291±1284	0.26	0.51
G050.2213	11.0	6.2±1.8	4.0±1.2	0.9±0.2	1.1	3.8±1.0	11.3±3.0	259±74	3.14	0.07
G078.1224	15.0	8.9±0.6	5.8±0.4	1.9±0.3	1.5	3.9±0.3	30.0±5.1	354±23	0.74	0.13
G079.1272	21.5	2.7±0.4	1.7±0.3	0.8±0.1	0.2	7.7±1.1	24.4±4.6	12.3±1.8	0.73	0.04
G079.8749	17.5	2.3±0.5	1.5±0.3	<0.5	–	–	<8.4	23±5	1.36	0.04
G079.8749-OFF	14.0	9.5±0.8	6.2±0.5	<0.5	–	–	–	363±30	0.99	0.12
G081.7133	–	27.2±7.2	17.7±4.7	1.5±0.3	2.8	2.0±0.2	8.4±1.3	237±24	3.64	0.06
G081.7220	–	11.9±0.5	7.7±0.3	4.4±0.6	3.4	2.3±0.1	80.0±13.3	1980±74	0.97	0.20
G081.7522	–	5.1±0.3	3.3±0.2	0.9±0.3	1.5	3.3±0.2	4.9±1.2	256±18	0.49	0.13
G081.7522-OFF	–	5.6±0.3	3.6±0.2	<0.6	1.0	3.7±0.4	–	223±24	0.55	0.12

Continued on next page

Table 2.5 – continued from previous page

Source Name	T_{ex} (K)	$N_{H^{13}CO^+}$ (cm^{-2}) ($\times10^{12}$)	N_{HCO^+} (cm^{-2}) ($\times10^{14}$)	N_{SiO} (cm^{-2}) ($\times10^{13}$)	N_{H_2} (cm^{-2}) ($\times10^{24}$)	A_{HCO^+} ($\times10^{-10}$)	A_{SiO} ($\times10^{-9}$)	Mass $M_\odot$	n_{H_2} (cm^{-3}) ($\times10^6$)	D_{Radius} pc
G081.7624-OFF	–	3.5±0.5	2.3±0.3	1.8±0.3	1.24	1.9±0.3	16.0±2.8	258±35	0.70	0.12
G081.8652-OFF	24.0	14.4±0.3	9.4±0.2	3.0±0.1	3.8	2.4±0.1	11.4±0.5	2329±40	1.05	0.21
G083.0936	11.8	3.8±1.2	2.5±0.9	<0.4	–	–	<5.3	31±12	4.89	0.03
G083.7071-OFF	23.6	1.7±0.4	1.1±0.3	<0.6	–	–	–	13.8±4	2.19	0.03
G083.7962	16.0	4.5±0.9	2.9±0.6	<0.6	–	–	<41	36.5±7.4	5.79	0.03
G103.8744	32.2	2.6±0.8	1.7±0.3	<0.7	0.2	8.3±1.8	<5.2	14.5±3	0.58	0.05
G109.8715	23.4	12.9±0.4	8.4±0.3	2.9±0.4	2.7	3.0±0.1	7.8±1.2	525±16	1.31	0.12
G192.6005	24.4	8.5±0.5	5.6±0.3	1.1±0.3	0.9	6.2±0.4	14.5±3.7	99±6	1.99	0.06
G194.9349	11.5	5.9±2	3.8±1.3	<0.6	–	–	<13.1	96±33	5.27	0.04
G203.3166	21.1	4.32±0.2	2.8±0.2	0.8±0.2	1.0	2.8±0.1	88±19	136±7	0.59	0.10
G203.3166-OFF	15.1	6.2±0.5	4.0±0.3	1.0±0.2	1.7	2.4±0.2	–	126±10	1.41	0.07
G207.2654	12.0	9.1±1.3	5.9±0.9	1.0±0.3	1.4	4.1±0.6	23.7±6.0	96±14	1.68	0.06
No CO Outflow										
G080.8645	–	3.6±0.3	2.3±0.2		2.4	1.0±0.1		327±28	14.75	0.03
G080.9383	–	<1.1	<0.7	–	–	–	–	<4	–	–
G081.7131	–	<1.2	<0.8	–	–	–	–	<3	–	–
G196.4542	19.8	2.1±0.5	1.4±0.3		1.1	1.2±0.3	–	794±190	2.33	0.11
G217.3771	–	1.3±0.4	0.8±0.3	–	1.0	0.9±0.3	–	42±15	2.11	0.03
G233.8306	–	<1.2	<0.9	–	–	–	–	<18	–	0.07

2.3.4.1 HCO^+ (4-3) and $C^{18}O$ (3-2) Mass Comparison

The mass estimates derived from the HCO^+ emission are compared to the $C^{18}O$ (3-2) estimated masses presented in Maud *et al.* (2015a) and are shown in Figure 2.4. More than half of the masses estimated from the HCO^+ emission appear underestimated compared with the $C^{18}O$ (3-2) mass estimates. Only sources with an SiO detection are found to have mass estimates higher than the $C^{18}O$ (3-2) masses. However, given the higher critical density of HCO^+ compared with CO, it is likely that the HCO^+ emission arises from denser material than the CO emission. Moreover, comparison of the areas used to estimate the masses, reveals that for the SiO detected and non-detected samples the areas of the $C^{18}O$ (3-2) emission are $\sim$4, and 16 times larger respectively than those used in the HCO^+ mass estimate.

2.3.5 Far-IR Herschel 70μm Emission

Far-IR 70μm emission has been suggested as an indicator of possible evolution (e.g. Dunham *et al.* 2014). With this in mind, 70μm emission from PACS was extracted from the Herschel archive. The maps were cropped to the same size as the JCMT maps and the number of components and corresponding flux is determined from dendrogram fits again using the python package ASTRODENDRO. Herschel maps covering 27 of the 33 RMS sources were obtained from the archive. To determine the dendrogram fits, the minimum amount of contiguous pixels was set to the beam size of the map. In parallel scanning mode, which makes up the majority of the observations, the 70μm Herschel HPBW is $5.86'' \times 12.16''$. The minimum detection was set at 5σ. The identified

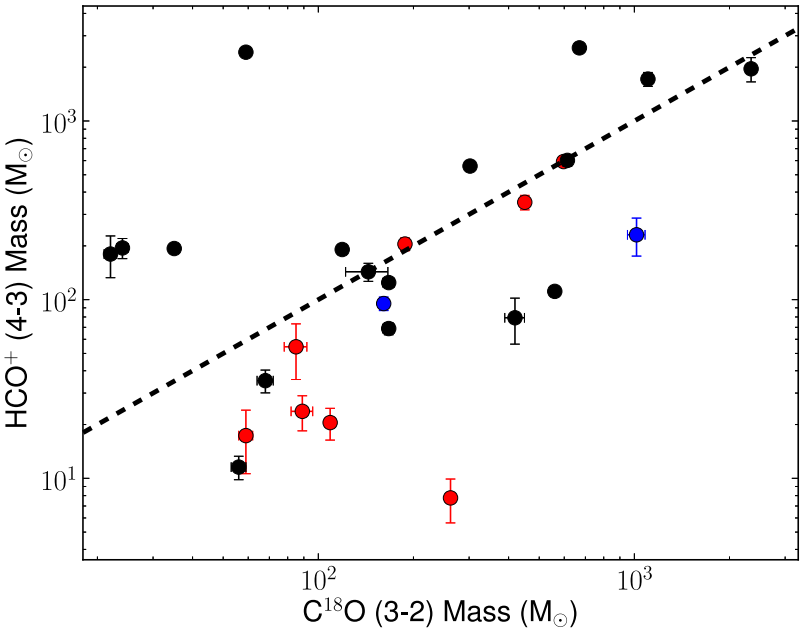

Figure 2.4: Comparison of the HCO^+ mass estimates with the $C^{18}O$ (3-2) mass estimates from Maud *et al.* (2015a). The HCO^+ masses are estimated considering the T_{ex} temperatures derived from the corrected HCO^+ Gaussian fits with the abundances derived from the HCO^+ and 850μm column densities. The black, red and blue circles represent SiO detected, SiO non-detected, and sources with neither SiO or CO detections respectively. The black dashed line is for a 1:1 ratio.

Herschel 70μm components were assigned with an $H^{13}CO^+$ component if the peak of the 70μm emission was within 10″ of the peak $H^{13}CO^+$ emission. The association of a Herschel 70μm component with a $H^{13}CO^+$ component is given in Table 2.3. Of the 27 RMS sources with available Herschel 70μm data, 25 have an associated Herschel peak within 10″ of the peak $H^{13}CO^+$ emission. Furthermore, all of the OFFSET sources have an associated 70μm component. The sum of the 70μm flux within the dendrogram limits is then converted to a luminosity through $L_{70_{\mu m}} = 4\pi d^2 . F_{70_{\mu m}}$, using a 10$\mu$m bandwidth in the Herschel

70μm PACS filter.

2.3.6 Properties of the SiO Detected and Non-Detected Sources

SiO is detected towards just under half of the sources. In more than half of the non-detected sources, the lack of an SiO detection does not appear to be due to sensitivity limitations or distance. Thus, are there differences in the properties of the sources with and without an SiO detection? Table 2.6 presents the average and median properties estimated for sources with and without an SiO detection, along with the results of KS-tests performed between the two samples to determine the likelihood that the values are from the same underlying population. As mentioned previously, there is no significant difference in the distances to the SiO detected and non-detected samples. Furthermore, the detection or non-detection of SiO does not appear dependent on the bolometric luminosity of the source.

The $H^{13}CO^+$ FWHM values for the SiO detected sources are $\sim$1 kms^{-1} greater on average than towards the SiO non-detected sample (see Figure 2.5). Furthermore, a KS-test between the two samples indicates a strong probability ($\sim$0.9) that the $H^{13}CO^+$ FWHMs are drawn from a different underlying population. The KS test of the FWHMs of the $C^{18}O$ (3-2) emission (p-value=0.35), similarly suggests that they are drawn from different populations, however, the dependence is less so when compared with the $H^{13}CO^+$ FWHM values.

The ^{12}CO total linewidths taken from Maud *et al.* (2015b) are notably different between the two populations, average values of $\sim$50 kms^{-1} , and $\sim$26 kms^{-1}

are found for the SiO detected and non-detected sources respectively. Furthermore, a KS test between the two populations returns a probability of 0.006, strongly suggesting the ^{12}CO (3-2) linewidths for the SiO detected and non-detected values are drawn from different distributions. Which may indicate the need for higher velocity shocks to excite SiO.

The estimated HCO^+ masses and column densities for the SiO detected and non-detected samples both give p-values<0.1 from the KS tests, suggesting that both the masses and column densities for the SiO detected and non-detected are from different underlying populations. Moreover, the mass and HCO^+ column density estimates both have higher average and median values in the SiO detected sources compared with the non-detected sources. The masses of the SiO detected sources are on average $\sim$5 times greater than the SiO non-detected sources. The average and median 70μm luminosities are $\sim$7500 $L_\odot$ and $\sim$1500 $L_\odot$ for the SiO detected sources respectively, compared with $\sim$1500 $L_\odot$ and $\sim$500 $L_\odot$ for the SiO non-detected sources. A KS test also gives a likelihood of <0.3 that the 70μm luminosities are from the same population. Whereas, considering only those sources within the original distance limits of the survey (i.e. ≤ 4.5 kpc) the average and median luminosity of the SiO detected sample are now $\sim$2000 $L_\odot$ and $\sim$1300 $L_\odot$ respectively. However, the KS test still gives p-values of $\sim$0.24 for the two distributions.

The HCO^+ abundance and N_{H_2} column densities show only a factor of two difference in their average values and approximately equivalent median values between the two samples. However, the KS tests show two noticeably different values depending on whether the sources without an SiO detection and a CO outflow detection are included or not. As only 3 of the 10 SiO non-detected

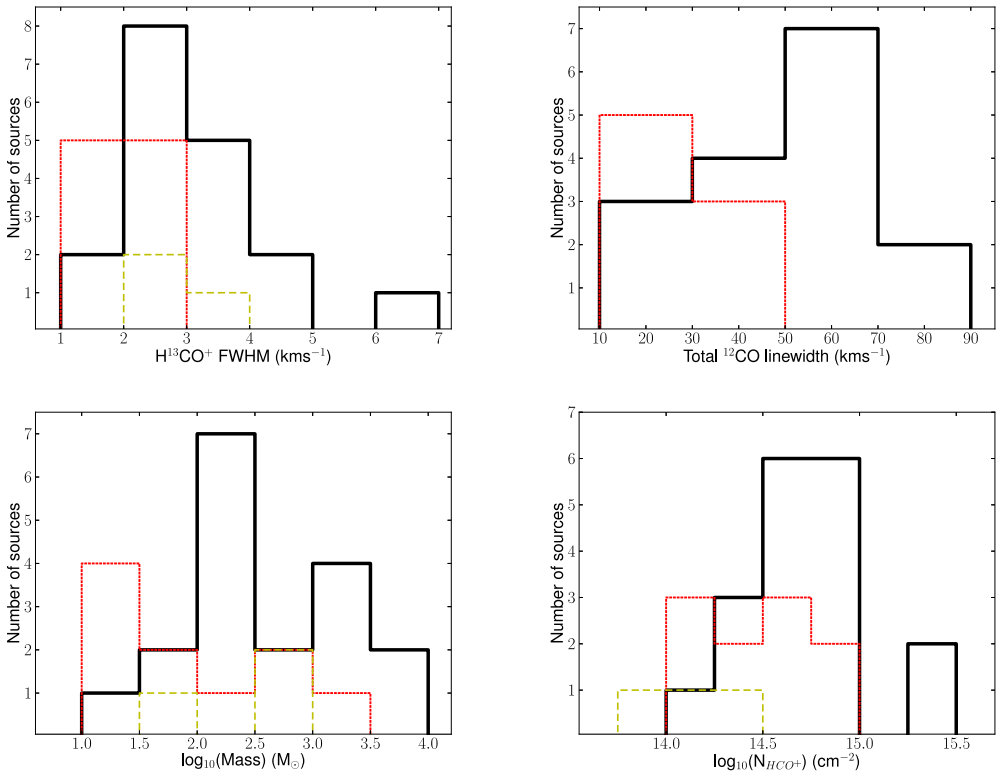

Figure 2.5: Histograms of the physical parameters with returned p-values of $\leq$0.2 for the SiO detected and non-detected samples. The black solid line represents the SiO detected sources, and the red-dotted and yellow dashed lines represent the SiO non detected with a CO outflow, and sources with no SiO or CO outflow emission respectively.

sources have available SCUBA data, the sample size for the HCO^+ abundances and N_{H_2} column densities is therefore lower. Figure 2.5 presents histograms of the SiO detected and SiO non-detected parameters that returned a p-value of $\leq$0.2 in the KS tests (i.e mass, N_{HCO^+}, $H^{13}CO^+$ FWHM, and total ^{12}CO (3-2) linewidths).

Table 2.6: Summary of properties between SiO detected and non-detected sources.

Source	SiO Detected		SiO Not Detected		No SiO or CO Detected		KS-test	
Properties	Average	Median	Average	Median	Average	Median	No SiO	No SiO or CO
Distance	2.2±1.7	1.4	1.6±0.3	1.4	2.5±1.6	1.4	0.57	0.70
$L_{\odot}$	20960±44850	9050	16500±28600	5800	31300±32600	13000	0.9	0.86
$H^{13}CO^{+}$ FWHM	3.1±1.1	2.8	2.0±0.5	1.9	2.7±0.5	2.5	0.04	0.08
$C^{18}O$ FWHM	3.1±0.9	2.8	2.6±0.7	2.7	2.4±0.7	2.3	0.35	0.36
^{12}CO linewidth	49±19	53	26±6	25	–	–	0.006	–
L70μm	7400±22300	1530	1470±2690	270	1020±620	700	0.25	0.17
Mass	1321±2100	259	251±357	67	338±310	327	0.06	0.09
$N_{HCO^{+}}(\times 10^{14})$	8.3±7.7	5.7	3.2±1.6	3.0	1.5±0.6	1.4	0.03	0.008
$A_{HCO^{+}}(\times 10^{-10})$	4.4±3.0	3.3	4.6±2.2	3.9	1.0±1.5	1.0	0.85	0.23
$N_{H_2}(\times 10^{24})$	1.9±1.2	1.5	0.8±0.5	0.8	1.5±0.6	1.1	0.17	0.27
Radius (pc)	0.15±0.11	0.12	0.08±0.07	0.05	0.07±0.03	0.08	0.03	0.06

2.3.7 Infall Properties Estimated from the $H^{13}CO^+$ and HCO^+ Spectra

As discussed previously, the $H^{13}CO^+$ and HCO^+ emission can provide information on the large scale kinematics of the region. Both HCO^+ and $H^{13}CO^+$ trace dense molecular gas with relatively high critical densities (see Table 2.1). Furthermore, the spectra from the optically thick HCO^+ transition can be compared with the spectra from the optically thin isotopologue $H^{13}CO^+$ to determine bulk gas motions, and provide an indication of infall depending on the asymmetry of the emission. Infall is interpreted when a double peaked line profile with a brighter blue asymmetry, offset from the rest velocity, is observed in HCO^+, and $H^{13}CO^+$ shows only a single peaked component at rest velocity. A single peak in the optically thin $H^{13}CO^+$ (4-3) line allows us to distinguish between self absorption and multiple line of sight components in the optically thick HCO^+ profile. An infall profile towards an individual object is not a confirmation of infall, as a combination of rotation and/or outflows could produce a similar profile. However, only infall will consistently produce a blue asymmetry (infall) profile over the whole sample of objects. The predominance of either a blue or red asymmetry is quantified by the skewness parameter. Following the procedure outlined in Mardones *et al.* (1997) the skewness parameter can be estimated from,

$$\delta\nu = \frac{v_{thick} - v_{thin}}{\Delta\, v_{thin}}, \tag{2.7}$$

where v_{thick} and v_{thin} are the LSR velocities at line peak for the optically thick HCO^+ (4-3) and optically thin $H^{13}CO^+$ (4-3) transitions respectively. The ve-

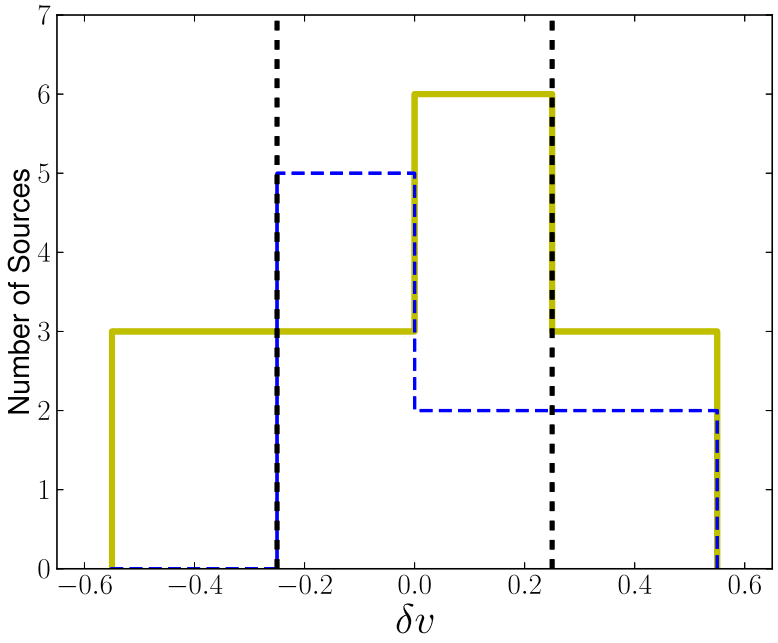

Figure 2.6: Histogram of the skewness parameter $\Delta\nu$ estimated from the $H^{13}CO^+$ and HCO^+ line profiles for sources with (solid yellow line) and without (blue dashed line) SiO detections. The black dashed lines represent the asymmetry limits for blue $\Delta\nu \leq 0.25$ and red $\Delta\nu \geq 0.25$ asymmetries.

locity difference is then normalized by the FWHM (Δv) of the optically thin $H^{13}CO^+$ line. The FWHM and the LSR velocity for $H^{13}CO^+$ are taken from the Gaussian fits presented in Table A.2 of Appendix A. Whereas, for the HCO^+ emission, the velocity is taken at the position of the brightest emission peak in the spectrum. The result is then the dimensionless parameter $\delta\nu$. A significant excess in either the blue or red asymmetry is defined as $\delta\nu \leq$-0.25 or $\delta\nu \geq 0.25$ respectively. In Figure 2.6, histograms showing $\delta\nu$, for both the SiO detected and non-detected sources, are presented. In total, 3 objects show a blue excess and 5 show a red excess. All 3 sources with a blue excess have a corresponding SiO detection and 3 of the 5 sources with a red excess have an

SiO detection (see Table 2.3 for individual sources). The significance of either the blue or red excess over the other was further quantified by Mardones *et al.* (1997) through the excess parameter,

$$E = \frac{N_{blue} - N_{red}}{N_{total}}. \tag{2.8}$$

For this sample the excess parameter is -0.25. Of the three sources with an identified blue excess, self absorption with a stronger blue peak is observed towards two sources, G203.3166-OFFSET and G081.7220. Following the method from Myers *et al.* (1996) the infall can be determined from the $H^{13}CO^+$ and HCO^+ line profiles. Using equation 9 of Myers *et al.* (1996) the infall velocity is estimated from,

$$V_{in} \approx \frac{\sigma^2}{v_{red} - v_{blue}} ln\Big(\frac{1 + e(T_{BD}/T_D)}{1 + e(T_{RD}/T_D)}\Big) \tag{2.9}$$

where σ is the velocity dispersion of the optically thin $H^{13}CO^+$ line, T_D is the brightness temperature of the dip and T_{BD} and T_{RD} are brightness temperature difference between height of the respective peak and the brightness of the dip, T_D, and v_{red} and v_{blue} are the velocities of the red and blue emission peaks respectively. The calculated infall velocity V_{in} can then be used to estimate the mass infall rate. Following the procedure outlined in Myers *et al.* (1996), the mass infall rates for the two sources with a double peaked blue asymmetric profile are estimated using

$$\dot{M} = 4\pi\, n_{H_2} \mu\, m_H r^2 V_{in}, \tag{2.10}$$

where μ is the mean molecular weight taken to be 2.35, m_H is the mass of hydrogen, and r is the radius of the emitting region, which is defined using the $H^{13}CO^+$ masks (assuming the mask to be circular), V_{in} is the infall velocity estimated from the HCO^+ and $H^{13}CO^+$ line profiles in Equation 2.9 and n_{H_2} is the ambient density, which is calculated for each source and given in Table 2.5. Infall velocities of 0.67 kms^{-1} and 1 kms^{-1} are found for G203.3166 and G081.7220 respectively along with mass infall rates of a few 10^{-3} $\dot{M}\,yr^{-1}$ for both sources. The estimated infall velocities and mass infall rates are consistent with previous values found for high mass star forming regions (e.g. Klaassen *et al.* 2012; Fuller *et al.* 2005) on size scales similar to these observations $\sim$0.1 pc.

2.4 Discussion

2.4.1 SiO Emission with Source Properties

The correlation statistics and linear regression fits to the estimated source properties (e.g. Mass, $H^{13}CO^+$ FWHM) as a function of the SiO luminosity are presented in Table 2.7. The STSDAS package part of the IRAF software was used to derive the P-values, and were calculated considering the 3σ upper limits for the SiO luminosities. A sources property is determined to be correlated if the P-value$\leq$0.01 and the linear correlation coefficient $>$0.5 (see Table 2.7). The $H^{13}CO^+$ and $C^{18}O$ FWHMs, ^{12}CO (3-2) total linewidth, 70μm luminosity, mass and HCO^+ column density are found to show a correlation with the SiO luminosity, whereas the HCO^+ abundance and N_{H_2} column density show no correlation with the SiO luminosity. Those properties showing a correlation with

the SiO luminosity are presented in Figure 2.7.

The $H^{13}CO^+$ FWHM displays the strongest correlation (R=0.75) with the SiO luminosity. As the CO linewidth was used in several sources to integrate the SiO emission, a correlation of the linewidth with the SiO luminosity may not be surprising. What is more noticeable is that only sources with an SiO detection have a respective total ^{12}CO (3-2) linewidth >35 kms^{-1} , which points towards SiO emission being a more efficient tracer of high velocity shocks. Gibb *et al.* (2007) also found a preference for SiO being detected towards the higher velocity outflows in their sample, suggesting that the presence of SiO is therefore an indication of a high velocity outflow. Of the mass, column density and 70μm luminosity, the mass and column densities are similarly linearly correlated with correlation coefficients of R=0.69, and R=0.67 respectively. The 70μm luminosity is also found to show a slight correlation with the SiO luminosity of $\sim$0.6. For the HCO^+ masses, over half of the non-detected SiO sources have a mass less than $\sim$40M$_\odot$, compared with only $\sim$10% of the SiO detected sample. Removing those sources with mass estimates lower than $\sim$40M$_\odot$ from both samples now gives a p-value in the KS test of 0.8 that the remaining SiO detected and non-detected sources are drawn from the same distribution. It is therefore possible that there are two populations in the non-detected sources. To test the possibility of an underlying causality in the correlation between SiO detectability and mass and ^{12}CO velocity dispersion and whether there is an underlying relationship between the two parameters (i.e. could the brighter SiO be due to faster shocks which happen to occur in the higher mass stars), Figure 2.8 displays the estimated source mass from the HCO^+ emission as a function of the total ^{12}CO (3-2) velocity dispersion. The points are scaled to represent

the SiO luminosities so the potential underlying relationship can be explored. A linear regression fit of the mass with CO velocity gives a P-value of 0.01 and a linear coefficient of 0.5, which both just make the cut-off limits to be classed as a linear correlation. There is no obvious relationship between those sources with the highest mass being related to sources with the highest ^{12}CO (3-2) velocity dispersions. While sources with the highest velocities do not have the largest SiO luminosities, there is a preference for sources with higher velocity to have associated SiO emission. More than half of the SiO detected sources have a total ^{12}CO velocity of $>35\,\mathrm{kms}^{-1}$, while sources without an SiO detection are all below this value. Furthermore, while there appears to be a link between the most massive sources having the largest SiO luminosities and similarly the lowest mass sources having a preference for an SiO non-detection, towards over half of the sample there is no obvious link with SiO luminosity and mass of the region.

2.4.2 SiO Luminosity with Source Evolution

The sources were purposely selected to sample a range of evolutionary stages, and are categorised into two main stages of evolution in the RMS survey; MYSOs and HII regions (based on colours, and radio emission). Figure 2.9 displays a histogram of the SiO luminosity with source classification (sources where the $H^{13}CO^{+}$ peak was offset from the RMS source position are presented as OFFSET sources). The HII region, G045.0711 (which has an updated distance of 7.7 kpc since the observations were undertaken Wu *et al.* 2014) has the highest SiO luminosity and is the only source where the SiO luminosity lies out-

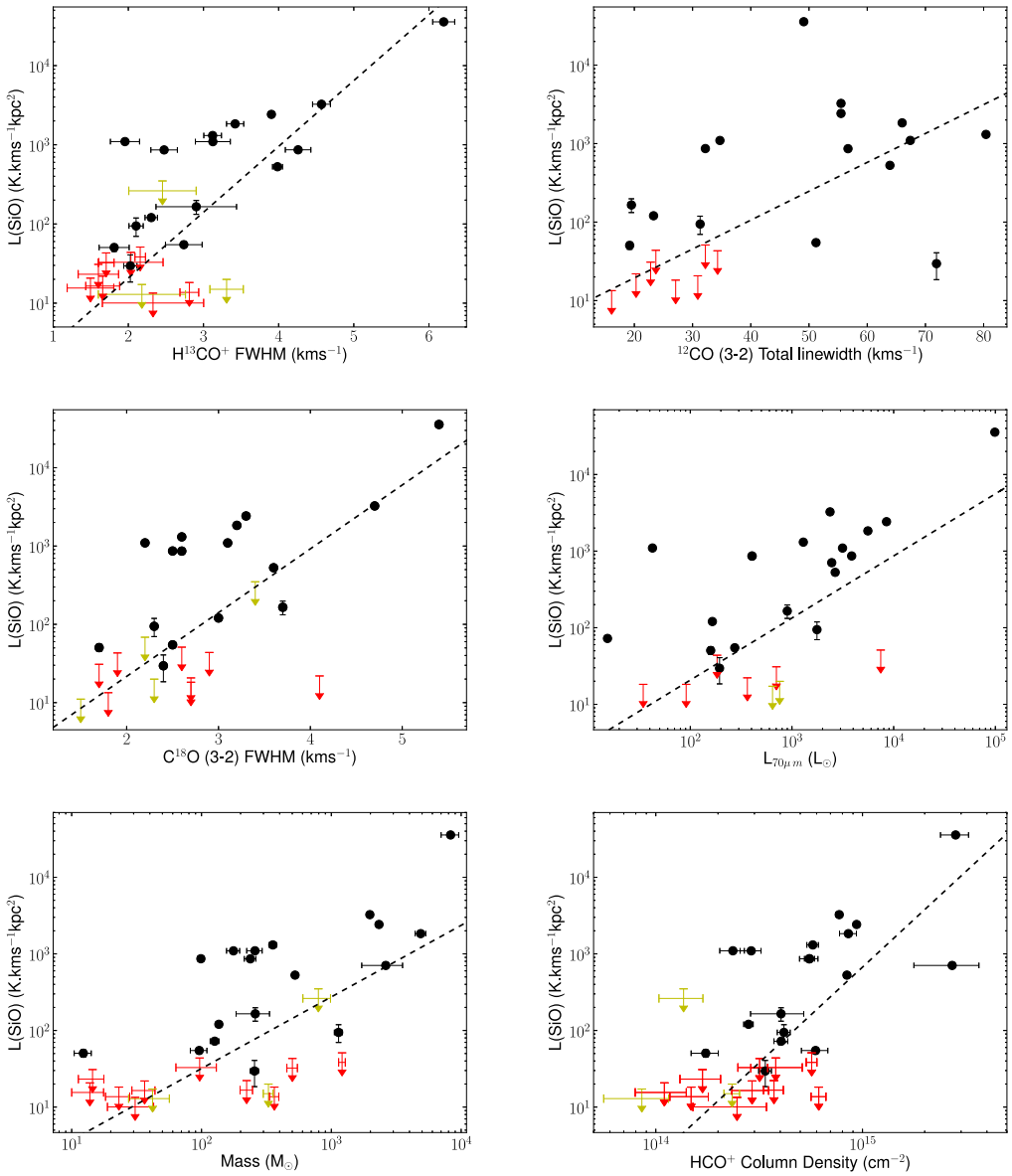

Figure 2.7: SiO Luminosity as a Function of the physical properties. The plots include the $H^{13}CO^+$ (4-3) and $C^{18}O$ (3-2) FWHM, ^{12}CO (3-2) linewidth, 70μm Luminosity, HCO^+ mass, and HCO^+ columns density. The black circles represent those sources with an SiO detection above 3σ that have a confirmed CO outflow detection in Maud *et al.* (2015b), and the red and yellow triangles represent the 3σ upper limits for those sources with and without an observed CO outflow in Maud *et al.* (2015b) respectively. The black dashed lines are linear regression fits to the data, including the 3σ upper limits and are provided in Table 2.7.

Table 2.7: Linear fit and correlation coefficients for SiO luminosity relationships. The linear fits are from the log10 of the SiO luminosity and the log10 of the source properties (apart from for the FWHM and linewdiths).

Correlation with L_{SiO}	P-value Spearman	Kendall	Cox	R	Linear fit
$H^{13}CO^+$ FWHM	0.0011	0.0001	0.001	0.75	y=0.83±0.13.x -0.34
$C^{18}O$ FWHM	0.040	0.012	0.011	0.6	y=0.81±0.17.x -0.29
^{12}CO linewidth	0.004	0.0095	0.0028	0.57	y=0.037±0.01.x+0.55
L70μm	0.0098	0.0069	0.019	0.61	y=0.81±0.15.x-0.30
Mass	0.0027	0.0016	0.0008	0.69	y=1.29±0.23.x-0.86
N_{HCO^+}	0.0005	0.0003	0.0001	0.67	y=2.49±0.52.x-34.61
A_{HCO^+}	0.46	0.63	0.15	0.29	–
N_{H_2}	0.0248	0.0221	0.0599	0.44	–

side of the YSO range for SiO luminosities. The remaining HII regions show no obvious difference in their SiO luminosity compared with the YSO class. The SiO luminosities of the OFFSET and HII/YSO sources also show no obvious differences compared with the YSO sample. In the ^{12}CO outflow sample by Maud *et al.* (2015b) (considering only sources with distances ≤ 4.5 kpc) ∼80% of the YSOs have confirmed ^{12}CO outflows compared with ∼40% of the HII regions. Of the sub-sample of those confirmed outflow sources 50% (4 of 8) of HII regions are found to have an SiO detection, compared with a ∼59% (10 of 17) SiO detection rate in the YSO sources.

The average and median values for each of the source properties (e.g. $L_\odot$, Mass, L_{SiO}) for each class are presented in Tables 2.8 and 2.9. The average 70μm luminosity for the YSO sources with an SiO detection is found to be ∼1800$L_\odot$, compared with ∼26000$L_\odot$ for the HII regions. However, this average includes G045.0711. Exclusion of this source, now gives a 70μm luminosity

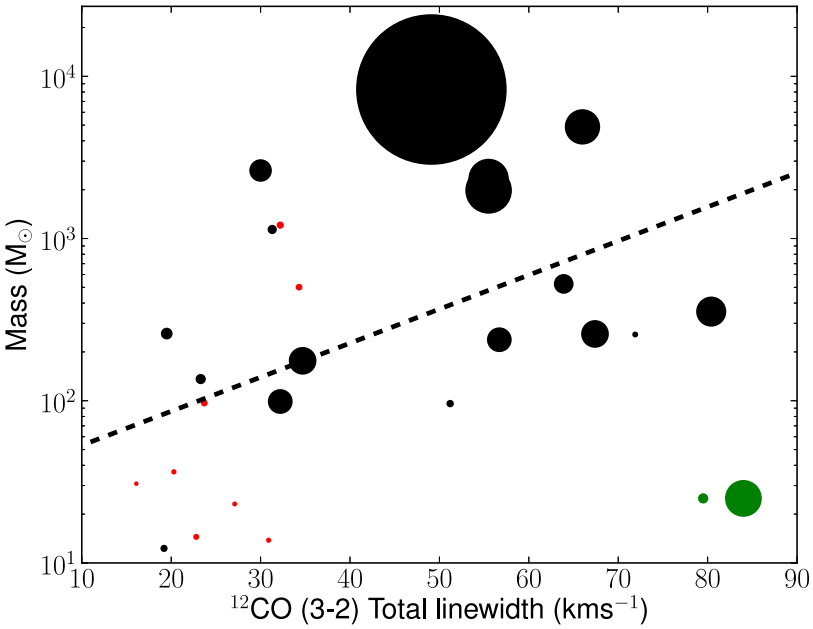

Figure 2.8: The derived masses from the HCO^+ emission as a function of the total ^{12}CO (3-2) velocity from Maud *et al.* (2015b). The black circles are SiO detected sources, and the red circles are SiO non-detected sources. The size of the circles relate to the SiO luminosities given in units of $K\,kms^{-1}$ kpc^2 (see Section 2.3.2) and the non-detected sizes relate to the 3σ upper limits. The green circles in the bottom right represent the average and median SiO luminosities for the whole sample and are $2000\,K\,kms^{-1}$ kpc^2 and $120\,K\,kms^{-1}$ kpc^2 respectively. The black dashed line is the resulting linear regression fit to the whole sample.

of $\sim$1750$L_\odot$ for the remaining HII regions, comparable with the YSO 70μm luminosities. Thus, there is little difference between 70μm luminosities towards the majority of either the HII regions or the YSOs.

2.4.2.1 Evolutionary Indicators

It is still not clear if outflows driven by massive stars follow the same evolutionary stages as outflows driven by low mass stars. In the low mass case the

momentum, force and energy of the jet/outflow is found to decline with age from class 0 to class I stages (e.g. Bontemps *et al.* 1996). As SiO emission is known to trace high velocity "active" jets, then the presence of SiO should decline with evolution in high mass stars if they have a similar driving mechanism to the low mass scenario. However, previous surveys have found both increasing (e.g. Klaassen *et al.* 2012; Leurini *et al.* 2014) and decreasing (e.g. Sanchez-Monge *et al.* 2013) SiO luminosities with proposed evolutionary stage. One method suggested to estimate the age of a given source is through the ratio of the bolometric luminosity to the mass ($L_{\odot}/M_{\odot}$). As a source evolves its luminosity will increase while the mass is expected to decrease due to mass loss from winds and jets. Thus, an increase in $L_{\odot}/M_{\odot}$ is a potential sign of evolution (e.g. López-Sepulcre *et al.* 2011; Leurini *et al.* 2014). Figure 2.10 displays the SiO luminosity as a function of the $L_{\odot}/M_{\odot}$ ratio, where the bolometric luminosity is taken from the RMS database, and the mass is taken from the HCO^{+} mass estimates (see Tables 2.2, and 2.5). No correlation is found between the SiO luminosity and $L_{\odot}/M_{\odot}$ ratio. However, what stands out is that all of the SiO non-detected sources are found towards higher values of $L_{\odot}/M_{\odot}$ (i.e. potentially more evolved sources), which is in agreement with the results of Sanchez-Monge *et al.* (2013) and López-Sepulcre *et al.* (2011), but is contrary to the results from Klaassen *et al.* (2012).

The ratio of the Herschel 70μm flux with the 22μm WISE flux[1] is plotted in Figure 2.11. As the source evolves and the emission moves to shorter wavelengths the F70/F22 colours should decrease. A correlation is found between the SiO luminosity and the F70/F22 colours, with the probability of false correlation

[1]The WISE flux is extracted directly from the RMS survey database

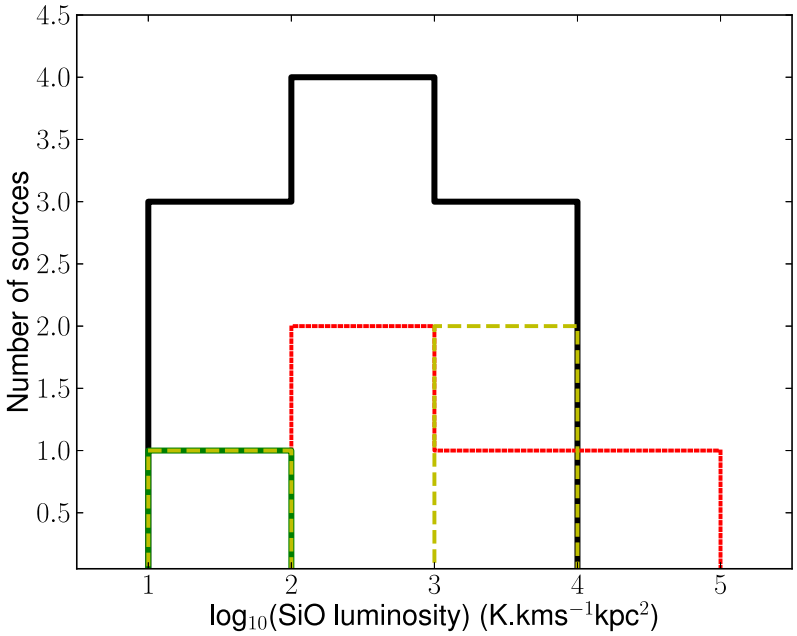

Figure 2.9: Histogram showing the SiO luminosity bins for a given class. The black solid line is the YSOs, the red line represnts the HII regions, and the yellow dashed and solid green lines are the OFFSET and HII/YSOs respectively.

given by <0.001 (see Table 2.7), and the corresponding linear correlation coefficient is 0.69 where the linear fit given by y=1.499(±0.37)x+0.76(±0.43). Thus, the SiO luminosity is stronger in the likely younger more embedded sources. The non-detected SiO sources all have lower colours, again suggesting that an SiO detection is an indication of youth. Klaassen *et al.* (2012) found an opposite trend in their survey of SiO (8-7), finding an increase of the SiO luminosity with evolution, which was also weakly observed by Leurini *et al.* (2014) in their sample. However, what is noticeable is that the HII sources with an SiO detection have redder colours, suggesting that the HII regions that have associated SiO emission may actually be younger. Davies *et al.* (2011) predict the life-

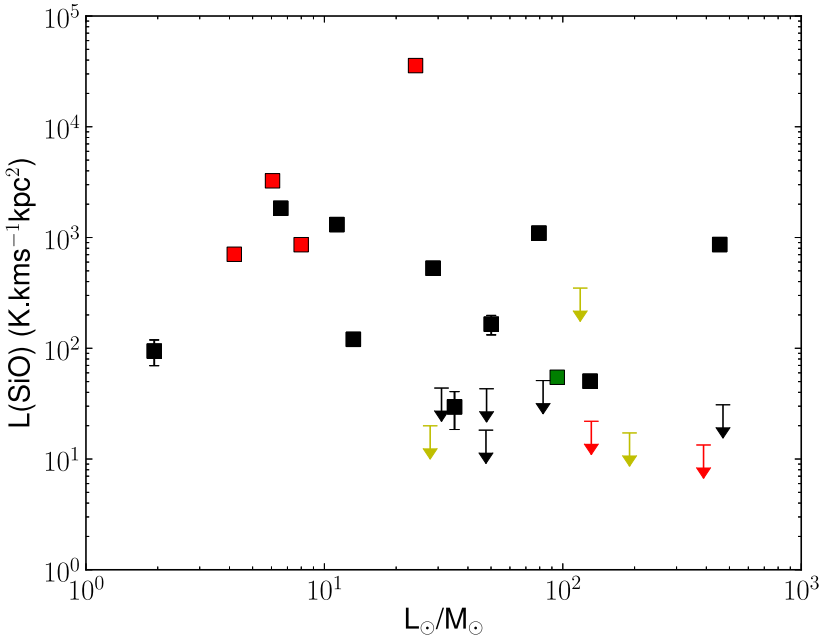

Figure 2.10: SiO luminosity as a function of $L_\odot/M_\odot$. The black, red, and green squares represent YSOs, HII, and HII/YSO sources with an SiO detection respectively. The triangles are the 3σ upper limits with the colours representing the same as above. The yellow upper limits are for sources without an SiO or CO detection. As no bolometric luminosities are available for the OFFSET sources, this classification is subsequently missing from the figure.

time for YSOs to dramatically drop for sources with $L_{bol}\sim10^{5.5}L_\odot$. The average bolometric luminosity of the sources in Klaassen *et al.* (2012) is of the order 10^4-$10^5L_\odot$, with several objects at a few $\times10^5L_\odot$. Thus, it is likely that some of the compact HII regions in Klaassen *et al.* (2012) will be relatively young and so the presence of SiO may decline with age in their sample, as seen by Sanchez-Monge *et al.* (2013), and consitient with the results presented in in this thesis.

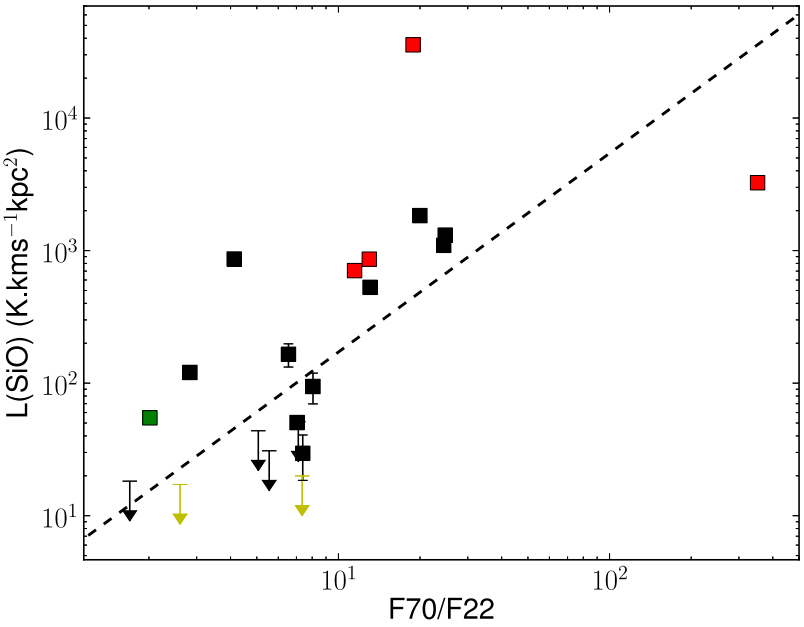

Figure 2.11: SiO luminosity as a function of the F70/F22 colours. The black, red, and green squares represent YSOs, HII, and HII/YSO sources with an SiO detection respectively. The triangles are the 3σ upper limits with the colours representing the same as above. The yellow upper limits are for sources without an SiO or CO detection. The offset sources are not included as their F22 flux is not available. The linear fit is shown by the black dashed line and has a correlation coefficient of R=0.69 and a linear fit given by $\log_{10}(y)=1.499(\pm0.37)\log_{10}(x)+0.76(\pm0.43)$. Furthermore, the HII regions with no SiO detection are not covered in the Herschel data, thus the sample size is smaller.

2.4.3 SiO Abundance Estimates

The SiO abundance is likely to be initially enhanced by the early protostellar jet. Previous observations (e.g. Sanchez-Monge *et al.* 2013) have observed a decrease in the SiO abundance with the age of the central driving source, suggesting a decrease in the outflow power with time. The SiO abundances are calculated following the same method as described above for the HCO^+ emission

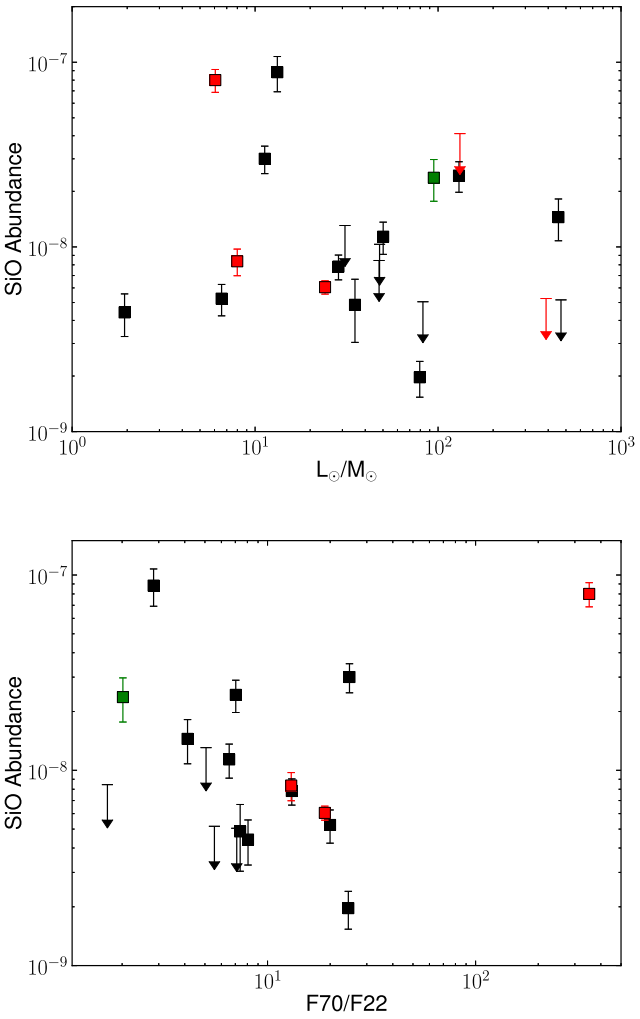

Figure 2.12: SiO Abundance as a function of $L_\odot/M_\odot$ (top panel) and F70/F22 colour (bottom panel). The black, red, and green squares represent YSOs, HII, and HII/YSO with an SiO detection respectively. The triangles are the 3σ upper limits with the colour representing the same as above. The OFFSET sources are not included as the bolometric luminosity and F22 fluxes are not available. No correlation is found between the SiO Abundance with either the $L_\odot/M_\odot$ or F70/F22 ratios.

(See Equation 2.3). The excitation temperature was taken to be 40 K (the derived excitation temperature from the ^{12}CO outflow emission by Maud *et al.* 2015b), and the SiO integrated intensity is taken from the sum of SiO emission over the derived velocity range (as described in Section 2.3.2). The SiO column density is then calculated following Equation 2.3, using the associated values for the SiO (8-7) transition. The fractional abundance is then calculated using the ratio of the derived SiO column densities with the average ^{12}CO column densities derived by Maud *et al.* (2015b) and assuming the standard value of 10^{-4} for the ^{12}CO to H_2 abundance ratio (Frerking *et al.* 1982). The beam averaged SiO abundances and column densities are given in Table 2.5. The average and median SiO abundances are 2.3×10^{-8} and 1.1×10^{-8} respectively. The estimated abundances are plotted as a function of the proposed evolutionary tracers (such as the $L_\odot/M_\odot$, and F70/F22) in Figure 2.12. The SiO abundance does not show any linear correlation with either of the possible evolutionary indicators. However, it should be stressed that the estimated SiO abundances are dependent on several parameters, such as the excitation temperature, the CO column density and the CO to H_2 abundance ratios, which will greatly affect the estimated values. In particular, the CO outflows are typically tracing a significantly larger area than the SiO emission, thus the average CO column densities may not represent the true density at the likely denser regions where SiO is emitted and the CO column densities may be an order of magnitude or more greater than used here. Furthermore, the temperatures used in the abundance estimate of 40 K may be underestimating the temperature of the SiO (8-7) emission, which has an E_{upper} temperature of $\sim$75 K.

Table 2.8: Summary of the average and median properties with source classification between SiO detected and non-detected sources for the YSO and HII regions.

	YSO				HII			
	SiO Detected		SiO Not Detected		SiO Detected		SiO Not Detected	
	Average	Median	Average	Median	Average	Median	Average	Median
$\log(L_{SiO})$	2.8±2.8	2.5	–	–	4.0±4.2	3.3	–	–
distance	2.0±1.1	1.7	1.9±0.2	2.0	3.7±2.6	2.8	1.4±0.0	1.4
$L_{\odot}$	4.1±4.1	4.0	4.5±4.6	4.2	3.8±3.6	3.7	4.7±4.9	4.1
$H^{13}CO^{+}$ FWHM	2.9±0.8	3.0	1.8±0.2	1.7	3.9±1.6	3.5	1.8±0.3	1.7
log(L70μm)	3.3±3.2	3.2	3.4±3.5	2.8	4.4±4.6	3.3	2.0	2.0
Mass	370±490	170	260±230	200	1200±1000	1150	17±3	17.3
$N_{HCO^{+}}(\times 10^{14})$	4.7±2.2	4.1	3.6±1.4	3.5	20.2±8.3	22	2.3±0.6	2.5
$A_{HCO^{+}}(\times 10^{-10})$	7.4±7.2	3.1	6.4±2.6	5.9	35.0±29.8	32.0	–	–
$N_{H_2}(\times 10^{23})$	8.1±6.3	6.8	5.8±2.4	5.8	15.7±13	11.4	–	–

Table 2.9: Summary of average and median properties with source classification between SiO detected and non-detected sources, for the OFFSET and HII/YSO sources.

	OFFSET				HII/YSO*
	SiO Detected		SiO Not Detected		
	Average	Median	Average	Median	
$\log_{10}(L_{SiO})$	3.1±3.0	3.04	–	–	1.7
distance	1.2±0.3	1.4	1.4±0.0	1.4	1.0
$\log_{10}(L_{\odot})$	–	–	–	–	4.0/3.1†
$H^{13}CO^+$ FWHM	2.8±0.8	2.5	2.4±0.6	2.8	2.7
$\log_{10}(L70\mu m)$	3.5±3.6	2.0	2.3±2.2	2.3	2.43
Mass	940±1150	194	110±80	130	35
$N_{HCO^+}(\times 10^{14})$	5.3±3.0	4.0	3.6±2.0	3.6	5.9
$A_{HCO^+}(\times 10^{-10})$	3.5±1.2	2.8	–	–	13.0
$N_{H_2}(\times 10^{23})$	17±13	8.1	–	–	4.6

(*) There is only a single HII/YSO region. (†) The luminosities are given for both the HII (first) and YSO (second)

2.4.4 Infall Properties

Only 3 sources show a blue asymmetry and only two of those with a double (stronger blue peaked) HCO^+ profile. However, the possibility of infall towards the remaining sources cannot be ruled out. Previous works (e.g. Fuller *et al.* 2005 and Rygl *et al.* 2013) found the lower energy HCO^+ transitions (e.g. J=1-0) showed a greater excess of blue asymmetry (i.e. indicating infall) compared with the higher energy transitions. Fuller *et al.* (2005) found transitions with higher critical densities show less infall signatures. They found 15% of their HCO^+ (4-3) line profiles showed a blue asymmetry compared with 30% in the 1-0 transition. Similarly Rygl *et al.* (2013) see a significant drop in sources observed with a blue excess with increasing energy of the transition (e.g. from HCO^+(1-0) to HCO^+(4-3)), finding a drop of 24 to 5 sources having a blue excess in the HCO^+ (1-0) to HCO^+ (4-3) samples respectively and from 14 to 4 in the red excess. This is compared with a $\sim$40% of the class 0 YSOs in Gregersen *et al.* (1997) having a blue asymmetry in the HCO^+ (4-3) line. The detection of 3 sources with a blue asymmetry ($\sim$11%) agrees with previous surveys towards high mass star forming regions at low spatial resolution. An important consideration is the sensitivity for infall asymmetry to line optical depth and excitation temperature. Smith *et al.* (2013) find an increase in the blue asymmetry of the optically thick line with decreasing beam size and suggest that matching the beam size with the energy of line transition will likely increase the detection of infall signatures. Future ALMA observations, at higher spatial resolution, will be able to directly test this.

2.4.4.1 Infall Candidates

Two sources G081.7220, and G203.3166-OFFSET are found to have a possible infall asymmetry with a double (stronger blue) peaked profile in the optically thick HCO^+ transition and a single peak in the optically thin component. However, the $H^{13}CO^+$ spectra, for both sources, hints at a possible blending of multiple components in the spectra. Towards G203.3166-OFFSET, the $H^{13}CO^+$ spectra is flattened at the top, and towards G081.7220 the $H^{13}CO^+$ spectra displays the broadest FWHM of the whole sample, along with a potential dip in the spectra. Furthermore, previous interferometric observations by Girart *et al.* (2013), have shown G081.7220 fragments into several cores on scales of $\sim$1000 AU. Thus, the $H^{13}CO^+$ and HCO^+ emission towards this source is likely due to multiple components that are not resolved. Towards G203.3166-OFFSET, previous interferometric observations (e.g. Peretto *et al.* 2007 and the work presented here in Chapter 3) show a single source (C-MM3) down to scales of $\sim$3000 AU. Furthermore, Peretto *et al.* (2007) suggest the parent cluster is possibly collapsing onto the this source, which resides at the centre of the parent cluster; NGC 2264-C. C-MM3, therefore, represents the best infall candidate in these observations.

2.5 Comparison to Outflows Driven by Low Mass Protostars

Observations of SiO towards low mass protostars (e.g. Gibb *et al.* 2004) suggest the strength of SiO emission declines towards more evolved sources. Gibb *et al.*

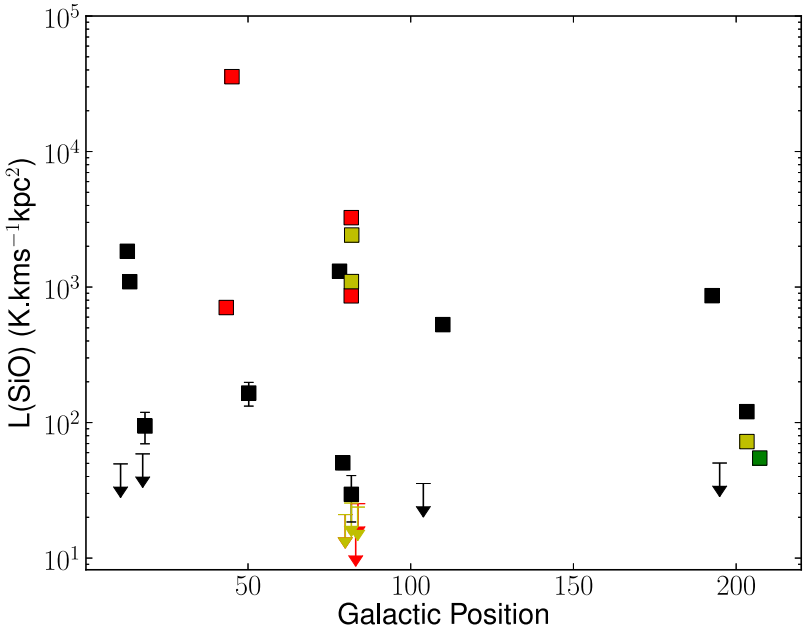

Figure 2.13: SiO Luminosity as a Function of Galactic Position. The black, red, yellow and green squares represent YSOs, HII, OFFSET and HII/YSO sources with an SiO detection respectively. The triangles are the 3σ upper limits with the colour representing the same as above.

(2004) find that 5 out of the 7 sources with SiO detections are class 0 sources. However, their overall detection rate of 28% is lower than ∼50% observed in this work. Furthermore, they suggest that the shock velocity and density play a role in the detection of SiO, finding only sources with an SiO detection at velocities above 30 kms^{-1} with the greatest SiO luminosities identified towards those sources with the highest corresponding velocities. This is consistent with the results presented in this work, where a higher percentage of the YSO sources have an SiO detection compared with the HII regions, and SiO detected sources are more prevalent towards regions with CO velocities above ∼35 kms^{-1}, and with redder F70/F22 colours.

2.5.1 Galactic Position

Whether the location of a star forming region in the Galaxy plays a significant role in its formation process is still a matter of debate. Figure 2.13 explores the effect of Galactic position on the detection and strength of the SiO emission. No obvious detection or lack of detected SiO or respective strength of the SiO emission is found to be dependant on Galactic position.

2.6 Conclusions

This Chapter has presented single dish molecular line data of the established outflow tracer SiO (8-7), and infall tracers $H^{13}CO^+$ (4-3) and HCO^+ (4-3), taken with the JCMT, towards a sample of 33 high mass star forming regions drawn from the RMS survey. The key results are detailed below:

1. Approximately 50% of sources have an associated SiO detection. Moreover, none of the sources without a confirmed CO outflow in Maud *et al.* (2015b) have an SiO detection, indicative of the association of the high SiO J transitions with outflows. Of the sources with a confirmed CO outflow; 50% (4 of 8) of HII regions are found to have an SiO detection, compared with 59% (10 of 17) of the YSOs. This suggests a higher prevalence of SiO emission towards YSOs compared with HII regions. However, of the HII regions that have an associated SiO detection, they appear to be relatively young. These results strongly suggest that SiO emission is more preferentially associated with young sources in massive star forming regions, consistent with the SiO observations towards low mass star

forming regions.

2. SiO emission is more preferentially observed towards sources with higher velocity ^{12}CO outflows. Only sources with a total ^{12}CO (3-2) velocity dispersion in Maud *et al.* (2015b) of greater than 35 kms^{-1} have a corresponding SiO detection. The SiO luminosity and detection or non-detection of SiO appears dependant on mass for only the most massive and lowest mass sources. Towards the three highest mass sources the highest SiO luminosities are found. Furthermore, over half of the non-detected sources have the lowest masses ($<$100M$_{\odot}$) compared with only one of the SiO detected sources. However, for the majority of sources the mass of a region does not appear to be linked to the resulting SiO luminosity. This could be due to the angular resolution of the observations. Given the spatial resolution multiple cores may be present within the beam, and so the mass of the core driving the outflow may not be directly linked to the overall mass of the region. There is also no apparent relation between those sources with higher ^{12}CO velocities having a higher mass.

3. In total 4 sources ($\sim$12% of the sample) show a blue asymmetry in the HCO$^+$ (4-3) and H^{13}CO$^+$ (4-3) emission, consistent with the previous surveys of HCO$^+$ (4-3) towards massive star forming regions. However, this is considerably lower than the amount of sources typically found with infall signatures towards low mass star forming regions at a similar resolution with this tracer. Smith *et al.* (2013) suggest that infall signatures should be more preferentially observed if the beam size of the observations and excitation conditions of the infall tracer are well suited. Future observa-

tions of either a lower HCO^+ J transition (e.g. HCO^+ (1-0) transition) at a similar resolution performed here, or the HCO^+ (4-3) transition but at a higher resolution may be better suited to trace infall in massive star forming regions. G203.3166-OFFSET is the most promising infall candidate presented in this data. This source (C-MM3, in G203.3166/NGC 2264-C) is part of the interferometric SMA observations presented in the following Chapter, and is found to drive a collimated outflow.

These results show that SiO is more strongly associated with the youngest sources and is more efficient at tracing higher velocity outflows. Thus, SiO is an excellent tracer of the youngest stages in massive star forming regions. This dataset provides an excellent base for future follow-up observations at higher spatial resolution.

Chapter 3

Submillimeter Array Observations Towards the Intermediate/High Mass Star Forming Region NGC 2264-C

This Chapter is formed from a manuscript currently in submission to Monthly Notices of the Royal Astronomical Society. This chapter presents high angular resolution ($\sim 3''$) Submillimeter Array (SMA) observations at 1.3 mm of NGC 2264-C, one of the nearest intermediate/high mass star forming regions in the RMS survey. The previous low resolution JCMT observations (discussed in Chapter 2) reveal the presence of multiple SiO outflows towards this region. The aim of these higher spatial resolution observations is to resolve the SiO emission as seen with the JCMT and so identify which source(s) in the region are driving active outflows. A particular goal is to assess the relationship of the

RMS source to the outflows seen at low angular resolution, and so to aid in the interpretation of low resolution outflow surveys. The observations presented in this chapter provide the first interferometric study of the outflow tracers SiO and CO towards NGC 2264-C.

3.1 Introduction

It is still not understood if the formation of high mass stars can be described as a scaled up version of the low mass star formation process. Jets and outflows play an important role in the star formation process, and their study provides a means of exploring the formation mechanism in both regimes. Observationally, YSOs of all mass are known to drive bipolar molecular outflows. Thus, a single outflow mechanism would imply that all stars acquire mass by a similar disc-accretion process that scales with source luminosity (e.g. Richer *et al.* 2000). The evidence for a single mechanism is an observed correlation, over five orders of magnitude, between the bolometric luminosity and outflow, force, power and mass flow rate (e.g.Cabrit & Bertout 1992).

Intermediate mass YSOs ($2\ M_{\odot} \leq M_{*} \leq 8\,M_{\odot}$) are the link between the low and high mass regimes, and as such may provide key insights into the transition of the outflow properties between the two regimes and whether they scale smoothly with the mass of the driving proto(star). However, an observational complication arises when going from the low to intermediate/high mass regime in that intermediate/high mass stars typically form in more complex and clustered environments (Lada & Lada 2003); as a result, it is not always unambiguously clear from observations which core(s) in a region are powering

the jet/outflow(s), particularly at lower spatial resolution. High angular resolution studies that can resolve individual cores and outflows are thus crucial to understanding jets/outflows from intermediate and high-mass stars. These high angular resolution observations aim to identify active outflows and their central driving sources, and to determine the relationship of these active outflows to the multiple outflows previously identified from the single dish JCMT observations.

3.2 An Overview of NGC 2264-C

Located in the Mon OB1 giant molecular cloud complex at a distance of 738^{+57}_{-50} pc (Kamezaki *et al.* 2014), NGC 2264-C is a comparatively well-studied region, with a wealth of ancillary data and known CO outflows, and H_2 jets (e.g. Buckle *et al.* 2012; Wang *et al.* 2002; Maury *et al.* 2009). AFGL 989-IRS1 (Allen 1972), a $9.5\,M_\odot$ B2 star, dominates the region in the IR. Thirteen millimetre continuum sources have been identified (Ward-Thompson *et al.* 2000; Peretto *et al.* 2006, 2007, see Figure 3.1), which have typical diameters of $\sim$0.04 pc and masses ranging from $\sim 2{-}40\,M_\odot$ (Peretto *et al.* 2006; Peretto *et al.* 2007). From comparing observations and SPH simulations, Peretto *et al.* (2007) suggest that NGC 2264-C is in a global state of collapse on to the central, most massive millimetre core, C-MM3 ($\sim 40\,M_\odot$). Maury *et al.* (2009) observed ^{12}CO (2-1) emission with the IRAM 30m ($\sim$11″), detecting a network of 11 outflow lobes with projected velocities ranging from 10-30 kms^{-1}, lengths of 0.2-0.8 pc and momentum fluxes in the range 0.5×10^{-5} to $50 \times 10^{-5}\,M_\odot\,kms^{-1}yr^{-1}$. However, the limited angular resolution meant that only a small minority of the detected outflow lobes could be unambiguously identified with driving sources (millimetre

continuum cores). Recent high resolution SMA observations by Saruwatari *et al.* (2011) focusing on the central class 0 protostellar core, C-MM3, identified a compact, young north-south bipolar outflow driven by this source in both ^{12}CO and CH_3OH emission, emphasising the power of high-resolution, multi-line observations.

The ambiguity in identifying outflow driving sources based on low-resolution single-dish observations calls for high angular resolution observations of a reliable jet/outflow tracer.

3.3 Observations

3.3.1 Submillimeter Array Observations

The Submillimeter Array (SMA)[1] observations were made with 8 antennas in the compact configuration on 2010 December 12. The pointing centre for the observations is R.A. (J2000) $06^h41^m10.13^s$, Dec. (J2000) $09°29'34.0''$. The observations were performed on-source for a total of ∼4 hours, spread over an 8 hour track to improve UV coverage. The system temperatures ranged from ∼ 100 - 180 K depending on source elevation. A typical value of $\tau_{(225GHz)}$ ∼ 0.1 - 0.15 was obtained during the observations. At 1.3 mm, the SMA primary beam is ∼ 55″, and the largest recoverable scale for the array in the compact configuration is ∼ 20″. The total observed bandwidth is ∼ 8 GHz, covering ∼216.8 - 220.8 GHz in the lower sideband and ∼228.8 - 232.8 GHz in the upper

[1]The Submillimeter Array is a joint project between the Smithsonian Astrophysical Observatory and the Academia Sinica Institute of Astronomy and Astrophysics and is funded by the Smithsonian Institution and the Academia Sinica.

sideband.

Initial calibration was accomplished in MIRIAD (Sault *et al.* 1995), with further processing undertaken in CASA[1]. The bandpass calibration was derived from observations of the quasar 3C454.3. The gain calibrators were J0530+135, J0532+075, and J0739+016, and the absolute flux calibration was derived from Uranus. The fluxes derived for the quasars were found to be within 20% of the SMA monitoring values, which suggests that the absolute flux calibration is good to within 20%. The upper and lower sidebands were treated individually during calibration. The line and continuum emission were separated using the command *uvcontsub* in CASA: only line-free channels were used to estimate the continuum. Self-calibration was performed on the continuum data in each sideband, with the solutions applied to the line data. The SMA correlator was configured to provide a uniform spectral resolution of 0.8125 MHz; the line data were resampled to a velocity resolution of $1.2\,\mathrm{km\ s^{-1}}$, then Hanning smoothed.

The continuum data from the lower and upper sidebands were combined to produce the final continuum image. The continuum image and line image cubes were cleaned using a robust weighting of 0.5. This results in a synthesised beam size of $\sim 3.06'' \times 2.69''$ with a P.A. of approximately -67 deg for the final 1.3 mm continuum image, which has a 1σ rms noise level of $\sim 2\,\mathrm{mJy\ beam^{-1}}$. In the Hanning-smoothed spectral line image cubes, the typical 1σ rms noise (per channel) is $\sim 40\,\mathrm{mJy\ beam^{-1}}$. Unless otherwise noted, images displayed in figures have not been corrected for the primary beam response of the SMA. All reported measurements were made from images corrected for the primary beam response.

[1]http://casa.nrao.edu

3.3.2 Archival Data

To complement the SMA and JCMT HARP observations, archival mid/far-infrared data was obtained. These archival data include PACS (Poglitsch *et al.* 2010) 70 μm observations (observational ID 1342205056, P.I. F. Motte) taken with the ESA *Herschel Space Observatory*[1] (Pilbratt *et al.* 2010), *Spitzer* MIPSGAL 24 μm observations (Rieke *et al.* 2004) and SCUBA 450 μm data (Di Francesco *et al.* 2008). The PACS Herschel 70 μm and SCUBA 450 μm maps are presented in Figure 3.1, overlaid with the positions of the brightest *Spitzer* MIPSGAL 24 μm point sources within the SMA field of view. The astrometry is corrected for the PACS archival data using the *Spitzer* MIPSGAL 24 μm images, which were calibrated against 2MASS point source positions (Skrutskie *et al.* 2006).

3.4 Results

3.4.1 1.3 mm Continuum Emission

The SMA 1.3 mm continuum image is presented in Figure 3.2. The structure of the 1.3 mm emission was characterised through the implementation of dendrograms (Rosolowsky *et al.* 2008). Dendrograms or structure tree diagrams can be used to define hierarchical structure in clouds. The dendrogram tree structures are comprised of three main components; a trunk, branches and leaves, which correspond to increasing levels of intensity in the dataset. The minimum threshold intensity required to identify a parent tree structure (e.g trunk) was

[1] *Herschel* is an ESA space observatory with science instruments provided by European-led Principal Investigator consortia and with important participation from NASA.

Table 3.1: Properties of Millimetre Continuum Sources

Source [a]	J2000.0 Coordinates[b]		J2000.0 Coordinates[c]		R_{eff} [d]	I_{peak} [e]	S_ν [f]
	$\alpha(^{hms})$	$\delta(^\circ\,'\,'')$	$\alpha(^{hms})$	$\delta(^\circ\,'\,'')$	(pc)	(mJy beam^{-1})	(mJy)
C-MM3	06 41 12.31	+09 29 11.50	06 41 12.28	+09 29 11.96	0.011	370	395
C-MM4	06 41 10.08	+09 29 21.70	06 41 09.95	+09 29 21.40	0.017	185	496
C-MM5	06 41 10.15	+09 29 33.70	06 41 10.14	+09 29 35.87	0.012	62	131
C-MM10	06 41 08.94	+09 29 44.56	06 41 08.75	+09 29 44.24	0.015	37	113
C-MM12	06 41 09.59	+09 29 54.64	06 41 09.63	+09 29 54.62	0.013	209	274
C-MM13	06 41 11.47	+09 29 17.47	06 41 11.51	+09 29 18.00	0.0099	34	53
SMA1	06 41 10.00	+09 29 49.25	06 41 10.12	+09 29 47.97	0.0079	15	21
SMA2	06 41 10.46	+09 29 39.66	06 41 10.46	+09 29 39.16	0.0057	27	22
SMA3	06 41 09.11	+09 29 26.50	06 41 09.16	+09 29 27.38	0.0093	17	27
SMA4	06 41 09.88	+09 29 14.53	06 41 09.88	+09 29 14.85	0.0053	48	27

Notes.

[a] Sources identified in the dendrogram analysis: C-MM- denotes previously known/named millimetre sources (Peretto *et al.* 2006, 2007); SMA- denotes new 1.3 mm detections.

[b] Position of millimetre continuum peak.

[c] Position of intensity-weighted centroid, computed using *Computing Dendrogram Statistics* (Astropy Collaboration *et al.* 2013).

[d] Effective radius, computed from the total leaf area using *Computing Dendrogram Statistics* (Astropy Collaboration *et al.* 2013), through $R_{eff} = \sqrt{Area/\pi}$ and assuming the distance of 738pc to NGC 2264-C.

[e] Peak intensity of 1.3 mm continuum emission, corrected for the primary beam response.

[f] Integrated 1.3 mm flux density, measured from the primary-beam-corrected continuum image using CASAVIEWER and the $3\,\sigma$ mask from the dendrogram fit to the uncorrected image (see Section 3.4.1).

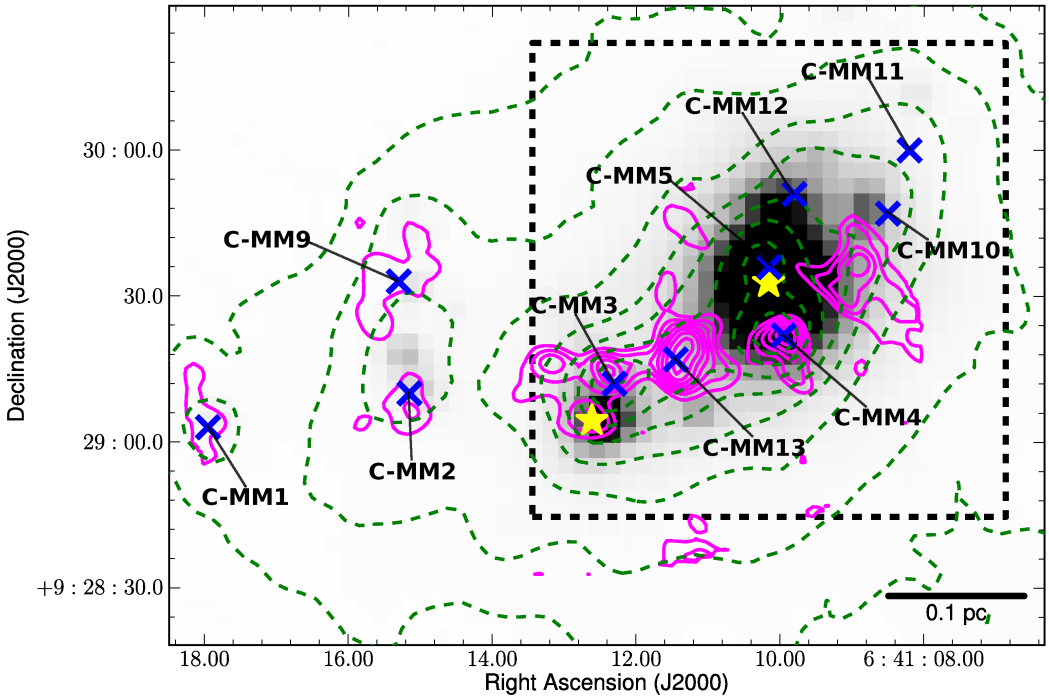

Figure 3.1: Overview of NGC 2264-C. Herschel PACS 70 μm emission (greyscale) overlaid with contours of SCUBA 450 μm emission (dashed green) and N_2H^+ (1-0) integrated intensity (PdBI, magenta). The N_2H^+ (1-0) integrated intensity map was presented in Peretto *et al.* (2007) and provided by N. Peretto. Blue crosses (x) mark the positions of millimetre sources (labelled C-MM) detected by Peretto *et al.* (2006, 2007); yellow stars mark the positions of the brightest 24 μm *Spitzer* point sources in the region. The dashed black square represents the FOV of the SMA observations presented in this chapter.

set to be 4 σ (in the continuum image prior to correction for the primary beam response; $\sigma \sim 2$ mJy beam^{-1}) and a minimum area of 18 contiguous pixels (the equivalent area of the synthesised beam). Further nested substructures (i.e. branches and leaves) require an additional 1 σ increase in intensity, again over a minimum of 18 contiguous pixels. The dendrograms were computed using the python implementation astrodendro[1].

[1]This research made use of astrodendro, a Python package to compute dendrograms of Astronomical data (http://www.dendrograms.org/)

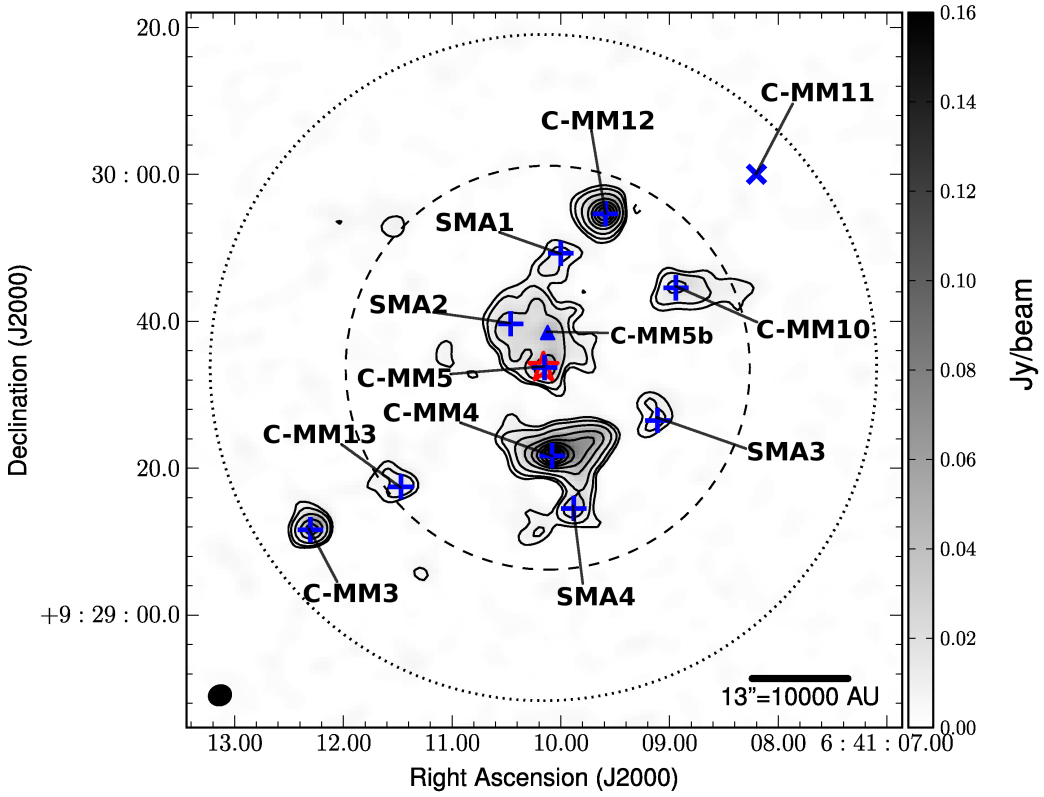

Figure 3.2: Map of the 1.3 mm continuum emission towards the section of NGC 2264-C observed with the SMA. The greyscale is the SMA 1.3 mm continuum emission from 0 to 0.16 Jy beam^{-1}; the peak flux in the field is 0.159 Jy beam^{-1}. The black contours represent (3, 5, 10, 20, 30, 40, 50, 60, 70, 80)$\times$ $\sigma = 2$ mJy beam^{-1}. The peak continuum positions for the 10 leaves (millimetre continuum peaks) identified in the dendrogram fit are marked with blue pluses (+) and labelled SMA- for new detections and C-MM- for previously detected sources. The blue triangle marks the peak position of the possible millimetre continuum peak C-MM5b. The red star represents the position of AFGL 989-IRS1 taken from the 2MASS data in the RMS Survey, and the blue cross (x) marks the position of C-MM11 from Peretto *et al.* (2007). The black dashed circle represents the FWHP of the SMA primary beam, and the outer black dotted circle represents the 10% power level of the SMA primary beam. The SMA synthesised beam ($3.06 \times 2.69''$, PA= -69.3) is shown at lower left.

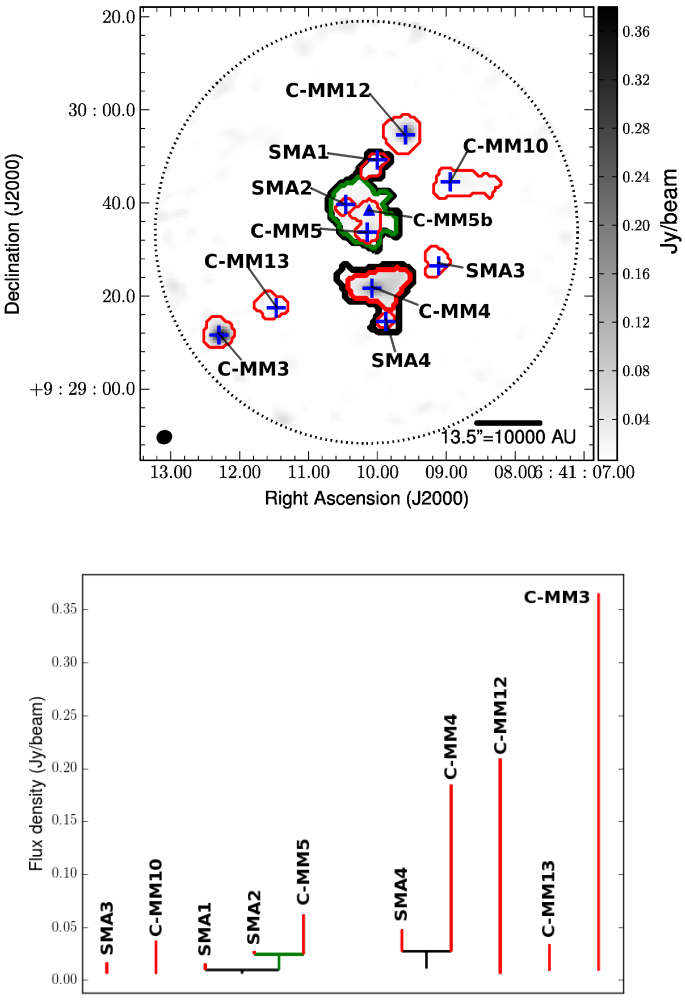

Figure 3.3: The dendrogram fit and tree structure diagram for NGC 2264-C. The top panel displays the 1.3 mm continuum image, corrected for the primary beam response, overlaid with the dendrogram fit to the data. As discussed in Section 3.4.1, structures are identified using a minimum threshold of $4\,\sigma$ ($1\sigma = 2$mJy/beam) and a minimum number of 18 contiguous pixels, with a step increase of 1σ for further substructure to be identified. The 10 emission peaks identified in the dendrogram fit are labelled. The red contours (top panel) and corresponding red lines (tree diagram, bottom panel) denote the highest level of a parent structure or of an independent structure with no further substructure if present. The green contour represents an additional branch within a parent structure. The black line gives marks the limit of the parent tree, of which the leaves and branches are nested within. Five sources (C-MM5, C-MM5, SMA1, SMA2 and SMA4) are nested within two trees, and five sources (C-MM3, C-MM10, C-MM12, C-MM13 and SMA3) are identified as independent structures with no further substructure.

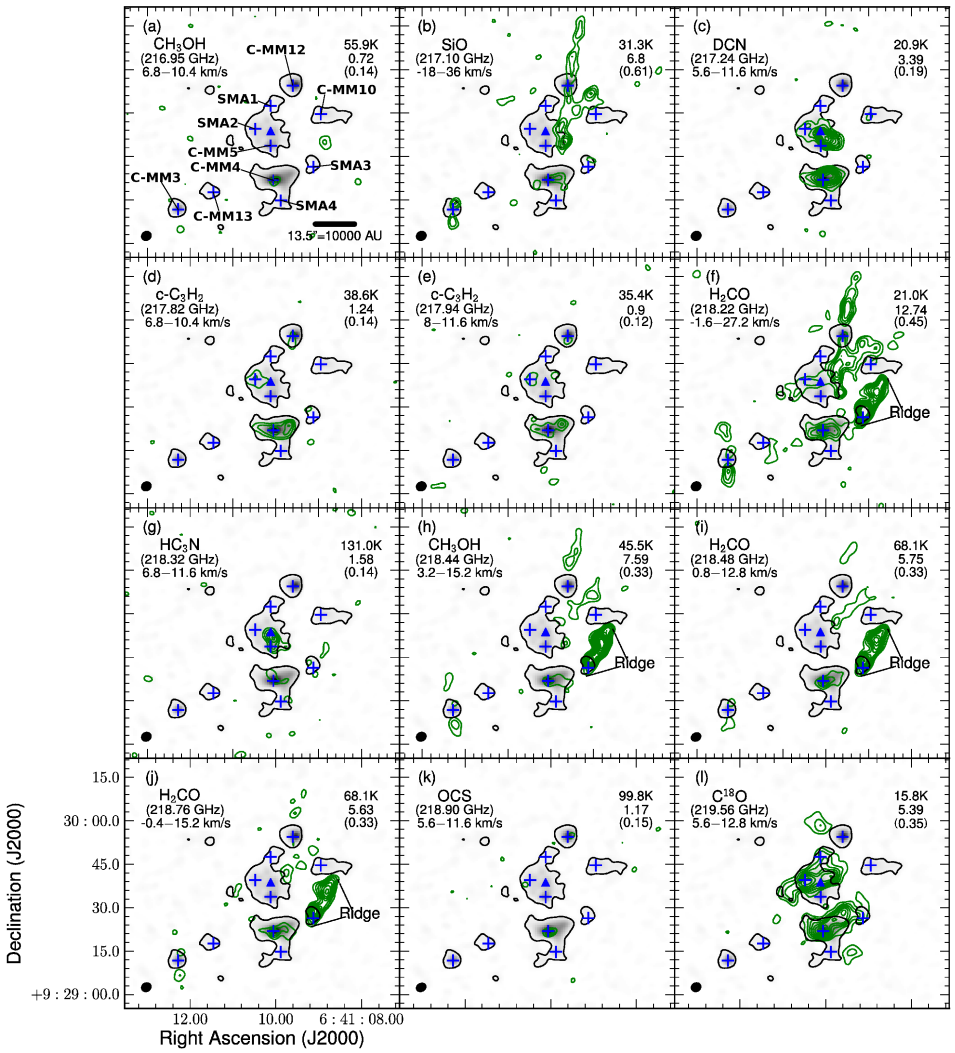

Figure 3.4: SMA integrated intensity maps (green contours) of detected molecular lines, overlaid on the 1.3 mm continuum emission (greyscale and black contour, contour level $3\sigma = 6$ mJy beam^{-1}). The integrated velocity range is given in the top left corner of each panel, along with the molecule and line rest frequency. E_{upper} for the transition and the peak and rms of each map (both in Jy beam^{-1} * km s^{-1}) are given at upper right in each panel. Blue pluses (+) mark the positions of the millimetre continuum peaks from Table 3.1, and the blue triangle marks the position of C-MM5b (see Section 3.4.1). Contour levels for the integrated intensity maps are from $3\,\sigma$ to peak in steps of $2\,\sigma$. (p) shows the CH_3CN emission integrated over the k=0-4 components.

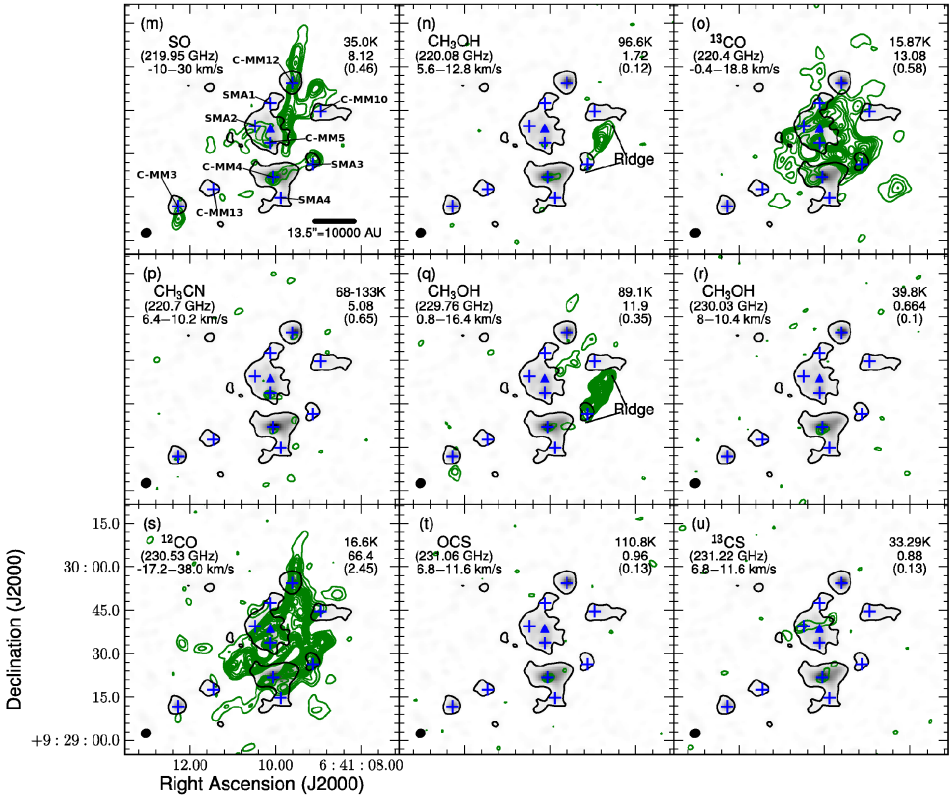

Figure 3.4– continued from previous page.

10 millimetre continuum sources are identified in the dendrogam fit in the SMA 1.3 mm image, of which four are new detections (labelled SMA1-SMA4 in Figure 3.2). The remaining six identified 1.3 mm continuum sources are previous detections (e.g. Peretto *et al.* 2006, Peretto *et al.* 2007, Ward-Thompson *et al.* 2000) and are labelled in Figure 3.2 according to the naming scheme of Peretto et al. (C-MM-). Of the ten 1.3 mm continuum sources identified in the dendrogram analysis, five are found as separate, independent parent structures with no substructure, and five are found nested into two tree structures. The two nested structures are comprised of C-MM4 and SMA4, and of C-MM5, SMA1, and SMA2, respectively (see Figure 3.3 for the dendrogram fit and re-

spective tree structure diagram). The parameters of the millimetre continuum sources (e.g. peak intensity, integrated flux density, and effective radius) were then extracted using the analysis code *Computing Dendrogram Statistics*[1] and the CASAVIEWER tool, and are presented in Table 3.1. All properties are estimated from the primary beam corrected 1.3 mm continuum image using a $3\,\sigma$ mask derived from the continuum image prior to correction for the primary beam response. This approach was taken to avoid including noise in the parameter estimates for millimetre continuum sources far from the pointing centre.

Of the sources reported by Peretto *et al.* (2006) and Peretto *et al.* (2007) that fall within the field of view shown in Figure 3.2, only C-MM11 –which lies outside the 20% power level of the SMA primary beam– is not detected in the SMA image. Our non-detection of C-MM11 is also consistent with the relative intensities of the millimetre continuum sources reported by Peretto *et al.* (2006, 1.2 mm IRAM 30-m observations): C-MM11 is the weakest Peretto et al. source within the SMA field (Figure 3.1). Thus, all of the previously identified millimetre continuum peaks are detected within the FWHP of the SMA primary beam.

The four new detections (e.g. SMA1, SMA2, SMA3, and SMA4) have the lowest integrated flux densities of the ten millimetre continuum sources: the brightest new detections (SMA3 and SMA4) have integrated flux densities that are approximately half that of the weakest previously reported source (C-MM13) in the SMA image (Table 3.1). This is consistent with SMA1-SMA4 not having been reported based on previous observations. However, it is noted that SMA4

[1]This research made use of Astropy, a community-developed core Python package for Astronomy (Astropy Collaboration *et al.* 2013)

is visible as a 3σ contour in Figure 1 of Peretto *et al.* (2007, PdBI 3.2 mm observations), but was considered a marginal detection and not studied further.

Inspection of the continuum map by eye reveals an additional millimetre continuum peak that is not identified by the dendrogram analysis. C-MM5 would be split into two cores: one at the peak position for C-MM5 tabulated in Table 3.1, and a second $\sim$4.5″ north (see Figure 3.2). The intensity of this second peak surpasses the dendrogram threshold for substructure, however the number of contiguous pixels is below the set limit, so the leaf is merged into C-MM5. If the number of contiguous pixels required is reduced to 77% of the area of the synthesised beam, C-MM5 is separated into two leaves by the dendrogram analysis. Inspection of the molecular line emission also indicates these two leaves may be separate objects (Section 3.4.2). It is therefore suggested that the northern leaf (hereafter C-MM5b) and C-MM5 are distinct millimetre continuum peaks, which at the current resolution cannot be unequivocally separated.

3.4.2 Molecular Line Emission

Molecular line emission is detected in 23 transitions of 13 species above $5\,\sigma$ with the SMA, including SiO, CO and its isotopologues (^{13}CO and C^{18}O), SO, OCS, H_2CO, CH_3OH, DCN, c-C_3H_2, ^{13}CS, HC_3N and CH_3CN. All lines detected at $>5\sigma$ have E_{upper} between $\sim$16 and 131 K. For each line detected towards NGC 2264-C, Table 3.2 lists the species, transition, rest frequency, E_{upper}, and whether the line is detected at $>5\,\sigma$ towards the millimetre continuum peak of each of the 11 cores (including C-MM5b, see Section 3.4.1). Table 3.3 presents

the parameters (peak line intensity, line centre velocity, linewidth, and integrated line intensity) obtained from single Gaussian fits to lines detected at $>5\,\sigma$, at each millimetre continuum peak. No fits are presented for ^{12}CO and ^{13}CO due to the complexity of the line profiles, which are strongly affected both by self absorption and by artefacts from poorly imaged large-scale emission.

Figure 3.4 presents integrated intensity maps for all detected transitions. The velocity range over which emission was integrated was determined for each transition, to encompass all channels with emission above 3σ. As shown in Figure 3.4, the morphology of the detected line emission is complex. For many transitions, the spatial morphology of the line emission differs markedly from that of the millimetre continuum. The emission in the integrated intensity maps falls into three main categories: (i) compact molecular line emission that directly traces millimetre continuum peaks (of which molecular line emission from the CH_3CN ladder transitions, both OCS transitions, HC_3N and the CH_3OH 5(1 , 4)- 4(2 , 2), CH_3OH 8(0 , 8)- 7(1 , 6) E and CH_3OH 3(-2, 2)- 4(-1, 4) E transitions are included); (ii) molecular line emission that overlaps but may not be clearly associated with millimetre continuum emission (e.g. may differ in morphology from the continuum emission and refers to emission from c-C_3H_2, DCN and C^{18}O); and (iii) spatially extended molecular line emission that is likely associated with outflows (of which line emission from SiO, SO, the H_2CO transitions and the CH_3OH 4(2 , 2)- 3(1 , 2), and CH_3OH 8(-1, 8)- 7(0 , 7) E transitions are included in this category). A distinct feature, which is labelled the "ridge", is also evident in Figure 3.4. The ridge is associated with the strongest H_2CO emission in the field, as well as the strongest emission in several CH_3OH transitions. While the southern edge of the ridge overlaps with

SMA3, the majority of the ridge structure does not appear to be associated with a millimetre continuum source. The nature of this intriguing feature is discussed in Section 3.5.2.

Table 3.2: Molecular line transitions detected towards the 11 (including C-MM5b) identified continuum peaks in NGC 2264-C. The line transition, rest frequency and upper energy (Columns 2, 3, and 4 respectively) are taken from Splatalogue (http://www.splatalogue.net/), Müller *et al.* (2005). A detection at $\geq 5\sigma$ is denoted by a Y, and N represents an non-detection (no emission at $\geq 5\sigma$). All measurements were made from image cubes corrected for the primary beam response, and a detection was determined from the spectra extracted from those beam corrected image cubes. The spectra are extracted from a single pixel at the respective peak continuum emission for each identified source. It should be noted that for sources far from the pointing centre such as C-MM3, the rms noise is higher.

Species	Transition	Frequency (GHz)	E_{upper} (K)	Detected										
				C-MM-							SMA-			
				3	4	5	10	12	13	5b	1	2	3	4
				LSB										
CH_3OH	5(1 , 4)- 4(2 , 2)	216.946	55.9	N	Y	N	N	N	N	N	N	N	N	N
SiO	(5 - 4)	217.105	31.3	Y	Y	N	N	Y	N	Y	N	N	N	N
DCN	(3 - 2)	217.239	20.9	N	Y	Y	Y	N	N	Y	N	Y	N	N
c-C_3H_2 [a]	6_{16} - 5_{05}	217.822	38.6	N	Y	N	N	Y	N	N	N	Y	N	N
c-C_3H_2 [a]	6_{06} - 5_{15}	217.822	38.6	N	Y	N	N	Y	N	N	N	Y	N	N
c-C_3H_2	5_{14} - 5_{23}	217.940	35.4	N	Y	N	N	N	N	N	N	Y	N	N
H_2CO	3(0, 3)- 2(0, 2)	218.222	21.0	Y	Y	N	Y	Y	N	Y	N	Y	Y	N
HC_3N	(24 - 23)	218.324	131.0	N	Y	Y	N	N	N	Y	N	N	N	N
CH_3OH	4(2 , 2)- 3(1 , 2)	218.440	45.5	N	Y	N	N	N	N	N	N	N	Y	N
H_2CO	3(2, 2)- 2(2, 1)	218.476	68.1	N	Y	N	N	N	N	N	N	N	Y	N
H_2CO	3(2, 1)- 2(2, 0)	218.760	68.1	Y	Y	N	N	Y	N	Y	N	Y	Y	N
OCS	(18 - 17)	218.903	99.8	N	Y	N	N	Y	N	N	N	N	N	N

Continued on next page

Table 3.2 – continued from previous page

Species	Transition	Frequency (GHz)	E_{upper} (K)	Detected										
				C-MM-							SMA-			
				3	4	5	10	12	13	5b	1	2	3	4
LSB														
$C^{18}O$	(2 - 1)	219.560	15.8	N	Y	N	Y	N	N	Y	Y	Y	Y	N
SO	6(5)-5(4)	219.949	35.0	N	Y	Y	N	Y	N	Y	N	Y	Y	N
CH_3OH	8(0 , 8)- 7(1 , 6) E	220.078	96.6	N	Y	N	N	N	N	N	N	N	N	N
CH_3CN	(12_4-11_4)	220.679	183.3	N	N	Y[b]	N	N	N	N	N	N	N	N
CH_3CN	(12_3-11_3)	220.709	133.3	N	Y[b]	Y[b]	N	N	N	N	N	N	N	N
CH_3CN	(12_2-11_2)	220.730	97.4	N	Y[b]	Y[b]	N	N	N	N	N	N	N	N
CH_3CN [c]	(12_1-11_1)	220.743	76.0	N	Y	Y	N	N	N	N	N	N	N	N
CH_3CN [c]	(12_0-11_0)	220.747	68.8	N	Y	Y	N	N	N	N	N	N	N	N
USB														
CH_3OH	8(-1, 8)- 7(0 , 7) E	229.759	89.1	N	Y	N	N	N	N	N	N	N	Y	N
CH_3OH	3(-2, 2)- 4(-1, 4) E	230.027	39.8	N	Y	N	N	N	N	N	N	N	N	N
^{12}CO	(2 - 1)	230.538	16.6	Y	Y	Y	Y	Y	Y	Y	Y	Y	Y	Y
OCS	(19 - 18)	231.061	110.8	N	Y	N	N	N	N	N	N	N	N	N
^{13}CS	(5 - 4)	231.221	33.29	N	Y	N	N	N	N	N	N	Y	N	N

([a]) The c-C_3H_2 components are blended in the spectra and cannot be separated. ([b]) CH_3CN components where emission is $<5\sigma$ but $>3\sigma$. ([c]) These CH_3CN components are blended in the spectra: 'Y' indicates emission $>5\sigma$ for the blended line.

Table 3.3: Gaussian Fits to Molecular Lines Detected at Each Millimetre Continuum Peak

Species	Transition	Frequency	E_{upper}	Fitted Line Parameters			
				Peak Intensity[a]	V_{centre} [a]	Linewidth [a]	$\int S\, dv$ [a]
		(GHz)	(K)	(Jy beam^{-1})	(km s^{-1})	(km s^{-1})	(Jy beam^{-1} km s^{-1})
				C-MM3			
H_2CO [b]	3(0, 3) - 2(0, 2)	218.222	21.0	0.91 (0.11)	6.60 (0.22)	3.93 (0.54)	3.80 (0.49)
H_2CO [b]	3(0, 3) - 2(0, 2)	218.222	21.0	0.44 (0.08)	-6.50 (0.33)	4.72 (0.98)	2.22 (0.40)
H_2CO	3(2, 1) - 2(2, 0)	218.760	68.1	0.58 (0.11)	8.22 (0.25)	2.68 (0.62)	1.66 (0.36)
				C-MM4			
CH_3OH	5(1 , 4) - 4(2, 2)	216.946	55.9	0.25 (0.03)	8.88 (0.15)	3.70 (0.35)	0.98 (0.12)
SiO [c]	(5 - 4)	217.105	31.3	0.22 (0.03)	15.04 (0.41)	5.33 (0.97)	1.26 (0.30)
DCN	(3 - 2)	217.239	20.9	0.87 (0.04)	8.53 (0.08)	3.54 (0.19)	3.29 (0.23)
c-C_3H_2	6_{16} - 5_{05}	217.822	38.6	0.55 (0.03)	7.77 (0.06)	2.54 (0.15)	1.50 (0.08)
c-C_3H_2	5_{14} - 5_{23}	217.940	35.4	0.24 (0.03)	8.70 (0.19)	2.92 (0.46)	0.74 (0.11)
H_2CO	3(0, 3) - 2(0, 2)	218.222	21.0	1.75 (0.03)	7.62 (0.03)	3.3 (0.07)	6.14 (0.11)
HC_3N	(24 - 23)	218.324	131.0	0.21 (0.03)	8.11 (0.20)	3.88 (0.49)	0.85 (0.14)
CH_3OH	4(2, 2) - 3(1, 2)	218.440	45.5	0.51 (0.03)	8.72 (0.11)	3.39 (0.26)	1.83 (0.13)
H_2CO	3(2, 2)- 2(2, 1)	218.476	68.1	0.55 (0.03)	7.82 (0.11)	3.85 (0.26)	2.24 (0.14)
H_2CO	3(2, 1)- 2(2, 0)	218.760	68.1	0.80 (0.03)	8.11 (0.06)	3.57 (0.14)	3.06 (0.11)
OCS	(18 - 17)	218.903	99.8	0.21 (0.02)	8.84 (0.33)	6.29 (0.89)	1.43 (0.18)
$C^{18}O$	(2 - 1)	219.560	15.8	2.59 (0.05)	8.03 (0.18)	2.38 (0.04)	6.57 (0.11)
SO	6(5)-5(4)	219.949	35.0	1.32 (0.05)	8.16 (0.05)	3.04 (0.13)	4.28 (0.17)

Continued on next page

Table 3.3 – continued from previous page

Species	Transition	Frequency	E_{upper}	Fitted Line Parameters			
				Peak Intensity[a]	V_{centre} [a]	Linewidth [a]	$\int S\, dv$ [a]
		(GHz)	(K)	(Jy beam^{-1})	(km s^{-1})	(km s^{-1})	(Jy beam^{-1} km s^{-1})
CH_3CN	(12_3-11_3)	220.709	133.3	0.10 (0.01)	5.77 (0.51)	2.76 (1.08)	0.28 (0.11)
CH_3CN	(12_2-11_2)	220.730	97.4	0.14 (0.01)	5.32 (0.4)	2.46 (0.80)	0.37 (0.10)
CH_3CN [d]	(12_1-11_1)	220.743	76.0	0.21 (0.01)	7.69 (0.28)	1.61 (0.53)	0.37 (0.10)
CH_3CN [d]	(12_0-11_0)	220.747	68.8	0.16 (0.01)	7.34 (0.29)	2.34 (0.59)	0.40 (0.10)
CH_3OH	8(0 , 8)- 7(1 , 6) E	220.078	96.6	0.21 (0.03)	7.96 (0.30)	4.70 (0.73)	1.07 (0.15)
CH_3OH	8(−1, 8)- 7(0 , 7) E	229.759	89.1	0.36 (0.03)	8.29 (0.15)	4.06 (0.37)	1.54 (0.13)
CH_3OH	3(−2, 2)- 4(−1, 4) E	230.027	39.8	0.22 (0.03)	8.32 (0.28)	4.35 (0.68)	1.02 (0.15)
OCS	(19 - 18)	231.061	110.8	0.27 (0.03)	8.42 (0.23)	4.07 (0.55)	1.19 (0.15)
^{13}CS	(5 - 4)	231.221	33.29	0.26 (0.04)	7.61 (0.30)	4.28 (0.74)	1.16 (0.19)
				C-MM5			
DCN	(3 - 2)	217.239	20.9	0.13 (0.02)	9.54 (0.22)	2.09 (0.56)	0.28 (0.10)
HC_3N	(24 - 23)	218.324	131.0	0.25 (0.02)	9.51 (0.08)	2.65 (0.28)	0.70 (0.06)
SO [b]	6(5)-5(4)	219.949	35.0	0.55 (0.05)	7.22 (0.70)	6.13 (1.73)	3.57 (1.06)
SO [b]	6(5)-5(4)	219.949	35.0	0.33 (0.01)	13.2 (0.08)	3.89 (0.21)	1.35 (0.09)
CH_3CN	(12_4-11_4)	220.679	183.3	0.12 (0.03)	8.82 (0.30)	2.68 (0.69)	0.34 (0.11)
CH_3CN	(12_3-11_3)	220.709	133.3	0.10 (0.02)	5.59 (0.46)	2.83 (1.20)	0.30 (0.10)
CH_3CN	(12_2-11_2)	220.730	97.4	0.11 (0.02)	7.26 (0.48)	4.05 (0.98)	0.49 (0.11)
CH_3CN [d]	(12_1-11_1)	220.743	76.0	0.12 (0.02)	7.51 (0.64)	2.78 (1.26)	0.35 (0.18)

Continued on next page

Table 3.3 – continued from previous page

Species	Transition	Frequency	E_{upper}	Fitted Line Parameters			
				Peak Intensity[a]	V_{centre} [a]	Linewidth [a]	$\int S\, dv$ [a]
		(GHz)	(K)	(Jy beam^{-1})	(km s^{-1})	(km s^{-1})	(Jy beam^{-1} km s^{-1})
CH_3CN [d]	(12_0-11_0)	220.747	68.8	0.20 (0.02)	8.51 (0.27)	3.61 (0.50)	0.78 (0.12)
				C-MM10			
DCN	(3 - 2)	217.239	20.9	0.38 (0.05)	7.80 (0.15)	2.07 (0.33)	0.84 (0.17)
H_2CO	3(0, 3) - 2(0, 2)	218.222	21.0	1.09 (0.11)	7.71 (0.09)	1.59 (0.19)	1.85 (0.30)
$C^{18}O$	(2 - 1)	219.560	15.8	0.25 (0.04)	7.83 (0.26)	3.56 (0.61)	0.96 (0.22)
				C-MM12			
SiO [c]	(5 - 4)	217.105	31.3	0.65 (0.05)	10.93 (0.16)	4.36 (0.47)	3.03 (0.28)
c-C_3H_2	6_{16} - 5_{05}	217.822	38.6	0.31 (0.06)	9.34 (0.20)	1.86 (0.38)	0.61 (0.12)
H_2CO	3(0, 3)- 2(0, 2)	218.222	21.0	0.57 (0.09)	11.18 (0.28)	3.55 (0.66)	2.17 (0.54)
H_2CO	3(2, 1)- 2(2, 0)	218.760	68.1	0.20 (0.02)	10.86 (0.14)	2.97 (0.33)	0.64 (0.10)
OCS	(18 - 17)	218.903	99.8	0.22 (0.02)	8.49 (0.18)	3.96 (0.42)	0.94 (0.13)
SO [b]	6(5)-5(4)	219.949	35.0	0.47 (0.06)	10.85 (0.29)	4.51 (0.70)	2.25 (0.46)
SO [b]	6(5)-5(4)	219.949	35.0	0.25 (0.03)	28.90 (0.28)	5.85 (0.67)	1.62 (0.24)
				SMA1			
$C^{18}O$	(2 - 1)	219.560	15.8	0.67 (0.08)	9.92 (0.11)	2.19 (0.29)	1.59 (0.28)
				SMA2			
DCN	(3 - 2)	217.239	20.9	0.36 (0.04)	9.95 (0.18)	3.23 (0.42)	1.23 (0.21)
c-C_3H_2 [e]	6_{16} - 5_{05}	217.822	38.6	0.27 (0.03)	9.42 (0.13)	2.78 (0.31)	0.81 (0.12)
c-C_3H_2	5_{14} - 5_{23}	217.940	35.4	0.25 (0.03)	10.38 (0.15)	2.54 (0.34)	0.67 (0.12)

Continued on next page

Table 3.3 – continued from previous page

Species	Transition	Frequency	E_{upper}	Fitted Line Parameters			
				Peak Intensity[a]	V_{centre} [a]	Linewidth [a]	$\int S\, dv$ [a]
		(GHz)	(K)	(Jy beam^{-1})	(km s^{-1})	(km s^{-1})	(Jy beam^{-1} km s^{-1})
H_2CO	3(0, 3) - 2(0, 2)	218.222	21.0	0.56 (0.04)	9.72 (0.10)	3.31 (0.25)	2.00 (0.20)
H_2CO	3(2, 1)- 2(2, 0)	218.760	68.1	0.19 (0.03)	9.88 (0.23)	2.89 (0.53)	0.58 (0.14)
$C^{18}O$	(2 - 1)	219.560	15.8	1.73 (0.06)	9.68 (0.05)	2.70 (0.11)	4.97 (0.27)
SO	6(5)-5(4)	219.949	35.0	0.80 (0.02)	9.52 (0.02)	2.16 (0.06)	1.82 (0.06)
^{13}CS	(5 - 4)	231.221	33.29	0.39 (0.05)	9.52 (0.12)	2.06 (0.28)	0.85 (0.15)
				SMA3			
H_2CO	3(0, 3)- 2(0, 2)	218.222	21.0	2.48 (0.08)	8.96 (0.08)	4.59 (0.18)	12.08 (0.63)
CH_3OH	4(2 , 2)- 3(1 , 2)	218.440	45.5	1.08 (0.07)	8.55 (0.08)	2.56 (0.20)	2.94 (0.30)
H_2CO	3(2, 2)- 2(2, 1)	218.476	68.1	1.30 (0.04)	8.83 (0.05)	3.47 (0.12)	4.80 (0.21)
H_2CO	3(2, 1)- 2(2, 0)	218.760	68.1	1.20 (0.04)	8.81 (0.05)	3.56 (0.12)	4.58 (0.12)
$C^{18}O$	(2 - 1)	219.560	15.8	0.39 (0.04)	8.83 (0.23)	4.84 (0.54)	2.01 (0.30)
SO [e]	6(5)-5(4)	219.949	35.0	0.43 (0.06)	9.93 (0.41)	6.26 (0.96)	2.84 (0.57)
CH_3OH	8(−1, 8) - 7(0, 7) E	229.759	89.1	0.97 (0.04)	8.60 (0.07)	3.40 (0.17)	3.52 (0.23)
				C-MM5b			
SiO	(5 - 4)	217.105	31.3	0.34 (0.03)	14.61 (0.16)	4.15 (0.37)	1.49 (0.17)
DCN	(3 - 2)	217.239	20.9	0.94 (0.05)	9.31 (0.07)	2.52 (0.17)	2.51 (0.22)
H_2CO	3(0, 3) - 2(0, 2)	218.222	21.0	0.68 (0.06)	8.93 (0.09)	2.22 (0.22)	1.60 (0.21)
HC_3N	(24 - 23)	218.324	131.0	0.44 (0.03)	8.97 (0.07)	2.11 (0.17)	0.99 (0.11)
H_2CO	3(2, 1) - 2(2, 0)	218.760	68.1	0.12 (0.02)	9.63 (0.22)	4.11 (0.52)	0.54 (0.09)

Continued on next page

Table 3.3 – continued from previous page

Species	Transition	Frequency	E_{upper}	Fitted Line Parameters			
				Peak Intensity[a]	V_{centre} [a]	Linewidth [a]	$\int S\, dv$ [a]
		(GHz)	(K)	(Jy beam^{-1})	(km s^{-1})	(km s^{-1})	(Jy beam^{-1} km s^{-1})
$C^{18}O$	(2 - 1)	219.560	15.8	1.54 (0.08)	9.28 (0.06)	2.39 (0.13)	3.92 (0.29)
SO [b]	6(5)-5(4)	219.949	35.0	0.39 (0.07)	9.83 (0.17)	2.18 (0.47)	0.90 (0.24)
SO [b]	6(5)-5(4)	219.949	35.0	0.14 (0.03)	15.32 (0.21)	3.12 (0.51)	0.48 (0.10)

([a]) 1-σ formal errors from the single Gaussian fits are given in the brackets (). ([b]) Two distinct velocity components are present in the spectrum; a single Gaussian fit is reported for each component. ([c]) Two velocity components appear to be present in the spectrum, but are not sufficiently well-separated in velocity to be fit separately. The reported fit is for the stronger component. ([d]) The k=0 and k=1 CH_3CN components are blended in the spectra. The reported parameters are from multiple-Gaussian fits using the GILDAS CLASS package. ([e]) Complex line profile, not well-fit by a single Gaussian.

3.4.2.1 Line Emission Associated with Millimetre Continuum Sources: Systemic Velocity Estimates

As shown in Figure 3.4, compact molecular line emission that peaks at the millimetre continuum peak is seen in only a few lines (OCS, CH_3CN, HC_3N and the 216.946 GHz, 220.078 and 230.027 GHz CH_3OH transitions), and only towards C-MM4, C-MM5, and C-MM5b (not all of these lines are detected towards all three sources; see Table 3.4). For these sources, $v_{\rm LSR}$ estimates for the individual millimetre continuum cores are given in Table 3.4, based on the fits (Table 3.3) to lines that exhibit spatially compact emission. For CH_3CN, the ladder transitions with a detection $<5\sigma$ are excluded from the $v_{\rm LSR}$ estimates.

The emission from DCN, $C^{18}O$ and c-C_3H_2 is found to be more extended (which is referred to as "diffuse", Table 3.4), coinciding with, and morphologically similar to, the millimetre continuum emission of C-MM4 and SMA2. For C-MM4, in particular, the similar morphologies of the line and millimetre continuum emission suggest that this more extended molecular line emission is associated with the millimetre continuum source. Strong DCN emission is also detected in the vicinity of C-MM5 and C-MM5b, but in this case the morphology of the line emission differs from that of the millimetre continuum, so it is not clear that the DCN emission is directly associated with the continuum source(s). Table 3.4 presents estimates of $v_{\rm LSR}$ based on fits to lines that exhibit "diffuse" emission and are detected at the position of a given core's millimetre continuum peak (including $C^{18}O$ as well as DCN and c-C_3H_2). It should be noted, that while this approach allows estimates of the $v_{\rm LSR}$'s for more sources, the results must be treated with greater caution than the estimates based on

the compact molecular line emission. The morphology of the $C^{18}O$ emission, for example, does not match that of the millimetre continuum, suggesting that the detected $C^{18}O$ may not arise from the dense gas of the millimetre continuum cores. In addition, the $v_{\rm LSR}$ estimates exclude lines that likely trace outflows and exhibit clearly extended emission (e.g. SiO, SO, H_2CO and the remaining CH_3OH lines).

The $v_{\rm LSR}$'s of the millimetre continuum sources, estimated as described above, range from $\sim$7.8 - 9.9 km s^{-1}. For C-MM4 and C-MM5 (which have the most data from line fits, Tables 3.3, and 3.4), the $v_{\rm LSR}$ estimates based on compact and "diffuse" tracers differ by up to $\sim$1 km s^{-1} (for C-MM5), and the standard deviation of the $v_{\rm LSR}$'s measured from individual lines is $\sim$0.5 km s^{-1} (Table 3.4).

Towards C-MM3, C-MM13, SMA1 or SMA4 no emission from lines that exhibit either compact or "diffuse" morphology is detected. As a result, the $v_{\rm LSR}$'s for these sources cannot be estimated from this SMA data. $v_{\rm LSR}$ estimates for C-MM3 and C-MM13 are of particular interest, given the outflow activity near C-MM3 (Section 3.4.2.2) and the velocity gradient reported by Peretto *et al.* (2007) in NGC 2264-C (spanning C-MM2, C-MM3, C-MM13, and C-MM4). For C-MM4, where the most compact emission is detected, the estimated $v_{\rm LSR}$ of 8.3 kms^{-1} is used for the remaining analysis. However, since estimates of the $v_{\rm LSR}$ cannot be obtained for the remaining continuum sources from this SMA data (and only a small minority of sources have robust $v_{\rm LSR}$ estimates based on compact molecular line emission), the following approach is adopted. For C-MM3, and C-MM13, the $v_{\rm LSR}$'s reported by Peretto *et al.* (2007) based on N_2H^+(1-0) emission (Table 3.4) are used. For all other millimetre continuum

sources (excluding C-MM4), the average $v_{\rm LSR}$ from the SMA data (averaged across all cores, for both compact and diffuse tracers) of 8.9 km s^{-1} is adopted. The $v_{\rm LSR}$ adopted for each continuum peak, and used throughout the remainder of this paper, is given in Table 3.4.

3.4.2.2 Extended and High Velocity Molecular Line Emission: Molecular Outflows

As shown in Figure 3.4, several species are characterised by collimated, extended emission: SiO, SO, CH_3OH, H_2CO, and ^{12}CO. The two most prominent collimated emission features in the integrated intensity maps (both elongated N-S) appear to be centred on C-MM3 and C-MM12. To investigate the nature of the extended molecular line emission, and its relation to outflows previously reported based in lower-angular-resolution data, the high resolution of these SMA observations is used to analyse the velocity structure of the emission. To identify any potential outflow axes, the well-known outflow tracer SiO is used (e.g. Gusdorf *et al.* 2008a,b; Guillet *et al.* 2009; Leurini *et al.* 2014, and references therein).

Figure 3.5 presents integrated intensity maps of the red- and blueshifted SiO emission observed with the SMA (SiO(5-4), resolution $\sim 3''$) and the JCMT (SiO(8-7), resolution $\sim 15''$). The comparison of the SMA and JCMT data will test whether the spatial filtering of the SMA misses any large-scale active outflows (which would be seen in SiO emission with the JCMT). The JCMT observations shown in Figure 3.5 (panel a) reveal two potential outflow systems: one encompassing both C-MM3 and C-MM13 (with the peak emission nearest to C-MM3), and a second that intersects both C-MM10 and C-MM12. In the

Table 3.4: Systemic Velocity Estimates for 1.3 mm Continuum Sources

Source	$v_{\rm LSR}$ (km s^{-1})			
	Compact[a]	Diffuse[b]	N_2H^+[c]	Adopted[d]
C-MM3	–	–	7.1	7.1
C-MM4	8.2 (0.5)	8.3 (0.4)	8.9	8.3
C-MM5	8.5 (1.0)	9.5	–	8.9
C-MM10	–	7.8 (0.02)	–	8.9
C-MM12	8.5	9.3	–	8.9
C-MM13	–	–	8.2	8.2
SMA1	–	9.9	–	8.9
SMA2	–	9.8 (0.4)	–	8.9
SMA3	–	8.8	–	8.9
SMA4	–	–	–	8.9
C-MM5b	9.0	9.3 (0.02)	–	8.9

Notes.
([a]) The average $v_{\rm LSR}$ estimates taken from the molecular line emission categorised as compact (see Section 3.4.2) and includes the CH_3CN ladder transitions (note only CH_3CN the ladder transitions with a detection $>5\sigma$ are included), both OCS transitions, HC_3N and the CH_3OH 5(1 , 4)- 4(2 , 2), CH_3OH 8(0 , 8)- 7(1 , 6) E and CH_3OH 3(-2, 2)- 4(-1, 4) E transitions (note not all of these lines are detected towards a given core; see Table 2 for details). The standard deviation is given in (). If no value is given, emission was detected only in one transition.
([b]) The average $v_{\rm LSR}$ estimates taken from molecular line emission categorised as diffuse (see Section 3.4.2) and includes $C^{18}O$ as well as DCN and c-C_3H_2 (again not all of these lines are detected towards a given core; see Table 2 for further details). The standard deviation is given in (). If no value is given, emission was detected only in one transition. ([c]) Taken from Peretto *et al.* (2007)
([d]) $v_{\rm LSR}$ assumed from each core for the remainder of this analysis.

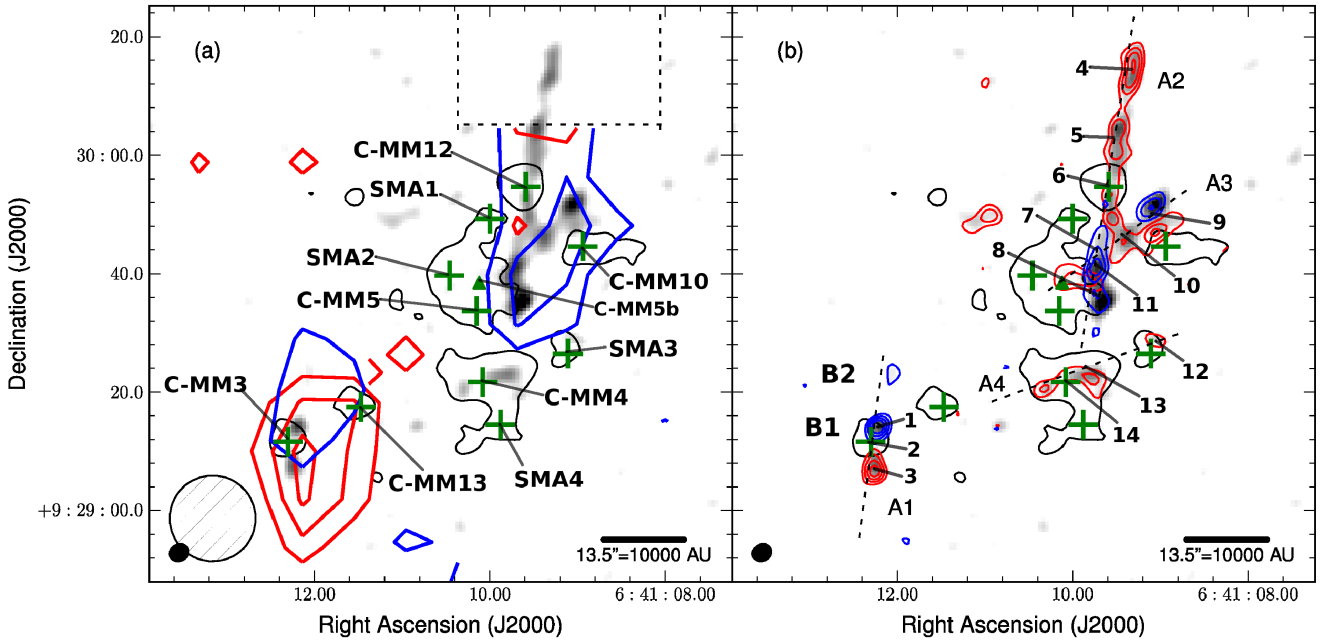

Figure 3.5: SMA SiO integrated intensity map (greyscale, integrated over the velocity range -20 to $37\,\mathrm{km s^{-1}}$) overlaid with contours of 1.3 mm continuum emission (black contour, level $3\sigma = 6\,\mathrm{mJy\ beam^{-1}}$) and blue/redshifted SiO emission from **(a)** the JCMT (SiO (8-7)) and **(b)** the SMA (SiO (5-4)). The velocity intervals for the blue/redshifted SiO emission are taken from $\pm 3\,\mathrm{km s^{-1}}$ from the v_{LSR} (7.1 km s^{-1} for C-MM3 and $8.3\,\mathrm{km s^{-1}}$ for C-MM4 and 8.9 km s^{-1} for C-MM12, see Section 3.4.2.1) and extend to the maximum outflow velocity. The velocity intervals are the same for the JCMT and SMA data and are: Blue: -20 to +4.1 km s^{-1} for C-MM3 (and C-MM13), -1.0 to $+5.3\,\mathrm{km s^{-1}}$ for C-MM4, and -20 to $+5.9\,\mathrm{km s^{-1}}$ for C-MM12 (and the other millimetre continuum cores); Red: +10.1 to $+37\,\mathrm{km s^{-1}}$ (C-MM3 and C-MM13), +11.3 to $+20\,\mathrm{km s^{-1}}$, and +11.9 to $+32\,\mathrm{km s^{-1}}$ (C-MM12 and other cores). In both panels, green pluses (+) mark the positions of the 10 millimetre continuum peaks from the dendrogram analysis and the green triangle marks the position of C-MM5b. **(a)** JCMT SiO(8-7) contour levels: (3,5,7,9) $\times\ \sigma = 0.2\,\mathrm{K.km\ s^{-1}}$. The 14.5″ JCMT beam (hatched circle) and the SMA synthesised beam (filled ellipse) are shown at lower left. The black dashed rectangle shows the area of missing data from the HARP receiver element H14. **(b)** SMA SiO(5-4) contour levels: (3,5,7,9) $\times\ \sigma = 0.36$ Jy beam^{-1} km s^{-1}. The thick dashed black lines represent possible outflow axes: A1, A2, A3, and A4. The numbered positions 1-14 mark the locations at which spectra shown in Figure 3.7 were extracted. The labels B1 and B2 mark components of the blueshifted outflow lobe of C-MM3 named by Saruwatari *et al.* (2011).

latter, only blueshifted emission is detected with the JCMT; however, receiver H14 was not operational during the observations, resulting in a gap in the JCMT map north of C-MM12. Figure 3.5b presents the higher spatial resolution SMA SiO (5-4) data. With the SMA, the SiO emission near C-MM3 and C-MM13 is clearly resolved, revealing a single bipolar outflow centred on C-MM3 (outflow axis A1, Figure 3.5b). The red and blueshifted lobes are spatially well-separated and are centred on the continuum source, indicating that the high-velocity SiO(5-4) emission traces a bipolar molecular outflow. The second potential outflow system identified in the JCMT data, towards C-MM12 and C-MM10, splits into multiple components at the higher spatial resolution of the SMA observations. As shown in Figure 3.5b, the SMA data reveal a collimated, bipolar outflow centred on C-MM12 (axis A2, Figure 3.5b): as in the C-MM3 outflow, the red and blueshifted lobes are spatially well-separated and centred on the millimetre continuum source. For both outflows, the sense of the velocity gradient is consistent in the SMA and JCMT observations (e.g. the blueshifted lobe is north of C-MM3, and the redshifted lobe south of C-MM3, in both the SMA and JCMT maps). The fact that the SMA SiO data recovers (and resolves) both of the SiO outflows identified with the JCMT is strong evidence that the SMA is not "missing" large-scale active outflows.

In addition to the two clear bipolar outflows driven by C-MM3 and C-MM12, two additional potential outflow axes are identified in Figure 3.5b. Outflow axis A3 is associated with a knotty structure, seen in red/blueshifted SiO(5-4) emission, that is located east/north-east of C-MM10 and is not obviously associated with a millimetre continuum source. Outflow axis A4 is defined by the redshifted SiO (5-4) emission observed towards C-MM4 and SMA3 (Figure 3.5b).

For reference the full channel maps for the SiO (5-4) emission are provided in Figure B.2.

To explore the nature and structure of the high velocity outflow emission in NGC 2264-C, four velocity regimes (e.g. Santiago-García *et al.* 2009): systemic ($v_{\rm LSR}\pm3\,{\rm kms}^{-1}$), standard high velocity (SHV, $v_{\rm LSR}\pm3$ to $10\,{\rm kms}^{-1}$), intermediate high velocity (IHV, $v_{\rm LSR}\pm$10-30kms^{-1}), and extremely high velocity (EHV, $v_{\rm LSR}\pm$30-50kms^{-1}) are considered. Figure 3.6 presents SMA integrated intensity maps for the systemic, SHV, and IHV regimes for SiO (5-4), SO (6(5)-5(4)), H_2CO (3(0, 3)- 2(0, 2)) and ^{12}CO (2-1). These are the only four transitions in which emission is detected at velocities >10 km s^{-1} from the $v_{\rm LSR}$ (e.g. in the IHV regime). The EHV maps are not displayed as very little EHV emission is detected and the only $>3\sigma$ emission with $v - v_{\rm LSR} > 30\,{\rm kms}^{-1}$ is detected in ^{12}CO (2-1) at $\sim31\,{\rm kms}^{-1}$, towards the redshifted lobe of the C-MM3 outflow. As described in Section 3.4.2.1, $v_{\rm LSR}$'s of 7.1 km s^{-1} for C-MM3, $8.3\,{\rm kms}^{-1}$ for the region covering C-MM4 (including C-MM13) are adopted. For the rest of the region, the velocity ranges are with respect to a $v_{\rm LSR} = 8.9$ km s^{-1} (assumed for the other continuum cores, Section 3.4.2.1).

Low-velocity (systemic) emission is detected along the outflow axes A2, A3, and A4 for all four transitions shown in Figure 3.6. The exception is outflow axis A1, associated with C-MM3: in this case, only H_2CO is detected at low velocities. In addition, two CH_3OH lines (CH_3OH 4(2,2)−3(1,2) and CH_3OH 8(-1,8)-7(0,7)E) exhibit extended emission along the outflow axes only in the systemic and SHV regimes, and so are not shown in Figure 3.6. For reference, the systemic and SHV emission from CH_3OH 4(2,2)−3(1,2) and CH_3OH 8(-1,8)-7(0,7)E can be found in Figure B.3 of Appendix B.

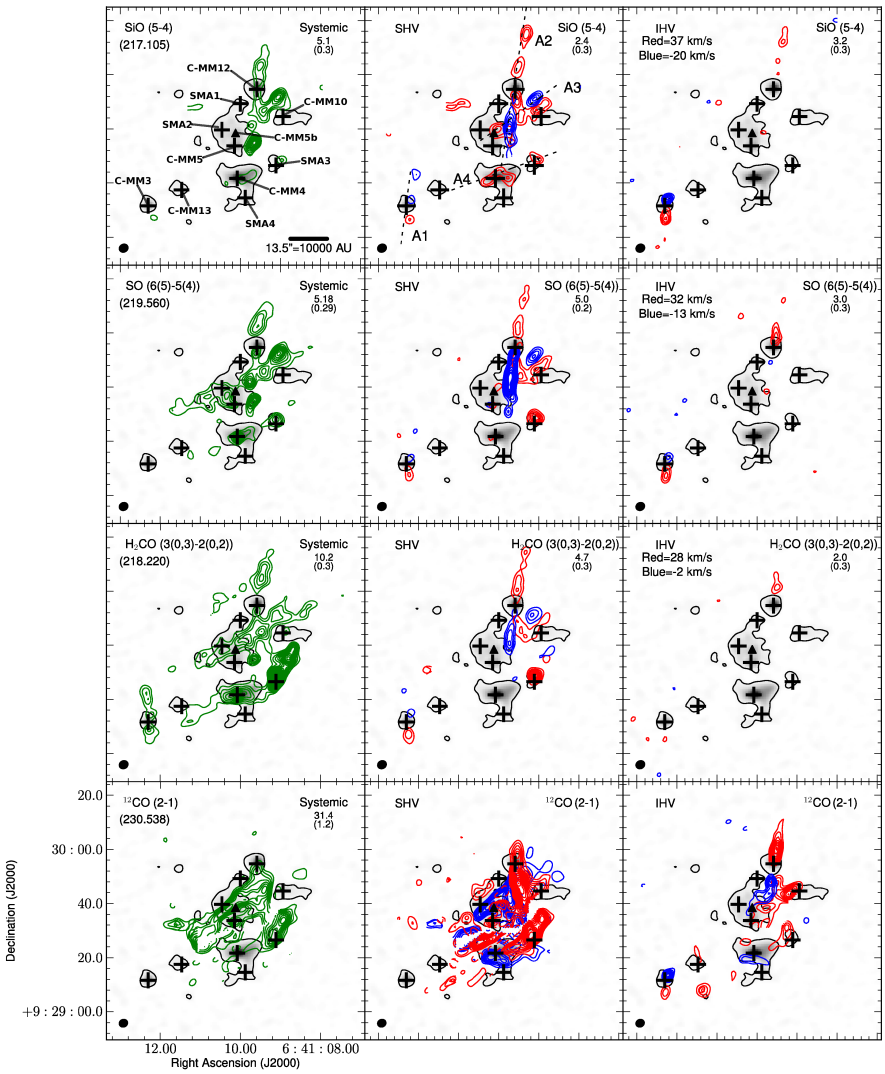

Figure 3.6: Integrated intensity maps (coloured contours) of emission at systemic (left column), SHV (middle column) and IHV (right column) velocities (see text for discussion) for the indicated transitions, overlaid on the SMA 1.3 mm continuum image (greyscale and black contour, contour level $3\sigma = 6$ mJy/beam). The velocity bins are taken with respect to the assigned $v_{\rm LSR}$'s (see Section 3.4.2.1 for a full discussion). The maximum velocity extent of the emission is given at top left in the IHV panels, except for ^{12}CO (2-1), where the maximum velocity differs significantly from outflow to outflow across the map (see Section 3.4.2.2). Contour levels are from $3\,\sigma$ to peak, in steps of $1\,\sigma$. The peak and rms (in Jy beam^{-1} km s^{-1}) are given at upper right in each panel, except for ^{12}CO. For ^{12}CO (2-1), the contoured rms levels are: SHV, red: 1.9 Jy.beam^{-1} km s^{-1} (C-MM3/C-MM13), 1.9 Jy.beam^{-1} km s^{-1} (other sources); SHV, blue: 1.4 Jy.beam^{-1} km s^{-1} (C-MM3/C-MM13), 1.9 Jy.beam^{-1} km s^{-1} (other sources); IHV, red: 1.0 Jy.beam^{-1} km s^{-1} (C-MM3/C-MM13), 1.4 Jy.beam^{-1} km s^{-1} (other sources); IHV, blue: 0.4 Jy.beam^{-1} km s^{-1} (C-MM3/C-MM13), 0.6 Jy.beam^{-1} km s^{-1} (other sources). In all panels, black pluses (+) mark the positions of the ten millimetre continuum peaks from the dendrogram analysis, and the black triangle marks the position of C-MM5b. The possible outflow axes shown in Figure 3.5 are overlaid for reference in the top, middle panel (the SHV emission of SiO).

In the SHV regime, collimated red- and blueshifted emission centred on C-MM3 and C-MM12 is detected in SiO, SO, and H_2CO. The ^{12}CO emission in the SHV regime is affected by poorly-imaged extended structure and confusion with the surrounding cloud, making it difficult to identify outflows in ^{12}CO in this velocity range. In the IHV regime, both lobes of the outflow associated with C-MM3 are detected in emission from SiO and SO, while no emission from H_2CO is observed towards this outflow. Towards C-MM12 only the redshifted lobe of the outflow associated with C-MM12 is detected and is traced by all three lines; SiO, SO, and H_2CO (Figure 3.6). The IHV ^{12}CO emission displays a similar morphology to the SiO and SO SHV and IHV molecular line emission tracing bipolar molecular outflows driven by C-MM3 and C-MM12.

While the high-velocity emission along the A1 and A2 axes can be clearly identified as bipolar molecular outflows driven by (respectively) C-MM3 and C-MM12, the nature of the emission along axes A3 and A4 is less clear. Along axis A3, red- and blueshifted emission is detected in the SHV regime in multiple tracers (SiO, SO and H_2CO), but cannot clearly be traced back to a driving source. In the IHV regime, only redshifted ^{12}CO is detected, with no obvious blueshifted counterpart. Along axis A4, redshifted SHV SiO emission is observed towards both C-MM4 and SMA3, while (redshifted) SO and H_2CO emission are only observed towards SMA3. In the IHV regime, only ^{12}CO is detected in the vicinity of axis A4: while both redshifted (near SMA3) and blueshifted (south of C-MM4) emission are present, these potential lobes are not centred on a millimetre continuum source. The velocity extents of the A3 and A4 emission are also more modest than those of the A1 and A2 outflows. For ^{12}CO (2-1), the maximum redshifted velocity is $\sim$38 kms^{-1}, 32 kms^{-1}, 28 kms^{-1}

and 24 kms^{-1} for A1 (C-MM3 outflow), A2 (C-MM12 outflow), A3, and A4, respectively. The minimum velocity for blueshifted ^{12}CO emission is $-17.2\,\mathrm{kms}^{-1}$ for A1 (C-MM3 outflow) and $-2.8\,\mathrm{kms}^{-1}$ for A2 (C-MM12 outflow) and A4 respectively.

To examine the outflow kinematics in greater detail, Figure 3.7 presents SiO, SO, H_2CO and ^{12}CO spectra at the positions labelled in Figure 3.5 (positions are numbered 1-14), along the potential outflow axes A1, A2, A3, and A4. Work by Codella *et al.* (2014), Tafalla *et al.* (2010), and Lee *et al.* (2010) has identified similarities between SiO and SO emission at high velocities, and if this is also the case in NGC 2264-C is explored here. As shown in Figure 3.6, SiO and SO exhibit similar morphologies; the spectra, however, reveal a number of differences. For example, towards C-MM4, along axis A4, the SO emission is considerably stronger than the SiO emission (the SiO emission along axis A4 is >50% weaker than the SiO emission along the other three potential outflow axes). The SO emission is also stronger towards position 7 along axis A2, over the velocity range $\sim$0-9 kms^{-1}. Elsewhere in the field, the SiO emission is stronger than the SO emission. This is most prominent at the continuum peak of C-MM12 (position 6) and at the northernmost position on the A2 axis (position 4). Close examination of the line profiles also reveals a velocity gradient in ^{12}CO along axis A4, from redshifted at position 12 to blueshifted at position 14. This ^{12}CO emission is lower-velocity than observed towards axes A1 and A2 and the SiO emission is also considerably narrower towards A4 than along A1 or A2.

It should be noted that SiO(5-4) emission associated with outflows from low-mass (proto)stars is unlikely to be detected as extended, collimated structures in these SMA observations. Scaling the results of Gómez-Ruiz *et al.* (2013)

and Codella *et al.* (2014) to the distance of NGC 2264-C and adjusting for the difference in beam sizes, the strongest SiO (5-4) emission from either of those previous works, would only be detected here at the $\sim$4-8 σ level. In addition, in both the JCMT and SMA observations, the width of the collimated emission appears to be limited by size of the beam.

3.4.2.3 Candidate Millimetre CH_3OH Masers

A notable feature of Figure 3.4 is the very strong 229.759 GHz CH_3OH emission associated with the "ridge". The 229.759 GHz CH_3OH 8(-1, 8)-7(0, 7)E transition is a known Class I methanol maser, first reported towards DR21 (OH) and DR21 West by Slysh *et al.* (2002) based on observations with the IRAM 30-m telescope. Probable maser emission in this transition is often seen in SMA observations of massive star-forming regions (e.g. Qiu & Zhang 2009; Fontani *et al.* 2009; Fish *et al.* 2011; Cyganowski *et al.* 2011, 2012, and references therein). Most recently, Hunter *et al.* (2014) directly demonstrated the maser nature of 229.759 GHz CH_3OH emission in NGC6334I(N), by showing that the observed line brightness temperature (T_B) is greater than the upper energy of the transition ($E_{\rm upper}$) in very high-resolution SMA observations.

To investigate the nature of the 229.759 GHz CH_3OH emission in NGC 2264-C, Figure 3.8 presents integrated intensity maps and corresponding line profiles for the CH_3OH 8(-1, 8)- 7(0 , 7) E, CH_3OH 8(0, 8)- 7(1 , 6) E and CH_3OH 3(-2, 2)- 4(-1, 4) E transitions at three locations where the CH_3OH 8(-1, 8)- 7(0 , 7) E 229.759 GHz emission is strongest. These are the ridge, along with the redshifted outflow lobes of both C-MM3 and C-MM12. As shown in Figure 3.8, the 229.759 GHz CH_3OH emission in the ridge is more than twice as strong as

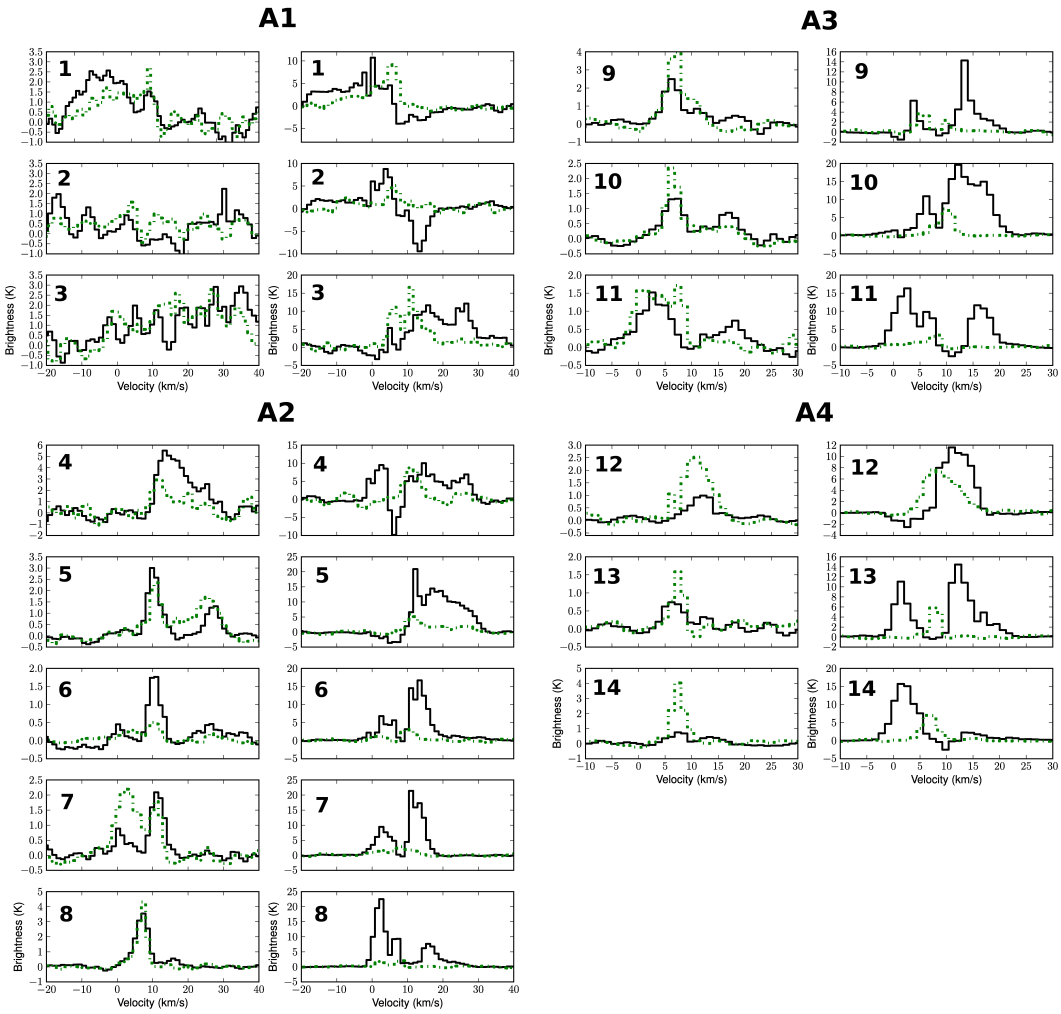

Figure 3.7: Spectra of SiO (5-4), SO 6(5)-5(4), H_2CO 3(0, 3)- 2(0, 2) and ^{12}CO (2-1) extracted at the positions labelled in Figure 3.5. The spectra are grouped by (potential) outflow axis, with the position number given in the top left corner of each panel. For each position, the left panel shows SiO (5-4) (solid black line) and SO 6(5)-5(4) (dashed green line) and the right panel shows ^{12}CO (2-1) (solid black line) and H_2CO 3(0, 3)- 2(0, 2) (dashed green line). The H_2CO 3(0,3)- 2(0, 2) emission has been scaled up by a factor of two in all spectra.

that towards the redshifted outflow lobes of either C-MM3 or C-MM12.

Like most previous 229 GHz studies (with the notable exception of Hunter *et al.* 2014), these SMA observations do not have sufficient angular resolution to establish masing in the 229.759 GHz line based on its brightness temperature. Slysh *et al.* (2002) proposed the ratio of the 229.759 and 230.027 GHz CH_3OH lines as a diagnostic of maser emission, with values of 229.759/230.027>3 indicating nonthermal 229.759 GHz emission. However, it should be noted, that the 230.027 GHz line is undetected at all three positions, and the 3σ limit is used to calculate the line ratios (see Table 3.5 for the 3σ limits towards each position). At two positions in the field, this line ratio is >3: towards the redshifted lobe of the C-MM3 outflow and towards the strongest 229.759 GHz emission in the ridge feature, where the ratio is considerably higher at >45. Furthermore, throughout the ridge structure the line ratio is consistently greater than 8. By comparison, the line ratio towards the C-MM4 continuum peak is < 2, consistent with thermal emission from warm gas (Section 3.5.1.1). As the rms noise increases towards the edge of the beam, the 3σ limits for the 230.027 GHz line for both C-MM3 and C-MM12 are considerably higher than found for the ridge. However, if the 3σ limit from 230.027 GHz line at the position of C-MM3 is instead used for the line ratio at the ridge position, a line ratio of $\sim$9 would still be obtained towards the ridge. Table 3.5 presents fits to the 220.078, 229.759, and 230.027 GHz CH_3OH lines at the three positions shown in Figure 3.8. Emission from 229 GHz CH_3OH masers often coincides spatially and spectrally with emission in lower-frequency Class I CH_3OH maser transitions (e.g. Cyganowski *et al.* 2011, 2012; Fish *et al.* 2011).

Class I CH_3OH maser emission, in the from of the 44 GHz transition, was

initially observed to the west of IRS1 in the direction of the ridge feature by (Haschick *et al.* 1990). More recently, Slysh & Kalenskii (2009) have identified three 44 GHz maser spots with the VLA (resolution 0.15″) coinciding spatially with the ridge (positions shown in Figure 3.8). The strongest of these three 44 GHz maser spots is coincident with the position of the strongest 229 GHz candidate maser emission found here. Furthermore, the 229/230 GHz ratio is found to be >15 at the position of all three 44 GHz maser spots. The $v_{\rm LSR}$ velocities of the 229 GHz emission at each of the three maser spots are 8.53 $\rm kms^{-1}$, 8.68 $\rm kms^{-1}$, and 8.48 $\rm kms^{-1}$, (for increasing declination in Figure 3.8) and are within $\sim$1 $\rm kms^{-1}$ compared with the 44 GHz $v_{\rm LSR}$ from Slysh & Kalenskii (2009) of 7.22 $\rm kms^{-1}$, 7.59 $\rm kms^{-1}$, and 7.72 $\rm kms^{-1}$ respectively. The coincidence of the class I 44 GHz CH_3OH maser spots, both spatially and spectrally with the 229.759 GHz emission in the ridge, supports the interpretation that the 229.759 GHz transition is masing in the ridge.

3.5 Discussion

3.5.1 Nature of the Millimetre Continuum Peaks

3.5.1.1 Temperature Estimates from the Molecular Line Emission

Methyl cyanide (CH_3CN) is commonly used to estimate the temperature of warm/hot gas in star forming regions. Using the method of rotational diagrams and assuming optically thin emission and LTE (e.g. Loren & Mundy 1984, Zhang *et al.* 1998), gas temperatures may be derived from the relative integrated intensities of the K-ladder components. Compact CH_3CN emission is identified

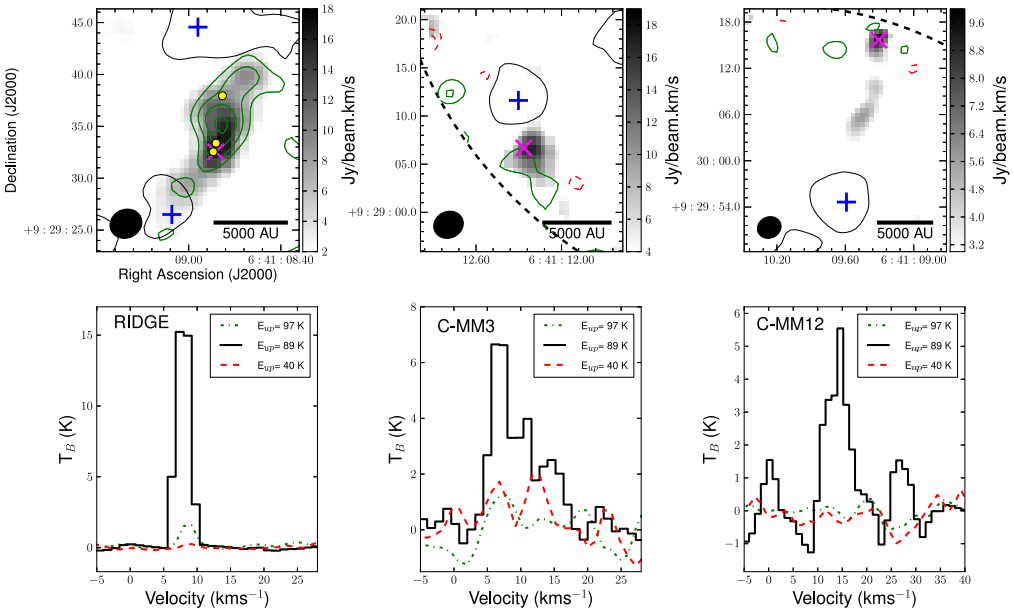

Figure 3.8: Top: Zoom views of integrated intensity maps, corrected for the primary beam response, of CH_3OH 8(-1, 8)- 7(0 , 7) E (229.759 GHz, greyscale), CH_3OH 8(0, 8)-7(1, 6) E (220.078 GHz, solid green contours) and CH_3OH 3(-2, 2)- 4(-1, 4) E (230.027 GHz, dashed red contours) towards the ridge feature, and the redshifted outflow lobes from C-MM3 and C-MM12. The integrated velocity ranges are the same as in Figure 3.4. Contour levels: CH_3OH 8(0, 8)- 7(1 ,6) E (220.078 GHz): 3, 6, 9, 12 σ, for 1 σ values of 0.2, 0.6 and 0.6 Jy beam^{-1} km s^{-1} towards the ridge, C-MM3 and C-MM12, respectively. CH_3OH 3(-2, 2)- 4(-1, 4) E (230.027 GHz): 3, 5 σ for 1 σ values of 0.2, 0.4 and 0.5 Jy beam^{-1} km s^{-1} towards the ridge, C-MM3 and C-MM12, respectively. The synthesized beam is shown at lower left in each panel. The blue pluses (+) mark the positions of the millimetre continuum peaks; the solid black line is the 3σ contour of the 1.3 mm continuum emission. The thick dashed line in the C-MM3 and C-MM12 images is the 10% level of the primary beam response. The yellow circles show the positions of the three 44 GHz CH_3OH maser spots detected in Slysh & Kalenskii (2009). Bottom: Spectra of the three CH_3OH transitions. The spectra are extracted at the position of the peak CH_3OH 8(-1, 8)-7(0 , 7) E (229.759 GHz) emission towards the ridge, and the outflows of C-MM3 and C-MM12, marked by a magenta cross (x) (see Table 3.5 for the coordinates of these positions).

Table 3.5: Methanol Line Fits at positions of Candidate 229.759 GHz CH_3OH Masers in NGC 2264-C

Methanol Transition	ν (GHz)	E_{upper} (K)	RA (J2000)	DEC (J2000)	Fitted Line Parameters: Intensity[a] (Jy.beam^{-1})	V_{centre} [a] (kms^{-1})	Width[a] (kms^{-1})	$\int S dv$ [a] (Jy.beam^{-1} kms^{-1})
Ridge								
8(0 , 8)- 7(1 , 6) E	220.078	96.6	06 41 08.8	+09 29 32.5	0.66 (0.03)	8.63 (0.04)	2.29 (0.11)	1.63 (0.10)
8(-1, 8)- 7(0 , 7) E	229.759	89.1	06 41 08.8	+09 29 32.5	6.64 (0.14)	8.53 (0.03)	2.45 (0.06)	17.31 (0.58)
3(-2, 2)- 4(-1, 4) E	230.027	39.8	06 41 08.8	+09 29 32.5	<0.14*	–	–	–
C-MM3 Outflow								
8(0 , 8)- 7(1 , 6) E	220.078	96.6	06 41 12.3	+09 29 06.7	<0.55*	–	–	–
8(-1, 8)- 7(0 , 7) E	229.759	89.1	06 41 12.3	+09 29 06.7	2.24 (0.4)	8.16 (0.58)	5.79 (1.63)	13.84 (4.81)
3(-2, 2)- 4(-1, 4) E	230.027	39.8	06 41 12.3	+09 29 06.7	<0.74*	–	–	–
C-MM12 Outflow								
8(0 , 8)- 7(1 , 6) E	220.078	96.6	06 41 09.3	+09 30 15.7	<0.50*	–	–	–
8(-1, 8)- 7(0 , 7) E	229.759	89.1	06 41 09.3	+09 30 15.7	1.74 (0.21)	14.70 (0.30)	4.85 (0.70)	8.99 (1.70)
3(-2, 2)- 4(-1, 4) E	230.027	39.8	06 41 09.3	+09 30 15.7	<0.90*	–	–	–

Notes.

[a] The formal errors from the single Gaussian fits are given in ().

* Non detection, the value given is the 3σ limit. This is taken from the rms in the spectra extracted from the beam corrected image cubes at each position.

towards two 1.3 mm continuum peaks, C-MM4 and C-MM5. The highest-energy K component detected (at $>3\sigma$) is K = 3 towards C-MM4 and K = 4 towards C-MM5, with an upper-level energies of E_{upper} =133 K and E_{upper} =183 K respectively. Following the procedure in Araya *et al.* (2005), estimated temperatures of $\sim$90 $\pm$48 K, $\sim$108 $\pm$36 K and CH_3CN column densities of $\sim 8.6\times10^{12}$ cm^{-2} and $\sim 1.6\times10^{13}$ cm^{-2} , are derived for C-MM4 and C-MM5 respectively from a linear regression fit (accounting for the uncertainties in the line integrated intensities) to the rotational diagrams, shown in Figure 3.9. Since fewer K components are detected towards C-MM4 (and the K=3 detection is marginal, at $\sim 3\sigma$), the temperature for this source is also estimated from the five detected CH_3OH transitions, by applying the rotation diagram method (e.g. Goldsmith & Langer 1999). The E_{upper} of the five detected CH_3OH transitions ranges from $\sim$40-100 K; following Cyganowski *et al.* (2011), a rotation temperature, from a linear regression fit, of $\sim$46$\pm$11 K is estimated for C-MM4. This suggests the CH_3OH emission is somewhat more spatially extended than the CH_3CN emission for this source.

3.5.1.2 Mass Estimates from the SMA 1.3 mm Continuum Emission

Thermal emission from dust, and free-free emission from ionised gas can both contribute to the observed continuum flux at millimetre wavelengths. To estimate the contribution from ionised gas, the 3.6 cm VLA flux densities from Reipurth *et al.* (2004) are extrapolated to 1.3 mm, assuming $S_\nu \propto \nu^{-0.1}$. VLA2 (see Table 2 from Reipurth *et al.* 2004) is coincident with the continuum peak C-MM4, and VLA3, and VLA4 fall within the 15σ continuum contour level

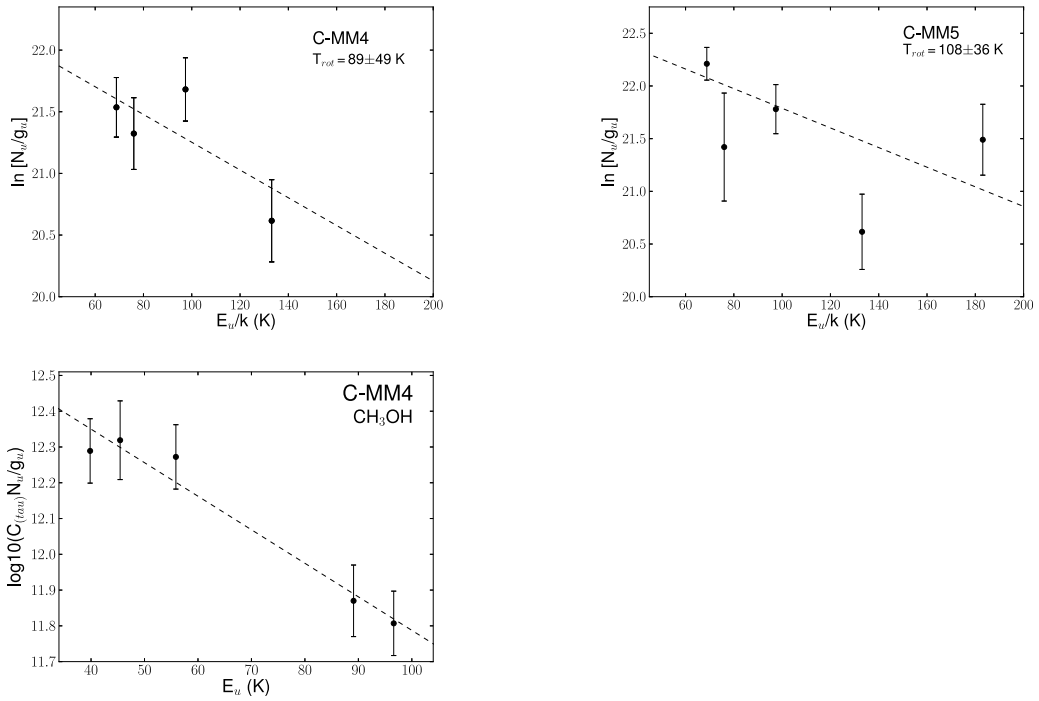

Figure 3.9: Rotation diagrams for the CH_3CN J=12_K-11_K transition observed towards the continuum peaks of CMM4, and C-MM5 (top two panels), along with the CH_3OH transitions of C-MM4 (bottom panel).

of C-MM5 with VLA4 coincident with the peak of the continuum emission. Extrapolating the 3.6cm emission from the component VLA2 for C-MM4, and total emission from both VLA3 and VLA4 for C-MM5, indicates the estimated ionised component is negligible for both C-MM4 and C-MM5 (<1% contribution at 1.3 mm from free-free emission). Therefore, the thermal contribution from the dust dominates the emission at 1.3 mm and the gas masses are estimated assuming a simple isothermal model of optically thin dust emission using,

$$M_{gas} = \frac{RF_\nu D^2}{\kappa_m(\nu)B_\nu(T_d)}, \tag{3.1}$$

where R is the gas to dust mass ratio (assumed to be 100), F_ν is the flux density, D is the distance to the region, $\kappa_m(\nu)$ is the dust opacity, $B_\nu(T_d)$ is the Planck function and T_d is the (assumed) dust temperature. A value of κ_m =1.0 cm^2g^{-1} at 1.3 mm is adopted, which assumes grains with ice mantles in high density regions ($10^8 cm^{-3}$; Ossenkopf & Henning 1994).

Table 3.6 presents mass estimates for a range of assumed dust temperatures, based on greybody fits to the large-scale dust emission (Ward-Thompson *et al.* 2000). Two temperature components –of 17 K and 38 K– were required to fit the SED (Ward-Thompson *et al.* 2000), and they are adopted as the lower and upper-limit temperatures for the mass estimates. This approach is adopted because, for the majority of the dust continuum sources (C-MM4 and C-MM5 excepted, Section 3.5.1.1), gas temperatures cannot be estimated from this SMA data. For C-MM4 and C-MM5, Table 3.6 also presents mass estimates assuming T_{dust} =T_{gas} and the gas temperatures from Section 3.5.1.1. It should be noted that the dust temperatures at the scales probed by these SMA observations are likely to be higher than those measured by Ward-Thompson *et al.* (2000) from single-dish data. As a result, the mass estimates obtained assuming the single-dish dust temperatures (which range from $\sim$0.1$-$7 $M_\odot$) are likely upper limits for the SMA cores.

Despite the (considerable) uncertainties introduced by the dust temperature, C-MM3, C-MM4, and C-MM12 appear as the three most massive 1.3 mm continuum sources: they are the only sources with estimated masses >1 $M_\odot$ for all assumed temperatures. Notably, the outflow-driving sources C-MM3 and C-MM12 are both spatially compact, in contrast to C-MM4 (Table 3.1, Figure 3.2). Furthermore, the mass estimate for C-MM5 in Table 3.6 encompasses

Table 3.6: Mass estimates for 1.3 mm continuum sources in NGC 2264-C. The first column gives the source name, and the second and third columns provide mass estimates assuming temperatures of 17 K and 38 K respectively. The fourth and fifth columns provide mass estimates (where possible) using the temperatures derived from the CH_3CN and CH_3OH rotation diagrams.

Source	Mass 17 K ($M_\odot$)	Mass 38 K ($M_\odot$)	Mass CH_3CN ($M_\odot$)	Mass CH_3OH ($M_\odot$)
C-MM3	5.4	2.0	–	–
C-MM4	6.8	2.5	$1.0^{+1.3}_{-0.4}$	$2.0^{+0.8}_{-0.4}$
C-MM5	1.8	0.7	$0.21^{+0.1}_{-0.1}$	–
C-MM10	1.6	0.6	–	–
C-MM12	3.8	1.4	–	–
C-MM13	0.7	0.3	–	–
SMA1	0.3	0.1	–	–
SMA2	0.3	0.1	–	–
SMA3	0.4	0.1	–	–
SMA4	0.4	0.1	–	–

both C-MM5 and C-MM5b, and so may be an overestimate for the mass of C-MM5 alone. The newly identified millimetre continuum sources (e.g. SMA1, SMA2, SMA3, and SMA4) have the lowest estimated masses, $\leq 0.4\,M_\odot$. The $5\,\sigma$ sensitivity limit of the observations corresponds to $\sim 0.14\,M_\odot$ and $\sim 0.05\,M_\odot$ for 17 and 38 K, respectively.

3.5.1.3 Notes on Individual Millimetre Continuum Sources

The 1.3 mm continuum sources in NGC 2264-C display a wide range of associated molecular line emission in the SMA data. C-MM4 exhibits the richest line emission, with a hot-core-like spectrum, while C-MM3, C-MM13, and SMA-4 are not associated with any molecular line emission that can be directly associ-

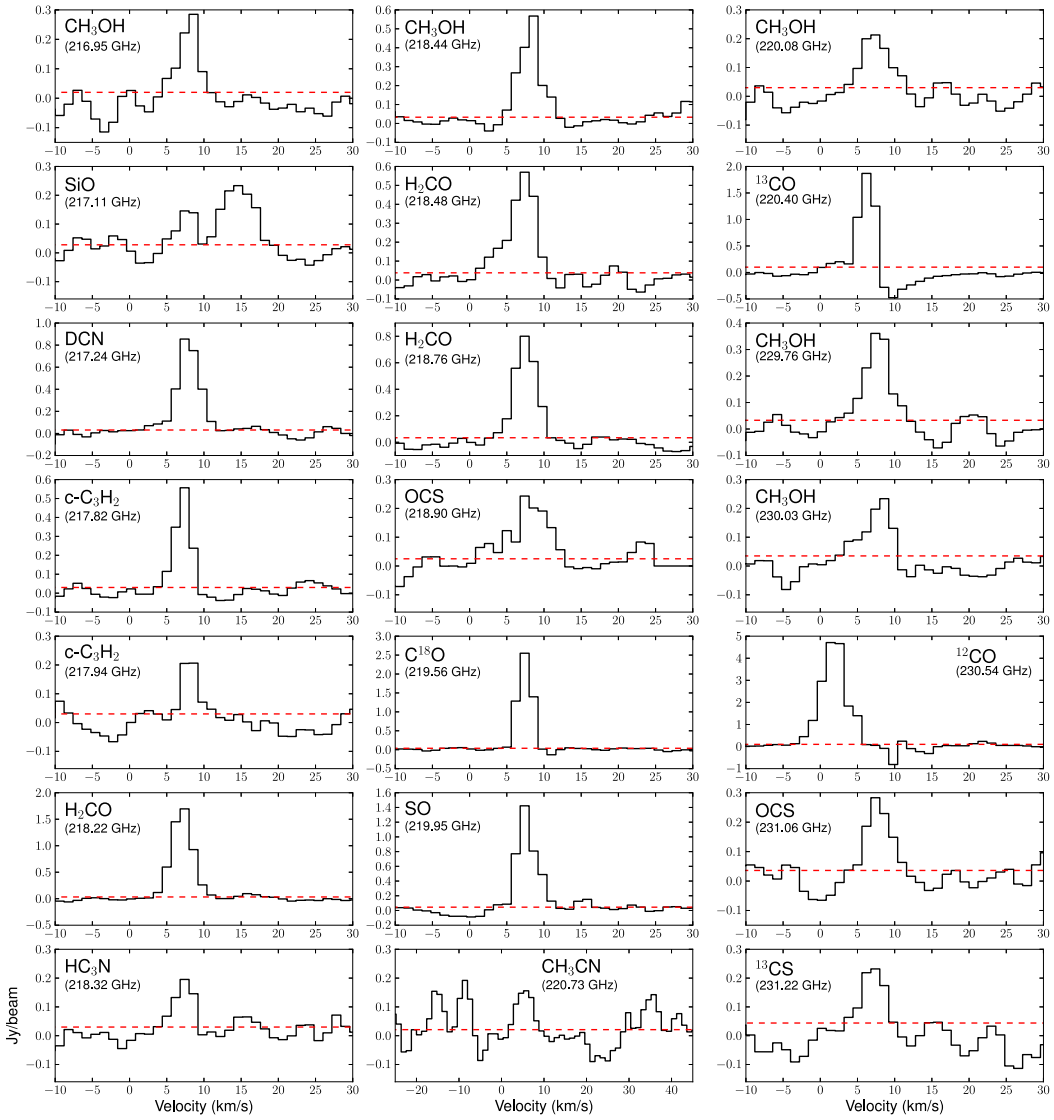

Figure 3.10: Spectra of transitions detected at the continuum peak of C-MM4. The spectra are extracted from a single pixel (at the continuum peak of C-MM4) in the beam corrected image cubes from each transition detected above 5σ. The CH_3CN ladder, centred on the K=2 transition, is shown and includes all K ladder transition detected at >3 and $< 5\ \sigma$. The horizontal red dashed line is the spectral rms noise. The transition and rest frequency are presented in the top left corner of each panel.

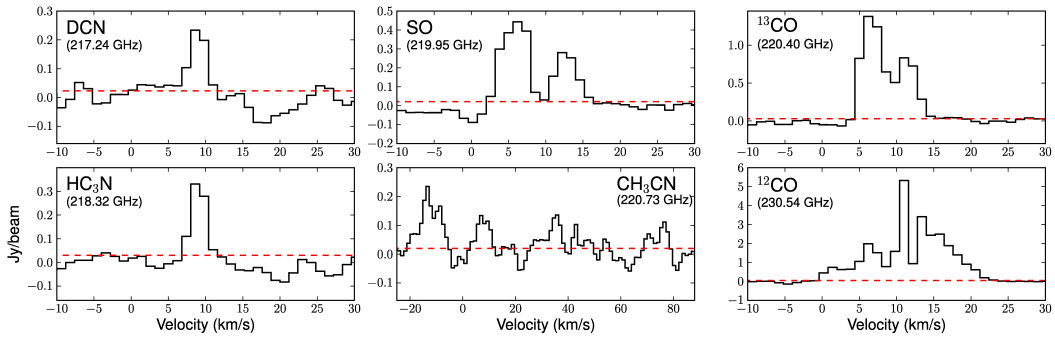

Figure 3.11: Spectra of transitions detected at the continuum peak of C-MM5, extracted from a single pixel from the beam corrected image cubes, of each transition detected above 5σ. The CH_3CN ladder, centred on the K=2 transition, is shown and includes transitions detected at >3 and < 5 σ. The horizontal red dashed line is the spectral rms noise. The transition and rest frequency are presented in the top left corner of each panel.

ated with the millimetre continuum cores (as opposed to e.g. outflow emission, Section 3.4.2.1). The presence/absence and relative strengths of molecular lines detected in wide-bandwidth interferometric observations may be indicative of evolutionary state; however, there is a degeneracy with core mass (e.g. Zhang *et al.* 2007; Galván-Madrid *et al.* 2010; Cyganowski *et al.* 2012; Wang *et al.* 2014). The nature of the individual 1.3 mm continuum sources in NGC 2264-C is discussed below, with reference to their molecular line emission (or lack thereof) and their 24/70μm properties (also indicative of evolutionary state, e.g. Battersby *et al.* 2011).

CMM-3: The molecular line emission observed in the vicinity of CMM-3 with the SMA is associated with the outflow driven by this millimetre continuum core (Section 3.4.2.2, see also Saruwatari *et al.* 2011). No compact molecular line emission is detected coincident with the millimetre continuum source; this may, however, be due to sensitivity limitations, as CMM-3 is located at the

$\sim$20% power level of the SMA primary beam. No Herschel PACS 70μm or Spitzer MIPSGAL 24μm emission is detected towards CMM-3[1], indicating that CMM-3 is likely young; the detection of N_2H^+ (1-0) (Peretto *et al.* 2007) and the enhancement of SCUBA 450 μm emission are also consistent with youth.

C-MM3 is one of the most massive cores in NGC 2264-C (based on these SMA mass estimates, Section 3.5.1.2). The SMA observations recover about $\sim$30% of the 1.3 mm single dish flux density (e.g. Peretto *et al.* 2006; Ward-Thompson *et al.* 2000). The mass estimate obtained here for C-MM3 is lower than those of Saruwatari *et al.* (2011)[2], Peretto *et al.* (2006), Peretto *et al.* (2007), and Ward-Thompson *et al.* (2000), due to differences in spatial filtering (when comparing interferometric and single-dish data), and in assumed opacities and dust temperatures (along with the recently revised distance to the region). If the temperature, opacity (scaled to 1.3mm), and distance assumed by Peretto *et al.* (2007) is adopted, the mass estimate from this data for C-MM3 is now comparable to the mass estimate Peretto *et al.* (2007) from based on their PdBI observations. Interestingly, Peretto *et al.* (2007) suggest that C-MM3 harbours a disc of mass 1.1 $M_\odot$, which would be a substantial fraction of the estimated mass of $\sim$2-5 $M_\odot$ (Table 3.6).

C-MM4 is the most molecular line rich core, displaying a hot core like spectrum. Compact molecular line emission with E_{upper} temperatures of 55-133 K from typical hot core tracers such as OCS, CH_3CN, CH_3OH and HC_3N is coincident with the continuum peak on scales of $\sim$0.01 pc. Figure 3.10 displays the

[1]Strong 70μm, 24μm, and 2.2μm emission are observed to the south-east of C-MM3. This emission is not directly associated with C-MM3, but is from a separate star with a weak, diffuse nebulosity surrounding it.

[2]The measured flux density for C-MM3 agrees within $\sim$20% with that reported by Saruwatari *et al.* (2011) based on SMA observations with similar spatial resolution.

line profiles for all transitions observed towards the continuum peak of C-MM4. In addition to the compact emission, several transitions tracing more diffuse emission are also identified such as N_2H^+ (1-0) (Peretto *et al.* 2007), DCN, and $C^{18}O$. No clear outflow is identified in the molecular line emission towards this core. The FIR 70μm Herschel emission (see Figure 3.1) is dominated by the bright infrared source AFGL 989-IRS1 in this region. However, at the continuum peak of C-MM4 the 70μm flux is more than $\sim$50% brighter compared with the any other position at a similar radii from IRS1, suggesting that C-MM4 is contributing to the 70 μm flux. In addition, 3.6 cm emission (VLA2 in Reipurth *et al.* 2004) is detected coincident with the continuum peak. Although, no 24 μm emission is detected towards the continuum peak of C-MM4.

A 1.3 mm flux of 496 mJy is found for this source, which recovers approximately half of the single dish flux (e.g. Peretto *et al.* 2006; Ward-Thompson *et al.* 2000). Peretto *et al.* (2006) estimate a mass of 35 $M_\odot$ from their single dish observations, which is comparable to their single dish mass estimate for C-MM3 of $\sim$40$M_\odot$. However, the morphology of C-MM4, is noticeably more extended than C-MM3. The molecular line emission suggests C-MM4 is also likely warmer than C-MM3. The mass estimates for C-MM4 using the assumed temperatures from the CH_3CN and CH_3OH rotational diagrams are $\sim$1-2 $M_\odot$. These results indicate C-MM4 is potentially lower in mass and more evolved than C-MM3.

C-MM5 coincides with the position of the IR-bright B2 $\sim$2000 $L_\odot$ star AFGL 989-IRS1. This well studied source, dominates both the 24μm and 70μm emission in this region. Very little molecular line emission is detected towards this continuum peak. The molecular line emission detected towards the contin-

uum peak is shown in Figure 3.11. Furthermore, there is no obvious indication of the presence of an outflow driven by this source in any of the molecular line emission. In spite of this, a twisted jet feature was detected at 1.65μm, and 2.2μm by Schreyer *et al.* (1997) located to the north-west of this source. Moreover, this sources also drives a dense stellar wind (Bunn *et al.* 1995) that has excavated a low density cavity around AFGL 989-IRS1 (Schreyer *et al.* 2003). This may account for the lack of molecular line emission detected towards this source, if the low density cavity created by the wind/jet has removed part or all of the outer envelope. While molecular line emission from the lower energy transitions is lacking, compact emission from CH_3CN and HC_3N is coincident with peak of the continuum emission. Grellmann *et al.* (2011) have previously identified a disc towards this source. As emission from CH_3CN is well known to trace discs (e.g. Cesaroni *et al.* (2014) and references therein), the emission from CH_3CN and HC_3N may be related to the presence of a disc in AFGL989-IRS1. On the other hand, as C-MM5, unlike C-MM4, does not display a typical hot core like spectrum, and given CH_3CN has also been previously detected in low velocity shocks and in outflows (e.g. Bell *et al.* 2014; Csengeri *et al.* 2011), the emission in C-MM5 from these compact tracers could also be due to shocks. An additional indication of evolution towards AFGL 989-IRS1/C-MM5 is the detection of 3.6 cm emission (VLA sources 3 and 4 Reipurth *et al.* 2004).

The 1.3 mm continuum flux towards C-MM5 only recovers $\sim$25% of the single dish flux. However, the 1.3 mm flux is taken from C-MM5 and not the entire parent structure which also includes the new detections SMA1 and SMA2. Peretto *et al.* (2006) estimate a mass of $\sim$18$M_\odot$ from the single dish observations. If the gas mass is calculated using the temperature estimated from

the rotational diagrams of the CH_3CN ladder, a mass of $\sim$0.2 $M_\odot$ is found for C-MM5 which is lower than for C-MM3 or C-MM4. Furthermore, this mass estimate potentially incorporates an additional source, C-MM5b, and the gas mass estimated from the 1.3 mm emission for C-MM5 may be lower again. As discussed previously in section 3.4.1, it is suggested that C-MM5b is likely a separate source which at the current resolution cannot be spatially resolved. The presence of the strongest 70μm, 24μm, 1.65μm, and 2.2μm, along with the previous detection of a disc, in addition to 3.6 cm radio continuum, suggest that C-MM5 is likely the most evolved source in this data.

C-MM10 displays very little molecular line emission. However, 70μm emission is observed towards the continuum peak (see Figure 3.1). This source is notably extended (see Figure 3.2) compared with the compact morphology of cores such as C-MM3 and C-MM12. Furthermore, only $\sim$10% of the single dish flux reported in Peretto *et al.* (2006) is recovered, which may suggest that the bulk of the 1.3 mm emission associated with this source is from an extended region that is currently resolved out. C-MM10 is likely a low mass source, but its exact nature is unclear.

CMM-12 lacks emission from typical hot core tracers. Only compact emission from OCS (E_{upper} =99.8 K) is detected towards the continuum peak. Furthermore, the majority of the molecular line emission in the vicinity of this source (such as from SiO, H_2CO and SO) is from the outflow driven by this millimetre continuum core, and not directly associated with the core. As emission from OCS has previously been suggested to be tracing the inner regions of the outflow (e.g. Cyganowski *et al.* 2011), the OCS emission is likely also tracing the outflow, rather than the continuum peak. C-MM12 also lacks any

obvious 70μm or 24μm emission. The estimated mass for this source is 1.4-3.8 $M_\odot$, approximately half of the estimated mass for C-MM3. A noticeably high proportion of the single dish flux ~90% is recovered. The single dish mass is estimated to be ~9 $M_\odot$ Peretto *et al.* (2006). These results suggest C-MM12 is likely a low/intermediate mass protostar.

C-MM13 displays one of the most molecular line poor spectra. Furthermore, there is no enhancement of 450 μm, 70 μm or 24 μm emission towards C-MM13. However, the N_2H^+(1-0) line displays the strongest emission coincident with this peak (Peretto *et al.* 2007) (see Figure 3.13). The estimated mass for C-MM13 is in the range 0.3-0.7 $M_\odot$, compared with ~8 $M_\odot$ from Peretto *et al.* (2007). If the mass is estimated assuming the parameters from Peretto *et al.* (2007), the mass would be ~2 $M_\odot$, which is approximately 4 times less. Furthermore, C-MM13 is not detected in the single dish observations. These results suggest C-MM13 is a low mass, likely young protostar. However, its nature, as with the continuum peak C-MM10, is unclear.

SMA1, SMA2, SMA3, and SMA4 are all new (>4σ) 1.3 mm detections. None of these newly detected 1.3 mm continuum peaks display enhancements in either the 450μm, 70 μm or 24μm emission, and only towards SMA4 is there N_2H^+(1-0) emission (Peretto *et al.* 2007). While SMA2 and SMA3 are the most molecular line rich of the four, no emission from the compact tracers is detected towards any of the four new sources. The mass estimates are <0.4 $M_\odot$ for all four, regardless of the gas temperature assumed. Three of the four new detections are nested within a parent tree structure. SMA1 and SMA2 are part of the same parent structure as AFGL 989-IRS1/C-MM5, and SMA1 is spatially coincident with the twisted jet feature to the north of this source.

SMA4 forms part of the same parent structure as C-MM4. Recent observations by Kamezaki *et al.* (2014) have identified an associated water maser towards SMA4. In addition, they note the association of the X-ray source (FMS2-1269) (Flaccomio *et al.* 2006) towards this continuum peak, suggesting that it is an X-ray emitting class 0 source and assign it as C-MM4S. SMA3 is the only new detection that is found as an independent structure. It is spatially coincident with the southern edge of the ridge feature.

3.5.2 Nature of the Ridge

As noted in section 3.4.2.3, a prominent feature in the SMA line observations is the so called "ridge". This feature is detected in all three H_2CO transitions, and three CH_3OH transitions; CH_3OH 4(2 , 2)- 3(1 , 2) (218.440 GHz), CH_3OH 8(0 , 8)- 7(1 , 6) E (220.078 GHz) and CH_3OH 8(−1, 8)- 7(0 , 7) E (229.759 GHz). In all of these transitions the emission is stronger towards the position of the ridge than towards any other location in the region. The emission from these transitions, typically extends over a spatial scale of ∼15000 AU in length (taken along the PA=150 degrees), with a width perpendicular of ∼2000-5000 AU. It is noted that along the length of ridge, the width varies and is not always spatially resolved by the beam. Furthermore, the ridge is not clearly associated with a millimetre continuum peak, only the southern edge of the ridge spatially coincides with the continuum peak SMA3. At this position, compact redshifted emission traced by SiO, SO and H_2CO in the SHV regime, and ^{12}CO emission in the IHV regime is observed. While no blueshifted counterpart is found towards the ridge, there is a possible blueshifted component traced by ^{12}CO along axis

A4 which is also coincident with C-MM4. Thus, the redshifted emission at the southern edge of the ridge may be from an outflow along axis A4 where the associated driving source is not obvious.

Class I masers are typically believed to be associated with outflows (e.g. Plambeck & Menten 1990; Kurtz *et al.* 2004; Cyganowski *et al.* 2009). The ratio of the 229/230 GHz CH_3OH emission (discussed in section 3.4.2.3) is an indication of the non-thermal nature of the 229 GHz emission for ratios>3. The ratio towards the strongest 229 GHz emission in the ridge to be ∼50, compared with ∼3 and <2 towards the outflows of C-MM3 and C-MM12 respectively. While the line ratio towards the ridge is considerably higher than towards C-MM3, it falls within the range of line ratios, 7-100, identified towards the outflow lobes of two extended green objects in Cyganowski *et al.* (2011). Thus, the detection of possible class I CH_3OH maser emission from the 229 GHz transition in this data, in addition to the detection of 44 GHz class I methanol masers (Slysh & Kalenskii 2009), suggests that the nature of the ridge could be due to an outflow. However, the peak position of the potential 229 GHz CH_3OH maser emission is offset from the compact redshifted emission. Voronkov *et al.* (2010) and Voronkov *et al.* (2014) have suggested that class I masers could also be excited in the shocks formed from an expanding HII region. As the ridge sits on the edge a low density cavity driven by AFGL 989-IRS1 (e.g. Schreyer *et al.* 2003; Nakano *et al.* 2003), the maser emission in the ridge could be the result of the dense stellar wind from IRS1 (Bunn *et al.* 1995) colliding with a region of high density ambient material.

3.5.3 Outflow Properties

Two unambiguous, high velocity bipolar outflows, traced by SiO, SO, H_2CO, CH_3OH and ^{12}CO are identified, and are driven by C-MM3 and C-MM12. Furthermore, high velocity ^{12}CO (2-1) emission, in the IHV regime, is found along axes A3 and A4.

Table 3.7, presents the outflow parameters (e.g. outflow length, maximum velocity and dynamical timescale) estimated from both the SiO (5-4) and ^{12}CO (2-1) emission, towards the two clearly defined bipolar outflows in this region driven by C-MM3 and C-MM12. The dynamical timescale is given as T_{dyn}=l_{flow}/v_{max}, where l_{flow} is the observed maximum outflow length on the sky, and v_{max} is given by $v_{max} = |v_{maxchannel} - v_{\rm LSR}|$, where $v_{maxchannel}$ is the velocity of the maximum/minimum channel in the image cube with a 3σ detection. The inclination of the outflow to the line of sight affects both the estimate of the outflow length ($l_{flow(corrected)}$=$l_{flow}/\sin(i)$), maximum velocity ($v_{max(corrected)}$=$v_{max}/\cos(i)$), and thus dynamical timescale. In Table 3.7, the outflow properties are presented for inclinations of both 45 and 60 degrees. Towards C-MM3, the two spatially separated blueshifted components, B1 and B2 (identified by Saruwatari *et al.* (2011) see Figure 3.5), are treated independently and dynamical timescale estimates are provided for both components. For both the blueshifted component B1 and the redshifted lobe, similar maximum lengths, and velocity estimates are found from the SiO (5-4) emission. The dynamical timescales estimated from SiO (5-4) are comparable at ∼300-500 yrs and ∼400-700 yrs for B1 and the redshifted lobe of C-MM3 respectively. In addition, the outflow properties estimated from the ^{12}CO (2-1) emission are

Table 3.7: SiO (5-4) and ^{12}CO (2-1) outflow properties for both the redshifted and blueshifted lobes of the outflows driven by C-MM3 and C-MM12.

Outflow	L ($''$)	v_{max} (kms^{-1})	$v_{(\lvert v_{max}-v_{\rm LSR}\rvert)}$ (kms^{-1})	i ($^\circ$)	l_{flow} (AU)	v_{max} (kms^{-1})	T$_{dyn}$ (years)	S$_v$ ^{b} (Jy.kms^{-1})
SiO (5-4)								
C-MM3 red lobe	6	36.8	29.7	45-60	6200-5100	42-60	700-410	21
C-MM3 B1 ^{a}	4	-19.6	26.7	45-60	4200-3400	38-53	520-300	13
C-MM3 B2 ^{a}	13	-5.2	12.3	45-60	13600-11000	17-25	3700-2100	6
C-MM12 red lobe	22	32.0	23.0	45-60	23000-18700	32-46	3400-2000	67
C-MM12 blue lobe	22	-1.6	10.6	45-60	23000-18700	15-22	7300-4200	20
^{12} CO (2-1)								
C-MM3 red lobe	6	38.0	30.9	45-60	6200-5100	44-62	680-390	68
C-MM3 B1^a	3	-17.2	24.3	45-60	3100-2500	34-49	430-240	30
C-MM3 B2^a	11	-5.2	12.3	45-60	11500-9300	17-25	3100-1800	1
C-MM12 red lobe	19	32	23.0	45-60	19800-16200	33-46	2900-1700	179
C-MM12 blue lobe	17	-2.8	11.8	45-60	17700-14500	17-24	5000-2900	79

Notes.
(^{a}) B1 and B2, which are labelled in Figure 3.5 and mark components of the C-MM3 outflow named by Saruwatari *et al.* (2011). (^{b}) Total integrated intensity calculated from the beam corrected image maps. For SiO, the emission is integrated from the $v_{\rm LSR}$ (7.2 kms^{-1}, and 8.9 kms^{-1} for C-MM3 and C-MM12 respectively) to maximum velocity of the respective lobe see note *c* above. For ^{12}CO (2-1), the emission is integrated over the velocity ranges stated in Table 3.8, which excludes emission at low velocities close to systemic due to confusion. For the B2 component the velocity range is taken from -5.2-0.8 kms^{-1}

Table 3.8: ^{12}CO (2-1) Outflow Properties

Outflow	i [a] (°)	Δv [b] (kms^{-1})	M$_{out}$ (10^{-3}M$_\odot$)	P$_{out}$ [c] (M$_\odot$ kms^{-1})	E$_{out}$ [c] (erg) ($\times 10^{43}$)	$\dot{M}_{out}$ [c] M$_\odot$yr^{-1}) ($\times 10^{-6}$)	$\dot{P}_{out}$ [c] (M$_\odot$ kms^{-1}yr^{-1}) ($\times 10^{-5}$)
C-MM3 red lobe	45-60	15.2-38.0	2.5	0.06-0.08	1.53-3.0	3.6-6.4	8.8-20.5
C-MM3 blue lobe [d]	45-60	−17.2-0.8	1.1	0.02-0.03	0.5-1.0	2.6-4.6	4.6-12.5
C-MM12 red lobe	45-60	16.4-32.0	6.5	0.12-0.17	2.5-4.9	2.2-3.8	4.1-10.0
C-MM12 blue lobe	45-60	-2.8-0.8	2.8	0.04-0.05	0.5-0.9	0.6-1.0	0.8-1.7

Notes.
([a]) Inclination from line of sight the outflow properties are estimated assuming both an inclination of 45° and 60°. ([b]) The velocity range used to estimate the outflow properties. ([c]) Values are calculated from the dynamical timescale estimates from the ^{12}CO (2-1) emission presented in Table 3.7. ([d]) The values presented for the blueshifted outflow lobe of C-MM3 are from the sum of B1 and B2 outflow components shown in Figure 3.5 and $\dot{M}_{out}$ and $\dot{P}_{out}$ are calculated from the dynamical timescale of the B1 component.

similar to the SiO (5-4) estimated outflow properties. The blueshifted emission from B1 is also a slightly lower velocity compared with the redshifted emission, and is approximately $3\,\mathrm{kms}^{-1}$ and $6\,\mathrm{kms}^{-1}$ slower for the SiO (5-4) and ^{12}CO (2-1) emission respectively.

At the position of the more northern blueshifted component, B2, in the C-MM3 outflow, a lower maximum velocity of $\sim$12 kms^{-1} is found. The dynamical timescale for this component is estimated to be $\sim$2000-3500 yrs for both the SiO (5-4) and ^{12}CO (2-1) emission. In both tracers, B2, is approximately an order of magnitude older compared with either the higher velocity blueshifted (B1) or redshifted components. It is suggested, that the outflow driven by C-MM3 may be impacting with dense material, at this position, which is causing it to slow further from the central core. In addition to the B1 and B2 blueshifted components, Saruwatari *et al.* (2011) also identified a second weaker, lower velocity redshifted component (which they labelled R2, see Figure 2 in Saruwatari *et al.* 2011) which is similarly offset and has a similar velocity to B2. However, R2 is outside of the 10% level of the SMA primary beam for these observations. If both the red and blueshifted lobes are similarly slowed due to the impact with ambient material, then C-MM3 may be centrally located in a dense envelope.

The red- and blueshifted outflow lobes driven by C-MM12 have a similar maximum length on the sky of $\sim$20$''$ ($\sim$15000 AU) in both the SiO (5-4) and ^{12}CO (2-1) emission. However, the blueshifted lobe has a considerably lower maximum velocity compared with the redshifted lobe in both tracers. This results in noticeably longer dynamical timescale estimates for the blueshifted outflow lobe, which may indicate that the blueshifted lobe is slowed, possibly due to an impact with ambient material. Moreover, the integrated SiO (5-4)

flux of the lower velocity blueshifted lobe is significantly lower than the integrated SiO (5-4) flux towards the higher velocity, redshifted lobe (see Table 3.7). This result again points towards SiO (5-4) being a more efficient tracer of high velocity shocks.

Assuming the ^{12}CO (2-1) emission is optically thin at high velocities, the outflow masses are estimated following the procedure outlined in Cyganowski *et al.* (2011) using,

$$M_{out} = \frac{1.186 \times 10^{-4}\, Q(T_{ex})\, e^{\frac{E_{upper}}{T_{ex}}} D^2 \int S_\nu d\nu}{\nu^3 \mu^2 S \chi}, \tag{3.2}$$

where M_{out} is the outflow gas mass given in units of $M_\odot$, T_{ex} is the excitation temperature in Kelvin, $\mathrm{Q}(\mathrm{T}_{ex})$ is the partition function, ν is the frequency in GHz, χ is the abundance relative to H_2, D is the distance to NGC 2264-C in kpc, and S_ν is the line flux in Jy. If the same excitation temperature as used by Maury *et al.* (2009) of 20 K is adopted here, then $Q(\mathrm{T}_{ex}) = 7.23$ K assuming a rotational constant of 2.765 K for ^{12}CO. The standard value of 10^{-4} is used for the ^{12}CO to H_2 abundance ratio (Frerking *et al.* 1982). Following the procedure from Qiu *et al.* (2009), the outflow momentum and energy can then be estimated from

$$P_{out} = \sum M_{out}(\Delta v)\Delta v \tag{3.3}$$

and

$$E_{out} = \frac{1}{2} \sum M_{out}(\Delta v)(\Delta v)^2, \tag{3.4}$$

where $\mathrm{M}_{out}(\Delta v)$ is the outflow mass calculated for a given channel of velocity $\Delta v = |v_{channel} - v_{\mathrm{LSR}}|$. Table 3.8, provides estimates of M_{out}, P_{out} and E_{out} for

the red- and blueshifted outflow lobes driven by C-MM3 and C-MM12. The values presented for the blueshifted lobe driven by C-MM3, are taken from the total contribution of the B1 and B2 components. Only the high velocity gas is considered in the estimates of the outflow mass, momentum and energy and the respective velocity ranges assumed for each lobe are presented in Table 3.8. In addition, the mass and momentum outflow rates $\dot{M}_{out} = M_{out}/\mathrm{t}_{dyn}$ and $\dot{P}_{out} = P_{out}/\mathrm{t}_{dyn}$ respectively are estimated from the dynamical timescales presented in Table 3.7. Given the blueshifted component, B1, contains more than 90% of the total mass contained in both the B1 and B2 components for the blueshifted lobe of C-MM3, the dynamical timescale estimated for B1 is used to derive the mass and momentum outflow rate estimates presented in Table 3.8 for C-MM3. All properties are corrected for inclinations of $i = 45°$ and $60°$. The estimated outflow mass, momentum and energy for C-MM3 are within $\sim$20% for the redshifted, and $\sim$40% for the blueshifted lobe, of the previous estimates from Saruwatari *et al.* (2011) assuming the same inclination.

The outflow driven by C-MM12 is found to be more than twice as massive and contains approximately twice the momentum and energy compared with the outflow from C-MM3. However, the mass and momentum outflow rates estimated for the outflow driven by C-MM3 are more than double those found towards the outflow from C-MM12. Given these results and the fact the dynamical time is found to be shorter for C-MM3 compared with C-MM12, this suggests that the more massive core C-MM3 may be driving a younger, less massive outflow compared with lower mass core C-MM12. However, it should be noted, that inclination effects have not been fully accounted for, and inclination differences between the outflows can significantly effect the estimation

of the dynamical timescale. In both outflows there is an apparent asymmetry between the outflow properties of the higher velocity, redshifted and lower velocity, blueshifted outflow lobes. The redshifted lobes are at least twice as massive, containing approximately 3 times more momentum and energy when compared with their respective blueshifted lobes.

3.5.3.1 Comparison with Previous Single Dish Observations of Outflows in NGC 2264-C

One of the main goals of this research is to use the higher resolution SMA observations to unambiguously identify what is driving the high velocity outflows seen in the single dish observations. Maury *et al.* (2009) previously-identified five outflow lobes (F1, F2, F5, F7, F11; see Figure 3.12) within the FOV observed here, from their lower spatial resolution ^{12}CO (2-1) observation, suggesting either C-MM3 or C-MM13 as the most likely candidates to be driving the outflow emission from the collimated outflow lobes F1 and F2.

However, no obvious outflow emission, from any the high velocity outflow tracers is identified along F1 or F2. Furthermore, towards C-MM13 no high velocity emission is observed. While a high velocity outflow is driven by C-MM3, the compact red- and blueshifted lobes are found to be in the opposite direction to the extended red and blueshifted emission from F1 and F2 respectively. This is also apparent from the single dish JCMT SiO (8-7) observation towards C-MM3 (see Figure 3.5), where the red- and blueshifted emission is to north and south respectively. These results suggest neither C-MM3 or C-MM13 are driving the F1 and F2 lobes observed in Maury *et al.* (2009). An extended, poorly collimated redshifted lobe (F11) is observed by Maury *et al.* (2009) to

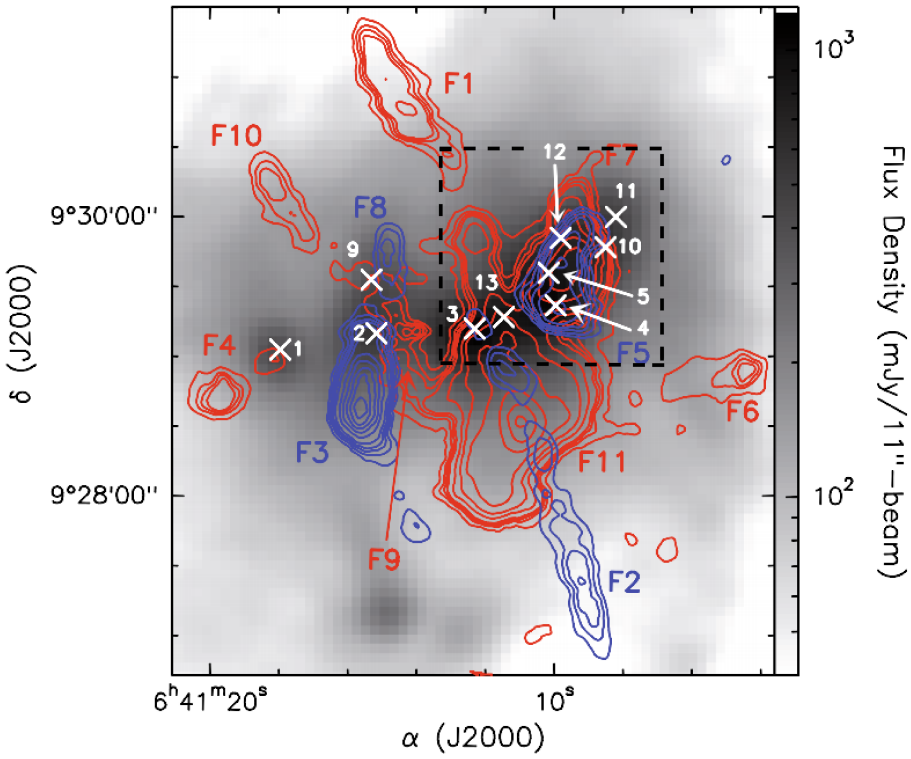

Figure 3.12: Previous observations by Maury *et al.* (2009) of the ^{12}CO (2-1) red and blueshifted emission in NGC 2264-C taken with the IRAM-30m telescope. This figure has been taken directly from Figure 2 of Maury *et al.* (2009), with the FOV covered in this SMA data defined by a black dashed square. The blue contours were integrated over the velocity range $-27\,\mathrm{kms}^{-1}$ and $2\,\mathrm{kms}^{-1}$ and the redshifted emission from $13\,\mathrm{kms}^{-1}$ to $34\,\mathrm{kms}^{-1}$. The contour levels go from 5-98 K kms^{-1} and 5-110K kms^{-1} for the blue- and redshifted emission respectively, and the greyscale is the 1.2 mm continuum from Peretto *et al.* (2006), with the continuum peaks identified by Peretto *et al.* (2006) and Peretto *et al.* (2007) given represented with white crosses.

the south of C-MM3. However, it is significantly extended compared with the compact redshifted emission we observe towards C-MM3.

The red- and blueshifted lobes F7 and F5 extend over several continuum peaks at the lower spatial resolution, and it is not obvious exactly which continuum peak(s) are responsible for the emission. However, at the higher spatial resolution of the SMA observations presented here, a collimated bipolar out-

flow driven by C-MM12 is revealed. Thus, the outflow lobes, F7 and F5, are associated with an the outflow driven by C-MM12. Furthermore, as previously mentioned, the fact that this SMA SiO data recover (and resolve) both of the SiO outflows identified with the JCMT data is strong evidence that the SMA observation is not "missing" any large-scale active outflows.

If the outflow mass estimates for the blue- and redshifted emission from C-MM12, calculated in Table 3.8, are compared to the estimates from Maury *et al.* (2009), only ∼10% and ∼30% of the red and blueshifted emission from F7 and F5 respectively is recovered. However, the mass estimates shown in Table 3.8 do not include emission with velocities lower than $16.4\,\mathrm{kms}^{-1}$ as the emission gets too confused and difficult to separate from systemic gas. Furthermore, the redshifted emission to the south of C-MM12 has not been included. As shown previously, to the south of C-MM12 there is another potential outflow axis (axis A3 see Figure 3.6), which at the lower spatial resolution is blended. If the lower velocity emission, and the redshifted emission to the south of C-MM12 is now included, the total outflow mass is now $\sim 20\times10^{-3}\mathrm{M}_{\odot}$ which is still only ∼30% of the mass estimated by Maury *et al.* (2009). However, given the spatial resolution in these SMA observations is ∼4 times greater than Maury *et al.* (2009), the difference in mass estimates is likely due, in part, to spatial filtering, but also due to the ability to more accurately separate emission not directly associated to the outflow at higher resolution.

3.5.4 Relative Evolutionary State

The two dominant bi-polar outflows are being driven by the IR-dark, compact, millimetre bright, and potentially youngest sources, C-MM3 and C-MM12. The lack of 70μm and 24μm emission towards either source and the associated outflow emission indicates that both of these sources are likely at a very early stage of evolution. In comparison, no obvious active outflow emission from either SiO (8-7), SiO (5-4), or high velocity ^{12}CO (2-1) is associated with C-MM5, which is coincident with the most evolved star in the region, AFGL989-IRS1 a 9.5 $M_{\odot}$ star. Thus, the presence of an SiO outflow appears to decline with evolution for this region. Klaassen *et al.* (2012) found an opposite trend in their survey of SiO (8-7), finding an increase of the SiO luminosity with evolution, which was also weakly observed by Leurini *et al.* (2014) in their sample. Davies *et al.* (2011), predict the lifetime for YSOs to dramatically drop for sources with $L_{bol}\sim10^{5.5}L_{\odot}$. The average bolometric luminosity of the sources in Klaassen *et al.* (2012) is of the order 10^{4}-$10^{5}L_{\odot}$, with several objects at a few $\times10^{5}L_{\odot}$. In comparison, AFGL989-IRS1 has a bolometric luminosity of $\sim10^{3}L_{\odot}$. Thus, it is likely that some possible compact HII regions in Klaassen *et al.* (2012) will be the same age or possibly younger than the most evolved source in our region, AFGL 989-IRS1, and so the presence of SiO may decline with age, as seen by Sanchez-Monge *et al.* (2013), consistent with the low mass scenario of the jet declining with age. In addition, the most evolved sources observed by Klaassen *et al.* (2012) and Leurini *et al.* (2014) may also host younger objects given the coarse angular resolution of the datasets.

3.5.4.1 Bolometric Luminosity Estimate

The IR emission in this region is dominated by AFGL989-IRS1. However, as C-MM3 is sufficiently spatially offset ($\sim$40$''$) from this source, it is possible to identify any IR emission that is associated with C-MM3, and obtain an estimate of its bolometric luminosity. Emission from five wavelengths (70μm, and 160μm Herschel PACS archive data (ID 1342205056, P.I. F. Motte), 450μm, and 850μm SCUBA data taken from Di Francesco *et al.* (2008), along with the 1.3 mm single dish flux from IRAM quoted in Ward-Thompson *et al.* (2000), is used to fit an SED for C-MM3. This is done using the online SED fitting tool described in Robitaille *et al.* (2007). The 70μm emission is not enhanced towards the position of C-MM3 but does peak nearby (see section 3.5.1.3). An upper limit for the 70μm emission towards this source is used. Two estimates for the bolometric luminosity of 71 $L_\odot$ and 102 $L_\odot$ are found for inclinations angles ranging from near edge on to $\sim$50°, and are consistent with a previous estimate of 50$\pm$10 $L_\odot$ by Maury *et al.* (2009) for C-MM3, using the online SED tool and three points (70μm, 450μm and 1.3 mm). The remaining outflow driving source, C-MM12, is however too close to AFGL-989 IRS1 to unambiguously identify any associated IR emission towards this position. A crude estimate of the bolometric luminosity for this source is estimated assuming that the luminosity ratio between C-MM3 and C-MM13 (e.g. $L_{bol}^{C-MM12}/L_{bol}^{C-MM3}$) is equal to the 1.3 mm flux density ratios. This gives an estimate of the C-MM12 bolometric luminosity of between $\sim$ 50-70$L_\odot$.

3.5.4.2 Comparison of Outflow Properties with Literature

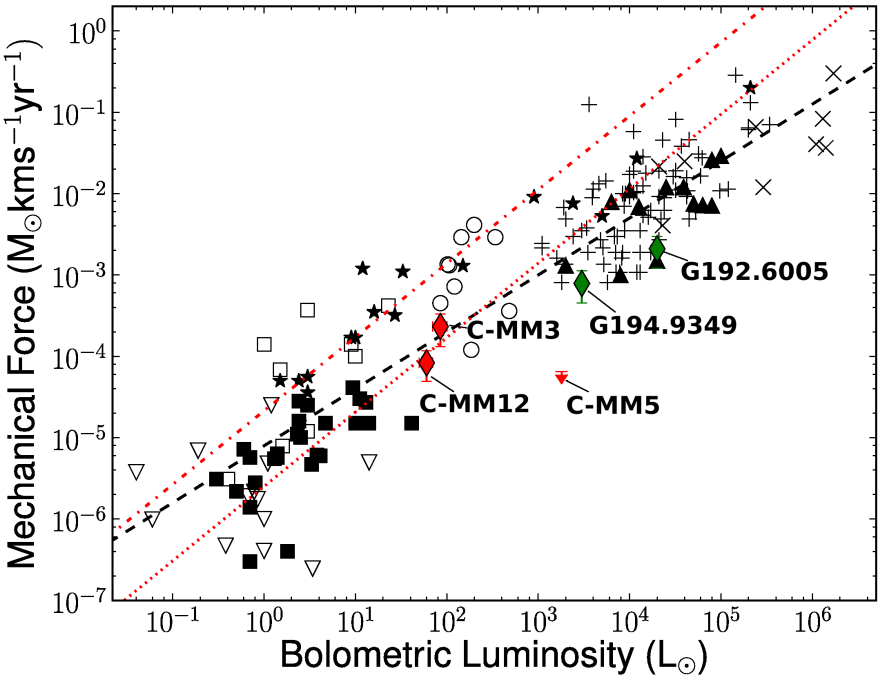

Figure 3.13: Outflow force vs bolometric luminosity taken from previous outflow studies. The black triangles are outflow sources from Beuther *et al.* (2002), the black stars are values taken from Cabrit & Bertout (1992), the black crosses (x) represent sources from López-Sepulcre *et al.* (2009), the upside down open triangles are values from van der Marel *et al.* (2013), and the black pluses (+) are values taken from Maud *et al.* (2015b) from a sample of RMS sources. The open and filled squares are Class 0 and Class I low mass outflow sources from Bontemps *et al.* (1996), and the open circles are intermediate-mass class 0 analogues from Duarte-Cabral *et al.* (2013). The correlations from the low mass class 0 and class I sources from Bontemps *et al.* (1996) are plotted as red dot-dash and dotted lines respectively. The black dashed line is the result of a linear regression fit including all of the previous literature values presented. The red diamonds mark the positions of C-MM3 and C-MM12. The error bars are the upper and lower limits for each value with the main point representing the average value. The upper limit of the outflow force estimated for AFGL989-IRS1/C-MM5 is also shown. The outflow forces presented, for all three sources, represent the total outflow emission in both red- and blueshitfed outflow lobes. The green diamonds represent the outflow forces for G192.6005 and G194.9349 and are discussed in Chapter 4.

Cabrit & Bertout (1992) initially observed a correlation, over five orders of magnitude, between the outflow properties and source bolometric luminosity. Since then, many subsequent, independent observational studies have added to this relationship extending it to over 6 orders of magnitude (e.g. Beuther *et al.* 2002; Maud *et al.* 2015b; Bontemps *et al.* 1996; van der Marel *et al.* 2013; Duarte-Cabral *et al.* 2013; López-Sepulcre *et al.* 2009; Cabrit & Bertout 1992), of which Figure 3.13 shows the resultant correlation. As mentioned in Section 1.3, the correlation between outflow force along with outflow energy and mass with the source bolometric luminosity is suggested as an indication of a similar driving mechanism between the low and high mass regimes. While a linear correlation is found extending from the low to high mass regime (black dashed line, Figure 3.13), there is an order of magnitude scatter about this fit. The linear correlations of the low mass class 0 and class I sources taken directly from Bontemps *et al.* (1996) are plotted (red dot-dash and dotted lines respectively) and are extended up to the luminosities in the high mass regime. Both fits have a similar gradient, however, the class 0 fit is on average an order of magnitude greater compared with the class I fit. In the high mass end of the plot, the class I correlation is found to better fit the data, whereas the class 0 type intermediate stars from Duarte-Cabral *et al.* (2013) sit above this fit and are better represented by the class 0 fit.

As sources observed in the RMS sample are by selection IR-bright and thus relatively evolved compared with embedded typically younger class 0 sources, it may not be surprising that the class I correlation provides a better fit compared with the class 0 fit. However, Dunham *et al.* (2014) found that outflow properties estimated using ^{12}CO (3-2) emission tend to be about an order of

magnitude lower on average than the outflow properties estimated from the ^{12}CO (2-1) emission, in the same sample of sources. Thus, the outflow forces estimated using ^{12}CO (3-2) by Maud *et al.* (2015b) may be under estimated relative to the outflow properties Bontemps *et al.* (1996) estimate from the ^{12}CO (2-1) emission. However, as discussed in Maud *et al.* (2015b) the majority of the high mass sources, given the observed spatial resolution and distances, likely contain multiple sources, where the luminosity of the cluster is dominated by the IR-bright RMS source. Thus, the outflow forces plotted in Figure 3.13 are representing the total for the cluster assuming the RMS source is driving the high mass outflow, which is not necessarily the case. A combination of low/intermediate stars could be responsible for the observed total outflow force (e.g. Maud *et al.* 2015b and references therein). Klaassen *et al.* (2015) observed this relation towards IRAS 17233-3606, where they find multiple sources are responsible for the single large scale outflow. This is also true for NGC 2264-C presented here, where the complex outflow emission observed in the single dish CO observations, at the higher resolution of the SMA is found to contain two bipolar outflows of which neither are driven by the RMS source, and it is the likely younger, IR-dark, sources; C-MM3 and C-MM12 that actually drive the outflows in this region.

The derived bolometric luminosities and outflow forces ($\dot{P}$ see Table 3.8) for these two sources, C-MM3 and C-MM12 are plotted in Figure 3.13. Furthermore, the estimated upper limits for the outflow force of C-MM5/AFGL989-IRS1 are also crudely estimated. The outflow force is calculated assuming a $20''$ aperture centred on C-MM5, with the ^{12}CO (2-1) emission integrated over a similar velocity range as seen in C-MM3 and C-MM12. It is stressed that

this is a very approximate measurement for the outflow properties. This derived estimate of the outflow force for AFGL989-IRS1 is lower than expected given its bolometric luminosity (1800 $L_\odot$ taken from the RMS survey). This may be a result of the more evolved nature of this source. The estimated outflow forces for C-MM3 and C-MM12 are below what would be expected given their likely young class 0 type nature. However, as the class 0 low mass sample by Bontemps *et al.* (1996) was observed with a single dish telescope compared with the interferometric observations performed here, and even though the spatial resolution is the same (given the larger distance to NGC 2264-C, ∼738pc) the interferometric observations will miss flux. Furthermore, the outflow forces estimated for C-MM3 and C-MM12 here, have not been corrected for optical depth effects and are thus likely further underestimated by a factor or around 5-10 (e.g. Dunham *et al.* 2014; Offner *et al.* 2011). Maury *et al.* (2009) estimated a flux for the the lobes F5 and F7 (which at higher resolution of these observations are found to be associated to C-MM12) of $4.6\times10^{-4}M_\odot$ $kms^{-1}yr^{-1}$ compared with $1.1\times10^{-5}M_\odot$ $kms^{-1}yr^{-1}$ estimated here. Thus, the true value of the outflow force for C-MM12 likely lies somewhere in-between the value estimated in this work and that estimated by Maury *et al.* (2009) where the forces presented here are likely lower limits compared with upper limits for C-MM12 from Maury *et al.* (2009).

There are still major difficulties when trying to link the outflow properties between the low and high mass regimes; the areas probed are different, and particularly in the high mass regime it is not clear if a single or multiple sources are responsible for the emission. In the high mass sample the lowest force that could be detected from Maud *et al.* (2015b) would be down at a few $\times10^{-4}M_\odot$

$kms^{-1}yr^{-1}$ (private communication), and the forces typically associated with low mass outflows would not be probed by those observations. In addition, the different methods used to estimate outflow properties (e.g. dynamical timescale and optical depth), make it difficult to directly compare properties between surveys. As mentioned in Section 1.3 the perceived correlation may not be directly related to the actual driving mechanism. The larger masses present in the high mass regime would provide higher values regardless of underlying mechanism (e.g. Maud *et al.* 2015b, Beuther *et al.* 2002, Richer *et al.* 2000). While a linear fit may initially suggest a correlation from the low to high mass regimes, indicative of a similar scaled up formation mechanism, the order of magnitude scatter around these fits means it is difficult to eliminate a different possible formation mechanism (e.g. Competitive Accretion) for high mass stars. Complementary high resolution observations are required to fully probe the high mass regions, where the outflow properties of individual sources in these clusters can be obtained.

3.6 Conclusions

This chapter presents observations of the intermediate/massive star forming region NGC 2264-C, at an angular resolution of $\sim 3''$, taken with the SMA at 1.3 mm, providing the first interferometric observation of the outflow tracers SiO (5-4) and ^{12}CO (2-1) towards this region. Of the ten 1.3 mm continuum peaks identified, of which four are new detections, only two are clearly driving bipolar outflows. The SiO (5-4) observations unambiguously reveal two high velocity bipolar outflows driven by C-MM3 and C-MM12. Similarly, high velocity

emission from SO and ^{12}CO, and H_2CO, along with lower velocity emission from CH_3OH is found to trace both outflows, however, SiO is more efficient at tracing the higher velocity outflow material. Furthermore, only towards these two bipolar outflows is the emission from the higher SiO J transition, SiO (8-7) in the JCMT data observed. However, at the lower spatial resolution of the JCMT observations the outflow driving source is ambiguous, highlighting the need for higher resolution, interferometric observations to identify the driving source of the outflow emission.

There is an apparent evolutionary differentiation between the continuum sources present in NGC 2264-C. Comparison of the molecular chemistry, mid and far IR, mm, sub-mm, and radio emission reveals that it is the likely youngest, mm brightest sources, C-MM3 and C-MM12, that are driving the dominant bipolar outflows. Both of these cores are IR-dark and molecular line weak and have no detected radio emission, indicating that they are possibly at a very early stage of evolution. In contrast, the IR-bright, most evolved source in the region, the RMS source AFGL 989-IRS1, does not drive a molecular outflow. However, the wind from this source (Bunn *et al.* 1995) is likely driving a low density cavity (Schreyer *et al.* 2003) that may be responsible for the molecular line rich ridge feature observed.

Thus, these observations clearly emphasise the power of higher-resolution, multi-line observations at removing the ambiguity in identifying outflow driving sources in complex high mass star forming clusters. However, the single dish observations still remain crucial to obtain the total flux. Future complementary interferometric observations, expanding the number of regions observed at higher resolution is crucial to gaining an understanding of the properties of

outflows in the high mass regime in comparison to the low mass regime. As shown here it is not clear when observing at low resolution what is driving the outflows in high mass clusters. These observations show that SiO traces the higher velocity emission more efficiently and is unambiguously tracing outflows towards the likely youngest sources in a similar manner to SiO in the low mass regime. While SiO outflow emission is not observed towards all sources in NGC 2264-C its detection appears dependent on mass and evolution, with only the more massive young IR-dark sources showing collimated bipolar outflows traced by the SiO emission.

Chapter 4

High Resolution Follow Up Observations of G192.6005 and G194.9349; exploring potentially "active" and "fossil" outflows

4.1 Introduction

This Chapter presents high resolution follow-up SMA Observations ($\sim 3''$) utilising the outflow tracing species SiO and CO towards two regions selected from the JCMT survey (one region with an SiO (8-7) detection and one region without an SiO (8-7) detection; see Chapter 2). The aim is to further explore the differences in the outflows and their driving source(s) between two potential evolutionary stages (i.e. a region harbouring a potentially active outflow compared with a region containing a potentially fossil remnant outflow). The regions;

G192.6005 and G194.9349, both have known CO outflows Maud *et al.* (2015b). However, while G192.6005 has associated SiO (8-7) emission (i.e. a sign of a young, high velocity, active outflow), G194.9349 has no detected SiO (8-7) emission. Furthermore, both regions have similar outflow properties estimated in the ^{12}CO (3-2) observations by Maud *et al.* (2015b), providing a good test base to explore their relation with SiO. In addition, as both sources are at similar distances[1] ($\sim$2 kpc), a direct comparison in sensitivity and resolution can be made. The SMA observations presented in this chapter specifically target the outflow tracers ^{12}CO (2-1) and SiO (5-4). The higher resolution presented here will further aid in distinguishing the driving source(s) of the observed outflow emission, determining whether the IR bright source is responsible for driving the outflows observed in the single dish data. This chapter is presented as follows; the previous literature is discussed in Section 4.2, the SMA data towards both regions is presented in Section 4.4 and the discussion and summary of this data is given in Sections 4.5 and 4.6 respectively.

4.2 Previous Literature

Both regions have been classified as YSOs in the RMS survey, and have bolometric luminosities $>10^3 L_\odot$. The bolometric luminosity of G192.6005 is an order of magnitude higher at $2.8\times10^4\,L_\odot$, compared with $3.0\times10^3\,L_\odot$ for G194.9349. Previous works (e.g. Palla *et al.* 1991; Wood & Churchwell 1989; Molinari *et al.* 1996) have subdivided the early stages of massive star formation, before the

[1]It should be noted that since the observations were undertaken, trigonometric parallax measurements of methanol masers by Rygl *et al.* (2010) towards G192.6005 have corrected the distance to this region from 2 kpc to $1.59^{0.07}_{0.06}$ kpc

onset of an HII region, into two groups (*Low* and *High*) based on their IRAS colours. Sources with IRAS colours [25-12]>0.57, and [60-12]>1.3[1], the classification criteria for an UCHII region in Wood & Churchwell (1989), which do not have a detectable HII region are classed as *High* sources, whereas all remaining young MYSOs, again without a detectable HII region, are classed as potentially less evolved *Low* sources. Based on the IRAS colours of G192.6005 and G194.9349 they would fall into the classes of *Low* and *High* respectively. The previous observational data towards each region is discussed below.

4.2.1 G192.6005-IRAS 06099+1800/S255IR

G192.6005/S255IR is a well studied source, residing between two evolved HII regions S255 and S257, it forms part of one of three more compact 1.3 mm continuum components (S255N, S255IR, and S255S) nested in a larger filamentary structure (Minier *et al.* 2005 see Figure 4.1). S255IR contains the brightest IR sources of the three mm regions, and is the focus of SMA observations presented here. At the given distance to this region, $1.59^{0.07}_{0.06}$kpc (Rygl *et al.* 2010), the bolometric luminosity is estimated at $\sim 2\times10^4 L_\odot$. The region contains two dominant near-IR sources; NIRS 1 and NIRS 3 (e.g. see Figure 4.1 Tamura *et al.* 1991), of which NIRS 3 dominates the mid-IR emission at 24.5μm (de Wit *et al.* 2009). Both sources have associated scattered light lobes, extending to the north and south, where the emission associated with NIRS 1 shows a twisted feature and is suggested to be a possible indication of precession of the outflow (e.g. Simpson *et al.* 2009 and references therein). Furthermore, Simpson *et al.* (2009) suggest the scattered light lobe of NIRS 1 lies behind southern lobe of

[1]Where the IRAS colour is defined as $[\lambda_1\text{-}\lambda_2]=\log_{10}(F_{\lambda_1}/F_{\lambda_2})$.

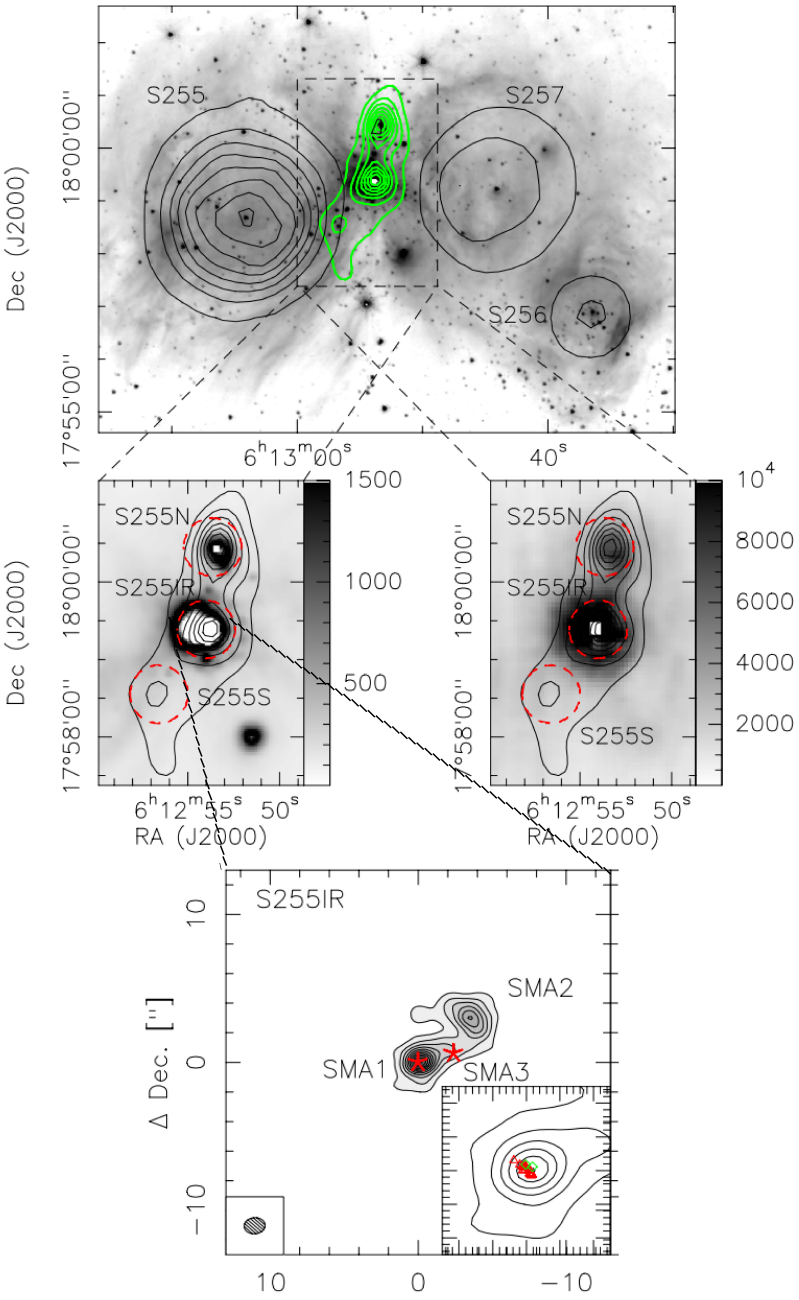

Figure 4.1: Taken from Figure 1 of Wang *et al.* (2011). The top panel displays SPITZER-IRAC 4.5μm emission, the black solid contours are 1.4 GHz emission and the green contours SCUBA 850μm emission. The greyscale in the middle left and right panels are the SPITZER-MIPS 24μm and 70μm emission respectively. The overlaid black solid contours are of the SCUBA 850μm emission. The bottom panel shows the SMA interferometric ($\sim$1.5$''$resolution) 1.3 mm continuum emission taken directly from Figure 3 of Wang *et al.* (2011). The black contours are the 1.3 mm emission and the red asterisk mark the position of NIRS 1 and NIRS 3 where (NIRS1 is coincident with SMA3 and NIRS 3 is coincident with SMA1). The zoomed image shows the continuum peak of SMA1, where the red triangles give the positions of water maser from Goddi *et al.* (2007) and the green diamonds give the positions of 6.7 GHz class II methanol masers emission from Xu *et al.* (2009).

NIRS 3. Interferometric mm observations by Wang *et al.* (2011) and Zinchenko *et al.* (2012) have identified further substructure within S255IR, with several continuum peaks reported. They both identify two dominant continuum peaks (SMA1 and SMA2), of which SMA1 is coincident with NIRS 3 (see Figure 4.1). SMA1 is also associated with class II CH_3OH maser emission (Xu *et al.* 2009) and H_2O maser emission (Goddi *et al.* 2007). NIRS 3 is spatially located between the two continuum peaks, and is not unambiguously resolved in the mm continuum emission (labelled SMA3, Figure 4.1).

4.2.2 G194.9349 - IRAS 06103+1523

G194.9349 is less well studied. The only previous interferometric observation towards this region is VLA NH_3 (1,1), and (2,2) emission at $\sim 3''$ resolution (Lu *et al.* 2014). Figure 4.2 presents the rotational temperatures derived from the NH_3 (1,1) and (2,2) emission overlaid on the integrated NH_3 (1,1) emission. The rotational temperature is found to peak ($\sim$30 K) at the position of the IR bright IRAS source position. Lu *et al.* (2014) estimate a mass of $25 M_\odot$ from the NH_3 emission. Fontani *et al.* (2010) found no 6.7 GHz class II CH_3OH maser emission and only a marginal $\sim 3\sigma$ detection of the 44 GHz class I CH_3OH maser. Moreover, no OH maser emission (Edris *et al.* 2007), or H_2O maser emission (Sunada *et al.* 2007; Palla *et al.* 1991) is detected towards this region.

4.3 Observations

The SMA observations presented in this chapter were taken in the same observing run as NGC 2264-C (see Section 3.3.1). They were observed using

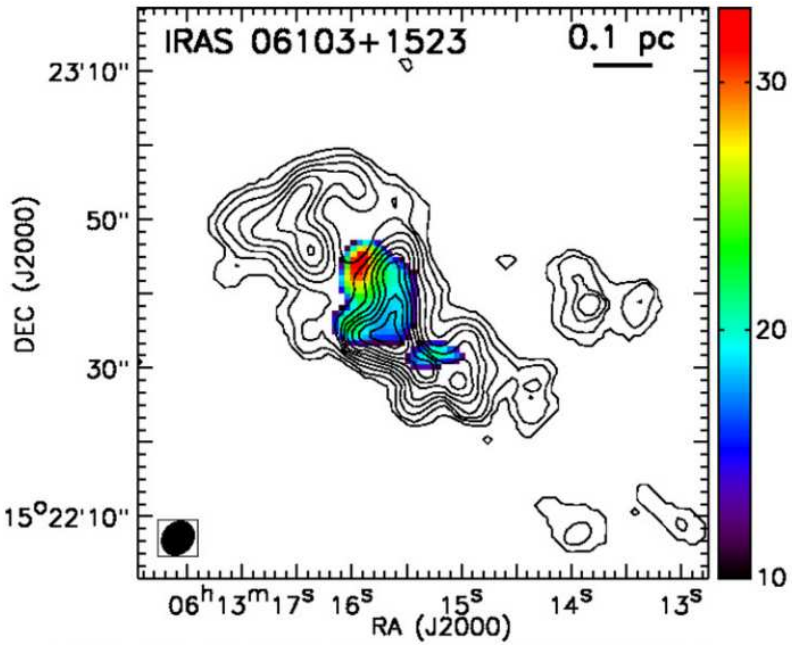

Figure 4.2: NH_3 (1,1) and (2,2) VLA emission towards G194.9349. This image is taken directly from Figure 8 of Lu *et al.* (2014). The colour scale is the rotational temperature in Kelvin derived from the NH_3 (1,1), and (2,2) emission. The black contours are the integrated intensity emission NH_3(1,1) emission (from 5% to 95% of the peak intensity in steps of 10%). The VLA synthesised beam ($\sim 3''$) is shown in the lower left hand corner.

the same frequency set-up. The gain calibrators were J0530+135, J0532+075, and J0750+125, and the absolute flux calibration was derived from Uranus. The pointing centre for G192.6005 is R.A. (J2000) $06^h12^m54.04^s$, Dec. (J2000) $+17°59'22.5''$, and is R.A. (J2000) $06^h13^m16.14^s$, Dec. (J2000) $+15°22'43.3''$ for G194.9349. The observations were performed on-each-source for a total of $\sim$4 hours, spread over an 8 hour track to improve UV coverage. Further details of the full reduction and cleaning procedure is described in Section 3.3.1.

4.4 Results

4.4.1 1.3 mm Continuum Emission

The 1.3 mm continuum images for both G192.6005 and G194.9349, corrected for the primary beam response, are shown in Figure 4.3. As with NGC 2264-C, the structure of the 1.3 mm emission is characterised through implementation of dendrograms, using the python based fitter astrodendro (Astropy Collaboration *et al.* 2013). The trees are fit using a minimum number of pixels set to the beam size ($\sim$17 pixels), for a minimum detection threshold of 4σ (in the non-beam corrected image), and further nested substructure identified for an additional increase of 1σ. The dendrogram trees for both sources are shown in Figure 4.4. For G192.6005, only one structure is identified with no nested substructure. Whereas G194.9349 contains three leaves, two of which belong to the same branch, nested in one parent trunk (see Figure 4.4).

The effects of reducing and increasing the minimum detection threshold to both 3σ and 5σ and increasing the limit for identifying further substructure from 1σ to 2σ are discussed below. Towards G192.6005, while the main structure remains the same regardless of either an increase or decrease, lowering the minimum limit to 3σ reveals two additional independent structures at $\sim3.5\sigma$. The first of these peaks is located $\sim40''$ to the north of the main component in G192.6005, at $\sim$25% level of the primary beam response. As a goal of these observations is to compare sources with a similar sensitivity, the source located at $\sim$25% level is not considered in the remainder of the analysis. The second source, located at $\sim$50% level of the primary beam response ($\sim20''$ to the north of the main component), is detected at $\sim3.5\sigma$ in the non-primary beam cor-

rected image and less than 5σ in the beam corrected image. Zinchenko *et al.* (2012) performed similar resolution observations with the SMA towards this region and did not identify this structure down to the $\sim 2\sigma$ level. However, they did identify a further source at $\sim 3\sigma$ (approximately $12''$ south of SMA1) which is not identified here. If the minimum detection threshold is lowered to $<3\sigma$, then an additional continuum peak is identified within a few arcseconds of the continuum peak (see Figure 1 of Zinchenko *et al.* 2012 where the peak is labelled SMA4). However, given the uncertainty and low detection threshold for these sources they are not currently considered as unambiguous detections, and are not discussed further. For the remaining single structure that is detected, higher spatial resolution SMA data (i.e. $\sim 1.5''$resolution Wang *et al.* 2011) clearly separates the 1.3 mm continuum emission into two peaks (see Figure 4.1). Similarly, the 1.3 mm continuum emission in these observations does suggest two separate enhancements, that at the current resolution the dendrogram fit cannot unambiguously resolve them. Furthermore, the chemistry towards the two peaks is different, suggesting that they are likely two individual sources (see Section 4.4.2 below for further discussion). Thus, for the remainder of this analysis it is assumed that there are two seprerate 1.3 mm sources present in G192.6005, which are labelled under the same nomenclature as Wang *et al.* (2011); SMA1 and SMA2 (see Figure 4.3) for the remainder of the analysis.

Towards G194.9349, the three identified continuum peaks remain unchanged regardless of either an increase or decrease in the detection thresholds. It is noted that towards G194.9349-SMA2 the 1.3 mm continuum appears to show two separate enhancements, which are currently identified as one component in the dendrogram fit. As there are no higher resolution observations towards this

region, G194.9349-SMA2 is treated as one component.

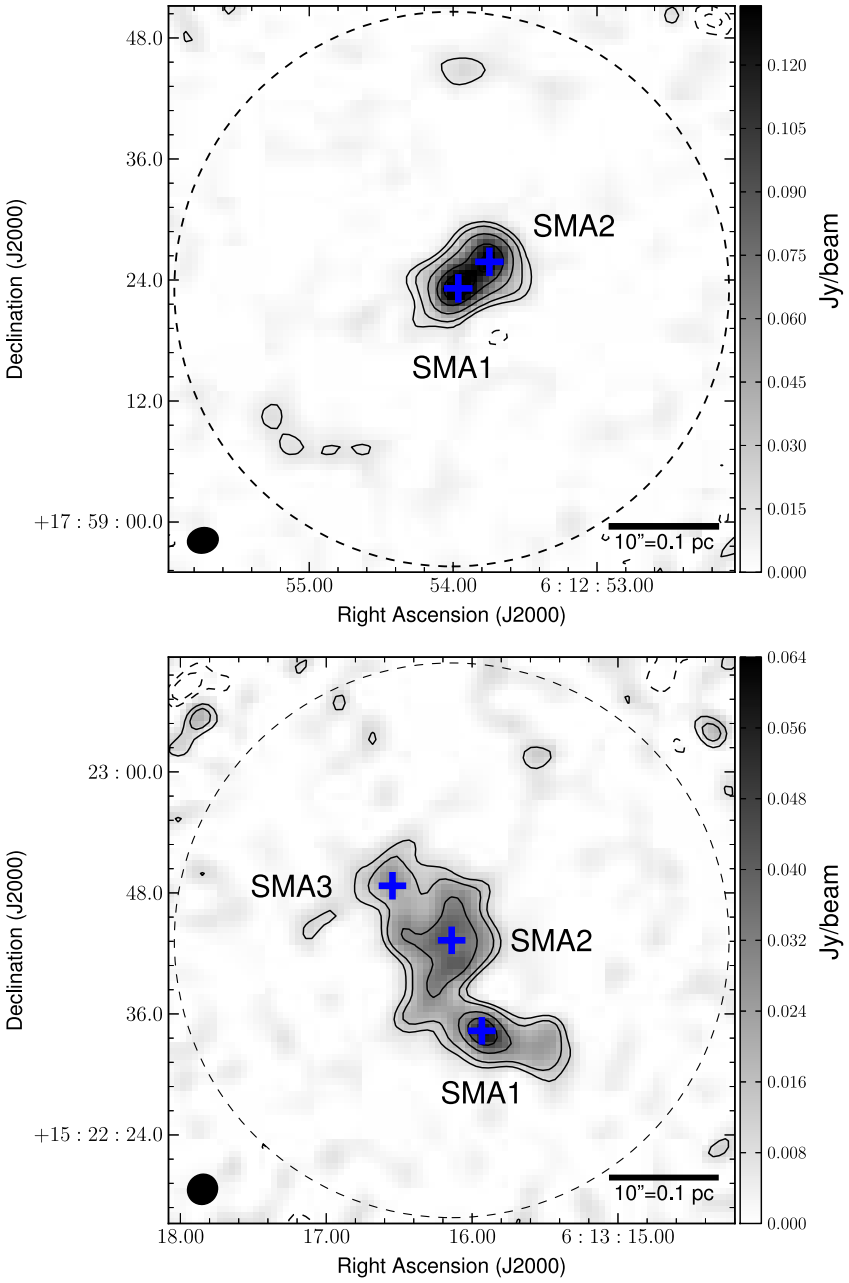

Figure 4.3: Maps of the 1.3 mm continuum emission towards G192.6005 (top panel) and G194.9349 (bottom panel), both maps are corrected for the primary beam response. The grey scale is the 1.3 mm SMA continuum emission with the scale for each region given in the colour-bar. The black solid contours represent (3,5,10,15,20,25,30)$\times$ $\sigma = 4.0$mJybeam^{-1} for G192.6005, and (3,5,10,15,20)$\times$ $\sigma = 3.0$mJybeam^{-1} for G194.9349. The dashed black contours are the negative contour levels representing (-3,-5)$\times \sigma$, where sigma is the same as above. The peak of each identified source is labelled with a blue plus (+), in G192.6005 two sources are identified; G192.6005-SMA1 and G192.6005-SMA2, in G194.9349 three sources are identified; G194.9349-SMA1, G194.9349-SMA2, and G194.9349-SMA3. The dashed black circle is the FWHP of the SMA primary beam, and the solid black circles in the lower left hand corners are the synthesised beams.

Table 4.1: Properties of the 1.3 mm individual continuum sources, along with the properties for the region as a whole (i.e. G192.6005-TOTAL and G194.9349-TOTAL).

Source [a]	J2000.0 Coordinates[b]		J2000.0 Coordinates[c]		R_{eff} [d]	I_{peak} [e]	S_ν [f]
	$\alpha(^{hms})$	$\delta(^\circ\,'\,'')$	$\alpha(^{hms})$	$\delta(^\circ\,'\,'')$	(pc)	(mJy beam^{-1})	(mJy)
G192.6005-SMA1	06 12 54.00	+17 59 23.09	06 12 53.97	+17 59 23.38	0.025	183	332
G192.6005-SMA2	06 12 53.79	+17 59 25.47	06 12 53.77	+17 59 25.77	0.027	165	304
G192.6005-TOTAL	06 12 54.00	+17 59 23.09	06 12 53.90	+17 59 24.23	0.044	183	597
G194.9349-SMA1	06 13 15.93	+15 22 34.32	06 13 15.88	+15 22 33.71	0.031	61	103
G194.9349-SMA2	06 13 16.18	+15 22 43.90	06 13 16.22	+15 22 42.50	0.042	41	185
G194.9349-SMA3	06 13 16.56	+15 22 48.74	06 13 16.56	+15 22 48.54	0.014	29	17
G194.9349-TOTAL	06 13 15.93	+15 22 34.32	06 13 16.12	+15 22 40.26	0.083	61	498

([a]) Sources identified. ([b]) Position of millimetre continuum peak. ([c]) Position of intensity-weighted centroid, computed using *Computing Dendrogram Statistics* (Astropy Collaboration *et al.* 2013), along with the CASAVIEWER, for G192.6005-SMA1, and G192.6005-SMA2. ([d]) Effective radius, computed from the total leaf area using *Computing Dendrogram Statistics* (Astropy Collaboration *et al.* 2013), through $R_{eff} = \sqrt{Area/\pi}$ and assuming the distance of 1.6 kpc and 2.0 kpc for G192.6005 and G194.9349 respectively. ([e]) Peak intensity of 1.3 mm continuum emission, corrected for the primary beam response. ([f]) Integrated 1.3 mm flux density (corrected for the primary beam response), computed using *Computing Dendrogram Statistics* (Astropy Collaboration *et al.* 2013).

Table 4.1 provides the coordinates, peak and integrated 1.3 mm fluxes and effective areas for the 5 detected sources (SMA1 and SMA2 in G192.6005, and SMA1, SMA2 and SMA3 in G194.9349). The total integrated flux is similar (within 20%) for both regions, with G192.6005 having a higher total flux at 597 mJy. However, the peak fluxes are noticeably different between the two regions. Towards G192.6005 the peak flux is approximately 3 times greater than found towards G194.9349. G192.6005 is also more compact than G194.9349; the effective radius of G192.6005 is approximately half of the radius identified for G194.9349.

G192.6005-SMA1 is the strongest 1.3 mm source in both regions, while G194.9349-SMA3 is the weakest. Towards G192.6005 both sources have similar peak and integrated 1.3 mm flux densities along with similar sizes. Towards G194.9349, SMA1 is the strongest mm source, however, SMA2 has the highest total integrated flux. G194.9349-SMA1 is more compact compared with G194.9349-SMA2 (as noted previously, towards G194.9349-SMA2 there is potentially a second source within this peak however it cannot currently be resolved).

4.4.2 Molecular Line Emission

The full LSB and USB line cubes (corrected for the primary beam response) were initially extracted from the peak pixel towards each identified continuum peak and inspected. Any potential line emission was then converted to a rest frequency using the respective $v_{\rm LSR}$'s of 7.8 $\rm kms^{-1}$ for G192.6005 and 15.6 $\rm kms^{-1}$ for G194.9349 (estimated from Gaussian fits to the $H^{13}CO^{+}$ (4-3) emission ob-

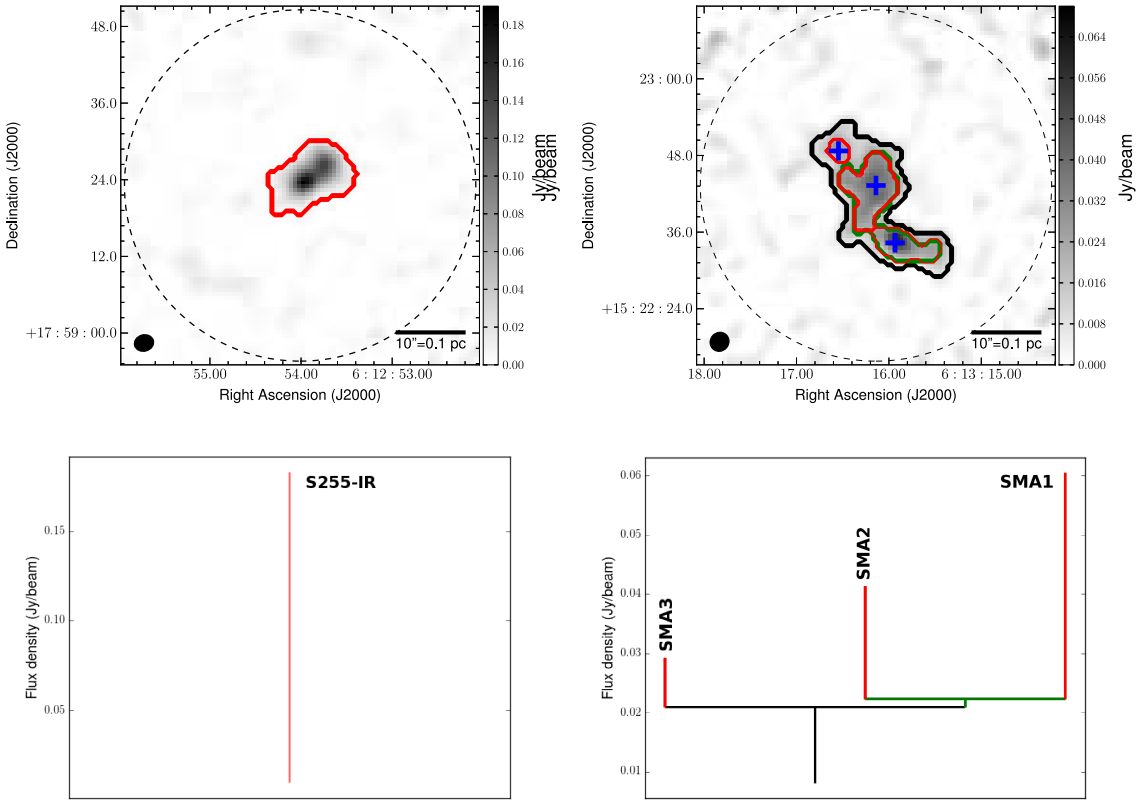

Figure 4.4: The dendrogram fits and tree diagrams for G192.6005 (top and bottom left hand panels respectively) and G194.9349 (top and bottom right hand panels respectively). The top panels show the 1.3 mm continuum emission (greyscales) with the dendrogram fit overlaid using a 3σ minimum threshold, where the red contours are the highest level structures; in the case of G192.6005 this is the parent as there is no nested substructure, and they represent the individual leaves in G194.9349. The green contour in G194.9349 is the branch where G194.9349-SMA1 and G194.9349-SMA2 are nested. The black contour is the parent structure in G194.9349 where all three leaves are nested. The lower panels provide a schematic of the tree diagram, where the y axis is the flux density in units of Jy/beam.

tained for each region in Chapter 2). The line rest frequencies were then compared against the transitions detected in NGC 2264-C. For additional lines, not detected in NGC 2264-C the rest frequencies were checked in the Splatalogue catalogue[1] and compared against previous SMA molecular line papers towards similar regions (e.g. Wang *et al.* 2011; Wang *et al.* 2012). Each identified line was then cleaned individually. Table 4.2 provides the rest frequencies, specific transitions and upper energies of the molecular line species detected above 3σ, along with the association of a transition with a given source. The results of a single Gaussian fit are presented for all transitions detected above 3σ, towards each continuum peak in Tables 4.3 and 4.4.

4.4.2.1 Molecular Lines Emission Towards G192.6005

Towards G192.6005, 39 molecular line transitions from 13 species are detected, with upper energies ranging from ∼16-600 K. This includes all of the transitions detected towards NGC 2264-C (see Table 3.2 in Chapter 3), with the exception of the *c*-C_3H_2 transitions. An additional 16 molecular lines (e.g. HNCO, and SO_2) are detected in G192.6005 (which were not detected in NGC 2264-C), all of which are tracing compact, unresolved emission centred on the continuum peak of G192.6005-SMA1. In comparison, towards G192.6005-SMA2, only 15 molecular lines (all of which were also observed in NGC 2264-C) are detected above 5σ.

Figure 4.5 displays the integrated intensity maps for the transitions detected above 5σ in G192.6005 that were also detected in NGC 2264-C. The 16 additional transitions detected towards G192.6005-SMA1 are not shown as they all

[1]http://www.cv.nrao.edu/php/splat/

trace similarly, compact unresolved emission, spatially centred on the continuum peak of SMA1 and are not observed towards any other location in the region. The Gaussian fits to these transitions are however listed in Table 4.3.

Several transition such as H_2CO, a number of the CH_3OH transitions, and SO trace extended emission in the region. There appears to be two main extensions in the emission, one running across both SMA1 and SMA2 (axis A1 Figure 4.5), and a second perpendicular to this, cutting primarily through G192.6005-SMA2 (axes A2 in Figure 4.5). Only four transitions; SO (6-5), SiO (5-4), ^{12}CO (2-1), and ^{13}CO (2-1) have emission covering a velocity range of $>20\,\mathrm{kms}^{-1}$. The most notable velocity range is observed in the ^{12}CO emission, where the velocity extends over $\sim100\,\mathrm{kms}^{-1}$. Interestingly, SiO does not show any extended emission over this region, however, several weak, compact components are observed, the brightest of which is found coincident with G192.6005-SMA1.

4.4.2.2 Molecular Lines Emission Towards G194.9349

Towards G194.9349, considerably less molecular line emission is detected. Only 8 molecular line transitions from four species; CO, H_2CO, SO and CH_3OH, are detected towards any of the continuum peaks. Furthermore, none of the higher energy tracers such as CH_3CN, HC_3N, or OCS are observed, and the majority of the detected lines appear to be tracing emission that is not directly associated with any of the continuum peaks. Figure 4.6 displays the integrated intensity maps for the transitions detected towards this region. Interestingly, all of the molecular emission trace a compact peak offset to north ($\sim4''$) of G194.9349-SMA2 where no continuum emission is detected. Further inspection of the LSB

and USB spectra at this position reveal the presence of two additional molecular transitions, the SiO (5-4) line and the CH_3OH (8(-1,8),-7(0,7)E) transition. This position is discussed as the molecular peak (G194.9349-MP) for the remainder of the analysis and the molecular line fits from a single Gaussian fit are presented in Table 4.4 for reference.

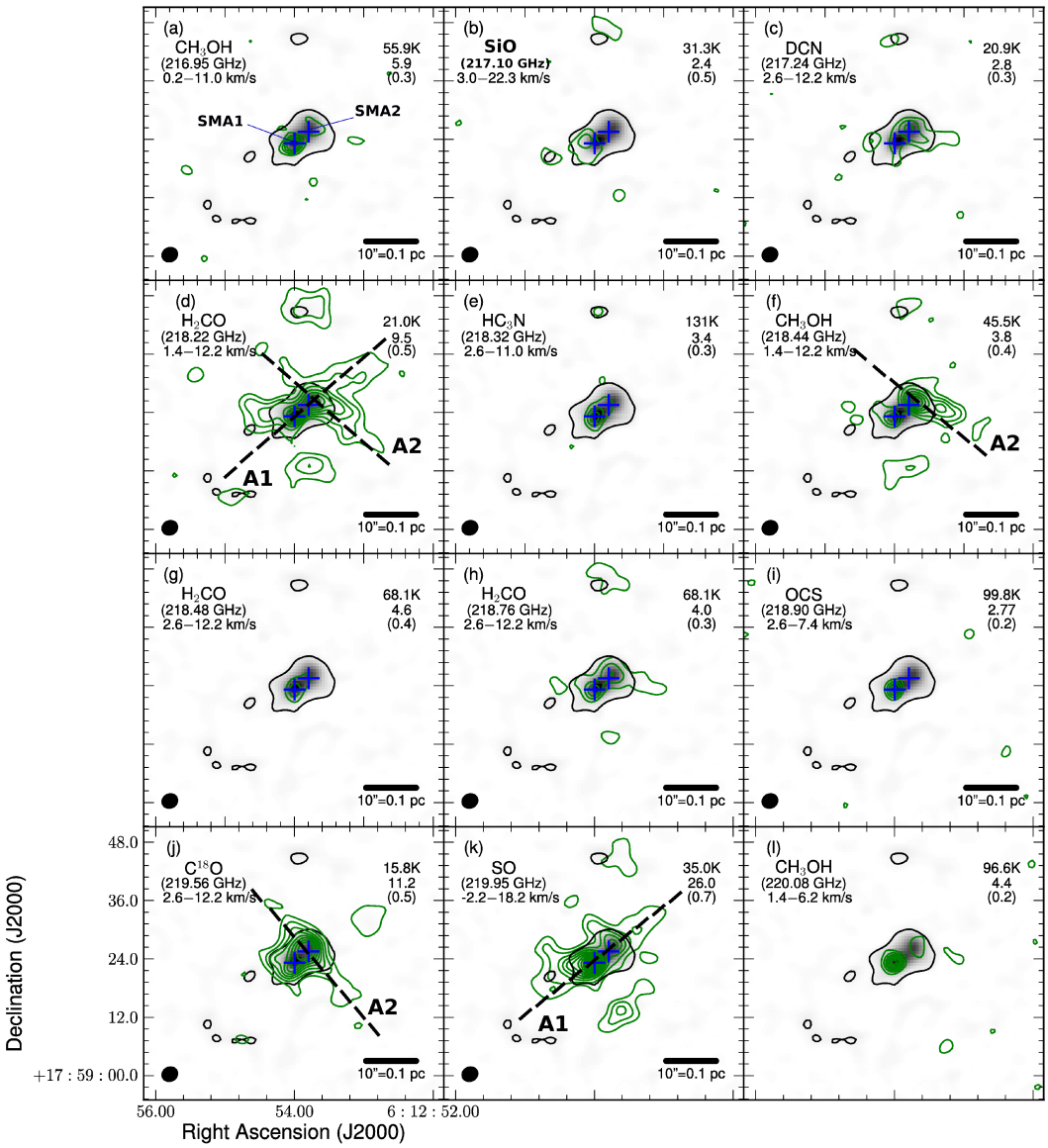

Figure 4.5: Integrated intensity maps for the molecular line transitions detected above $3\,\sigma$ towards G192.6005. The molecular line transition, rest frequency and velocity range integrated over are labelled in the top left corner of each panel. In the top right corner of each panel the E_{upper} temperature (K) of the respective transition, the peak flux (Jy/beam*km/s) and rms (Jy/beam*km/s) of the map is listed. The blue pluses represent the positions of the 2 continuum peaks, SMA1 and SMA2. The green contours are from $3\,\sigma$ to peak in steps of $2\,\sigma$. The grey scale in the 1.3 mm continuum emission and the black line represents the $3\,\sigma$ contour level ($3\sigma = 12$ mJy/beam) (taken Figure 4.3). The thick black dashed lines highlight the extension of the molecular emission towards several transitions, and are labelled A1 and A2.

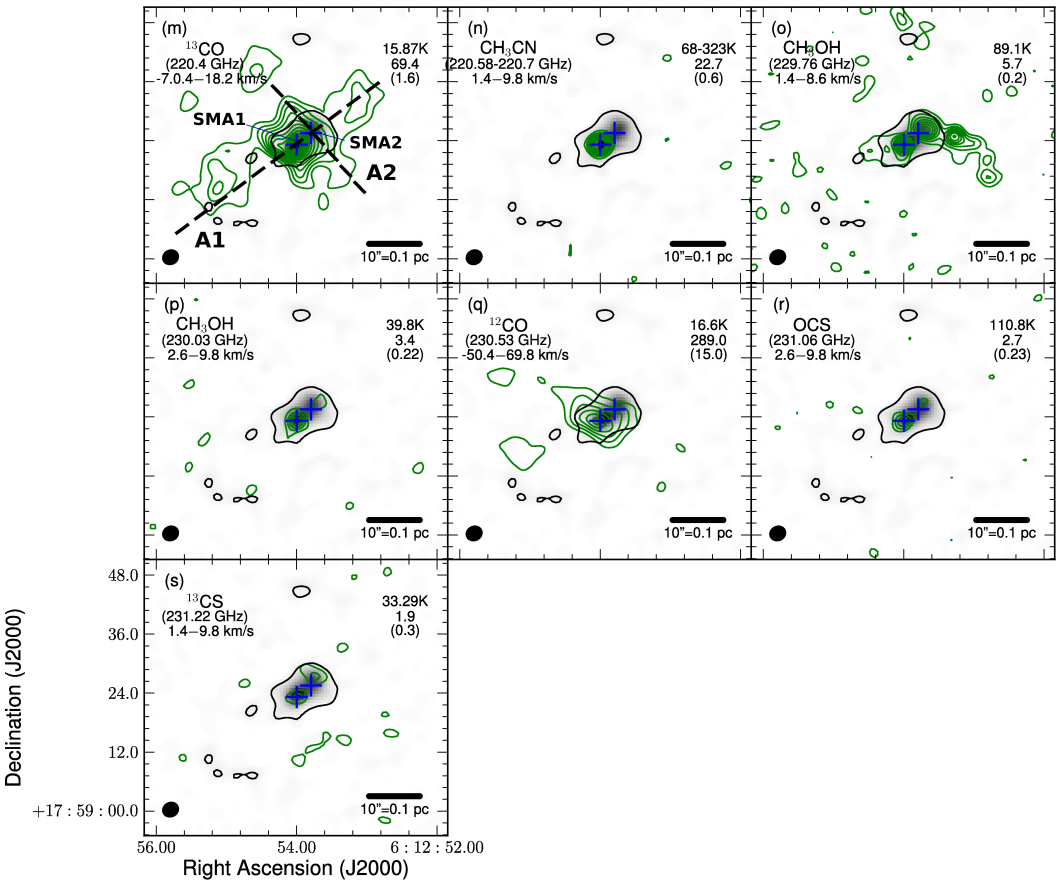

Figure 4.5–continued

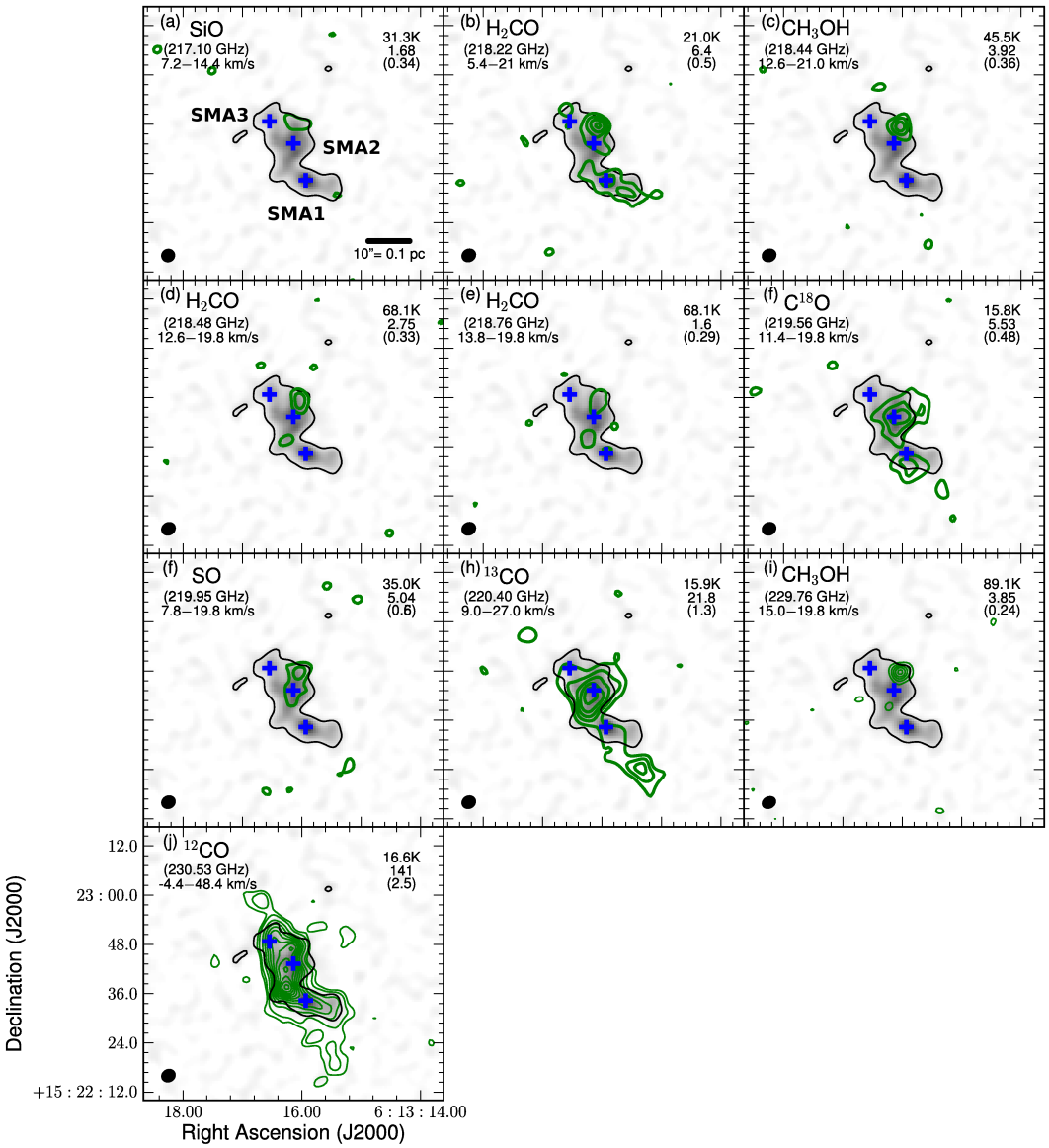

Figure 4.6: Integrated intensity maps for the molecular line transitions detected above $3\,\sigma$ towards G194.9349. The molecular line transition, rest frequency and velocity range integrated over are labelled in the top left corner of each panel. In the top right corner of each panel the E_{upper} temperature (K) of the respective transition, the peak flux (Jy/beam*km/s) and rms (Jy/beam*km/s) of the map is listed. The blue pluses represent the positions of the three continuum peaks; G194.9349-SMA1, G194.9349-SMA2, and G194.9349-SMA3. The green contours are from $3\,\sigma$ to peak in steps of $2\,\sigma$. The grey scale in the 1.3 mm continuum emission and the black line represents the $3\,\sigma$ contour level (3σ =11 mJy/beam) taken from Figure 4.3.

Table 4.2: Summary of the molecular line transitions detected towards individual continuum peaks along with the G194.9349-MP. The frequencies and upper energies are taken from Splatalogue (http://www.splatalogue.net/), (Müller *et al.* 2005). Y indicates emission detected at $\geq 5\sigma$, N indicates no detected emission (no emission at $\geq 5\sigma$). All measurements were made from image cubes corrected for the primary beam response, and a detection was determined from the spectra extracted from those beam corrected image cubes.

Species	Transition	Frequency	E_{upper}	G192		G194			
		(GHz)	(K)	SMA1	SMA2	SMA1	SMA2	SMA3	MP
				LSB					
CH_3OH *	5(1 , 4)- 4(2 , 2)	216.946	55.9	Y	Y	N	N	N	N
CH_3OCHO	20(1,20)- 19(0,19) E	216.96797	101	Y	N	N	N	N	N
SiO *	(5 - 4)	217.105	31.3	Y	Y	N	N	N	Y
DCN *	(3 - 2)	217.239	20.9	Y	Y	N	N	N	N
CH_3OH	6(1, 5)- 7(2, 6)	217.299	363.5	Y	N	N	N	N	N
H_2CO *	3(0, 3)- 2(0, 2)	218.222	21.0	Y	Y	Y	Y	Y	Y
HC_3N *	(24 - 23)	218.324	131.0	Y	Y	N	N	N	N
CH_3OH *	4(2 , 2)- 3(1 , 2)	218.440	45.5	Y	Y	N	N†	N	Y
H_2CO *	3(2, 2)- 2(2, 1)	218.476	68.1	Y	Y	N†	N†	N	Y
H_2CO *	3(2, 1)- 2(2, 0)	218.760	68.1	Y	Y	Y	N†	N	Y
OCS *	(18 - 17)	218.903	99.8	Y	N	N	N	N	N
HNCO	10(1,10)- 9(1, 9)	218.981	101.08	Y	N	N	N	N	N
$C^{18}O$ *	(2 - 1)	219.560	15.8	Y	Y	Y	Y	N	Y
HNCO [c]	10(2, 9)- 9(2, 8)	219.734	231	Y	N	N	N	N	N
HNCO [c]	10(2, 8)- 9(2, 7)	219.737	231	Y	N	N	N	N	N

Continued on next page

Table 4.2 – continued from previous page

Species	Transition	Frequency	E_{upper}	G192		G194			
		(GHz)	(K)	SMA1	SMA2	SMA1	SMA2	SMA3	MP
HNCO	10(0,10)- 9(0, 9)	219.798	58.0	Y	N†	N	N	N	N
SO *	6(5)-5(4)	219.949	35.0	Y	Y	N†	Y	N	Y
HCOOH	10(0,10)- 9(0, 9)	220.038	48.06	Y	N	N	N	N	N
CH_3OH *	8(0 , 8)- 7(1 , 6) E	220.078	96.6	Y	N†	N	N	N	N
^{13}CO *	(2-1)	220.398	15.9	Y	Y	Y	Y	Y	Y
HNCO ‡	10(1, 9)- 9(1, 8)	220.585	101.50	Y	N	N	N	N	N
CH_3CN‡	(12_6-11_6)	220.594	325.9	Y	N	N	N	N	N
CH_3CN	(12_5-11_5)	220.641	247.4	Y	N	N	N	N	N
CH_3CN *	(12_4-11_4)	220.679	183.3	Y	N	N	N	N	N
CH_3CN *	(12_3-11_3)	220.709	133.3	Y	N	N	N	N	N
CH_3CN *	(12_2-11_2)	220.730	97.4	Y	N†	N	N	N	N
CH_3CN *‡	(12_1-11_1)	220.743	76.0	Y	N	N	N	N	N
CH_3CN *‡	(12_0-11_0)	220.747	68.8	Y	N†	N	N	N	N
			USB						
SO_2	11(5, 7)-12(4, 8)	229.348	122.01	Y	N	N	N	N	N
$HCOOCH_3$	19(3,17)- 18(2,16) E	229.590	105.6	Y	N	N	N	N	N
CH_3OH *	8(-1, 8)- 7(0 , 7) E	229.759	89.1	Y	Y	N	N	N	Y
CH_3OH	19(5, 15)- 20(4, 16) ++	229.864	567.6	Y	N	N	N	N	N
CH_3OH	19(5, 14)- 20(4, 17) −−	229.939	567.6	Y	N	N	N	N	N
CH_3OH *	3(-2, 2)- 4(-1, 4) E	230.027	39.8	Y	Y	N	N	N	N

Continued on next page

Table 4.2 – continued from previous page

Species	Transition	Frequency	E_{upper}	G192		G194			
		(GHz)	(K)	SMA1	SMA2	SMA1	SMA2	SMA3	MP
^{12}CO *	(2 - 1)	230.538	16.6	Y	Y	Y	Y	Y	Y
OCS *	(19 - 18)	231.061	110.8	Y	N	N	N	N	N
^{13}CS *	(5 - 4)	231.221	33.29	Y	Y	N	N	N	N
CH_3OH	10(2, 9)- 9(3, 6) $--$	231.281	165.3	Y	N	N	N	N	N
$HCOOCH_3$	23(9,15)-23(8,16) E	232.422	392.4	Y	N	N	N	N	N

(*) Notes transitions that were also observed towards NGC 2264-C (see Table 3.2 for reference). (†) Notes molecular lines where the emission is $<5\sigma$ but detected above $>3\sigma$. (‡) These CH_3CN components are blended in the spectra. The K=0 is blended with the K=1 and the K=6 is partially blended with the HNCO 10(1, 9)- 9(1, 8) transitions.

Table 4.3: Gaussian fits to molecular lines detected at each millimetre continuum peak in G192.6005 detected above 3σ. Standard 1-σ errors from the single Gaussian fits are given in the brackets ().

Species	Transition	Frequency	E_{upper}	Fitted Line Parameters			
				Peak Intensity	V_{centre}	Linewidth	$\int$ S dv
		(GHz)	(K)	(Jy beam^{-1})	(km s^{-1})	(km s^{-1})	(Jy beam^{-1} km s^{-1})
				G192-SMA1			
CH_3OH^*	5(1 , 4) - 4(2, 2)	216.946	55.9	1.01 (0.04)	4.36 (0.11)	5.68 (0.27)	6.13 (0.38)
CH_3OCH	$20_{1,20}$-$19_{0,19}$0 E	216.968	101	0.37 (0.03)	7.10 (0.29)	6.68 (0.74)	2.65 (0.37)
SiO^* $^\diamond$	(5 - 4)	217.105	31.3	0.29 (0.03)	9.76 (0.38)	8.74 (0.88)	2.68 (0.36)
DCN^*	(3 - 2)	217.239	20.9	0.40 (0.10)	4.39 (0.21)	2.03 (0.67)	0.86 (0.35)
CH_3OH^*	6(1, 5)- 7(2, 6)	217.299	363.5	0.66 (0.02)	4.10 (0.08)	4.65 (0.20)	3.26 (0.18)
H_2CO^*	3(0, 3) - 2(0, 2)	218.222	21.0	1.47 (0.14)	5.33 (0.27)	5.69 (0.65)	8.91 (1.34)
HC_3N^*	(24 - 23)	218.324	131.0	0.45 (0.03)	6.66 (0.26)	7.66 (0.60)	2.65 (0.38)
CH_3OH^*	4(2, 2) - 3(1, 2)	218.440	45.5	0.78 (0.04)	4.73 (0.12)	4.37 (0.29)	3.64 (0.31)
H_2CO^*	3(2, 2)- 2(2, 1)	218.476	68.1	0.88 (0.05)	5.04 (0.14)	5.07 (0.32)	4.74 (0.39)
H_2CO^*	3(2, 1)- 2(2, 0)	218.760	68.1	0.80 (0.06)	5.00 (0.16)	4.58 (0.39)	3.92 (0.44)
OCS *	(18 - 17)	218.903	99.8	0.64 (0.03)	4.70 (0.13)	5.09 (0.30)	3.47 (0.27)
HNCO	10(1,10)- 9(1, 9)	218.981	101.08	0.45 (0.02)	4.70 (0.16)	7.38 (0.38)	3.54 (0.24)
$C^{18}O$	(2 - 1)	219.560	15.8	1.92 (0.06)	7.83 (0.08)	5.55 (0.19)	11.37 (0.52)
$HNCO^\diamond$	10(2, 9)- 9(2, 8)	219.734	231	0.32 (0.03)	7.43 (0.42)	9.64 (1.01)	3.33 (0.46)
HNCO	10(0,10)- 9(0, 9)	219.798	58.02	0.48 (0.03)	4.44 (0.38)	11.04 (0.89)	5.59 (0.59)
SO^*	6(5)-5(4)	219.949	35.0	2.97 (0.08)	7.11 (0.10)	8.05 (0.23)	25.48 (0.99)

Continued on next page

Table 4.3 – continued from previous page

Species	Transition	Frequency	E_{upper}	Fitted Line Parameters			
				Peak Intensity	V_{centre}	Linewidth	$\int S\, dv$
		(GHz)	(K)	(Jy beam^{-1})	(km s^{-1})	(km s^{-1})	(Jy beam^{-1} km s^{-1})
HCOOH	10(0,10)- 9(0, 9)	220.03797	48.0	0.32 (0.04)	4.00 (0.23)	6.16 (0.56)	2.07 (0.24)
CH_3OH *	8(0 , 8)- 7(1 , 6) E	220.078	96.6	0.93 (0.03)	5.18 (0.07)	4.82 (0.16)	4.78 (0.21)
HNCO	10(1, 9)- 9(1, 8)	220.585	101.50	0.39 (0.04)	5.11 (0.39)	8.58 (0.94)	3.60 (0.52)
CH_3CN	(12_6-11_6)	220.594	325.90	0.36 (0.04)	4.27 (0.25)	6.65 (0.61)	2.55 (0.30)
CH_3CN	(12_5-11_5)	220.641	247.40	0.37 (0.04)	4.44 (0.26)	5.33 (0.61)	2.12 (0.32)
CH_3CN *	(12_4-11_4)	220.679	183.3	0.49 (0.04)	5.32 (0.27)	5.56 (0.71)	2.19 (0.43)
CH_3CN *	(12_3-11_3)	220.709	133.3	0.74 (0.03)	5.06 (0.10)	5.61 (0.26)	4.44 (0.26)
CH_3CN *	(12_2-11_2)	220.730	97.4	0.72 (0.03)	4.76 (0.06)	5.52 (0.17)	4.22 (0.30)
CH_3CN *‡	(12_1-11_1)	220.743	76.0	0.84 (0.03)	4.64 (0.26)	5.39 (1.01)	4.82 (0.91)
CH_3CN *‡	(12_0-11_0)	220.747	68.8	0.68 (0.03)	4.56 (0.46)	3.75 (0.81)	2.73 (0.84)
SO_2	11(5, 7)-12(4, 8)	229.3476	122.01	0.39 (0.02)	6.42 (0.13)	5.56 (0.30)	2.31 (0.29)
$HCOOCH_3$	19(3,17)- 18(2,16) E	229.5904	105.6	0.88 (0.03)	6.12 (0.07)	5.23 (0.17)	4.92 (0.21)
CH_3OH *	8(-1, 8)- 7(0 , 7) E	229.759	89.1	1.22 (0.04)	5.00 (0.08)	4.61 (0.19)	5.99 (0.33)
CH_3OH	19(5, 15)- 20(4, 16) ++	229.864	567.6	0.31 (0.02)	4.23 (0.25)	7.70 (0.68)	2.57 (0.28)
CH_3OH	19(5, 14)- 20(4, 17) −−	229.939	567.6	0.28 (0.04)	3.60 (0.28)	4.56 (0.67)	1.35 (0.26)
CH_3OH *	3(-2, 2)- 4(-1, 4) E	230.027	39.8	0.78 (0.04)	4.40 (0.12)	4.69 (0.28)	3.95 (0.32)
OCS *	(19 - 18)	231.061	110.8	0.59 (0.03)	4.97 (0.10)	5.44 (0.25)	3.40 (0.20)
^{13}CS *	(5 - 4)	231.221	33.29	0.30 (0.03)	2.77 (0.44)	9.24 (1.19)	2.98 (0.48)
CH_3OH	10(2, 9)- 9(3, 6) −−	231.281	165.3	0.98 (0.06)	4.77 (0.14)	4.85 (0.33)	5.09 (0.46)

Continued on next page

Table 4.3 – continued from previous page

Species	Transition	Frequency	E_{upper}	Fitted Line Parameters			
				Peak Intensity	V_{centre}	Linewidth	$\int S\, dv$
		(GHz)	(K)	(Jy beam^{-1})	(km s^{-1})	(km s^{-1})	(Jy beam^{-1} km s^{-1})
$HCOOCH_3$	23(9,15)-23(8,16) E	232.422	392.4	0.36 (0.03)	3.18 (0.21)	5.00 (0.49)	1.94 (0.25)
				G192-SMA2			
CH_3OH*	5(1 , 4) - 4(2, 2)	216.946	55.9	0.26 (0.03)	8.73 (0.25)	4.20 (0.59)	1.15 (0.21)
SiO *	(5 - 4)	217.105	31.3	0.21 (0.04)	9.31 (0.29)	3.24 (0.69)	0.74 (0.20)
DCN *	(3 - 2)	217.239	20.9	0.95 (0.03)	9.46 (0.04)	3.21 (0.10)	3.23 (0.13)
H_2CO*	3(0, 3) - 2(0, 2)	218.222	21.0	2.59 (0.11)	9.03 (0.07)	3.41 (0.17)	9.42 (0.60)
HC_3N *	(24 - 23)	218.324	131.0	0.39 (0.03)	9.55 (0.15)	3.69 (0.36)	1.55 (0.19)
CH_3OH*	4(2, 2) - 3(1, 2)	218.440	45.5	1.66 (0.04)	8.51 (0.04)	3.08 (0.10)	5.43 (0.22)
H_2CO*	3(2, 2)- 2(2, 1)	218.476	68.1	0.75 (0.04)	8.74 (0.08)	3.35 (0.20)	2.66 (0.21)
H_2CO*	3(2, 1)- 2(2, 0)	218.760	68.1	0.83 (0.06)	8.69 (0.11)	3.13 (0.25)	2.76 (0.30)
$C^{18}O$ *	(2 - 1)	219.560	15.8	4.42 (0.09)	9.37 (0.03)	2.98 (0.07)	14.05 (0.45)
HNCO †	10(0,10)- 9(0, 9)	219.798	58.02	0.18 (0.03)	8.52 (0.18)	1.85 (0.30)	0.35 (0.08)
SO *	6(5)-5(4)	219.949	35.0	2.25 (0.10)	9.08 (0.07)	3.38 (0.17)	8.13 (0.54)
CH_3OH *†	8(0 , 8)- 7(1 , 6) E	220.078	96.6	0.23 (0.04)	8.57 (0.25)	3.02 (0.60)	0.74 (0.19)
CH_3CN *†	(12_2-11_2)	220.730	97.4	0.17 (0.04)	9.22 (0.22)	2.48 (0.53)	0.45 (0.13)
CH_3CN *†	(12_0-11_0)	220.747	68.8	0.21 (0.03)	9.46 (0.20)	2.15 (0.48)	0.48 (0.14)
CH_3OH *	8(-1, 8)- 7(0 , 7) E	229.759	89.1	0.77 (0.06)	8.55 (0.15)	3.45 (0.35)	2.84 (0.38)
CH_3OH *	3(-2, 2)- 4(-1, 4) E	230.027	39.8	0.25 (0.04)	8.88 (0.17)	2.84 (0.40)	0.75 (0.14)
^{13}CS*	(5 - 4)	231.221	33.29	0.39 (0.08)	8.84 (0.25)	2.29 (0.58)	0.94 (0.31)

(*) Notes transitions that were also observed towards NGC 2264-C (see Table 3.2 for reference). (†) Notes molecular lines where the emission is $<5\sigma$ but detected above $>3\sigma$. (‡) These CH_3CN components are blended in the spectra. The K=0 is blended with the K=1 and the K=6 is partially blended with the HNCO 10(1, 9)- 9(1, 8) transitions, The reported parameters are from multiple-Gaussian fits using the GILDAS CLASS package. (⋄) Two velocity components appear to be present in the spectrum, but are not sufficiently well-separated in velocity to be fit separately. The reported fit is for the stronger component.

Table 4.4: Gaussian fits to molecular lines detected at each millimetre continuum peak in G194.9349 detected above 3σ. Standard 1-σ errors from the single Gaussian fits are given in the brackets (). It is noted that all transitions given were also observed towards NGC 2264-C (see Table 3.2 for reference).

Species	Transition	Frequency	E_{upper}	Fitted Line Parameters			
				Peak Intensity	V_{centre}	Linewidth	$\int S\, dv$
		(GHz)	(K)	(Jy beam^{-1})	(km s^{-1})	(km s^{-1})	(Jy beam^{-1} km s^{-1})
				G194-SMA1			
H_2CO	3(0, 3) - 2(0, 2)	218.222	21.0	1.09 (0.06)	15.03 (0.06)	3.01 (0.20)	3.50 (0.30)
H_2CO †	3(2, 2)- 2(2, 1)	218.476	68.1	0.18 (0.03)	14.91 (0.14)	2.64 (0.32)	0.52 (0.08)
H_2CO	3(2, 1)- 2(2, 0)	218.760	68.1	0.35 (0.04)	14.87 (0.16)	1.96 (0.30)	0.72 (0.15)
$C^{18}O$	(2 - 1)	219.560	15.8	0.84 (0.08)	15.31 (0.12)	2.53 (0.28)	2.26 (0.33)
SO †	6(5)-5(4)	219.949	35.0	0.26 (0.07)	15.25 (0.28)	2.00 (0.61)	0.55 (0.22)
				G194-SMA2			
H_2CO	3(0, 3) - 2(0, 2)	218.222	21.0	0.64 (0.09)	16.94 (0.18)	2.43 (0.43)	1.66 (0.39)
CH_3OH †	4(2, 2) - 3(1, 2)	218.440	45.5	0.26 (0.03)	16.61 (0.20)	3.26 (0.49)	0.93 (0.18)
H_2CO †	3(2, 2)- 2(2, 1)	218.476	68.1	0.28 (0.06)	16.73 (0.33)	3.40 (0.77)	1.01 (0.31)
H_2CO †	3(2, 1)- 2(2, 0)	218.760	68.1	0.27 (0.09)	16.21 (0.41)	1.70 (0.61)	0.49 (0.24)
$C^{18}O$	(2 - 1)	219.560	15.8	1.61 (0.10)	16.29 (0.10)	3.02 (0.23)	5.14 (0.55)
SO	6(5)-5(4)	219.949	35.0	0.75 (0.04)	16.10 (0.09)	3.31 (0.20)	2.65 (0.22)
				G194-SMA3			
H_2CO	3(0, 3) - 2(0, 2)	218.222	21.0	0.36 (0.04)	12.93 (0.13)	2.45 (0.31)	0.94 (0.16)
				G194-MP			

Continued on next page

Table 4.4 – continued from previous page

Species	Transition	Frequency	E_{upper}	Fitted Line Parameters			
				Peak Intensity	V_{centre}	Linewidth	$\int S\, dv$
		(GHz)	(K)	(Jy beam^{-1})	(km s^{-1})	(km s^{-1})	(Jy beam^{-1} km s^{-1})
SiO $^{\diamond}$	(5 - 4)	217.105	31.3	0.23 (0.03)	10.77 (0.55)	9.56 (1.38)	2.34 (0.31)
H_2CO	3(0, 3) - 2(0, 2)	218.222	21.0	1.06 (0.10)	17.44 (0.20)	4.49 (0.50)	5.07 (0.73)
CH_3OH	4(2, 2) - 3(1, 2)	218.440	45.5	0.80 (0.07)	16.83 (0.19)	4.40 (0.46)	3.72 (0.51)
H_2CO	3(2, 2)- 2(2, 1)	218.476	68.1	0.39 (0.06)	15.52 (0.50)	6.81 (1.21)	2.85 (0.66)
H_2CO	3(2, 1)- 2(2, 0)	218.760	68.1	0.54 (0.07)	17.14 (0.16)	2.58 (0.37)	1.48 (0.28)
$C^{18}O$	(2 - 1)	219.560	15.8	0.49 (0.10)	16.37 (0.46)	4.52 (1.13)	2.37 (0.77)
SO $^{\diamond}$	6(5)-5(4)	219.949	35.0	0.75 (0.07)	16.03 (0.26)	5.34 (0.60)	4.25 (0.64)
CH_3OH	8(-1, 8)- 7(0 , 7) E	229.759	89.1	0.99 (0.05)	17.23 (0.09)	3.52 (0.22)	3.72 (0.30)

(†) Notes molecular lines where the emission is $<5\sigma$ but detected above $>3\sigma$. ($\diamond$) Two velocity components appear to be present in the spectrum, but are not sufficiently well-separated in velocity to be fit separately. The reported fit is for the stronger component.

4.4.2.3 $v_{\rm LSR}$ Estimates

The $v_{\rm LSR}$ is estimated, for both G192.6005-SMA1 and G192.6005-SMA2, from Gaussian fits to the detected molecular transitions, using only transitions that trace compact emission directly associated with the mm continuum peaks (see Table 4.3 for the resulting Gaussian fit parameters to all lines). The following transitions are defined as compact: CH_3CN, HC_3N, OCS, and the CH_3OH transitions with rest frequencies of 216.946 GHz, 220.078 GHz and 230.027 GHz. In addition, for G192.6005-SMA1 all the molecular transitions that were not detected in NGC 2264-C (such as HNCO, and the higher energy CH_3OH transitions) are also included in the $v_{\rm LSR}$ estimate as they all trace compact emission coincident with the mm continuum emission. For G192.6005-SMA1 the average (including the standard deviation) and median $v_{\rm LSR}$'s are $4.8\pm0.9\,{\rm kms}^{-1}$ and $4.7\,{\rm kms}^{-1}$ respectively. For G192.6005-SMA2 only one compact tracer (CH_3OH 216.946 GHz) is detected above 5σ, which has a $v_{\rm LSR}$ of $8.7\,{\rm kms}^{-1}$. If the emission from tracers detected below 5σ but above 3σ is also considered (e.g. HNCO and CH_3CN), then the average and median $v_{\rm LSR}$ estimates for G192.6005-SMA2 are now $8.9\pm0.4\,{\rm kms}^{-1}$ and $8.8\,{\rm kms}^{-1}$ respectively. The CH_3OH line at 216.946 GHz is the only transition detected above 5σ towards both sources, and the $v_{\rm LSR}$ estimates are $4.36\ {\rm kms}^{-1}$ and $8.73\ {\rm kms}^{-1}$ for G192.6005-SMA1 and G192.6005-SMA2 respectively (see Tables 4.3, and 4.4). Thus, there is an $\sim4\,{\rm kms}^{-1}$ difference between the $v_{\rm LSR}$ estimates for the two mm continuum peaks. The $C^{18}O$ emission towards G192.6005-SMA1 is slightly offset from the continuum peak, having a higher estimated $v_{\rm LSR}$ of $7.8\,{\rm kms}^{-1}$, while for G192.6005-SMA2 it is consistent with the other tracers ($9.4\,{\rm kms}^{-1}$). The

$v_{\rm LSR}$ estimated in from the JCMT $H^{13}CO^+$ (4-3) emission (see Chapter 2) is 7.8 $\rm kms^{-1}$, consistent with $C^{18}O$ towards G192.6005-SMA1. The $C^{18}O$ at this position may therefore be tracing the bulk gas rather than the individual cores. Wang *et al.* (2011) suggest $C^{18}O$ is tracing a velocity gradient across the cores. Considering only the compact emission the $v_{\rm LSR}$ for G192.6005-SMA1 and G192.6005-SMA2 is taken as 4.8 $\rm kms^{-1}$ and 8.9 $\rm kms^{-1}$ respectively.

Towards G194.9349, none of the detected molecular line emission appears to directly trace any of continuum peaks in this region. There is also a lack of emission from the higher energy transitions such as OCS or from any of the complex organic molecules. Only one transition, H_2CO 3(0,3)-2(0,2), is detected towards all three cores. However, as also observed in Chapter 3, this transition is likely not directly tracing core material. The previous NH_3 observations by Lu *et al.* (2014) find an estimate for the $v_{\rm LSR}$ of the main NH_3 (1,1) component of 15.6 $\rm kms^{-1}$, which is the same as found from the average of the $H^{13}CO^+$ (4-3) emission over the region. Without having an estimate of any compact emission, and given the remaining transitions are likely not directly tracing the continuum cores, the $v_{\rm LSR}$ is taken to be 15.6 $\rm kms^{-1}$ for all three cores.

4.4.3 Outflows

4.4.3.1 High Velocity Emission Towards G192.6005

Figure 4.7 shows the integrated red and blueshifted maps for SiO, SO, and ^{13}CO towards G192.6005. As G192.6005-SMA1 and G192.6005-SMA2 have a difference of $\sim$4 $\rm kms^{-1}$ in their respective $v_{\rm LSR}$ estimates, the high velocity emission is integrated from the lowest $v_{\rm LSR}$ estimate (G192.6005-SMA1 = 4.8 $\rm kms^{-1}$)

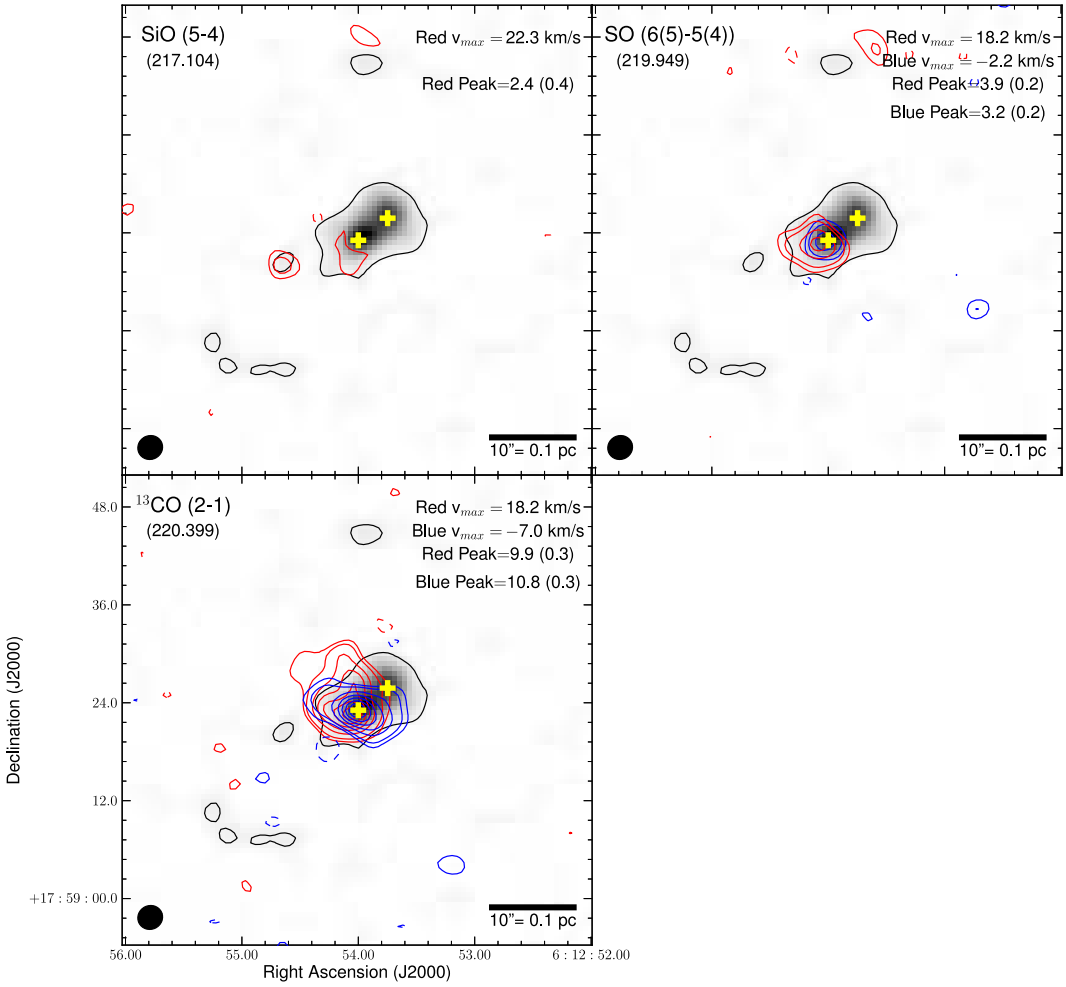

Figure 4.7: Integrated intensity maps for SiO (5-4), SO (6(5)-5(4), and ^{13}CO towards G192.6005. The transition and given rest frequency is given in the top left of each panel. The maximum red and blue shifted velocity of the line is given in the top right corner of each panel. Below these values are the red and blue peak fluxes given in Jy beam^{-1} km s^{-1} along with the 1 σ rms values given in the brackets.

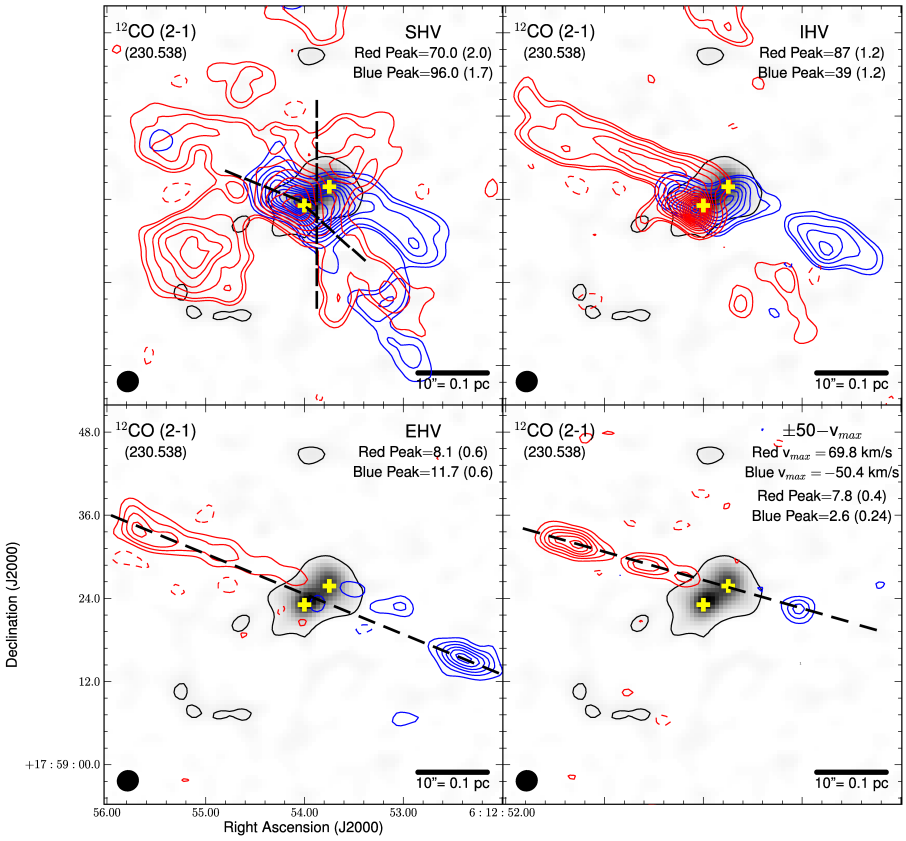

Figure 4.8: Integrated intensity of the ^{12}CO emission for SHV, IHV, EHV and emission >50 kms^{-1} velocity ranges towards G192.6005, using the $v_{\rm LSR}$ estimate for G192.6005-SMA1 for reference. The red- and blueshifted contours display the red and blue shifted emission with respect to the $v_{\rm LSR}$ of 4.8 kms^{-1}. The given velocity bin is labelled in the top right corner of each panel, for the lower right panel the maximum velocity is given. The peak of the red and blue shifted integrated emission and corresponding 1σ rms noise for each velocity bin is given in the top right corner of each panel in units of Jybeam^{-1}.kms^{-1}. The greyscale is the 1.3 mm continuum and the single black contour represents the 3σ contour of the 1.3 mm emission not corrected for the primary beam response. The yellow pluses mark the positions of the two identified cores G192.6005-SMA1 and G192.6005-SMA2. In the top left panel the black dashed lines represent the orientation of the scattered light lobes from Simpson *et al.* (2009). In the lower two panels the black dashed lines show a straight line joining the peak of the red- to blue-shifted emission.

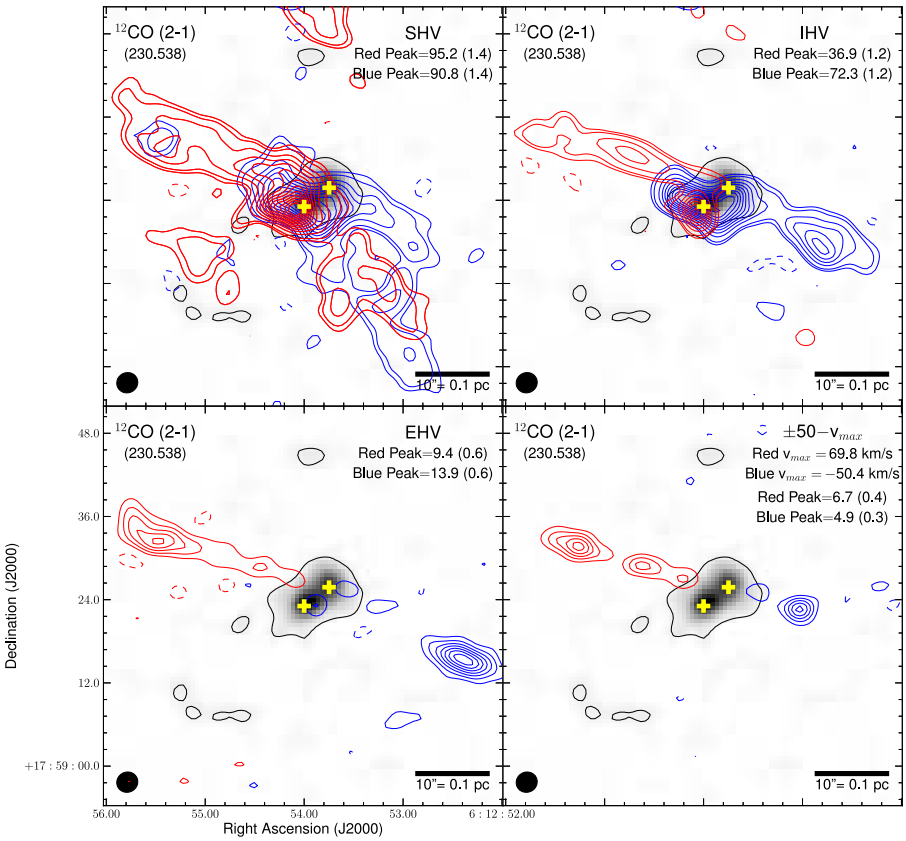

Figure 4.9: Integrated intensity of the ^{12}CO emission for SHV, IHV, EHV and emission >50 kms^{-1} velocity ranges towards G192.6005, using the $v_{\rm LSR}$ estimate for G192.6005-SMA2 for reference. The contours and greyscale, and labels are the same as described in Figure 4.3.

minus 3 kms^{-1} and highest $v_{\rm LSR}$ estimate (G192.6005-SMA2 = 8.9 kms^{-1}) plus 3 kms^{-1} to the minimum and maximum channel in the respective channel maps of each transition. This should avoid including systemic material as potential outflow emission. SiO traces only weak redshifted emission offset from G192.6005-SMA1, whereas both SO and ^{13}CO show red- and blueshifted emission coincident with this continuum peak. No high velocity emission is observed towards the continuum peak of G192.6005-SMA2.

Figures 4.8, and 4.9 display the high velocity red and blue-shifted ^{12}CO emis-

sion integrated over several velocity bins; $\pm$ 3-10 kms^{-1} (SHV), $\pm$ 10-30 kms^{-1} (IHV), $\pm$ 30-50 kms^{-1} (EHV) and >50 kms^{-1} with respect to the $v_{\rm LSR}$'s of G192.6005-SMA1 (4.8 kms^{-1}) and G192.6005-SMA2 (8.9 kms^{-1}) respectively. The only noticeable difference when using the respective $v_{\rm LSR}$ estimates of the sources is in the SHV regime, less emission is found along axis A1 (see Figure 4.5) when using the $v_{\rm LSR}$ of G192.6005-SMA2. However, in both cases the ^{12}CO emission is complex. Towards the higher velocity bins (e.g. SHV and EHV) there is no obvious difference when using either $v_{\rm LSR}$. The ^{12}CO high velocity emission is notably more complex and extended compared with the higher velocity SO, SiO and ^{13}CO emission, which all trace emission coincident with G192.6005-SMA1. The velocity range of the ^{12}CO emission extends over $\sim$100 kms^{-1}. In the lower velocity regimes (e.g. SHV and IHV regimes) ^{12}CO traces the extended red- and blueshifted emission centred on G192.6005-SMA1. However, when going to the higher velocity regimes (e.g. EHV and >50 kms^{-1}) extended emission is again observed, but there is no longer any obvious emission coincident with G192.6005-SMA1. In all of the velocity regimes the ^{12}CO emission displays extended, collimated red and blue-shifted emission, extending from to the north east (NE) and south west (SW) respectively (See axes in Figure 4.8).

In the top left panel of Figure 4.8 the axis of the scattered light lobes from Simpson *et al.* (2009) are overlaid on SHV emission. Wang *et al.* (2011) suggest the low velocity red-shifted emission extending to the south is likely a result of the outflow lobe associated with NIRS 1, and that the more collimated extended emission running from the NE to SW is associated with an outflow driven by SMA1/NIRS 3. They also highlight H_2O maser emission detected by Goddi *et al.* (2007) is also aligned in the NE-SW direction (see Figure 4.1). However,

if a straight line is crudely drawn from the peak of the blue- to the peak of the redshifted emission the position at which it cuts through the continuum emission changes from NIRS 1 (the near IR source that is located between SMA1 and SMA2) to SMA2 when going from the EHV regime to the emission with velocities $>50\,\mathrm{kms}^{-1}$, respectively. In addition, the angle of the line also changes by several degrees. This may be due to precession from both scattered light lobes, in particular the lobe associated with NIRS 1 shows twisted emission in the northern lobe (Simpson *et al.* 2009). While G192.6005-SMA1 is likely responsible for the compact red- and blueshifted emission, it is still not unambiguously clear at this resolution what is responsible for the outflow emission.

4.4.3.2 High Velocity Emission Towards G194.9349

Several of the transitions (e.g. H_2CO and CH_3OH in Figure 4.6) show two components in the emission, appearing to be centred on G194.9349-SMA2. SiO is weakly observed in the more northern of these components, at the position of G192.9349-MP. However, only the emission from ^{12}CO (2-1) has a high velocity range which extends over $\sim 50\,\mathrm{kms}^{-1}$.

Figure 4.10 displays the red- and blueshifted integrated intensity maps of SiO, SO, H_2CO and ^{13}CO emission. The emission is integrated from $15.6\pm3\,\mathrm{kms}^{-1}$ to minimum and maximum velocity of the lowest and highest velocity in the channel maps of each given transition. Only the ^{13}CO emission shows any velocity gradient, with blue-shifted emission to the north of G194.9349-SMA2 and red-shifted to the south, however the emission is not well collimated. In contrast, SiO, SO and H_2CO trace only a single component coincident with the position of G194.9349-MP.

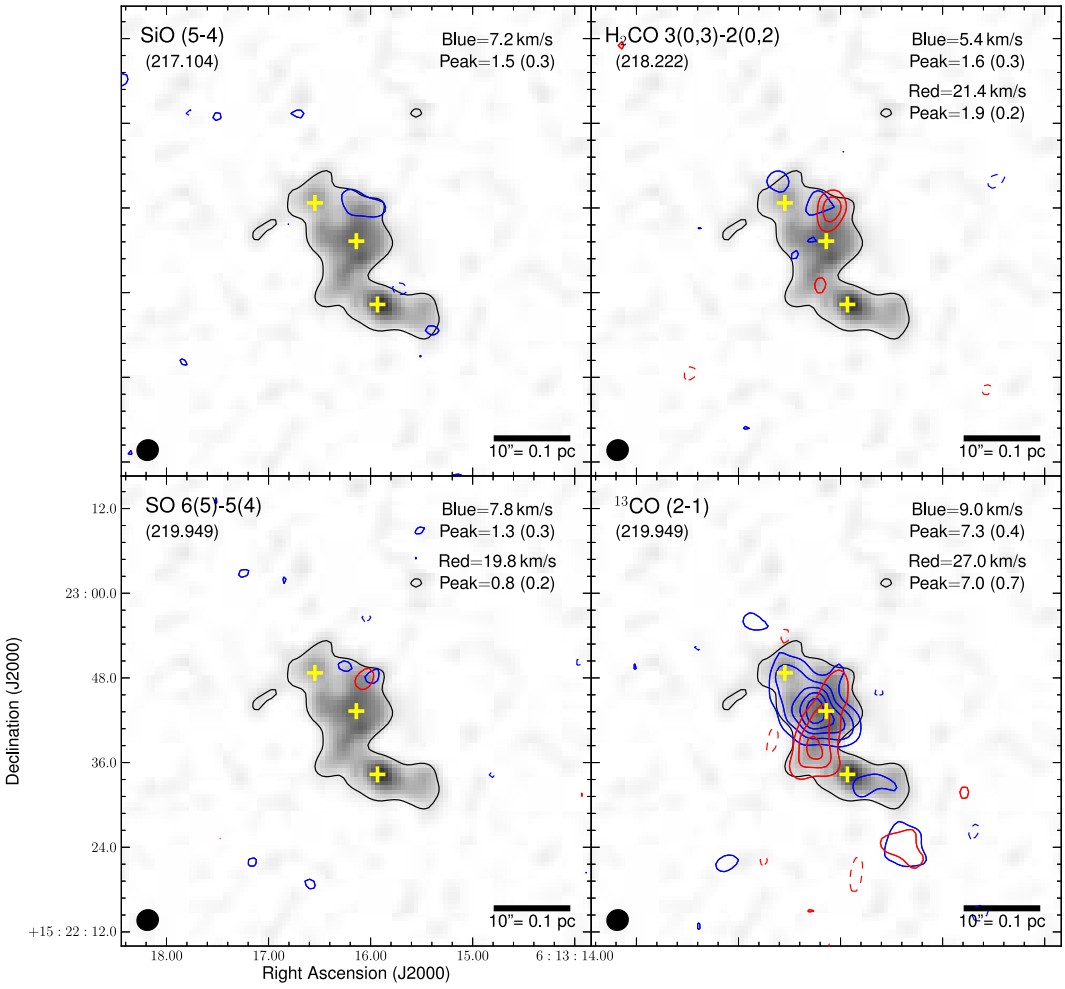

Figure 4.10: Integrated intensity maps for SiO (5-4), H_2CO 3(0,3)-2(0,2), SO (6(5)-5(4), and ^{13}CO towards G194. The transition and given rest frequency is given in the top left of each panel. The respective maximum velocity used for the integration are given in the top right corner of each panel along with the peak and σ rms noise level given in the brackets (e.g. Peak=). The emission is integrated from 15.6±3 kms^{-1} to maximum red and blueshifted velocity for each transition.

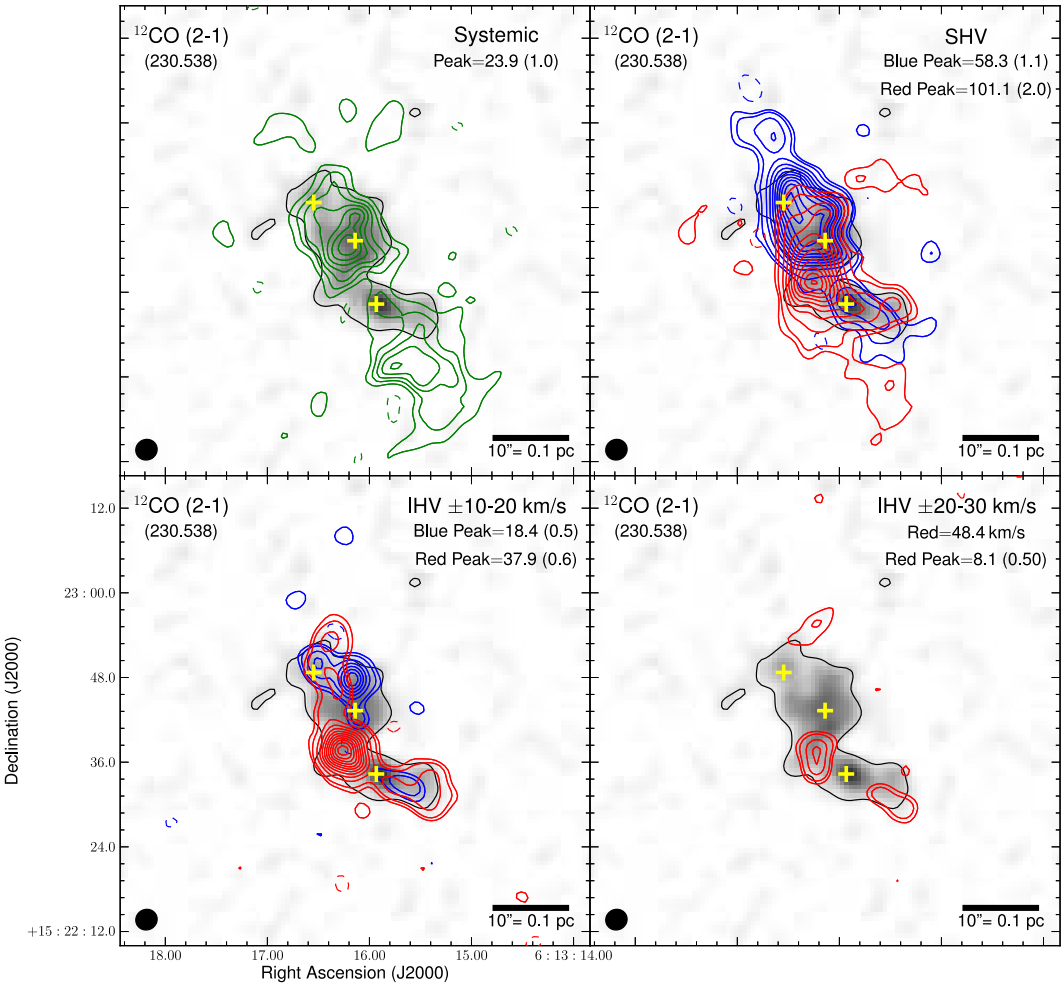

Figure 4.11: Integrated intensity of the ^{12}CO emission for systemic, SHV, and IHV velocity ranges towards G194.9349. The green contours are the systemic emission, while the red- and blueshifted contours display the red and blue shifted emission with respect to the $v_{\rm LSR}$ of 15.6 kms^{-1}. The velocity bin is labelled in the top right corned of each panel, along with the maximum velocity if the velocity range does not extend over the entire bin. The peak and 1σ rms noise for each velocity bin for both the red- and blueshifted emission is also given in the top right corner of each panel in units of Jybeam^{-1}.kms^{-1} (e.g. Red Peak = value () for redshifted integrated intensities and, Blue Peak=value() for the blueshifted integrated intensities). The greyscale is the 1.3 mm continuum and the single black contour represents the 3σ contour of the 1.3 mm emission not corrected for the primary beam response. The yellow pluses mark the positions of the three identified cores.

Figure 4.11 displays the ^{12}CO emission towards G194.9349 integrated over the systemic $v_{\rm LSR}\pm 3\,{\rm kms}^{-1}$, $\pm$ 3-10 $\,{\rm kms}^{-1}$ (SHV), and $\pm$ 10-30 $\,{\rm kms}^{-1}$ (IHV) velocity ranges (the IHV velocity range is split into $\pm$ 10-20 $\,{\rm kms}^{-1}$ and $\pm$ 20-30 $\,{\rm kms}^{-1}$ velocity bins) all with respect to the assumed $v_{\rm LSR}$ of 15.6 $\,{\rm kms}^{-1}$. Unlike G192.6005, there is no emission above >30 $\,{\rm kms}^{-1}$ from the $v_{\rm LSR}$ (e.g. in the EHV range or >50 $\,{\rm kms}^{-1}$) on G194.9349. The SHV and IHV ($\pm$ 10-20 $\,{\rm kms}^{-1}$) velocity bins both show red- and blue shifted emission to the south and north of G194.9349-SMA2 respectively. The strongest blueshifted emission in the IHV ($\pm$ 10-20 $\,{\rm kms}^{-1}$) velocity bin is coincident with the position of G194.9349-MP. Furthermore, there appears to be a hint of red- and blueshifted emission towards the position of G194.9349-SMA1 and in the highest velocity bin (e.g. IHV $\pm$ 20-30 $\,{\rm kms}^{-1}$ bin) redshifted emission is still observed at this position. It is suggested that the bulk of the high velocity ^{12}CO emission is tracing a bipolar outflow centred on G194.9349-SMA2. However, the emission is complex, containing multiple high velocity red and blueshifted components that are not obviously associated with a continuum peak. Thus, at the current resolution the ^{12}CO emission is still complex and it is difficult to dissect exactly what is contributing to the high velocity emission.

4.4.4 Far IR Herschel 70μm emission

The Herschel 70μm emission towards both G192.6005 and G194.9349 (taken from the Herschel archive) is presented in Figure 4.12. Towards G192.6005 the 850μm emission from SCUBA is also overlaid (taken from Di Francesco *et al.* 2008). Towards G192.6005, the brightest 70μm emission is coincident

with G192.6005-SMA1, while the 450μm emission is coincident with G192.6005-SMA2, suggesting G192.6005-SMA2 is potentially younger than G192.6005-SMA1. It is noted that in the 850μm SCUBA emission there are two additional enhancements in the emission; towards the position of SMA4 (Zinchenko *et al.* 2012) (where the 1.3 mm continuum emission is detected at $\sim$3.5σ in the beam corrected image), and the position to the north at $\sim$50% of the primary beam.

Towards G194.9349, the 70μm emission is coincident with G194.9349-SMA2. However, there is no obvious enhancement in the 70μm emission towards either G194.9349-SMA1, or G194.9349-SMA3. There is no SCUBA 450μm emission available for this source.

4.5 Discussion

4.5.1 Temperature and Mass Estimates

G192.6005-SMA1 is considerably molecular line rich. Molecular emission from several high energy complex organic molecules (COMs) is observed towards this source. In particular, the CH_3CN (12-11) ladder is detected up to the K=6 (E_{upper} =326 K) above 5σ. As discussed in Section 3.5.1.1, the CH_3CN ladder is commonly used to estimate the temperature. Following the same method the temperature is estimated through a rotational diagram for G192.6005-SMA1. The temperature is found to be 200$\pm$56 K when fitting up to the K=5 ladder transition, and 306$\pm$51 K when fitting up to the K=6 ladder transition. The high temperature estimates are probably only representing disc emission, which the CH_3CN emission is likely tracing, and not the bulk gas. As such, it will not

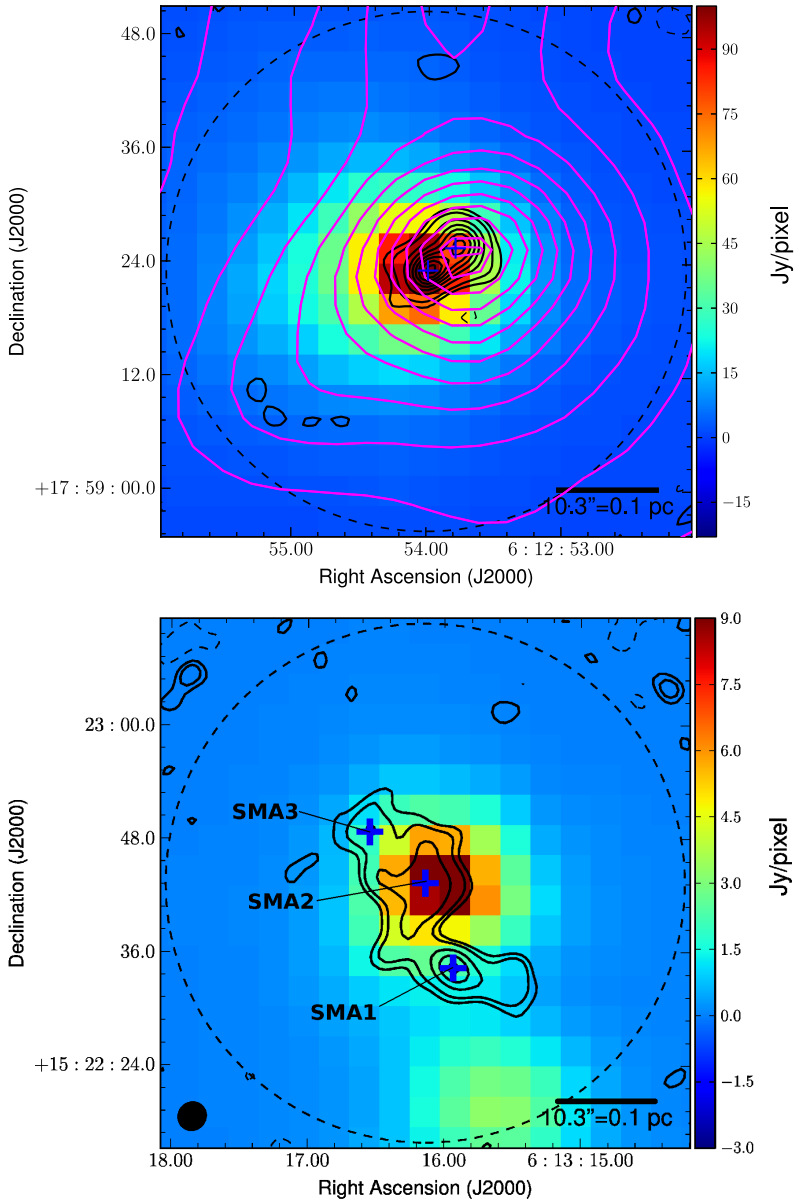

Figure 4.12: Herschel 70μm and SCUBA 850μm emission towards both regions. The colour scale is the 70μm Herschel emission taken from the archive. The solid magenta contours are the 850μm SCUBA data. The black contours are the 1.3 mm emission as shown and the black dashed contours are the FWHP of the SMA beam as shown in Figure 4.3.

represent the temperature of the dust traced by the 1.3 mm emission.

Towards G194.9349, considerably fewer molecular lines are detected. Furthermore, the molecular lines that are detected are typically lower energy (e.g. H_2CO. CH_3OH, $C^{18}O$, E_{upper} ∼16-68 K) and are likely associated with the outflow lobes, and not directly tracing material associated with the continuum peaks. None of the CH_3CN K-ladder transitions are detected. Previous interferometric observations by Lu *et al.* (2014) (see Figure 4.2) provide an estimate of the kinetic temperature derived from the NH_3(1,1) and (2,2) emission in the range of 8-43 K. However, they indicate a greater uncertainty for temperature estimates above 30 K, suggesting them as an upper limit. The highest temperature is found towards the continuum peak of G194.9349-SMA2, dropping to ∼20 K towards G194.9349-SMA1, with no emission towards G194.9349-SMA3. For G194.9349-SMA1, and G194.9349-SMA2 the mass is estimated using the kinetic temperature estimates from the NH_3 data of 30 K, and 20 K respectively. As no other temperature estimate is possible for G194.9349-SMA3 a temperature of 20 K is also assumed for this source.

Following the procedure from Section 3.5.1.2, assuming the emission is optically thin, a gas to dust ratio of 100, and the dust opacity to be κ_m =1.0 cm^2g^{-1} the masses are estimated for each continuum peak using the temperature estimates discussed above. For G192.6005, masses of 5.1 $M_\odot$ and 3.3 $M_\odot$ are estimated for G192.6005-SMA1 and G192.6005-SMA2 respectively (based on temperatures of 40 K). For G194.9349, masses of 8.4 $M_\odot$, 9.0 $M_\odot$ and 1.4 $M_\odot$ are estimated for G194.9349-SMA1, G194.9349-SMA2 and G194.9349-SMA3 respectively (based on temperatures of 30 K, 20 K and 20 K).

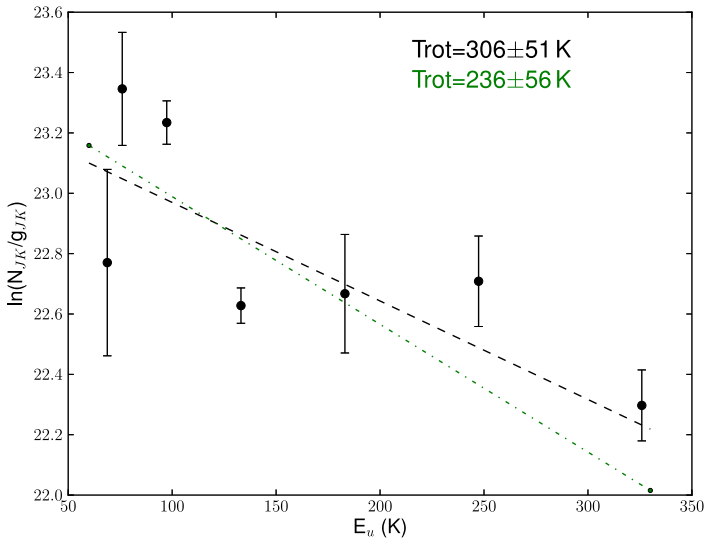

Figure 4.13: Rotation diagrams for the CH_3CN J=12_K-11_K towards G192.6005-SMA1. The error bars are from 1σ errors to the Gaussian fits of the individual transitions. The black dashed line represents the linear regression fit including all transitions up to K=6 and the green dot-dashed line gives the linear regression fit including transitions up to the K=5 transitions. The two fits are provided as the K=6 ladder transition is partly blended with the HNCO 10(1,9)-9(1,8) transition at 220.585 GHz.

4.5.2 Individual Sources - Possible Evolution

G192.6005-SMA1 (NIRS 3) is by far the most molecular rich of the continuum peaks observed. It shows a very typical hot core spectrum, characterised by numerous complex organic species with upper temperatures in excess of 200 K. Furthermore, the temperature estimate from the CH_3CN emission is in excess of 200 K. Previous observations have revealed both H_2O (Goddi *et al.* 2007) and 6.7 GHz class II CH_3OH (Xu *et al.* 2009) maser emission toward this continuum peak. The brightest 7.9μm (Longmore *et al.* 2006), 24.5μm (de Wit *et al.* 2009) and 70μm emission is also coincident with SMA1. The mm continuum estimate

is in agreement with previous, similar resolution, interferometric observations by Zinchenko *et al.* (2012). Furthermore, red- and blueshifted emission from several tracers is coincident with this continuum peak, suggesting it is likely driving a bipolar outflow.

G192.6005-SMA2 is less molecular line rich. In particular, none of the higher energy COMs are detected, however, emission is weakly observed from lower energy CH_3CN, and CH_3OH transitions. Furthermore, no 24.5μm emission or an obvious enhancement in the 70μm emission is found towards G192.6005-SMA2. Yet the 850μm SCUBA emission (see Figure 4.12) is coincident with this continuum peak. No high velocity emission potentially tracing an outflow is directly associated with this source, however the axis of the high velocity red- and blueshifted ^{12}CO emission (see Figure 4.8) appears to run through the centre of SMA2. The 1.3 mm emission is also similar for both SMA1 and SMA2. These results suggest G192.6005-SMA2 is likely less evolved than G192.6005-SMA1. It is noted that a second NIR source (NIRS 1) is observed in this region, located between SMA1 and SMA2 (which also shows mid and near IR emission Longmore *et al.* 2006; de Wit *et al.* 2009), however, this is not directly associated with SMA2. Furthermore, there is no obviously associated 1.3 mm emission with NIRS 1.

Towards **G194.9349** there is less molecular emission. Of the three continuum peaks identified; G194.9349-SMA3 is notably molecular line weak (only H_2CO is detected) and the 1.3 mm continuum is considerably weaker than for the other two continuum peaks. There is also no 70μm emission towards G194.9349-SMA3. Towards G194.9349-SMA1 and G194.9349-SMA2, the molecular and 1.3 mm continuum emission is similar between the two sources. The

significant difference between these two sources is the coincidence of the 70μm emission with G194.9349-SMA2, while no enhancement is found towards G194.9349-SMA1. There is no 450μm available for this region. Furthermore, the bulk of high velocity ^{12}CO emission is centred on G194.9349-SMA2. It is suggested that G194.9349-SMA2 is the most evolved source in this region and is driving the dominant CO outflow. However, it should be noted that there is a hint of two 1.3 mm continuum peaks within G194.9349-SMA2 and future higher resolution observations may reveal two or more sources at this position. G194.9349-SMA2 and G194.9349-SMA1 have similar mass estimates of $\sim$10M$_\odot$, whereas G194.9349-SMA3 is lower in mass ($\sim$1 M$_\odot$). An interesting feature in G194.9349 is the MP, which coincides with the only SiO emission detected in this region. There appears to be no enhancement in the mm continuum towards this position. However, the bulk emission from the parent structure is detected at $\sim5\sigma$ towards the MP. If the upper limits for continuum emission associated with the MP is assumed to be at the 5σ level, then a mass estimate of $\sim$1M$_\odot$ is obtained. The MP may be the result of a low mass core that is currently not resolved, or it could be caused by molecular emission excited along the outflow from G194.9349-SMA2. Inspection of the NIR emission towards the position of the MP is dominated by the emission from G194.9349-SMA2. Emission from the CH_3OH (229 GHz) line (i.e. which is potentially masing in the ridge feature observed in NGC 2264-C; see Section 3.4.2.3), is only observed towards the MP. Observations at higher sensitivity and resolution would be required to resolve any potentially associated continuum peak, and distinguish the nature of the MP.

Table 4.5: Outflow properties estimated from the ^{12}CO (2-1) high velocity emission.

Source	i [a] (°)	$\lvert v_{max}\text{-}v_{LSR}\rvert$ [b] (kms^{-1})	l (pc)	T_{dyn} (yrs)	M_{out} ($10^{-3}M_\odot$)	P_{out} [c] ($M_\odot$ kms^{-1})	E_{out} [c] (erg) ($\times10^{43}$)	$\dot{M}_{out}$ [c] $M_\odot$yr^{-1}) ($\times10^{-5}$)	$\dot{P}_{out}$ [c] ($M_\odot$ kms^{-}yr^{-1}) ($\times10^{-4}$)
G192-Red lobe	45-60	65	0.33-0.26	3500-2000	81	2.3-3.3	95-190	2.3-4.1	6.5-16.5
G192-Blue lobe	45-60	55	0.33-0.26	4100-2400	121	3.0-5.0	58-116	3.5-6.0	5.6-13.3
G194-Red lobe	45-60	33	0.23-0.19	4900-2800	130	1.7-2.4	25-51.0	2.6-4.6	3.5-8.6
G194-Blue lobe	45-60	21	0.27-0.22	9100-5300	89	1.0-1.4	11-23	1.0-1.7	1.0-2.6

([a]) Inclination from line of sight the outflow properties are estimated assuming both an inclination of 45° and 60°. ([b]) The velocity range used to estimate the outflow properties. ([c]) Values are calculated from the dynamical timescale estimates from the ^{12}CO (2-1).

4.5.3 Outflow Properties

Following the same procedure as described in Section 3.5.3, the outflow properties are estimated from the ^{12}CO (2-1) emission. Table 4.5.2 gives the calculated properties such as outflow mass and momentum for the red- and blueshifted emission towards each region. For G192.6005, the outflow properties are estimated from the high velocity emission over the velocity ranges of 15.6−69.6 kms^{-1} for the redshifted emission and -50.4−0 kms for the blueshifted emission. Towards G194.9349, the high velocity red- and blueshifted emission coincident with G194.9349-SMA1 is excluded from the outflow estimates, and the outflow properties are determined using red- and blueshifted emission in the velocity ranges of 22.4−48.8 kms^{-1} and -5.2−9.2 kms^{-1} respectively.

4.5.3.1 Comparison of Outflow Properties

Towards both regions similar outflow properties are estimated. The most notable difference is in the velocity ranges traced by the ^{12}CO emission between the region. Towards G192.6005, both the velocity in the red- and blue-shifted lobes (at 65 kms^{-1} and 55 kms^{-1} respectively) is approximately twice the velocity from the red- and blueshifted lobes of G194.9349 (at 33 kms^{-1} and 21 kms^{-1} respectively). It should be noted that the same outflow inclinations have been used for both regions, and may not represent the true inclination. As the dynamical timescale is dependant on the inverse of the maximum velocity, and given the outflow sizes are similar between both regions, the dynamical timescale for G194.9349 is approximately twice that of G192.6005. The total outflow masses are approximately the same in both regions at $\sim$0.1M$_\odot$. The average outflow

forces are $1\times10^{-3}\,M_{\odot}\,kms^{-1}\,yr^{-1}$ and $8\times10^{-4}\,M_{\odot}\,kms^{-1}\,yr^{-1}$ for G192.6005 and G194.9349 respectively. The mass and outflow forces are $\sim$50 and 2 times lower respectively than the single dish ^{12}CO (3-2) estimates from Maud *et al.* (2015b). However, there is a difference of $\sim$5 in the spatial resolution between the SMA and the JCMT observations. Furthermore, as the SMA is not sensitive to emission on scales $\geq20''$, it is expected that emission will be lost due to spatial filtering. However, while the masses are considerably different between the SMA and JCMT observation, the forces are similar as the maximum outflow velocities observed in these SMA observations are greater than seen by Maud *et al.* (2015b).

The derived outflow forces and bolometric luminosities taken from the RMS survey are plotted in Figure 3.13 (see Section 3.5.4.2). For both sources the derived outflow forces fall below the linear fit to all of the data, and also sit below the linear correlation extended from the class I sources from Bontemps *et al.* (1996). However, as with NGC 2264-C, the outflow properties have not been corrected for optical depth or potential missing flux, and are thus likely lower limits. However, even using the single dish outflow force for G192.6005 and G194.9349 estimated from Maud *et al.* (2015b) of $5.2\times10^{-3}\,M_{\odot}\,kms^{-1}\,yr^{-1}$ and $3.8\times10^{-3}\,M_{\odot}\,kms^{-1}\,yr^{-1}$ respectively they would now sit around the class I correlation. Both sources have previous ^{12}CO (2-1) single dish observations from (Wang *et al.* 2011; G192.6005, IRAM 30m ^{12}CO (2-1)) and (Kim & Kurtz 2006b; G194.9349) and in both cases the outflow force is an order of magnitude higher in the ^{12}CO (2-1) estimates compared with the ^{12}CO (3-2) derived outflow forces, similar to that found by Dunham *et al.* (2014). If the ^{12}CO (2-1) outflow forces from the literature are now added to Figure 3.13 the sources would now sit

near the line representing the class 0. Thus, depending on the tracer, observing method and applied correction the outflow forces can differ by more than an order of magnitude.

4.5.4 SiO Emission

In both regions the SiO emission is found to be compact, tracing only one or two positions, and is not found to be extended along the outflow axes. Considering the typical strength of the SiO emission observed towards the outflows driven by C-MM3 and C-MM12 in NGC 2264-C (see Section in 3) the emission would be expected to be detected at 0.18 Jy/beam and 0.11 Jy/beam in G192.6005 and G194.9349 respectively (corrected for the distances of 1.6 kpc and 2 kpc). Given the 1σ rms noise per channel in the SiO maps is $\sim$0.06 Jy/beam for both G192.6005 and G194.9349, then the extended SiO emission would be present at $\sim$3, and $<2\sigma$ respectively. The lack of extended SiO emission may then be due to sensitivity in the observations. However, in both regions at the position where compact SiO is detected, it is detected at approximately 3 times greater intensity than what is expected from the strongest SiO emission in NGC 2264-C. Furthermore, the emission from transitions such as CH_3CN, OCS and H_3CN is observed to be more than 10 times brighter in G192.6005 than expected (again from scaling the emission in NGC 2264-C to the distance of 1.6 kpc). This suggests that the lack of SiO emission along the extent of the outflow axis may be real in G192.6005. In G194.9349 emission from transitions such as CH_3CN, OCS HC_3N is not observed, and compared with the typical strength of the emission in NGC 2264-C it would be expected to fall below the sensitivity

limit. However, the detected transitions (e.g. H_2CO, SO, and CH_3OH) are all stronger than predicted from the emission in NGC 2264-C. Thus, it is less clear if the lack of SiO emission in this region is due to sensitivity limitations. Moreover, the nature of the MP is also ambiguous. If it is the result of a low mass core, given the typical detections of SiO emission in low mass regions it would not expected to be detected. It may then represent a denser region along the outflow driven by G194.9349-SMA2. In the JCMT observations (Chapter 2), SiO is detected towards G192.6005, but not towards G194.9349. However, in these higher resolution SMA observations SiO is now observed towards both regions. Thus, complementary higher resolution observations are critical in fully understanding the picture of massive star formation. However, even at the spatial scales resolved here ($\sim$5000 AU) it is difficult to identify the exact nature of the SiO emission, and it is currently not possible to identify if the outflows in both regions are potentially "active" or "fossil". Both higher sensitivity and resolution observations would be required, in both regions, to confirm the lack of SiO emission tracing collimated emission along the outflows

4.5.5 The Outflow Driving Sources

In both regions the 70μm bright sources are coincident with the centre of the red- and blueshifted ^{12}CO (2-1) outflows, and it appears that the most evolved source in each region is driving an outflow. However, it is stressed that both regions are complex, and currently the resolution and sensitivity are not sufficient to fully understand the picture. In particular, the high velocity outflow emission in G192.6005 is not clearly associated with any source and an argument could

be made for either SMA1 or SMA2 as the driving source.

While G192.6005, is classed as a *low* source, compared with G194.9349 which is identified as a *High* source (see section 4.2), G192.6005 is only slightly below the *High* source cut-off ([25-12]=0.5 for G192.6005). Furthermore, radio continuum emission is observed (3.1 mJy at 15 GHz) (Ojha *et al.* 2011) towards G192.6005-SMA1. However, taking the flux at 15 GHz and scaling assuming the emission is optically thin gives an expected 8 GHz luminosity of $L_\nu(8\,\mathrm{GHz})=\sim 9\times10^{11}$, which is comparable to the typical values of MYSOs with similar bolometric luminosities (e.g. see Figure 6 of Lumsden *et al.* 2013). The [70-22] colour, where the 70μm emission is taken from the Herschel archive data and the 22μm flux from WISE (taken from the RMS survey), is similar in both regions at 0.6 and 0.7 for G192.6005 and G194.9349 respectively. In contrast, the bolometric luminosity to mass ratio (using the mass estimates from the HCO^+ (4-3) emission in Chapter 2) gives a ratio of $\sim$500 for G192.6005 and $\sim$30 for G194.9349, which suggests G194.9349 is potentially less evolved than G192.6005. In comparison, the bolometric to mass ratio for C-MM3 (using the mass estimate for the offset source and the luminosity estimated in Chapter 3) is 0.79, thus C-MM3 is expected to be even less evolved than either of these regions. However, these properties are probing the global properties of the region, and particularly in the case of the colours they will be dominated by the IR bright RMS source which may not actually be the driving source of the outflow emission (as is the case for NGC 2264-C).

If the molecular emission between regions is also considered as a possible indication of evolution, then G192.6005-SMA1 would be expected to be most evolved. However, as previously mentioned, the presence and strength of molec-

ular emission is dependent on the mass and luminosity of the source. Thus, it is difficult to make a comparison between the molecular emission in G192.6005 which has a bolometric luminosity an order of magnitude larger than G194.9349. In particular, when scaling the emission from C-MM5 in NGC 2264-C, which has a similar bolometric luminosity ($1800 L_{\odot}$), the emission from the hot core tracers would fall below the 3σ sensitivity limit in G194.9349. Thus, it is difficult to distinguish the evolutionary nature of the outflow driving sources between regions.

4.5.6 Comparison with the Literature

One major difficulty when comparing outflow properties between surveys is the difference in spatial scales probed, particular when comparing the high and low mass regime. In addition, a still difficult task is establishing an age or evolutionary stage between sources of different mass and luminosity. There are currently limited examples of well resolved outflows in high mass regions with targeted observations of both CO and SiO (e.g. G24.78+0.08 Codella *et al.* 2013; and IRAS 17233-3606 Klaassen *et al.* 2015 and references therein). If the outflow forces estimated from these regions were placed on Figure 3.13, they would lie above the line of best fit with estimated forces of a few $\times 10^{-2}\,\mathrm{M_{\odot}\,kms^{-1}\,yr^{-1}}$. However, it is not unambiguously clear in Codella *et al.* (2013) what is driving the SiO emission.

4.6 Conclusions

This Chapter has presented SMA 1.3 mm at $\sim 3''$resolution towards G192.6005 and G194.9349, providing the first interferometric continuum, SiO and ^{12}CO observations towards G194.9349. The aim of the Chapter was to explore the differences between regions with and without SiO emission (i.e. of a potentially active and fossil outflow). The following key points are found:

- Towards each region a high velocity bipolar outflow traced by ^{12}CO ($>50\,\mathrm{kms}^{-1}$ in G192.6005) is observed. In both regions the outflows are most likely driven by the 70μm IR- bright RMS source. This is contrary to the outflows observed in NGC 2264-C where the IR bright RMS source has no associated outflow, and it is the IR-dark, mm bright, likely youngest sources that drive the outflows.

- Towards both regions no high velocity, extended SiO emission is tracing the outflows, and only weak lower velocity SiO emission is observed towards either G192.6005 or G194.9349. Thus, the lack of SiO emission in these sources may be due to the more evolved nature of the driving sources in G192.6005 and G194.9349 compared with the young sources driving the collimated outflows traced by SiO in NGC 2264-C. Whether, the lack of collimated high velocity SiO emission in both of these regions can be attributed to the sensitivity limitations of the data is not clear, and would require more sensitive observations to confirm this. However, particularly in the case of G192.6005, the source driving the outflow is molecular line rich, with a multidue of typical hot molecular core tracing species strongly detected, suggesting the lack of SiO emission may be real

in this source. The "active" or "fossil" nature of these outflows however cannot be confirmed by these observations alone.

- The estimated outflow forces for G192.6005, G194.9349 and NGC 2264-C (given that they have been calculated from the same observational setup and under the same assumptions), while only providing four points on the outflow force vs bolometric luminosity in Figure 3.13, would provide a linear fit with a less inclined slope than would be expected if the gradient from the class 0 and class I correlations was applied. Thus, if the high mass regime can be seen as a scaled up version of the low mass regime, this would suggest the outflows from G192.6005 and G194.9349 are more evolved than those in NGC 2264-C, which is in agreement with the results of multi-line observations presented in this thesis. However, this is very tentative and would require observations towards significantly more regions, where the outflow driving properties are known, to fill in this plot to either confirm or refute this.

- In both regions a clear evolutionary differentiation between the continuum sources is observed. In G192.6005 the NIR source, NIRS 1, is not coincident with SMA2 but is a separate source with no observed mm continuum emission, whereas SMA1 is coincident with the bright 70μm source NIRS 3. However, there is an order of magnitude difference in the bolometric luminosities of the two regions, and the lack of molecular emission towards G194.9349 may be due to the sensitivity, making it difficult to establish any potential evolutionary differences between the regions.

In the near future ALMA observations will provide the resolution, sensitivity and UV coverage required to disentangling the emission is these complex regions and enable an accurate comparison of the outflows and their driving sources not only between regions but between outflows residing within the same clusters

Chapter 5

CH_3CN Emission Towards a Sample of High Mass Star Forming Regions

5.1 Introduction

An established evolutionary sequence is still lacking towards massive stars. The increased complexity and short formation time-scales in the high mass regime make them more difficult to probe compared with the low mass regime. An important step in understanding the formation process in young massive stars is building an evolutionary picture of their early evolution.

The HMC phase represents one of the earliest observable stages in the evolution of a massive star. HMCs are associated with having a rich molecular line spectra (e.g. Purcell *et al.* 2006; Hatchell *et al.* 1998), and are readily seen in species such as CH_3OH, and CH_3CN. In particular, CH_3CN emission, given

its symmetric top nature, is a useful probe of the cloud conditions. The work presented in this chapter gives a snapshot survey spanning a full range in luminosity of 33 high mass star forming regions selected from the RMS survey, targeting the hot molecular core tracing transition CH_3CN (J=5-4). Table 5.1 presents the properties of the K ladder transitions observed, such as the rest frequency and the energy of the upper level.

5.2 Sample

The survey includes 33 massive star forming regions selected from the RMS survey. The sources cover a range in bolometric luminosity of $\sim 1\times10^3 L_\odot$-$1\times10^5 L_\odot$, and were selected to have a distance limit of $\sim$4.5 kpc. Of the 33 sources, the sample contains 23 classified YSOs, 3 HII regions, and 7 HII/YSOs. Table 5.2 presents the list of sources and their respective properties extracted from the RMS survey database. Column 1 gives the source name in Galactic coordinates, Columns 2, 3, and 4 are the RMS classification and RA and DEC of each source. The v_{LSR}, distance and bolometric luminosity is given in columns 5, 6, and 7 respectively. The last column gives the corresponding IRAS source name, along with the commonly used name(s) where possible.

5.3 Observations

The observations were taken with the 22 m MOPRA telescope providing a resolution of $\sim 37''$at the frequency of the CH_3CN (J=5-4) ladder. The observations were taken as a single pointing towards each source, centred on the position of

Table 5.1: Molecules observed in this survey, the transition is given in Column 2. The rest frequencies (Column 3), energies of the upper level above the ground state (Column 4), and the statistical weights in (Column 5).

Species	Transition	Frequency (GHz)	E_{upper}/k (K)	g_u
CH_3CN	(5_0-4_0)	91.987088	13.24	22
CH_3CN	(5_1-4_1)	91.985284	20.39	22
CH_3CN	(5_2-4_2)	91.980000	41.82	22
CH_3CN	(5_3-4_3)	91.971374	77.54	44
CH_3CN	(5_4-4_4)	91.959206	127.5	22

the RMS source (see Table 5.2 for a list of the RMS sources observed and their respective coordinates). The observations and initial data reduction (within ASAP) were carried out by Cormac Purcell.

5.4 Results

5.4.1 CH_3CN Data

The observations were taken with a single pointing centred on the RMS source position and thus provide a single spectrum for each source (spatial resolution is $\sim$37″at the frequency of the J=5-4 ladder). The single CH_3CN (J=5-4) spectra towards each source were then initially inspected within the GILDAS CLASS software package. A detection is determined for a given source if the emission is observed to be above the $3\,\sigma$ noise limit in the spectrum. Where the rms noise in the spectra is calculated from a baseline fit to the line free channels only. CH_3CN emission is detected in 22 of the 33 sources surveyed ($\sim$66%). Figure 5.1 displays the CH_3CN spectra (black solid line) towards those sources with

a $\geq 3\sigma$ detection. For those sources with a detection, the individual CH_3CN K-ladder transitions are then fit simultaneously with multiple Gaussian's using the GILDAS CLASS software package. The line separation between ladder components was set to the theoretical values, and the FWHM of the line was set to a single value for all ladder components. The resulting FWHM and integrated intensity of the individual K-ladder components are given in Table 5.3 with the resulting Gaussian fits overlaid on the CH_3CN spectra in Figure 5.1. Only K-ladder components where the total integrated intensities were detected above the expected 3σ integrated intensities (assuming the peak of the line is equal to $3\times$ the rms value in the spectra and using the FWHM from the K-ladder fit to estimate the expected 3σ limits for the integrated intensity) were included (see Table 5.3 for individual rms values and the FWHM).

Table 5.2: Properties of the sources observed in this MOPRA survey. The sources are labelled by their Galactic name (Column 1), with the given RMS survey classification (Column 2). The RA and DEC are given in Column 3 and Column 4 respectively. The source v_{LSR} and distance, and bolometric luminosity are presented in Column 5, Column 6, and Column 7 respectively. All properties are taken from the RMS survey. In Column 8, the IRAS name and/or more commonly used names for each source are provided where possible. For the HII/YSO sources the bolometric luminosities for both the HII and YSO components are given with the HII given first.

Source Name	Type	RA (J2000)	Dec (J2000)	v_{LSR} (kms^{-1})	D (kpc)	Bol Lum ($L_\odot$)	IRAS/Common Name
G010.3040-00.1466	HII	18:08:56.25	-20:05:43.4	13.0	2.1	6.6e+04	W31
G012.9090-00.2607	YSO	18:14:39.56	-17:52:02.3	36.7	2.4	3.2e+04	18117-1753/ W33A
G017.6380+00.1566	YSO	18:22:26.37	-13:30:12.0	22.1	2.2	1.0e+05	18196-1331
G018.3412+01.7681	YSO	18:17:58.11	-12:07:24.8	33.1	2.8	2.2e+04	18151-1208
G192.6005-00.0479	YSO	06:12:54.01	+17:59:23.1	7.4	2.0	4.5e+04	06099+1800/ S255 IR
G194.9349-01.2224	YSO	06:13:16.14	+15:22:43.3	15.9	2.0	3.0e+03	06103+1523
G196.4542-01.6777	YSO	06:14:37.06	+13:49:36.4	18.0	5.3	9.4e+04	06117+1350
G203.3166+02.0564	YSO	06:41:10.15	+09:29:33.6	7.4	0.7	1.8e+03	06384+0932/NGC2264-C
G217.3771-00.0828	HII	06:59:15.73	-03:59:37.1	25.1	1.3	8.0e+03	06567-0355
G224.6065-02.5563	YSO	07:03:43.16	-11:33:06.2	13.8	0.8	1.2e+03	07013-1128
G263.2283+01.5712	YSO	08:53:09.46	-42:13:07.6	5.4	0.7	1.2e+03	08513-4201
G263.7434+00.1161	YSO	08:48:48.64	-43:32:29.0	12.0	0.7	1.2e+03	08470-4321
G286.2086+00.1694	YSO	10:38:32.70	-58:19:14.3	-20.2	2.3	8.0e+03	10365-5803
G305.2017+00.2072	HII/YSO	13:11:10.45	-62:34:38.6	-41.0	4.0	3.0e+04	13079-6218
G305.5610+00.0124	YSO	13:14:26.36	-62:44:30.4	-38.8	4.0	1.2e+04	13111-6228

Continued on next page

Table 5.2 – continued from previous page

Source Name	Type	RA (J2000)	Dec (J2000)	v_{LSR} (kms^{-1})	D (Kpc)	Bol Lum ($L_\odot$)	IRAS Name
G307.6138-00.2559	HII/YSO	13:32:31.24	-62:45:17.0	-36.6	7.0	4.0e+4/3.9e+03	13291-6229
G310.0135+00.3892	YSO	13:51:37.85	-61:39:07.5	-39.7	3.2	6.7e+04	13481-6124
G313.7051-00.1895	YSO	14:22:34.74	-61:08:26.3	-42.4	8.5	1.8e+04	14188-6054
G318.0489+00.0854	HII/YSO	14:53:42.33	-59:08:52.3	-49.3	3.4	1.7e+04/7.3e+03	14498-5856
G318.9480-00.1969	HII/YSO	15:00:55.31	-58:58:52.6	-33.8	2.4	2.7e+03/1.0e+04	
G322.1729+00.6442	YSO	15:18:38.29	-56:37:30.9	-56.6	3.6	2.1e+04	
G323.7410-00.2552	HII/YSO	15:31:45.84	-56:30:50.8	-49.5	3.2	1.7e+04/1.1e+04	15278-5620
G326.4755+00.6947	YSO	15:43:18.94	-54:07:35.4	-41.6	1.8	4.1e+03	15394-5358
G326.6618+00.5207	YSO	15:45:02.84	-54:09:03.0	-39.6	1.8	1.4e+04	15412-5359
G333.0058+00.7707	YSO	16:15:13.79	-49:48:52.0	-48.3	3.2	2.9e+03	
G336.4917-01.4741	HII/YSO	16:40:01.14	-48:51:52.4	-23.4	2.0	2.3e+05/1.2e+04	16362-4845
G338.9196+00.5495	YSO	16:40:34.04	-45:42:07.9	-64.1	4.2	3.2e+04	
G339.6816-01.2058	YSO	16:51:05.95	-46:15:52.4	-28.0	2.4	6.5e+03	16474-4610
G341.1281-00.3466	HII/YSO	16:52:33.33	-44:36:10.6	-41.3	3.3	1.3e+03/4.7e+03	16489-4431
G341.2182-00.2136	YSO	16:52:17.93	-44:26:53.0	-43.2	3.4	5.6e+03	
G345.5043+00.3480	YSO	17:04:22.87	-40:44:23.5	-17.0	2.0	1.0e+05	17008-4040
G347.0775-00.3927	YSO	17:12:25.81	-39:55:19.9	-12.0	1.7	3.0e+03	17089-3951
G348.7250-01.0435	HII	17:20:08.13	-38:57:23.4	-12.7	2.8	4.7e+04	17167-3854

Table 5.3: Parameters of the fits to the CH_3CN lines.

Source Name	rms (K)	v_{LSR} * (kms^{-1})	δv (kms^{-1})	T_{MB}dv, K=0 ($K.kms^{-1}$)	T_{MB}dv, K=1 ($K.kms^{-1}$)	T_{MB}dv, K=2 ($K.kms^{-1}$)	T_{MB}dv, K=3 ($K.kms^{-1}$)	T_{MB}dv, K=4 ($K.kms^{-1}$)
G010.3040	0.008	12.9	5.59±0.10	1.31±0.03	1.15±0.03	0.35±0.02	0.31±0.02	–
G012.9090	0.015	36.2	4.71±0.10	1.13±0.04	0.96±0.04	0.54±0.04	0.44±0.04	–
G017.6380	0.010	–	–	–	–	–	–	–
G018.3412	0.010	31.3	2.45±0.17	0.18±0.02	0.14±0.02	0.06±0.02	–	–
G192.6005	0.009	6.56	2.22±0.17	0.16±0.02	0.15±0.02	0.09±0.02	–	–
G194.9349	0.010	–	–	–	–	–	–	–
G196.4542	0.010	–	–	–	–	–	–	–
G203.3166	0.010	7.48	2.67±0.10	0.29±0.02	0.25±0.020	0.08±0.018	–	–
G217.3771	0.007	–	–	–	–	–	–	–
G224.6065	0.009	–	–	–	–	–	–	–
G263.2283	0.007	–	–	–	–	–	–	–
G263.7434	0.008	–	–	–	–	–	–	–
G286.2086	0.007	-20.47	3.58±0.15	0.20±0.018	0.159±0.018	0.09±0.017	–	–
G305.2017	0.008	-41.66	5.85±0.22	0.51±0.03	0.53±0.03	0.23±0.03	0.21±0.03	–
G305.5610	0.013	-40.01	3.44±0.19	0.27±0.03	0.23±0.03	0.14±0.03	0.16±0.03	–
G307.6138	0.006	-36.89	3.24±0.18	0.15±0.02	0.13±0.02	0.08±0.02	–	–
G310.0135	0.010	–	–	–	–	–	–	–
G313.7051	0.010	–	–	–	–	–	–	–
G318.0489	0.046	–	–	–	–	–	–	–

Continued on next page

Table 5.3 – continued from previous page

Source Name	rms (K)	v_{LSR} * (kms^{-1})	FWHM (kms^{-1})	T$_{MB}$dv, K=0 (K.kms^{-1})	T$_{MB}$dv, K=1 (K.kms^{-1})	T$_{MB}$dv, K=2 (K.kms^{-1})	T$_{MB}$dv, K=3 (K.kms^{-1})	T$_{MB}$dv, K=4 (K.kms^{-1})
G318.9480	0.008	-33.48	4.08±0.07	0.68±0.02	0.67±0.02	0.33±0.02	0.25±0.02	–
G322.1729	0.011	-55.73	4.04±0.21	0.39±0.03	0.28±0.03	0.17±0.03	–	–
G323.7410	0.008	-50.02	4.60±0.07	0.60±0.02	0.58±0.02	0.30±0.02	0.27±0.02	0.09±0.02
G326.4755	0.011	-41.90	4.15±0.11	0.60±0.03	0.51±0.03	0.18±0.03	0.16±0.03	–
G326.6618	0.008	-39.49	3.60±0.15	0.26±0.02	0.23±0.02	0.10±0.02	–	–
G333.0058	0.008	-48.81	4.08±0.10	0.48±0.02	0.38±0.02	0.19±0.02	0.14±0.02	–
G336.4917	0.009	-23.6	3.22±0.14	0.25±0.02	0.24±0.02	0.12±0.02	0.11±0.02	–
G338.9196	0.013	-63.76	4.83±0.10	0.94±0.04	0.94±0.04	0.47±0.03	0.34±0.03	–
G339.6816	0.008	-28.52	3.99±0.11	0.42±0.02	0.38±0.02	0.12±0.02	0.10±0.02	–
G341.1281	0.008	-41.66	2.20±0.19	0.08±0.02	0.10±0.02	–	–	–
G341.2182	0.008	-43.08	4.23±0.12	0.47±0.02	0.37±0.02	0.13±0.02	0.09±0.02	–
G345.5043	0.007	-16.33	5.43±0.05	1.27±0.02	1.21±0.02	0.78±0.02	0.75±0.02	0.20±0.02
G347.0775	0.009	–	–	–	–	–	–	–
G348.7250	0.009	-13.79	4.72±0.09	0.68±0.02	0.64±0.02	0.33±0.02	0.32±0.02	0.12±0.02

(*) The v$_{LSR}$ is taken from the K=0 ladder fits.

5.4.2 CH_3CN K-ladder Detections

As mentioned, CH_3CN emission was detected towards 22 of the 33 sources surveyed ($\sim$66%). Of those 22 sources; 3 were detected in ladder transitions up to the k=4 transition, 11 sources were detected up to the k=3 ladder transition, 7 up to the K=2 ladder transition, and only one source showed emission up to the the K=1 ladder transition. The remaining 11 sources were not detected down to 3σ in any given ladder component. The results of the Gaussian fits for the individual CH_3CN ladder transitions are presented in Table 5.3, and the CH_3CN ladders with the Gaussian fits overlaid are presented in Figure 5.1.

5.4.3 The Effect of Distance or Luminosity on the Detection of CH_3CN Emission

The CH_3CN emission as shown in both Chapters 3, and Chapter 4, is generally tracing compact emission coincident with the continuum peak of the source (see also Hernández-Hernández *et al.* 2014 for a different sample of HMCs). CH_3CN emission is therefore likely tracing a much smaller region than that probed by the $\sim 37''$ beam obtained here. The non-detections may be a result of beam dilution effects, with sources that are further away more likely to suffer the effects of beam dilution. The average and median distances to sources with a CH_3CN detection are 2.9 kpc and 2.6 kpc respectively compared with 2.7 kpc and 2.0 kpc respectively for sources without a CH_3CN detection. A KS-test of the distances between the detected and non-detected sources yields a probability of $\sim$15% that the distances are drawn from the same population. However, as the non-detected sources are typically closer, then beam dilution does not appear to be

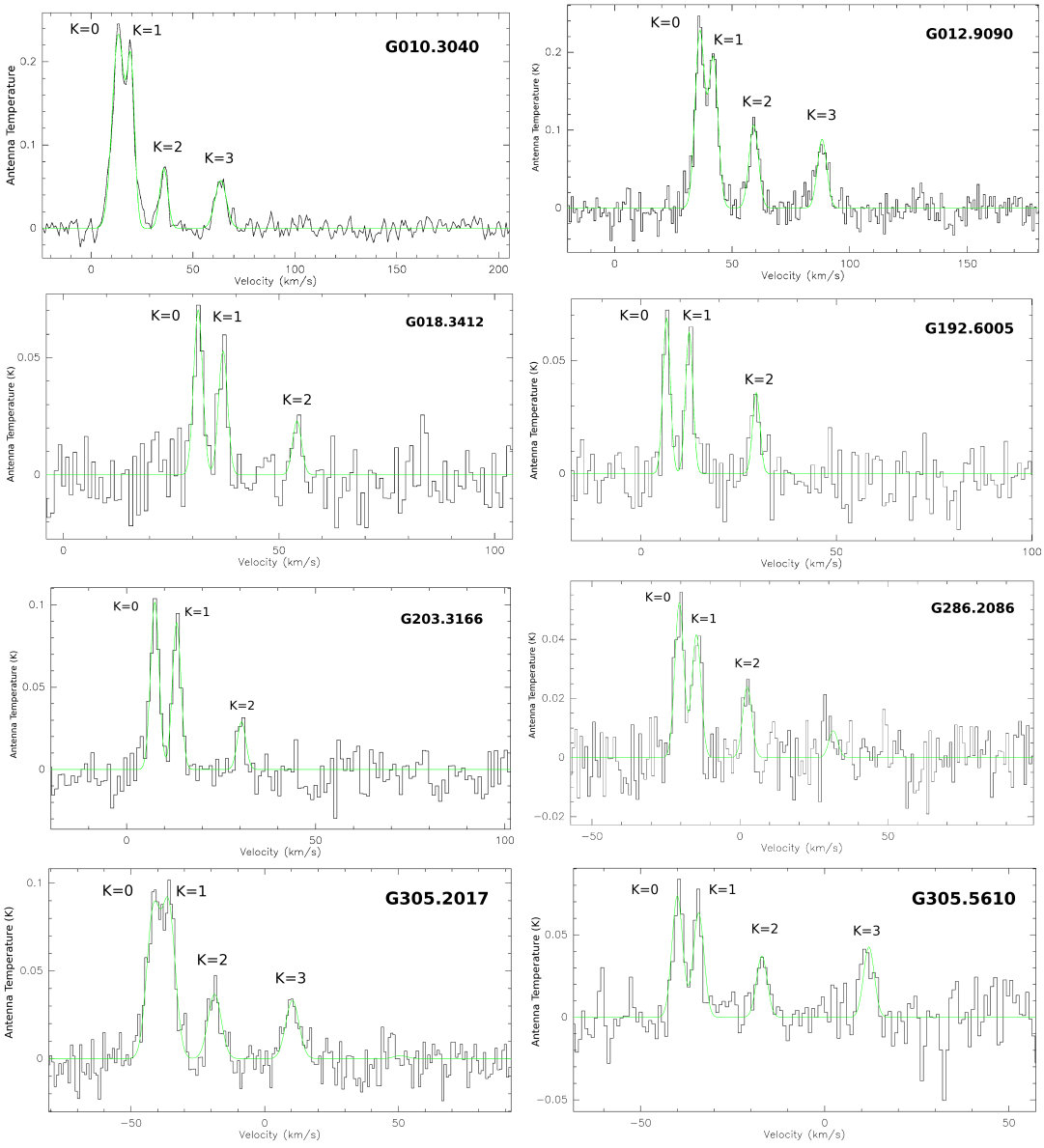

Figure 5.1: Spectra of the CH_3CN ladders with the Gaussian fits overlaid. The black solid line gives the CH_3CN spectra with the Gaussian fits are overlaid in green. Only the labelled ladder components are included in the rotational diagrams.

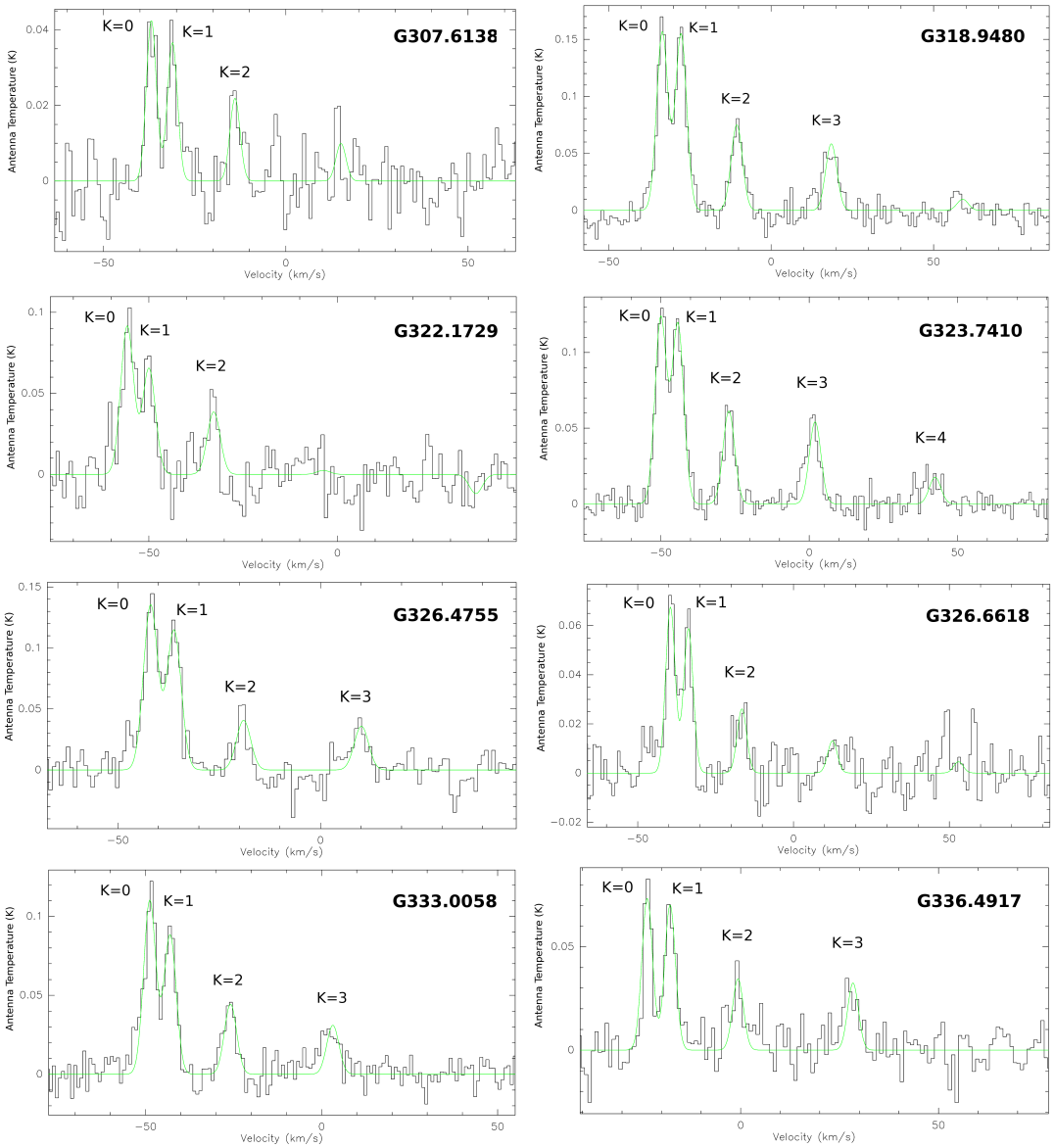

[]**Figure 5.1**–continued from previous page.

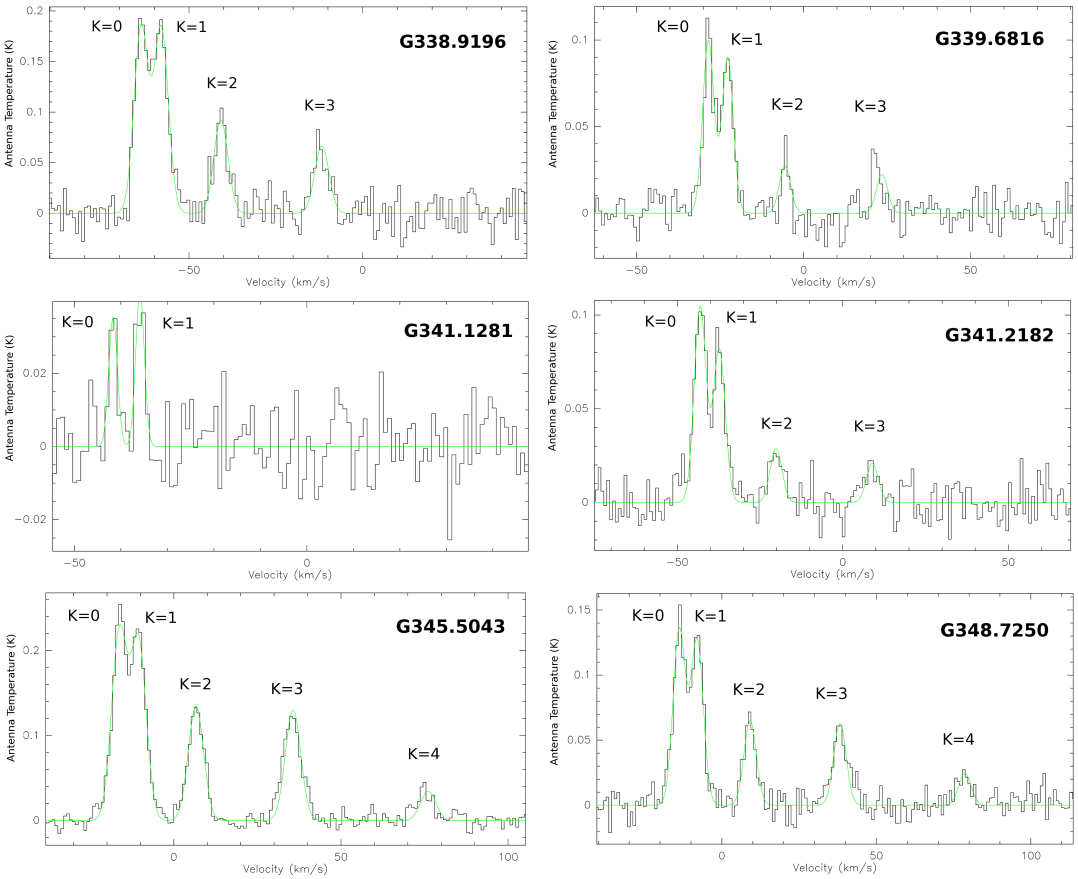

[]**Figure 5.1**–continued from previous page.

a significant factor in the non-detection of CH_3CN towards these sources.

The average and median bolometric luminosities (considering only the brightest of the two luminosities given for those sources classified as HII/YSO, see Table 5.2) of the sources with detected CH_3CN emission are found to be $\sim 3\times10^4 L_\odot$ and $1.9\times10^4 L_\odot$ respectively, compared with $\sim 3\times10^4 L_\odot$ and $8\times10^3 L_\odot$ for the non-detected sources respectively. Furthermore, a KS-test yields a probability of 22% that the luminosities of the detected and non-detected sources are drawn from the same population. Figure 5.2 displays histograms of the distances and luminosities of the of CH_3CN detected and non-detected sources. It is notable

that over half of the non-detected sources have the lowest luminosities of the observed sources. If only sources with a luminosity greater than $10^4 L_\odot$ are considered then the detection rate of CH_3CN would increase from ∼67% to 75%. Therefore, it seams likely that the detectability of CH_3CN may depend on the luminosity, but is not due to beam dilution, although it is stressed this cannot be formally proved.

5.4.4 CH_3CN Parameters

The CH_3CN rotational temperatures and column densities are derived in the same manner as in Section 3.5.1.1 which follows the procedure outlined in Araya *et al.* (2005). The CH_3CN rotational diagrams of $\ln(N_u/gu)$ as a function of E_u/k are presented in Figure 5.3, for all sources with a CH_3CN detection in at least 3 transitions. The resulting estimated rotation temperatures and column densities are presented in Table 5.4. Of the sources with detected CH_3CN emission, only one source, G341.1281, does not have 3 detected transitions and only the K=0, and K=1 transitions are detected towards this source. Therefore, a temperature or column density estimate is not given for this source. The errors given for the rotational temperature estimates are derived from the error in the slope taken from the linear regression fit. The average and median of the rotation temperatures are both ∼44 K (with a standard deviation of ∼12 K), and the average and median column densities are 1.1×10^{13}cm^{-2} and 0.75×10^{13}cm^{-2} respectively. Given the calibration errors, the column density estimates are likely to be correct to within a factor of 2.

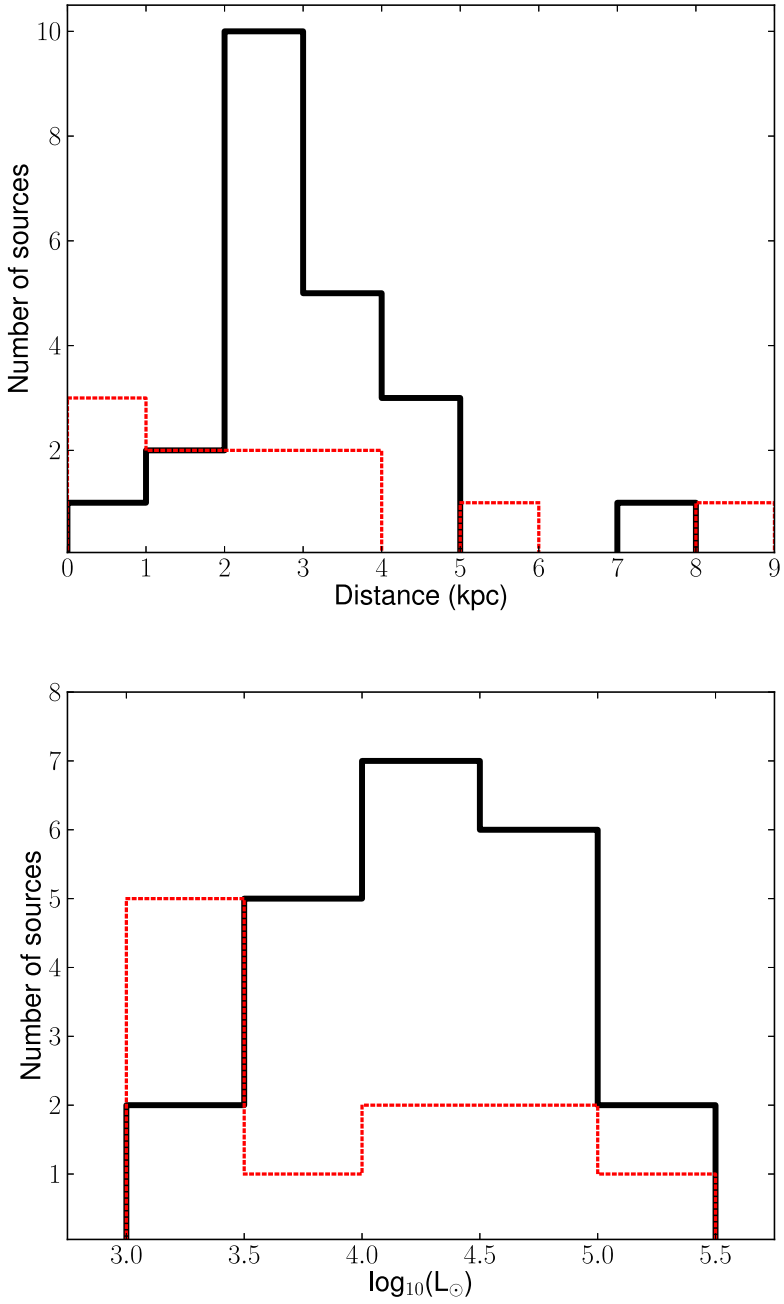

Figure 5.2: Histograms of the source distance (top panel) and bolometric luminosity (bottom panel) for CH_3CN detected and non-detected sources. The sources with CH_3CN emission are represented by a solid black line, whereas sources with no associated CH_3CN emission are shown by the red dashed line.

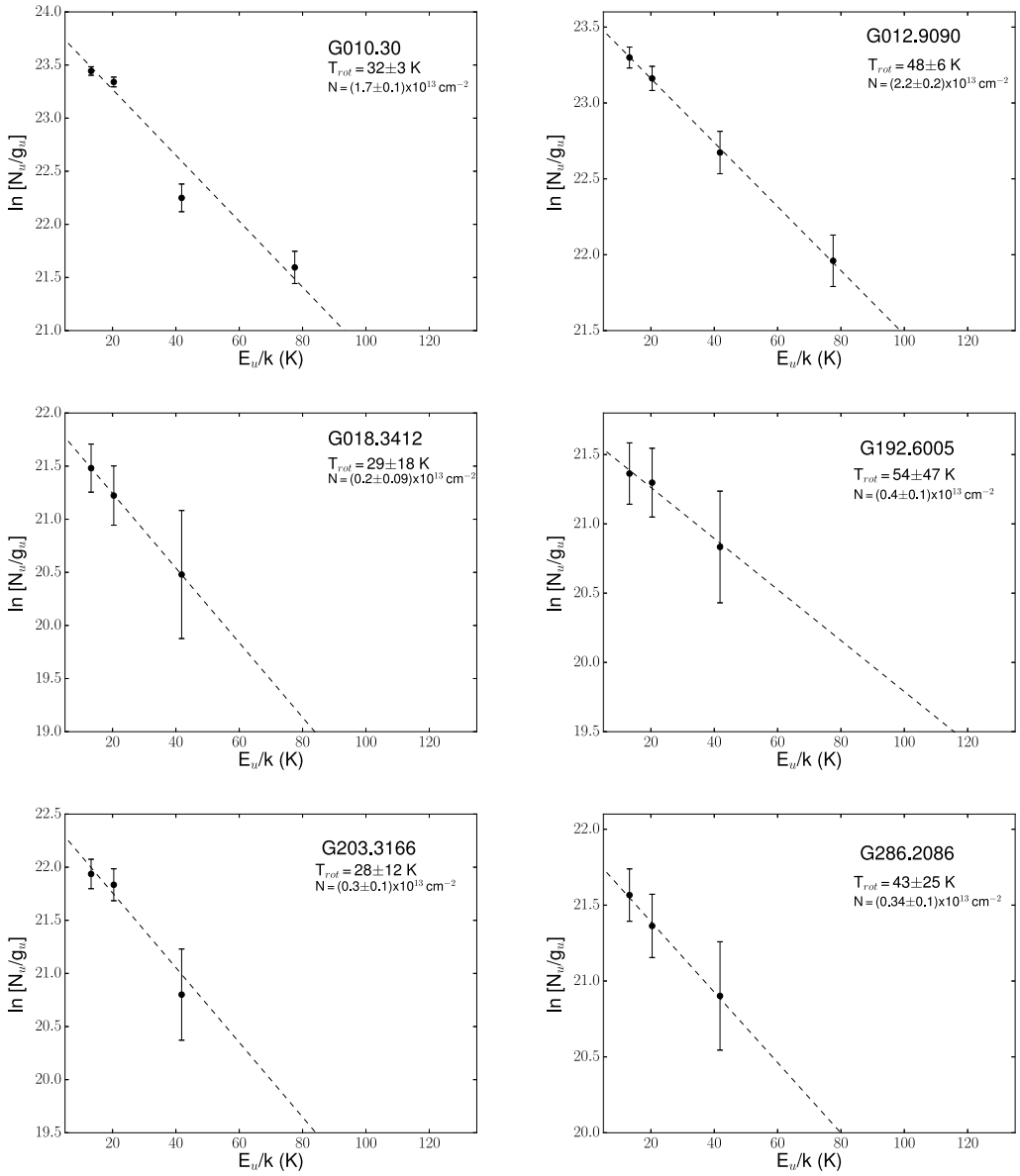

Figure 5.3: CH_3CN rotation diagrams for sources with CH_3CN emission detected up to at least the K=2 ladder transitions. The error bars are the 1σ errors of the Gaussian fits to the ladder transitions, and the black dashed line is the result of a linear regression fit, which takes account of the errors in the flux estimates. The respective source name, and results of the rotational diagram fit , are given in the top right corner of the plot.

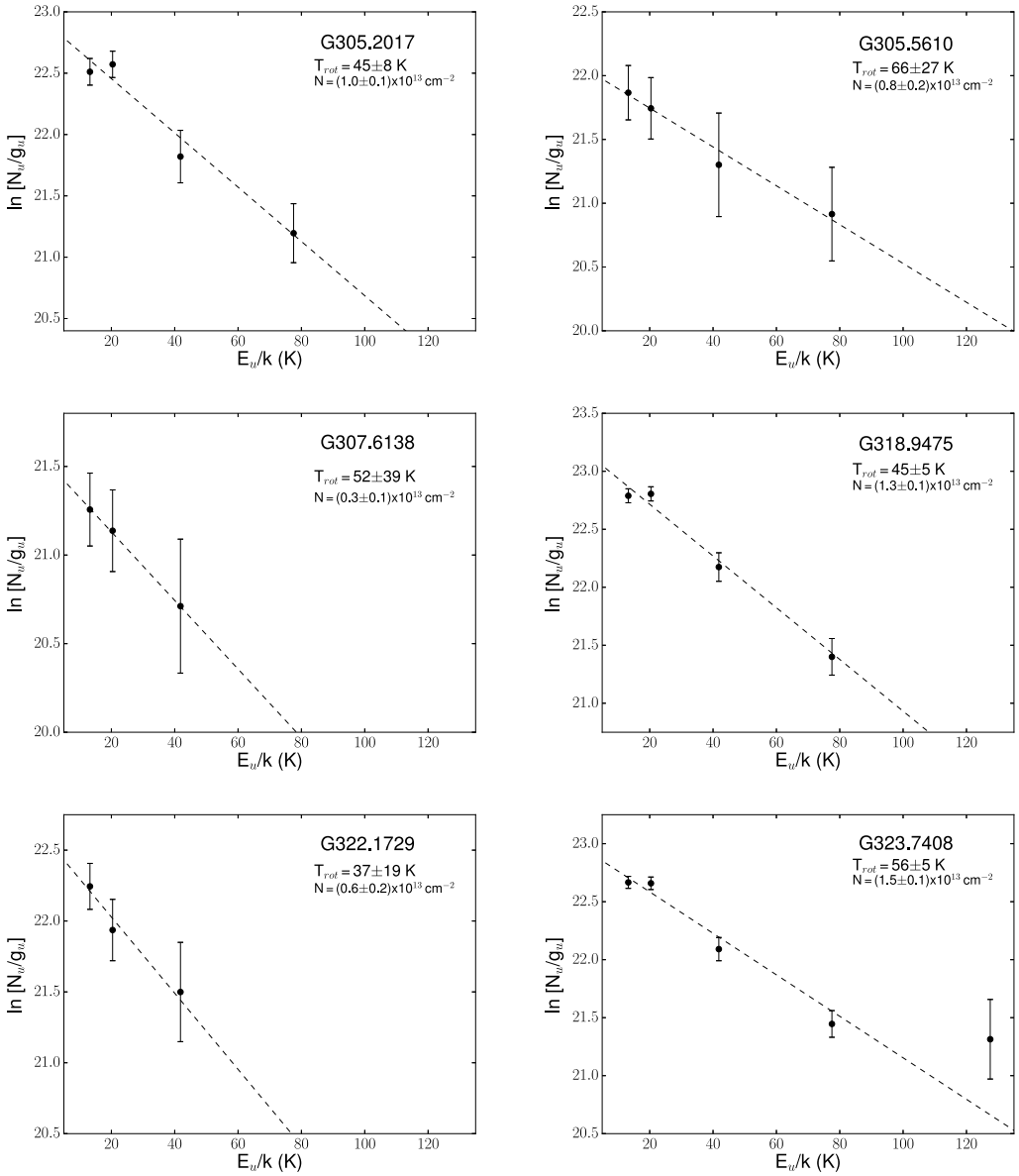

Figure 5.3 – continued from previous page.

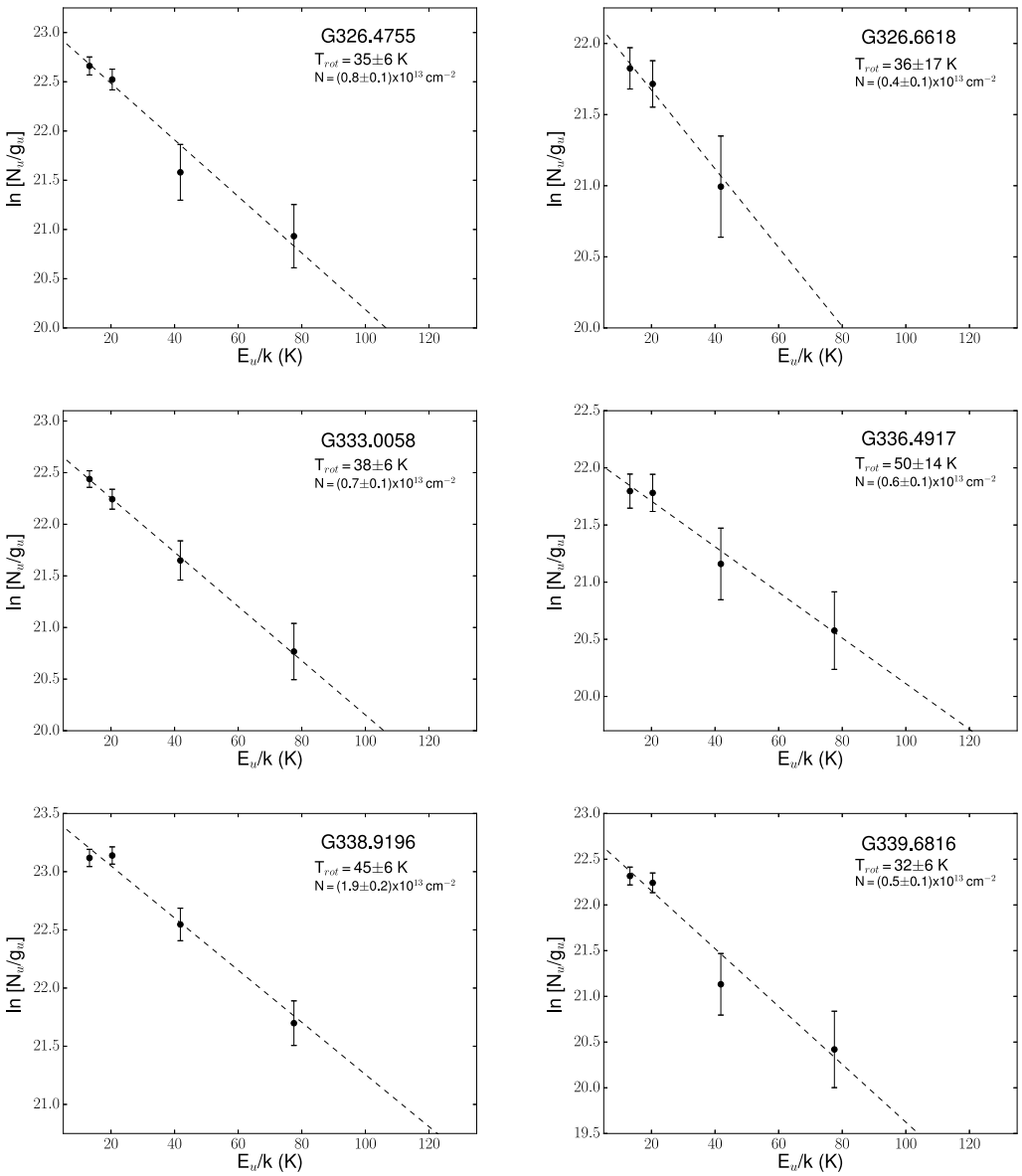

Figure 5.3 – continued from previous page.

Table 5.4: CH_3CN rotational temperature and column density estimates for sources with emission detected up to at least the K=2 ladder transition

Source	T_{rot} (K)	Column Density ($\times 10^{13}$cm^{-2})
G010.3040	32.2±2.3	1.7
G012.9090	47.4±6.0	2.2
G018.3412	28.5±17.5	0.2
G192.6005	54.3±47.3	0.4
G203.3166	28.4±11.9	0.3
G286.2086	43.1±25.1	0.3
G305.2017	45.2±7.9	1.0
G305.5610	65.7±27.1	0.8
G307.6138	51.7±39.5	0.3
G318.9480	44.9±4.9	1.3
G322.1729	37.2±18.5	0.6
G323.7410	55.9±5.1	1.5
G326.4755	34.8±5.8	0.8
G326.6618	36.1±17.4	0.4
G333.0058	38.1±5.8	0.7
G336.4917	50.1±13.7	0.6
G338.9196	44.6±5.9	1.9
G339.6816	31.6±6.0	0.6
G341.2182	29.8±5.3	0.5
G345.5043	70.9±4.2	4.3
G348.7250	62.9±7.6	1.9

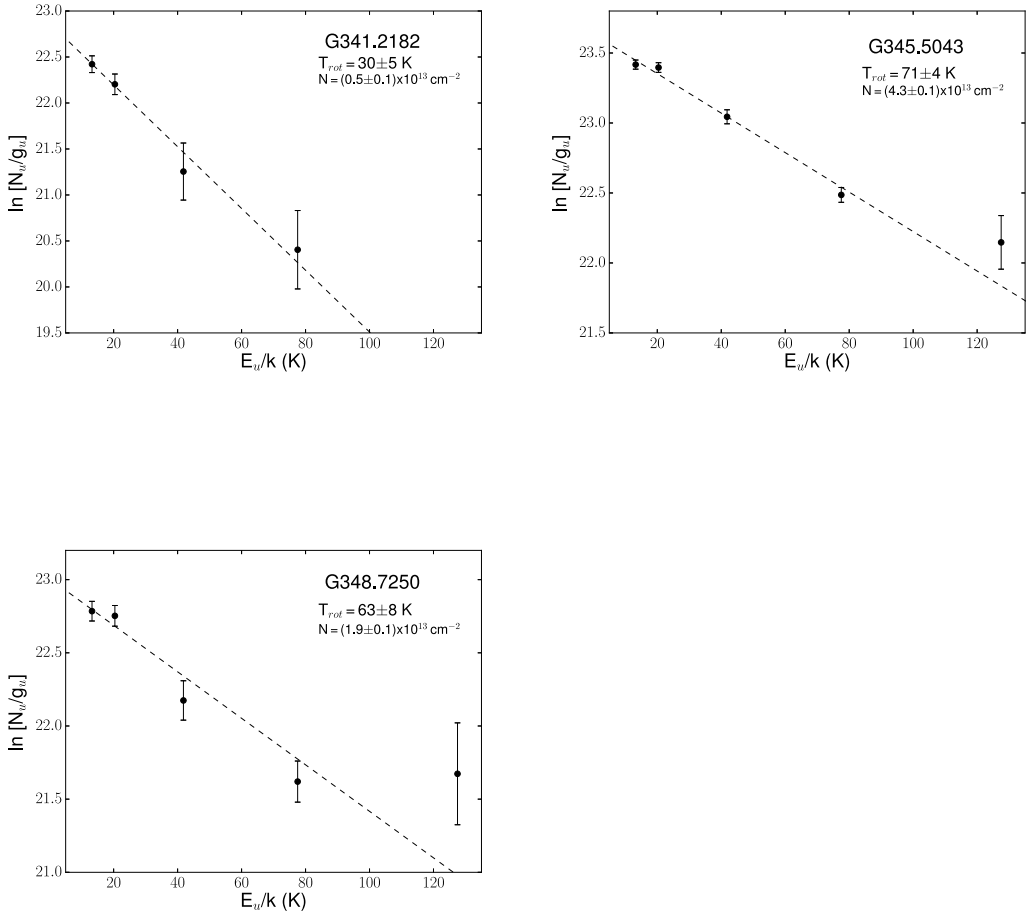

Figure 5.3 – continued from previous page.

5.5 Discussion

5.5.1 CH_3CN Detection and Source Properties with Evolution

The F22/F8 flux ratio can be used as an indication of potential evolution, with younger more heavily embedded regions expected to have redder colours on average. The 22μm WISE fluxes, and the 8μm fluxes were extracted directly from the RMS survey database. Figure 5.4 displays a histogram of the F22/F8

ratios for the CH_3CN detected and non-detected sources. A KS test also gives a probability of ∼30% that the colours towards the two samples are from the same population. Thus, there appears to be no obvious difference in the colours of CH_3CN detected and non-detected sources.

Figure 5.5 displays the estimated CH_3CN rotational temperatures as a function of the source bolometric luminosity, FWHM of the CH_3CN ladder fits, and F22/F8 colours. The rotational temperatures do no correlate with either the FWHM of the ladder fits, or the bolometric luminosities. However, there is a correlation of the rotational temperatures with the F22/F8 colours, suggesting the redder more heavily embedded, younger sources are hotter. However, further observations would be required to fully explore the evolutionary nature of the regions.

5.5.2 Comparison with Previous Literature

CH_3CN emission is detected in ∼67% of the sources observed. This is similar to a survey of massive star forming regions observed by Purcell *et al.* (2006) where ∼70% of the sources were found to have a CH_3CN emission detected in the J=5-4 ladder. They found a higher prevalence of CH_3CN emission towards the UCHII regions in their sample compared with radio dark sources. Furthermore, when only considering sources with bolometric luminosities above $10^4 L_\odot$ they found the detection rate of CH_3CN emission increased towards both samples, however there was still a prevalence towards UCHII regions over radio quiet sources.

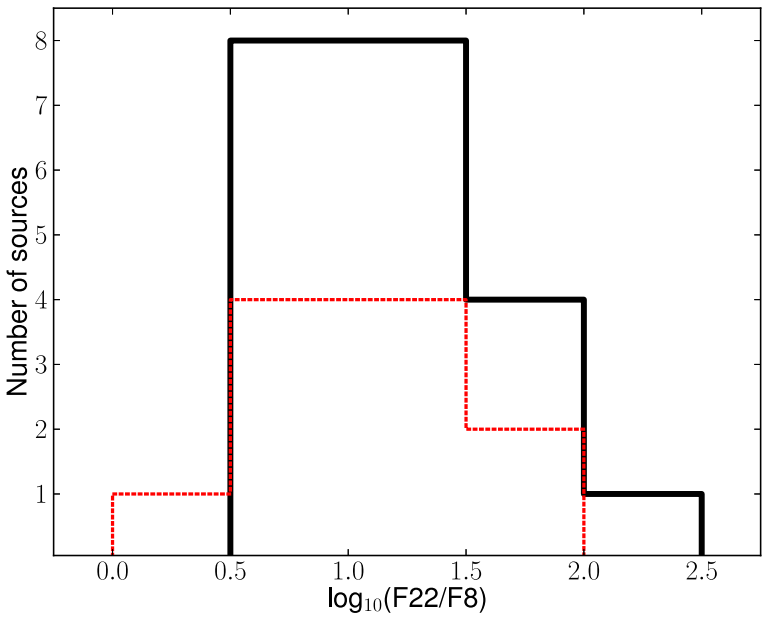

Figure 5.4: Histogram of the F22/F8 colours for the CH_3CN detected and non-detected sources. The solid black line represents sources with a CH_3CN detection, whereas the red dashed lines represents sources without a CH_3CN detection.

5.5.3 Comparison with Sources in the JCMT SiO Survey

There is an overlap of 9 sources (approximately 27% of the sample) between the sources observed here and those that were observed as part of the JCMT SiO outflow survey presented in Chapter 2. Of those 9 sources five (G010.3040, G012.9090, G018.3412, G192.6005, and G203.3166) have a CH_3CN detection and four (G017.6380, G194.9349, G196.4542, G217.3771) have no detected CH_3CN emission. Furthermore, for the five sources with a CH_3CN detection only one source, G010.3040, does not have a corresponding SiO detection, and all four sources without a CH_3CN detection likewise do not have an SiO detection. However, it should be noted that in the case of NGC 2264-C, the work

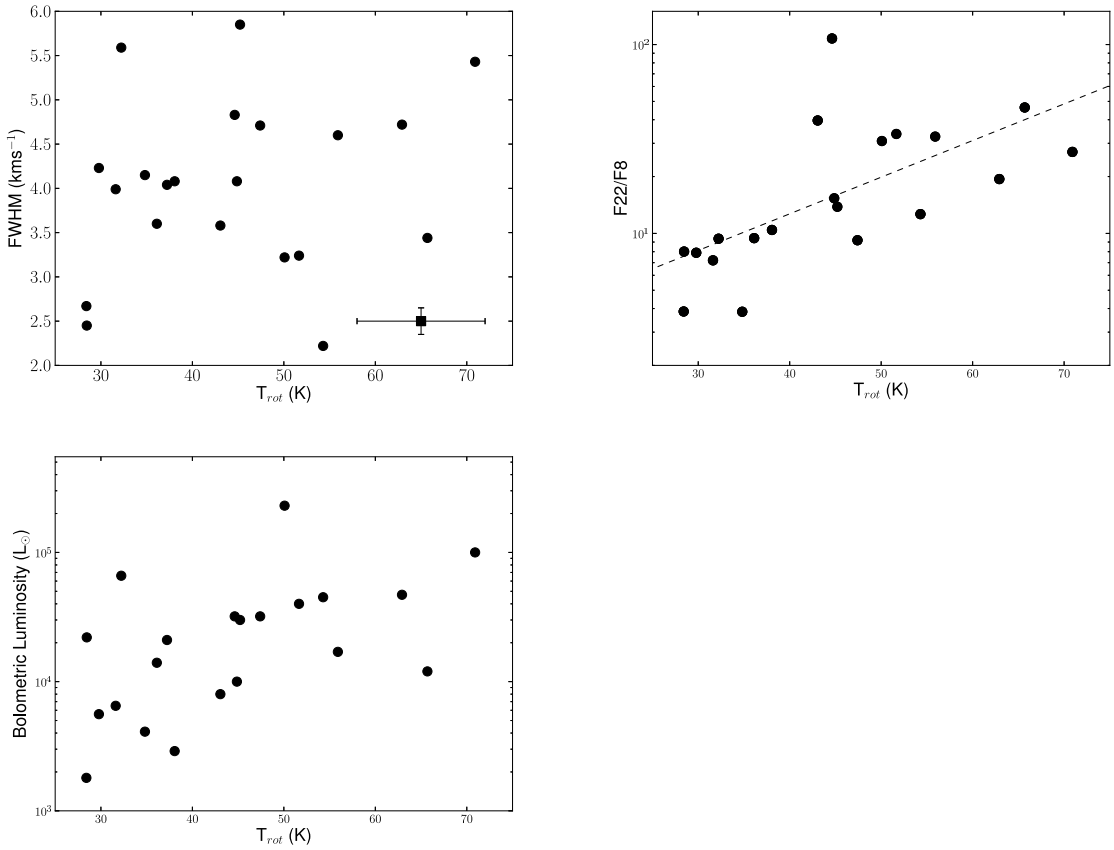

Figure 5.5: CH_3CN rotation temperature as a function of the; CH_3CN FWHMs from the Gaussian fits to the whole ladder (top left panel), F22/F8 colour (top right panel) and bolometric luminosity (bottom panel). The typical errors in the rotational temperature are shown in the top panel. For the HII/YSO sources the higher bolometric luminosity is plotted. The black dashed line in the middle panel represents the linear fit where the correlation coefficient is R=0.65 and the fit is given by $\log_{10}(y)=0.0194(\pm0.0043)x+0.3277(\pm0.1987)$.

presented in Chapter 3 clearly shows that the compact CH_3CN emission is not coincident with either of the outflow driving sources, but is coincident with the IR bright and likely more evolved sources in the region. In comparison, towards G192.6005 (see Chapter 4), the SiO emission appears coincident with CH_3CN emission. This again highlights the difficulty in comparing properties between single dish surveys. Where it is not always obvious exactly what the emission in the lower resolution observations is tracing in these complex environments.

5.6 Conclusions

This Chapter has presented a snapshot survey of CH_3CN emission towards 33 massive star forming regions drawn from the RMS survey. The key results are highlighted below:

- CH_3CN emission is detected towards 22 (66%) of the RMS sources observed. While high spatial resolution observations (e.g. those presented in Chapters 3, and 4 in addition to work from Hernández-Hernández *et al.* (2014) and references therein) have shown that CH_3CN emission is found to be compact and coincident with the cores, beam dilution does not appear to be a strongly contributing factor in the non-detected sample. However, the detection of CH_3CN may depend on the luminosity of the source, with more luminous sources showing a higher fraction of CH_3CN detections.

- The derived rotational temperatures show a linear correlation with the F22/F8 colours, thus redder potentially younger sources have higher tem-

peratures. This may suggest the CH_3CN emission, in these potentially younger regions, is located closer to the star. Future interferometric observations should be able to test this.

Higher sensitivity observations would be required to test whether the lack of CH_3CN detected emission is due to the lower luminosity in several of the sources.

Chapter 6

Conclusions and Future Work

6.1 Overview

The key findings from each of the chapters are summarised briefly below;

- **Chapter 2** presented SiO, $H^{13}CO^+$ and HCO^+ emission towards a sample of 33 massive star forming regions observed with the JCMT. SiO emission is detected in ∼50% of the massive star forming regions. Furthermore, the detection of SiO emission appears to be linked to the age of the RMS source, with the younger sources showing a stronger dependence with SiO. The presence of SiO also appears to be linked to the CO velocity, with SiO more efficiently tracing sources with higher velocity dispersions.

- **Chapter 3** presented the first interferometric SiO and ^{12}CO observations towards the massive star forming region NGC 2264-C. Both the SiO and ^{12}CO emission trace two collimated, bipolar, high velocity outflows in the region, of which both are driven by the brightest mm, IR-darkest and

molecular line weak, likely youngest cores. In contrast, the IR-bright RMS source has no associated SiO emission and shows no indication of a molecular outflow. Thus, the SiO emission is again an indication of youth in massive star forming regions.

- **Chapter 4** presented high spatial resolution observations towards two regions observed in the JCMT survey (one source with and SiO detection and one source without and SiO detection). At the higher resolution of these observations, both sources now show SiO emission. However, the nature of the SiO emission towards both regions is unclear and it does not trace any high velocity, collimated emission along the ^{12}CO outflow axis. However, both ^{12}CO outflows appear to be driven by the IR-bright RMS source, thus the lack of associated SiO emission may be a sign of age in these regions.

- **Chapter 5** presented MOPRA single dish CH_3CN emission towards a sample of 33 sources from the RMS survey. Approximately 66% of the sources were found to have CH_3CN emission. Furthermore, the derived CH_3CN temperatures are found to correlate with the F22/F8 colours which may possibly indicate the emission in these redder sources is closer to the central star.

6.2 Summary

The work presented in this thesis has focused on outflows towards massive star forming regions, exploring how their properties change with evolution or mass

of the driving source. It is still not known how massive stars form. Whether they can be seen as a scaled up version of the low mass scenario or form by some inherently different mechanism (e.g. Competitive Accretion) is still debated.

In the Competitive Accretion scenario it is suggested that the dynamic accretion and close interaction between cluster members would likely lead to disruption or possibly even destruction of the accretion discs (e.g. Tan *et al.* 2014; Bally & Zinnecker 2005). While the discs are likely to reform, they may not necessarily be aligned with the rotation plane of a protostellar system and their orientations would be expected to be randomly distributed. Thus, the associated outflows would also likely suffer from severe precession effects, and be poorly collimated again with a large distribution of orientation axes in a given cluster. Thus, in the Competitive Accretion scenario clusters could contain several less collimated outflows which are randomly orientated. In comparison, in the Core Accretion model, where a single bound core collapses to form a single star, there is likely to be less disruption to the disc-outflow system during accretion, and outflows should be more collimated and aligned to the accretion disc. However, whether outflows forming within the same cluster under Core Accretion are more likely to all show outflows aligned along the same plane or be randomly orientated is not clear. As discussed by Beuther & Shepherd (2005b), outflows from massive stars are thought to de-collimate with evolutionary stage, likely confusing interpretation between outflows associated to Competitive and Core Accretion models towards regions harbouring more evolved sources. De-collimation in outflows is still a matter of debate, with many examples of highly collimated outflows in the high mass regime existing (e.g. Carrasco-González *et al.* 2010), yet none are currently observed towards sources with bolometric

luminosities above $10^4 L_\odot$, which may indicate for the highest mass stars a different formation mechanism is required (e.g. Competitive Accretion). On the other hand as the formation timescale for a star above $10^4 L_\odot$ is considerably shorter, the class 0 stage would only last a short time, resulting in very few observational examples of collimated outflows towards sources with a bolometric luminosity $>10^4 L_\odot$. Furthermore, single dish observations which show a single outflow at low resolution could potentially be comprised of several cores driving outflows at higher resolution - as seen by Klaassen *et al.* (2015) and here towards NGC 2264-C - which will lead to confusion in determining the collimation in low resolution observations. Thus, using CO to trace collimation, particularly at low spatial resolution to determine the collimation of outflows is likely not a viable mechanism, and interferometric observations are likely required. Future observations probing a large sample of young massive star forming clusters at high resolution, where many single outflow/disc system can be resolved in the same cluster, could provide a viable means to test between Competitive and Core Accretion models.

The data presented in Chapter 3 utilised high resolution observations of the outflow tracers SiO and ^{12}CO towards the young intermediate/massive star forming region, NGC 2264-C. The observations revealed two collimated, high velocity young outflows in the region, driven by the IR-dark, brightest, likely young class 0 type intermediate/massive cores in the region, C-MM3 and C-MM12. In addition, both outflows are oriented along the same axes (i.e. they both extend from in the north south plane). Moreover, the lower limit to the collimation factors (the width of both outflows is currently not resolved and the minor axis is taken as the beam size) are 2-8 which are similar to those observed

in the low mass regime. Furthermore, the estimated forces for these outflows, if corrected for optical depth effects and missing flux, would lie between the class I and class 0 linear fits shown in Figure 3.13. C-MM3 represents the best candidate of localized infall of the sources presented in HCO^+ and $H^{13}CO^+$ emission in the JCMT observations presented in Chapter 2, with an estimated infall rate of a few $10^{-3}M_{\odot}yr^{-1}$. Peretto *et al.* (2006) also observed large scale infall motions towards this source and a velocity dispersion in the vicinity, proposing a formation mechanism intermediate between turbulent core accretion and protostellar mergers. The results presented here suggest the formation mechanism for this source is similar to the scaled up version of the low mass formation scenario, and thus best described by the Core Accretion model.

Towards G192.6005 and G194.9349, the outflow forces appear lower than expected, both sources also lack associated SiO emission tracing the outflow, suggesting they may be more evolved outflows. However, it is unclear if the lack of SiO emission can be attributed to the sensitivity of the observations. In all three regions further fragmentation is observed at higher resolution, and a clear spread in evolution is found between cores within the same region. Directly comparing the evolution between different regions is a complex task, even considering regions at a similar distance. On the face of it, G194.9349 appears less molecular line rich compared with G192.6005. However, the order of magnitude difference between their respective bolometric luminosities could mean that the emission from G194.9349 falls below the current sensitivity limits. This makes a direct comparison of the properties of the molecular emission related to the outflow emission difficult. This again becomes apparent in NGC 2264-C where the hot molecular cores are observed towards the IR brighter sources; however

the two sources driving the outflows are an order of magnitude less luminous, and so the emission from these tracers may fall below the sensitivity limits. This also appears to be the case for the CH_3CN emission presented in Chapter 5, where approximately half of the sources without a CH_3CN emission in the sample of 33 massive star forming regions have the lowest bolometric luminosities. Moreover, Vasyunina *et al.* (2011) also found no CH_3CN emission towards any of the single IRDCs in their observations; however, when the CH_3CN emission was avergaed over all of their sample a detection was obtained.

Towards both NGC 2264-C and G194.9349 there are chemically rich features in the regions (i.e. the "ridge" and the MP) where there is no obvious association with mm continuum emission. Both of these features have emission from the CH_3OH (229 GHz) transition which may be indicating potential class I maser emission. They may be highlighting sites where a shock from either a wind or jet is interacting with ambient medium.

As highlighted above it is still a difficult task even at high resolution to identify what is going on in these complex regions. In particular, G194.9349 which showed no SiO emission in the single dish observations, displays SiO in the higher spatial resolution observation. Lower resolution observations still provide an excellent tool to explore the bulk properties in a large sample of objects. As shown, the JCMT observations presented here, reveal the SiO emission is more prevalent towards younger sources, and sources with the highest velocity CO outflows, consistent with the picture of the jet properties declining with age as seen in the low mass case. While the SiO emission correlates with the F70/F22 colour, there is no correlation with the F22/F8 colour. Similarly, the CH_3CN emission in Chapter 4 shows no difference in the colours for sources with or

without CH_3CN emission. However, Cooper (2013) found a strong dependence on the F22/F8 colour and the presence of a jet in their NIR spectra towards MYSOs form the RMS survey. The lack of a correlation in this work is likely due to the colours probing the mid-IR bright sources in the regions, which are not necessarily the source of the outflow or hot core emission. As evidenced by the high resolution observation in this work showing the outflows in NGC 2264-C are driven by the mid-IR dark, likely youngest sources. A combination of complementary single dish and interferometric observations towards a large sample of regions, coving whole clusters, where the outflow, disc, and envelope can be identified towards a single core are required to fully probe the formation mechanism of high mass stars.

6.2.1 Future Work

The move to full capabilities with ALMA is expected to bring many exciting results and answers in the coming years to the currently unanswered questions. In particular, regarding the interplay of discs and outflows in massive star forming regions and their comparison with the low mass regime. This section discusses future extensions of this work.

6.2.1.1 High Angular Resolution Follow-up

The key to understanding jet/outflows from massive stars lies in high angular spatial resolution studies, where a single core and its associated outflow can be resolved. As the results in this thesis show, even at $3''$ resolution it is difficult to unambiguously identify the outflow driving source. Furthermore, the higher

resolution observations reveal multiple cores and in the case of NGC 2264-C it is not the IR bright, RMS source that drives the high velocity SiO outflows, but the younger cores. It would be interesting to take a larger sub-sample of the JCMT sources for follow-up observations at high resolution ($<3''$), and with high sensitivity to probe exactly where the SiO emission is coming from in these complex regions, and if there are differences in the outflows driven by younger cores compared with more evolved sources. The higher spatial resolution will also allow for the collimation of the outflows to be probed, helping to distinguish if the picture presented by Beuther & Shepherd (2005b), where the outflow decollimates with evolution holds. Furthermore, as suggested by Smith *et al.* (2013) infall signatures may be best matched to the beam size. Thus, the low detection of infall in HCO^+ (4-3) and $H^{13}CO^+$ emission in the Chapter 2 may be due to the beam size of the JCMT observations. High resolution follow-up observations of these tracers towards sources presented in Chapter 2 will be able to test this.

6.2.1.2 Maser Emission in MYSOs

Maser emission as a tool for probing evolution towards massive star forming regions has long been debated (e.g. Ellingsen *et al.* 2007; Voronkov *et al.* 2014). It is thought the class I (collisionally driven) masers should be present before the class II (radiatively driven) masers form (e.g. Ellingsen *et al.* 2007). Additionally, the 6.7 GHz maser emission is believed to be associated with the earlier phases of the star formation process. Breen *et al.* (2010) have indicated the increase in the class II luminosity with source age. Exactly which phase of the MYSO formation process 6.7 GHz maser emission traces is still unclear. Where

these masers are excited in relation to the MYSO and if the environments of MYSOs harbouring faint masers are different to those harbouring bright maser emission is still also not clear. To further explore these questions a sample of MYSOs (with no previously observed maser emission in the methanol multi-beam survey (MMB) survey Caswell *et al.* 2010) from the RMS survey were observed with ATCA (at 10 times greater sensitivity). This will allow us to identify if they are true non-detections or if they are potentially a different type of faint class II methanol maser, which will further aid in building an evolutionary picture of the early stages of massive star formation.

6.2.1.3 Probing the Colder Emission-Looking for the Youngest Sources

While the RMS survey provides the largest sample of MYSOs and UCHII regions, it is biased towards sources that are already bright in the mid-IR. Herschel has provided a wealth of far-IR data, but currently there are no large scale surveys in the mm regime with comparable spatial resolution to the Herschel 70μm emission, the best being ATLASGAL with a resolution of $\sim$19$''$(Schuller *et al.* 2009). The recently updated MUSTANG bolometer on the GBT will allow mm observations at a comparable resolution ($\sim$8$''$) to the 70μm Herschel data. This will allow the cooler emission to be explored in comparison the the warmer 70μm emission, likely highlighting regions in the youngest stages of evolution. As an initial step it would be interesting to follow-up the JCMT sample presented in this thesis. However, with impending release of the HOBYs (Motte *et al.* 2010) and Hi-gal (Molinari *et al.* 2010) Herschel surveys it would be interesting as a longer term goal to follow up these surveys with the GBT to help build-on the global properties on massive star formation in the Galaxy.

6.3 Final Remarks

The work in this thesis suggests that the SiO emission is observed towards younger regions in massive star forming regions, in a similar manner to the SiO emission observed in the low mass regime. Furthermore, this work highlights the need for higher spatial resolution, and sensitivity observations to fully understand the outflows and their driving sources in the complex high mass star forming regions. In addition, a comprehensive understanding of the age and evolutionary nature of the outflow driving sources is still required. In the case of NGC 2264-C the high velocity bipolar outflows are coincident with the likely younger, mm brightest, IR dark sources. In contrast, the IR-bright RMS source does not appear to drive an outflow in this region. Thus, it is not always clear from the single dish observations exactly what is responsible for the outflow emission in massive star forming clusters. Looking to the future high resolution observations where a single core and outflow can be resolved will play an important role in fully understanding how massive stars form.

Appendix A

HCO^+ and $H^{13}CO^+$ Integrated Intensity Maps and Line Fits

This Appendix provides additional information and Figures related to Chapter 2 of this thesis. Presented below are the 1σ rms noise achieved for each molecule towards each source from the JCMT survey. The resulting Gaussian fits to the $H^{13}CO^+$ spectra along with the HCO^+ and $H^{13}CO^+$ integrated intensity maps for each source and the extracted total spectra from the masked regions are shown.

Table A.1: The 1σ rms noise achieved for each molecule towards each source. Column 1 is the Galactic source name and Column 2 is the RMS source classification. In Columns 3 and 4 the corresponding RA and DEC positions are given. The achieved rms noise in each map for the for $H^{13}CO^+$, SiO , and HCO^+ cubes are given in Columns 5, 6 and 7 respectively, for a channel width of 0.42 kms^{-1} , 1.68 kms^{-1} and 0.05 kms^{-1} respectively.

Source Name	Type	RA (J2000)	Dec (J2000)	rms noise (K)		
				$H^{13}CO^+$	SiO	HCO^+
CO Outflow						
G010.8411-02.5919	YSO	18:19:12.09	- 20:47:30.9	0.08	0.04	0.70
G012.9090-00.2607	YSO	18:14:39.56	- 17:52:02.3	0.09	0.04	0.63
G013.6562-00.5997	YSO	18:17:24.38	- 17:22:14.8	0.07	0.04	0.62
G017.6380+00.1566	YSO	18:22:26.37	- 13:30:12.0	0.07	0.04	0.52
G018.3412+01.7681	YSO	18:17:58.11	- 12:07:24.8	0.07	0.04	0.51
G020.7617-00.0638	HII/YSO	18:29:12.36	- 10:50:38.4	0.09	0.04	0.54
G043.3061-00.2106	HII	19:11:16.97	+ 09:07:28.9	0.08	0.03	0.58
G045.0711+00.1325	HII	19:13:22.10	+ 10:50:53.4	0.09	0.04	0.55
G050.2213-00.6063	YSO	19:25:57.77	+ 15:02:59.6	0.08	0.04	0.54
G078.1224+03.6320	YSO	20:14:25.86	+ 41:13:36.3	0.08	0.04	0.49
G079.1272+02.2782	YSO	20:23:23.83	+ 41:17:39.3	0.08	0.04	0.56
G079.8749+01.1821	HII	20:30:27.45	+ 41:15:58.5	0.08	0.04	0.55
G081.7133+00.5589	YSO	20:39:02.36	+ 42:21:58.7	0.07	0.04	0.75
G081.7220+00.5699	HII	20:39:01.01	+ 42:22:50.2	0.18	0.09	0.76
G081.7522+00.5906	YSO	20:39:01.98	+ 42:24:59.1	0.09	0.04	–

Continued on next page

Table A.1 – continued from previous page

Source	Type	RA	Dec	rms noise (K)		
Name		(J2000)	(J2000)	$H^{13}CO^+$	SiO	HCO^+
G081.7624+00.5916	YSO	20:39:03.72	+42:25:29.6	0.09	0.04	–
G081.8652+00.7800	YSO	20:38:35.36	+42:37:13.7	0.09	0.04	0.39
G081.8789+00.7822	HII	20:38:37.71	+42:37:58.6	0.09	0.04	0.39
G083.0936+03.2724	HII	20:31:35.44	+45:05:45.8	0.09	0.04	0.38
G083.7071+03.2817	YSO	20:33:36.51	+45:35:44.0	0.08	0.04	0.70
G083.7962+03.3058	HII	20:33:48.02	+45:40:54.5	0.10	0.05	0.73
G103.8744+01.8558	YSO	22:15:09.08	+58:49:07.8	0.12	0.06	0.82
G109.8715+02.1156	YSO	22:56:17.98	+62:01:49.7	0.12	0.06	0.87
G192.6005-00.0479	YSO	06:12:54.01	+17:59:23.1	0.11	0.06	0.44
G194.9349-01.2224	YSO	06:13:16.14	+15:22:43.3	0.11	0.04	0.80
G203.3166+02.0564	YSO	06:41:10.15	+09:29:33.6	0.08	0.04	0.75
G207.2654-01.8080	HII/YSO	06:34:37.74	+04:12:44.2	0.1	0.05	0.43
No CO Outflow						
G011.9454-00.0373	HII	18:11:53.20	-18:36:21.8	0.10	0.05	0.75
G080.8645+00.4197	HII	20:36:52.16	+41:36:24.0	0.09	0.04	–
G080.9383-00.1268	HII	20:39:25.91	+41:20:01.6	0.09	0.04	–
G081.7131+00.5792	YSO	20:38:57.19	+42:22:40.9	0.07	0.09	0.76
G196.4542-01.6777	YSO	06:14:37.06	+13:49:36.4	0.09	0.04	0.40
G217.3771-00.0828	HII	06:59:15.73	-03:59:37.1	0.07	0.04	–
G233.8306-00.1803	YSO	07:30:16.72	-18:35:49.1	0.12	0.07	–

Table A.2: Fitted parameters from a single Gaussian fit of the $H^{13}CO^+$ (4-3) line emission extracted from the within $H^{13}CO^+$ (4-3) 5σ masked regions. Column 1 is the galactic name, Column 2 is the RMS classification, and Column 3 gives the number of pixels in the $H^{13}CO^+$ (4-3) used to extract the emission. Columns 4, 5, 6 and 7 give peak, central velocity, FWHM and integrated intensity from a single Gaussian fit to the sum of the $H^{13}CO^+$ (4-3) emission extracted from all pixels within the masked region.

Source Name	Type	No of pixels	T_{mb} (K)	V_{LSR} (kms^{-1})	δV (kms^{-1})	T_{mb}dv (K.kms^{-1})
CO Outflow						
G010.8411-02.5919	YSO	17	14.38±0.76	11.98±0.04	1.71±0.10	26.12±2.11
G012.9090-00.2607	YSO	38	19.94±0.58	37.32±0.05	3.42±0.11	72.65±3.21
G013.6562-00.5997	YSO	4	1.90±0.12	48.0±0.10	3.13±0.23	6.32±0.62
G017.6380+00.1566	YSO	33	27.57±0.77	22.33±0.03	2.16±0.07	63.38±2.71
G018.3412+01.7681	YSO	21	14.37±0.56	32.84±0.04	2.10±0.10	32.19±1.91
G043.3061-00.2106	HII	6	2.92±0.21	59.28±0.08	2.40±0.20	7.45±0.81
G045.0711+00.1325	HII	13	6.97±0.14	59.10±0.06	6.20±0.15	45.98±1.43
G050.2213-00.6063	YSO	4	0.96±0.15	40.36±0.23	2.90±0.54	2.97±0.72
G078.1224+03.6320	YSO	22	14.26±0.46	-3.32±0.05	3.12±0.12	47.39±2.35
G079.1272+02.2782	YSO	5	2.74±0.26	-1.58±0.09	1.81±0.20	5.28±0.77
G079.8749+01.1821	HII	5	2.16±0.29	-4.90±0.10	1.54±0.24	3.53±0.71
G079.8749+01.1821-OFFSET	–	19	12.84±0.49	-3.14±0.05	2.81±0.12	38.44±2.25
G081.7133+00.5589	YSO	8	8.63±0.53	-4.09±0.08	2.47±0.18	22.76±2.14
G081.7220+00.5699	HII	53	58.83±1.32	-3.17±0.05	4.57±0.12	286.36±9.84
G081.7522+00.5906	YSO	23	18.58±0.70	-4.04±0.04	2.03±0.09	40.11±2.29

Continued on next page

Table A.2 – continued from previous page

Source Name	Type	No of pixels	T_{mb} (K)	V_{LSR} (kms^{-1})	δV (kms^{-1})	T_{mb}dv (K.kms^{-1})
G081.7522+00.5906-OFFSET	–	20	13.02±0.51	-3.19±0.05	2.77±0.12	38.43±2.28
G081.7624+00.5916	YSO	19	11.11±0.94	-4.34±0.08	1.96±0.19	23.2±3.03
G081.8652+00.7800	YSO	–	–	–	–	–
G081.8652+00.7800-OFFSET	–	56	83.83±0.75	9.67±0.017	3.90±0.04	348.53±4.78
G081.8789+00.7822	HII	–	–	–	–	–
G083.0936+03.2724	HII	4	0.89±0.22	-3.50±0.29	2.33±0.67	2.22±0.84
G083.7071+03.2817	YSO	–	–	–	–	–
G083.7071+03.2817-OFFSET	–	4	1.95±0.35	-3.62±0.13	1.50±0.31	3.11±0.85
G083.7962+03.3058	HII	4	2.78±0.33	-4.31±0.10	1.66±0.23	4.91±0.88
G103.8744+01.8558	YSO	5	3.80±0.55	-18.30±0.11	1.60±0.27	6.49±1.44
G109.8715+02.1156	YSO	71	91.63±1.31	-10.80±0.03	3.99±0.07	388.87±8.49
G192.6005-00.0479	YSO	5	4.11±0.14	7.84±0.07	4.26±0.17	18.65±0.98
G194.9349-01.2224	YSO	4	1.48±0.27	15.61±0.18	2.03±0.43	3.20±0.89
G203.3166+02.0564	YSO	50	34.05±1.06	8.15±0.04	2.31±0.08	83.60±3.96
G203.3166+02.0564-OFFSET	–	28	15.87±0.56	7.55±0.04	2.54±0.10	42.96±2.32
G207.2654-01.8080	HII/YSO	12	5.77±0.45	12.58±0.10	2.74±0.24	16.83±1.98
No CO Outflow						
G080.8645+00.4197	HII	11	3.76±0.22	-2.75±0.095	3.31±0.22	13.26±1.17
G080.9383-00.1268	HII	–	–	–	–	–
G081.7131+00.5792	YSO	–	–	–	–	–

Continued on next page

Table A.2 – continued from previous page

Source Name	Type	No of pixels	T_{mb} (K)	V_{LSR} (kms^{-1})	δV (kms^{-1})	T_{mb}dv (K.kms^{-1})
G196.4542-01.6777	YSO	4	1.16±0.18	19.337±0.18	2.455±0.43	3.20±0.89
G217.3771-00.0828	HII	4	0.76±0.17	23.9344±0.25	2.18±0.58	1.76±0.62
G233.8306-00.1803	YSO	–	–	–	–	–

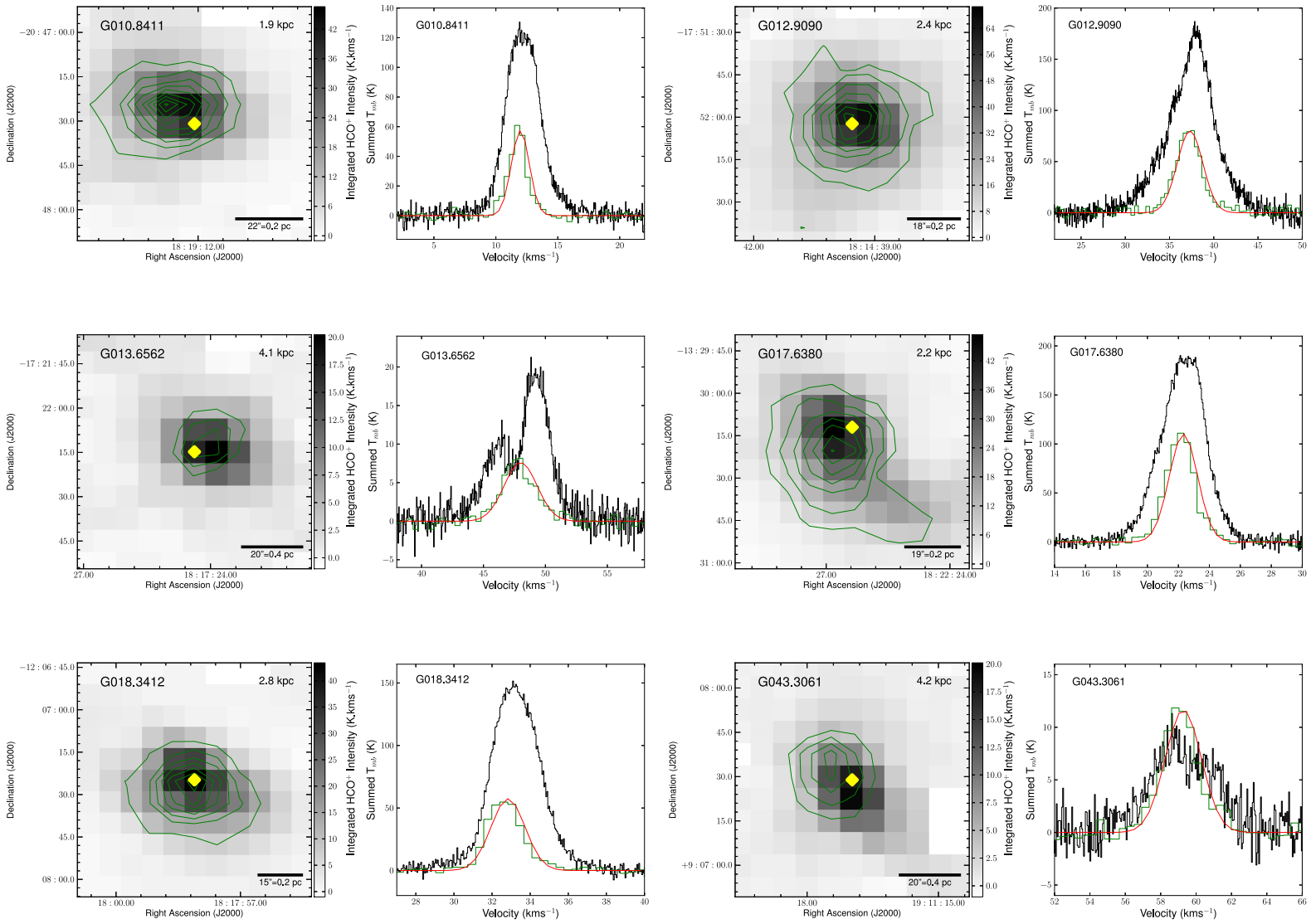

Figure A.1: The left panels show the HCO^+ (greyscale), and $H^{13}CO^+$ (solid green contours) integrated intensity maps. The green contours levels are given by 1σrms $\times$5,10,15,20,25,30,35,40,45,50 where the rms values for individual sources are given in Table A.1. The yellow diamond gives the position of the RMS source for OFFSET sources the yellow cross represents the peak of the $H^{13}CO^+$ emission in the offset component. The right panels, show the $H^{13}CO^+$ (green contours) and HCO^+ (black contours) spectra extracted from the pixels within the masked regions. The $H^{13}CO^+$ emission has been multiplied by a factor of 4. The red solid line displays the Gaussian fit to the $H^{13}CO^+$ emission also increased by a factor of 4 (see Table A.2 in Appendix A for the Gaussian fit parameters).

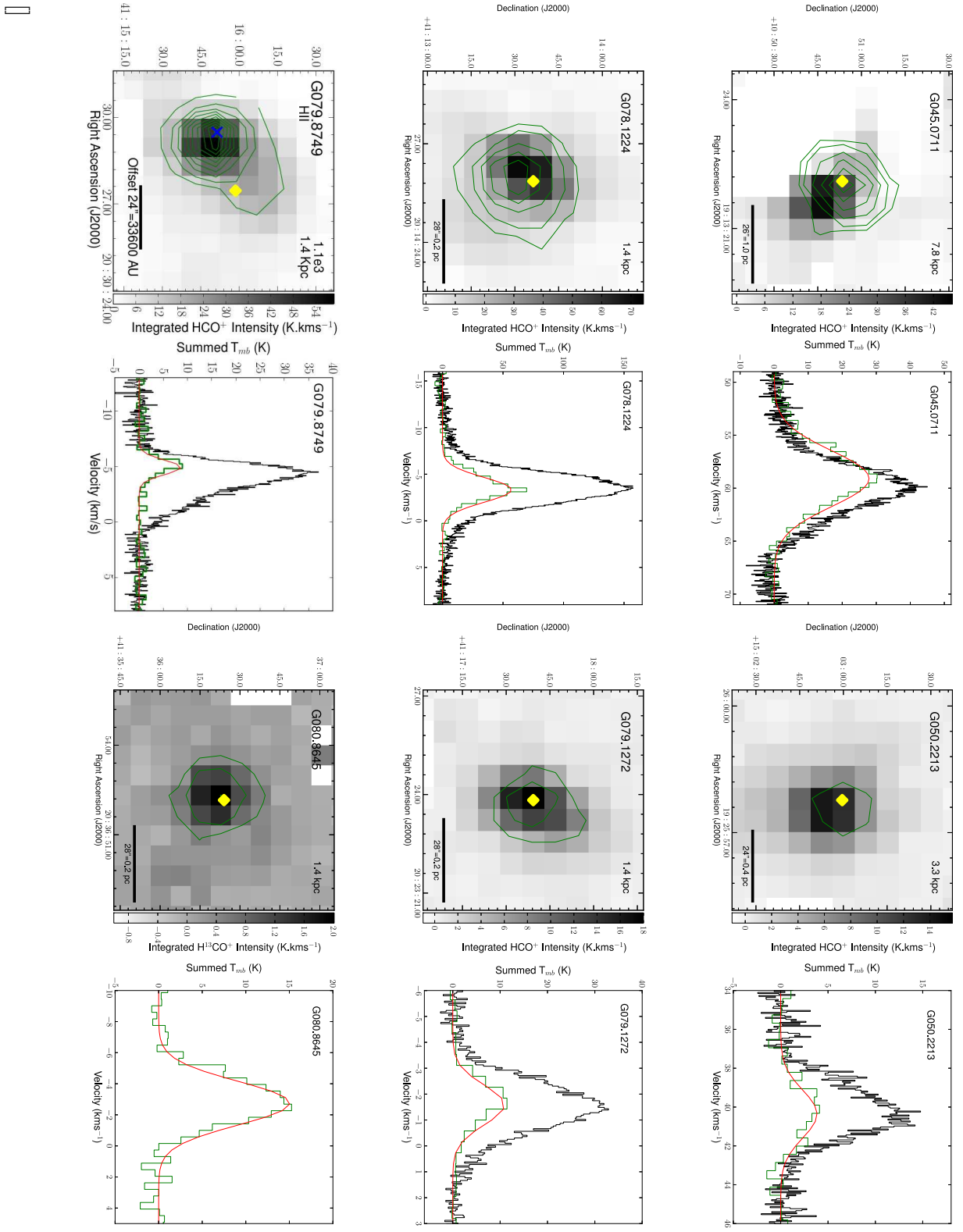
G045.0711
7.8 kpc
26"=1.0 pc
Integrated HCO+ Intensity (K.kms−1)
Summed Tmb (K)
Velocity (kms−1)
Declination (J2000)
Right Ascension (J2000)
G078.1224
1.4 kpc
28"=0.2 pc
G050.2213
3.3 kpc
24"=0.4 pc
G079.1272
1.4 kpc
28"=0.2 pc
G080.8645
1.4 kpc
28"=0.2 pc
Integrated H13CO+ Intensity (K.kms−1)
G079.8749
HII
1.1e3
1.4 Kpc
Offset 24"=33600 AU
Velocity (km/s)

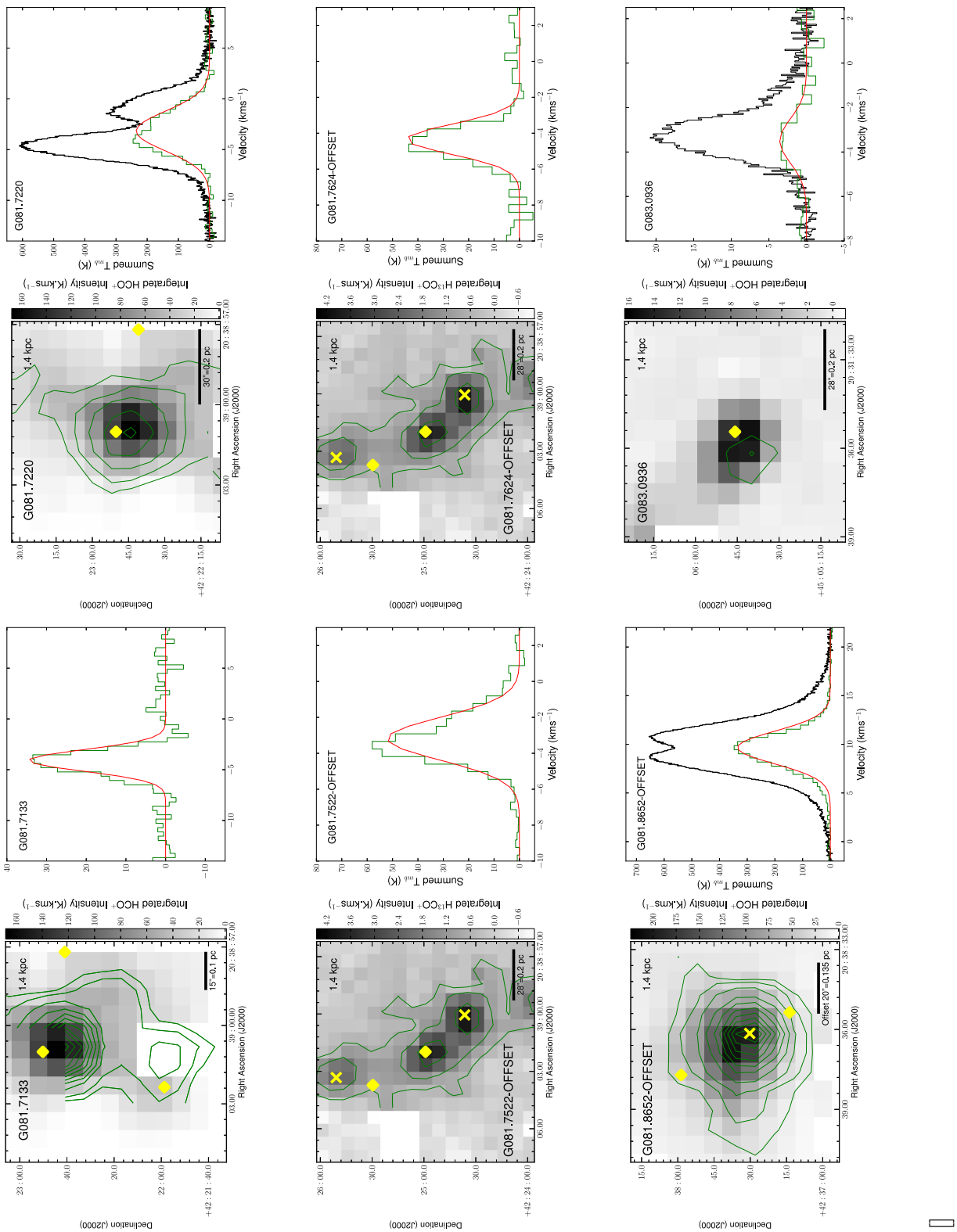
G081.7133
G081.7220
G081.7522-OFFSET
G081.7624-OFFSET
G081.8652-OFFSET
G083.0936
1.4 kpc
Right Ascension (J2000)
Declination (J2000)
Integrated HCO+ Intensity (K.kms−1)
Integrated H13CO+ Intensity (K.kms−1)
Summed Tmb (K)
Velocity (kms−1)
15″=0.1 pc
30″=0.2 pc
28″=0.2 pc
Offset 20″=0.135 pc

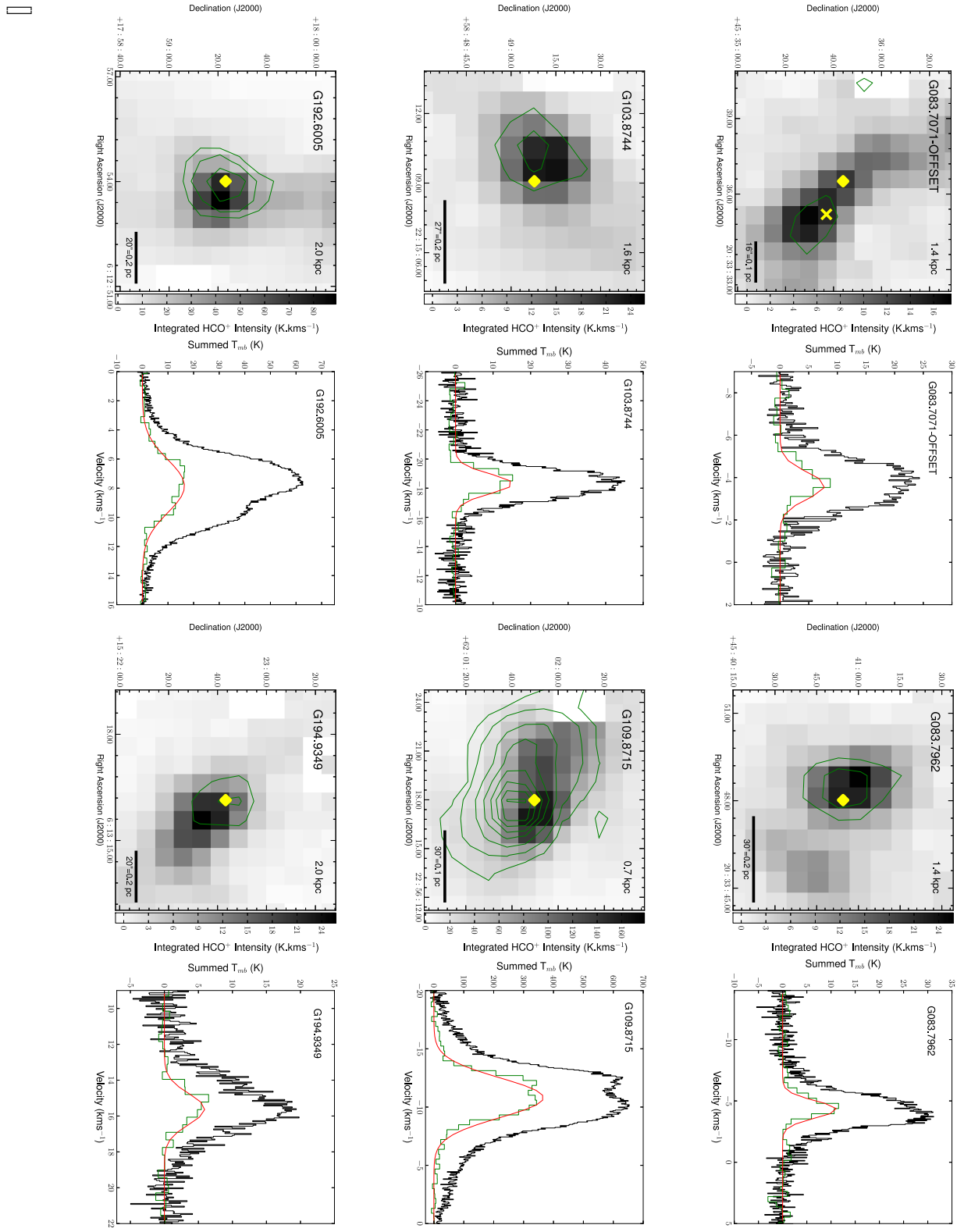
G083.7071-OFFSET
1.4 kpc
16"=0.1 pc
Declination (J2000)
Right Ascension (J2000)
Integrated HCO+ Intensity (K.kms−1)
Summed Tmb (K)
Velocity (kms−1)
G103.8744
1.6 kpc
27"=0.2 pc
G083.7962
1.4 kpc
30"=0.2 pc
G109.8715
0.7 kpc
30"=0.1 pc
G192.6005
2.0 kpc
20"=0.2 pc
G194.9349
2.0 kpc
20"=0.2 pc

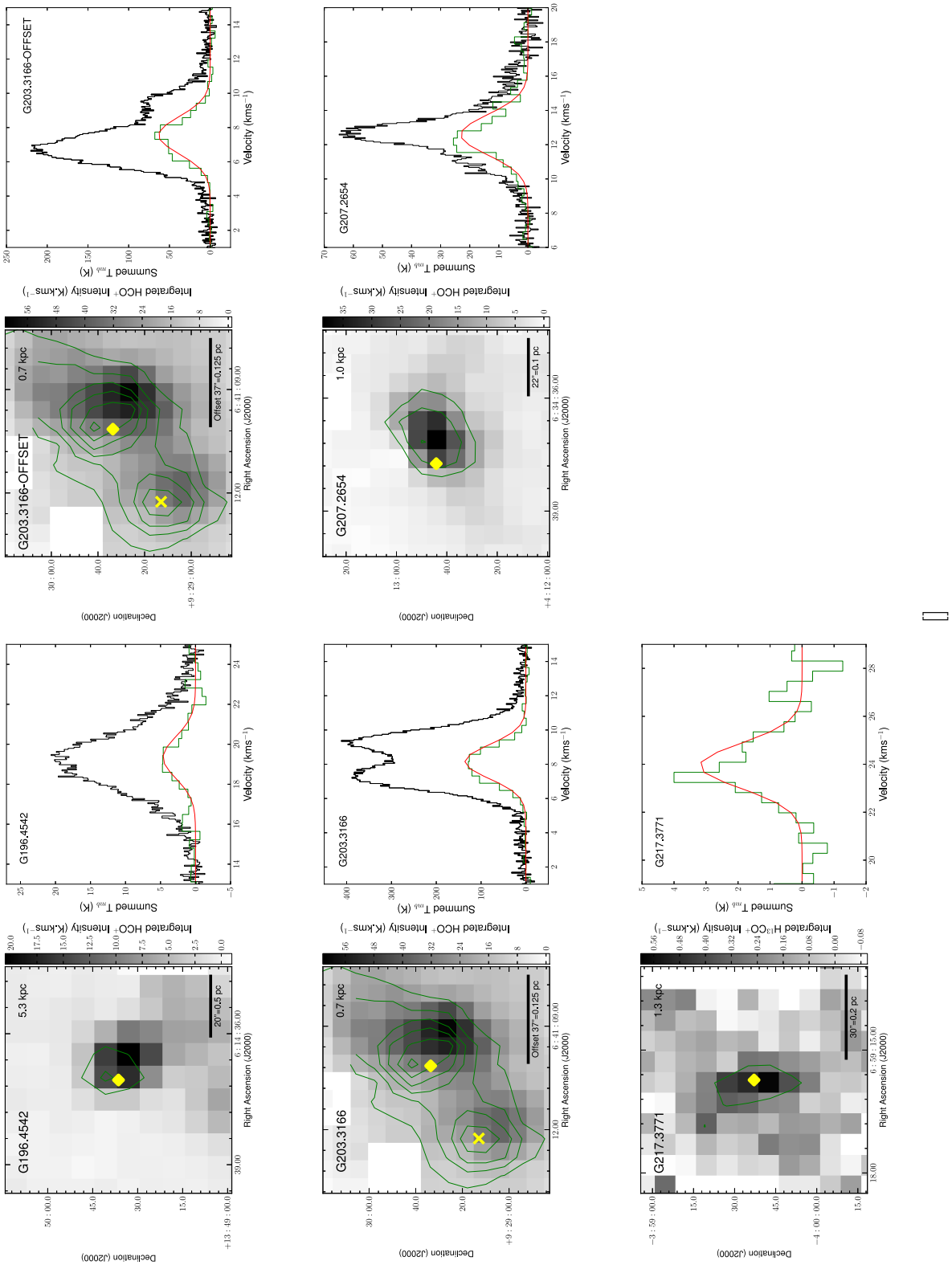
G196.4542
5.3 kpc
20"=0.5 pc
G203.3166-OFFSET
0.7 kpc
Offset 37"=0.125 pc
G203.3166
0.7 kpc
Offset 37"=0.125 pc
G207.2654
1.0 kpc
22"=0.1 pc
G217.3771
1.3 kpc
30"=0.2 pc
Integrated HCO+ Intensity (K.kms−1)
Integrated H13CO+ Intensity (K.kms−1)
Summed Tmb (K)
Declination (J2000)
Right Ascension (J2000)
Velocity (kms−1)

Appendix B

Full Molecular Line Spectra, SiO Channels Maps, and CH_3OH SHV maps towards NGC 2264-C

This Appendix presents additional, complementary Figures to Chapter 3. Provided below are the full LSB and USB spectra for the mm continuum peaks detected in NGC 2264-C, taken from the peak continuum pixel. In addition, the full SiO channel map is presented for a velocity resolution of $1.2\,\mathrm{kms}^{-1}$ per channel. The systemic and SHV emission for the two CH_3OH transitions tracing the outflows in NGC 2264-C are also provided.

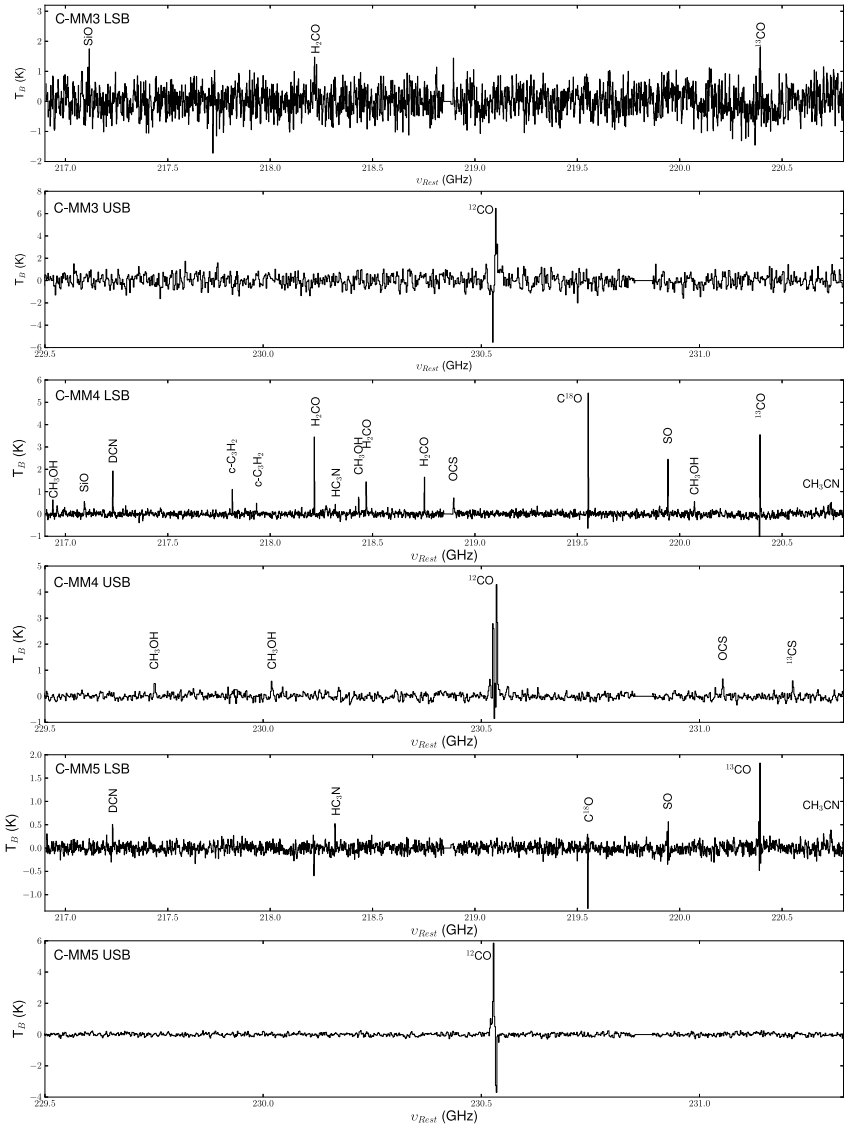

Figure B.1: The LSB and USB Spectra from the RMS observations towards the continuum peaks identified in NGC 2264-C. The source is given in the top left corner and the lines detected are labelled for the mm Continuum Peaks.

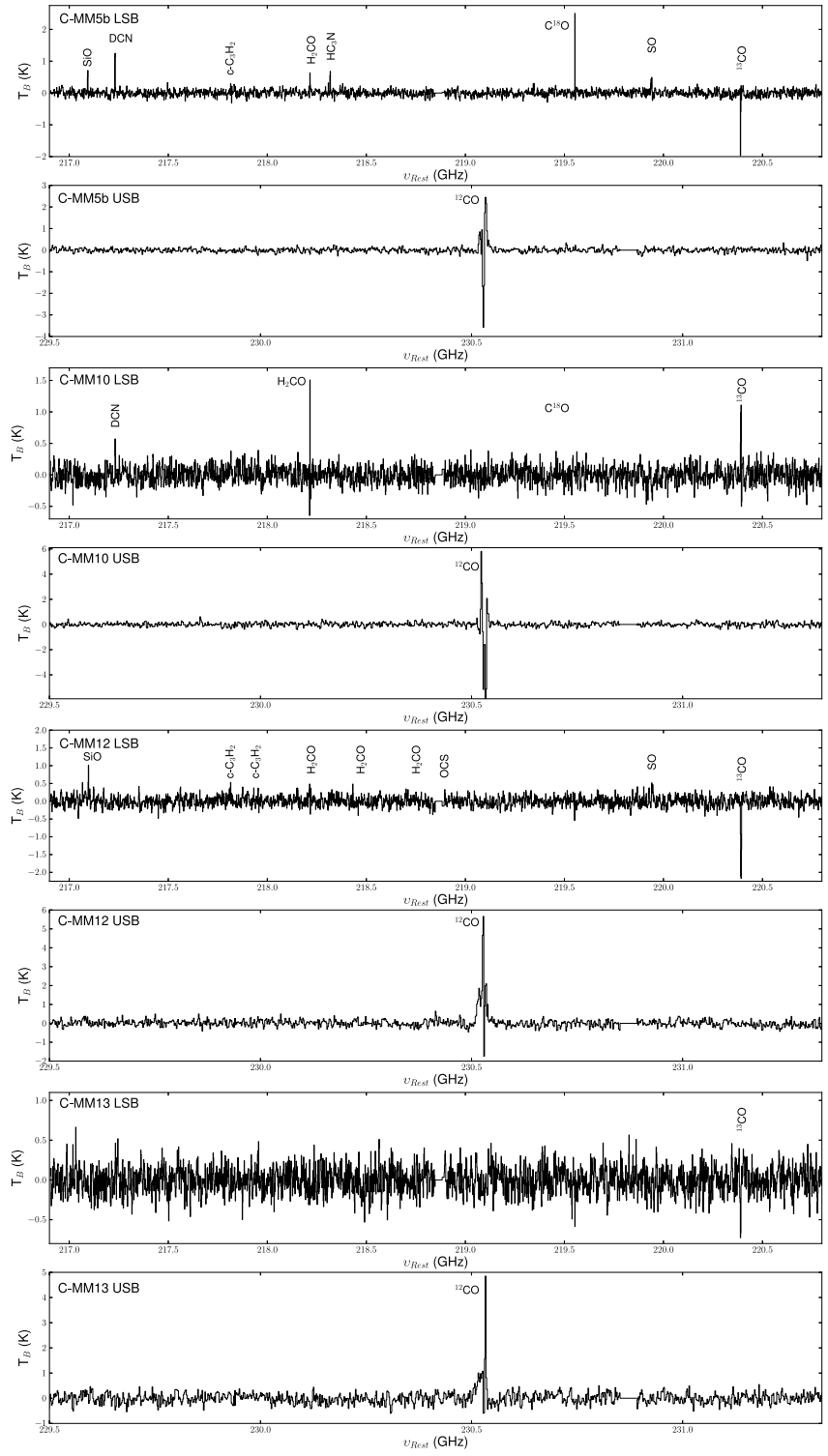
C-MM5b LSB
SiO
DCN
c-C3H2
H2CO
HC3N
C18O
SO
13CO
C-MM5b USB
12CO
C-MM10 LSB
DCN
H2CO
C18O
13CO
C-MM10 USB
12CO
C-MM12 LSB
SiO
c-C3H2
c-C3H2
H2CO
H2CO
H2CO
OCS
SO
13CO
C-MM12 USB
12CO
C-MM13 LSB
13CO
C-MM13 USB
12CO
T_B (K)
υ_Rest (GHz)

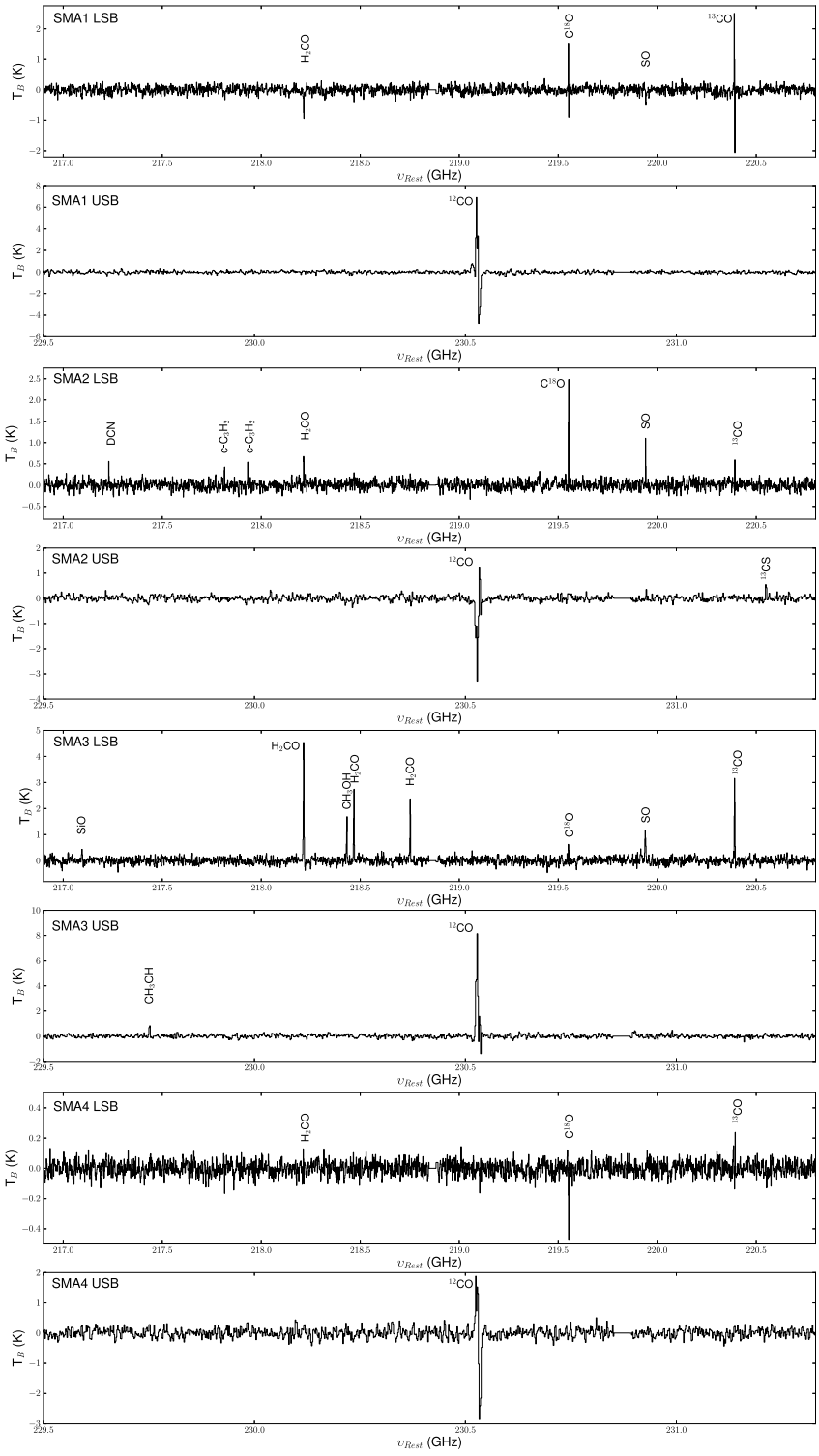
SMA1 LSB
H2CO
C18O
SO
13CO
SMA1 USB
12CO
SMA2 LSB
DCN
c-C3H2
c-C3H2
H2CO
C18O
SO
13CO
SMA2 USB
12CO
13CS
SMA3 LSB
H2CO
SiO
CH3OH
H2CO
H2CO
C18O
SO
13CO
SMA3 USB
12CO
CH3OH
SMA4 LSB
H2CO
C18O
13CO
SMA4 USB
12CO
TB (K)
υRest (GHz)

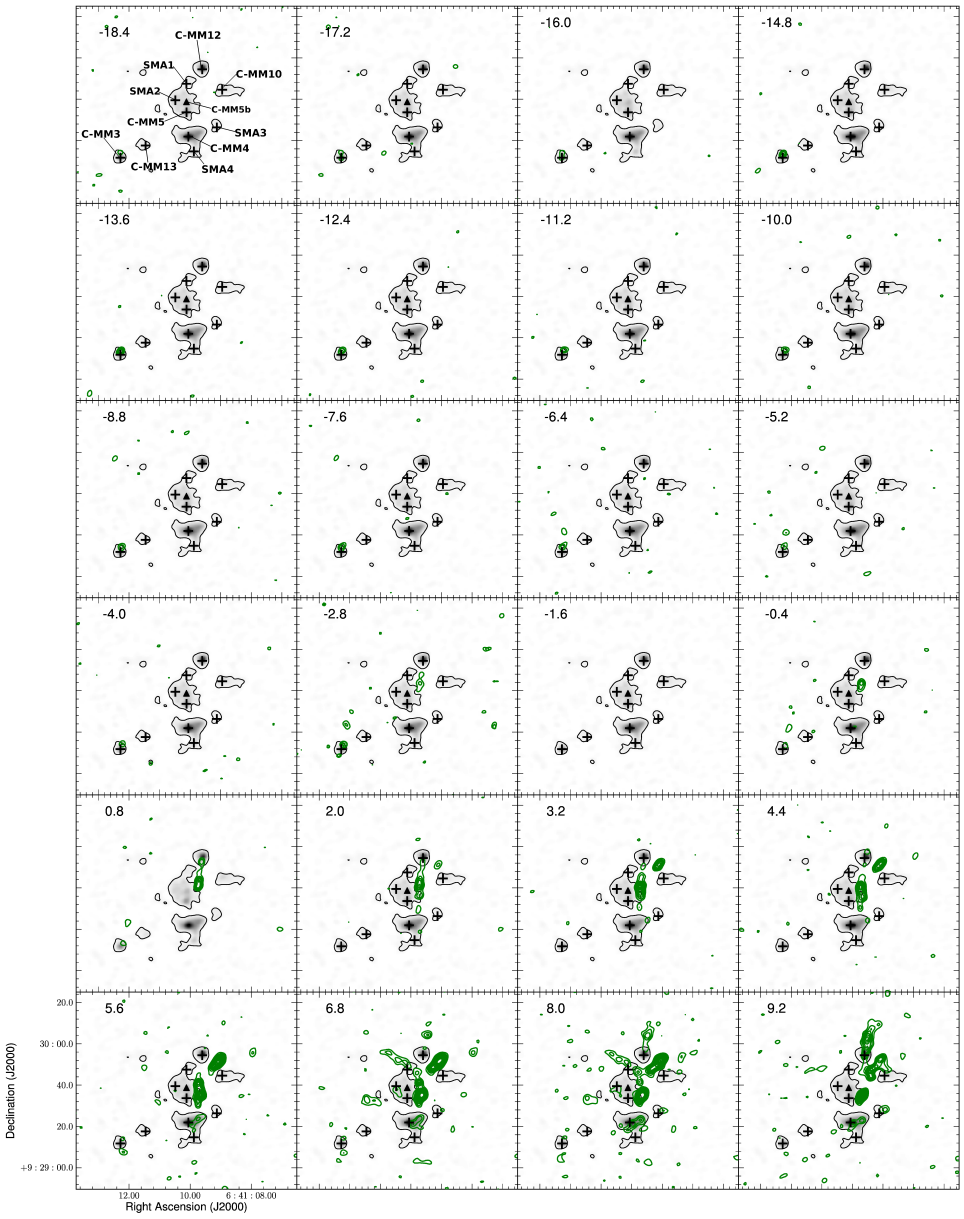

Figure B.2: Channel maps of the SiO (5-4) emission. The greyscale is the 1.3 mm continuum and the black contour is the 3σ level. The green contours are the SiO (5-4) emission starting at 3σ and increasing in steps of 2σ, where $1\sigma = 40$mJy/beam for each panel. The channels are all 1.2 kms^{-1} wide and the respective velocity for each channel is provided in the top left corner (units kms^{-1}).

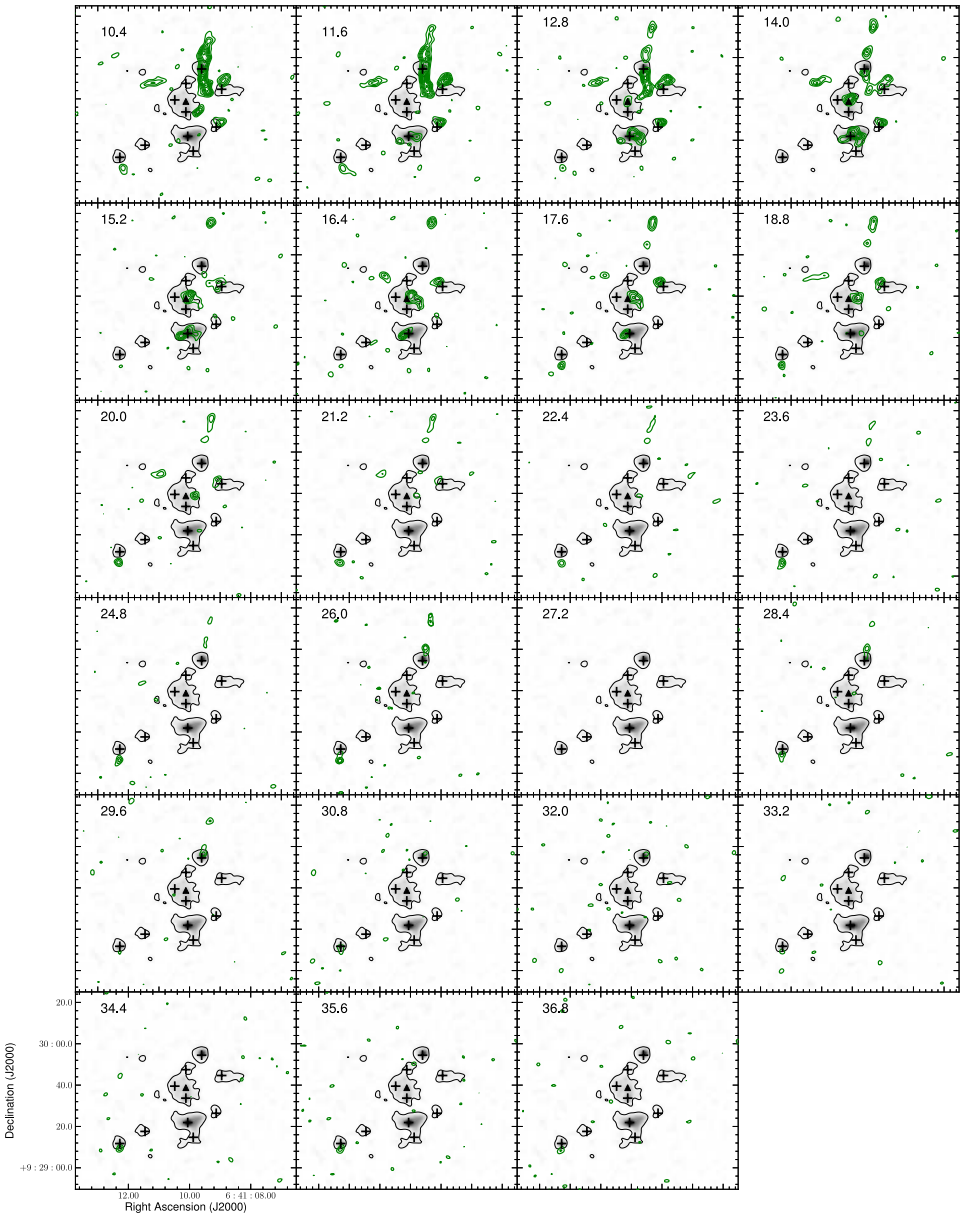
10.4
11.6
12.8
14.0
15.2
16.4
17.6
18.8
20.0
21.2
22.4
23.6
24.8
26.0
27.2
28.4
29.6
30.8
32.0
33.2
34.4
35.6
36.8
Declination (J2000)
20.0
30 : 00.0
40.0
20.0
+9 : 29 : 00.0
12.00
10.00
6 : 41 : 08.00
Right Ascension (J2000)

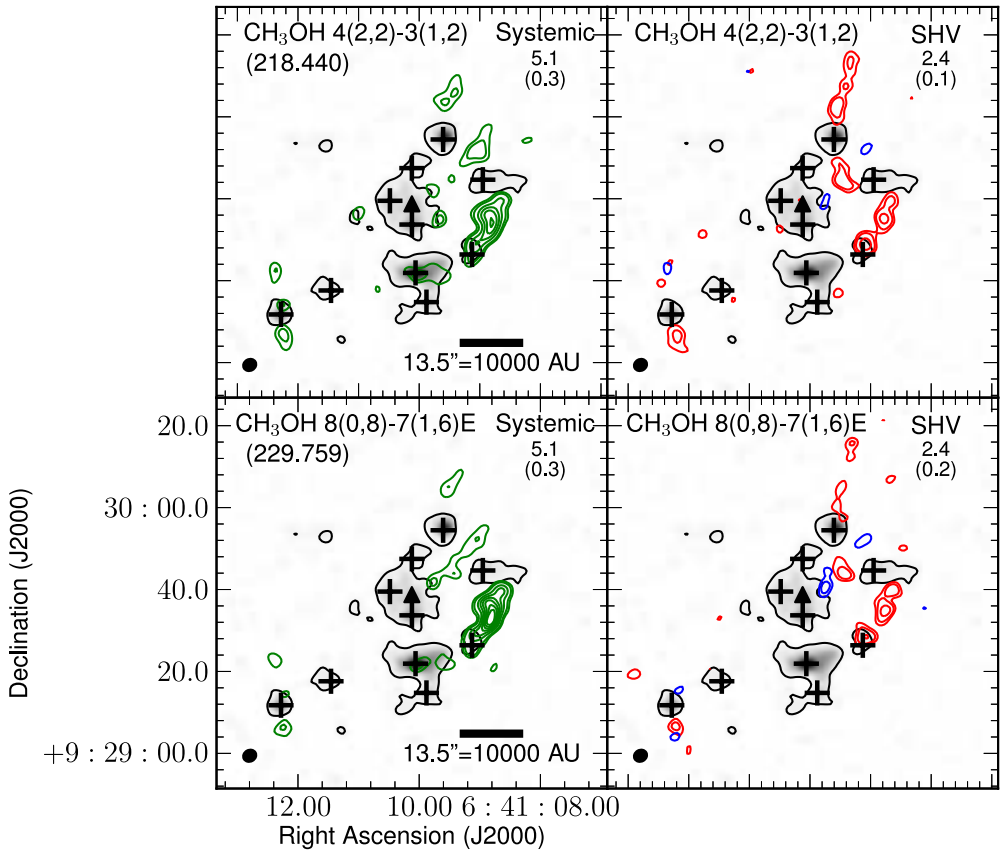

Figure B.3: CH_3OH systemic and SHV red and blueshifted emission in NGC 2264-C. The CH_3OH transition and rest frequency is given in the top left corner of the panels. The velocity regime and integrated intensity and 1σ rms are given in the top right of each panel. The black crosses mark the positions of the ten mm continuum peaks in NGC 2264-C.

References

Allen, D.A. (1972). Infrared Objects in H II Regions. *ApJL*, **172**, L55. 87

André, P. (2013). The Herschel View of Star Formation. *ArXiv e-prints*. 4

André, P., Men'shchikov, A., Bontemps, S., Könyves, V., Motte, F., Schneider, N., Didelon, P., Minier, V., Saraceno, P., Ward-Thompson, D., di Francesco, J., White, G., Molinari, S., Testi, L., Abergel, A., Griffin, M., Henning, T., Royer, P., Merín, B., Vavrek, R., Attard, M., Arzoumanian, D., Wilson, C.D., Ade, P., Aussel, H., Baluteau, J.P., Benedettini, M., Bernard, J.P., Blommaert, J.A.D.L., Cambrésy, L., Cox, P., di Giorgio, A., Hargrave, P., Hennemann, M., Huang, M., Kirk, J., Krause, O., Launhardt, R., Leeks, S., Le Pennec, J., Li, J.Z., Martin, P.G., Maury, A., Olofsson, G., Omont, A., Peretto, N., Pezzuto, S., Prusti, T., Roussel, H., Russeil, D., Sauvage, M., Sibthorpe, B., Sicilia-Aguilar, A., Spinoglio, L., Waelkens, C., Woodcraft, A. & Zavagno, A. (2010). From filamentary clouds to prestellar cores to the stellar IMF: Initial highlights from the Herschel Gould Belt Survey. *A&A*, **518**, L102. 4

Araya, E., Hofner, P., Kurtz, S., Bronfman, L. & DeDeo, S. (2005). CH_3CN Observations toward Southern Massive Star-forming Regions. *ApJS*, **157**, 279–301. 25, 124, 221

Arce, H.G. & Sargent, A.I. (2006). The Evolution of Outflow-Envelope Interactions in Low-Mass Protostars. *ApJ*, **646**, 1070–1085. 8, 14

Astropy Collaboration, Robitaille, T.P., Tollerud, E.J., Greenfield, P., Droettboom, M., Bray, E., Aldcroft, T., Davis, M. & Ginsburg, A. (2013). Astropy: A community Python package for astronomy. *A&A*, **558**, A33. 38, 91, 97, 161, 165

Bally, J. & Zinnecker, H. (2005). The Birth of High-Mass Stars: Accretion and/or Mergers? *ApJ*, **129**, 2281–2293. 235

Battersby, C., Bally, J., Ginsburg, A., Bernard, J.P., Brunt, C., Fuller, G.A., Martin, P., Molinari, S., Mottram, J., Peretto, N., Testi, L. & Thompson, M.A. (2011). Characterizing precursors to stellar clusters with Herschel. *A&A*, **535**, A128. 129

Baumgardt, H. & Klessen, R.S. (2011). The role of stellar collisions for the formation of massive stars. *MNRAS*, **413**, 1810–1818. 9

Bell, T.A., Cernicharo, J., Viti, S., Marcelino, N., Palau, A., Esplugues, G.B. & Tercero, B. (2014). Extended warm gas in Orion KL as probed by methyl cyanide. *A&A*, **564**, A114. 132

Beltrán, M.T., Sánchez-Monge, Á., Cesaroni, R., Kumar, M.S.N., Galli, D., Walmsley, C.M., Etoka, S., Furuya, R.S., Moscadelli,

L., Stanke, T., van der Tak, F.F.S., Vig, S., Wang, K.S., Zinnecker, H., Elia, D. & Schisano, E. (2014). Filamentary structure and Keplerian rotation in the high-mass star-forming region G35.03+0.35 imaged with ALMA. *A&A*, **571**, A52. 25

Bergin, E.A., Melnick, G.J. & Neufeld, D.A. (1998). The Postshock Chemical Lifetimes of Outflow Tracers and a Possible New Mechanism to Produce Water Ice Mantles. *ApJ*, **499**, 777–792. 18

Beuther, H. & Schilke, P. (2004). Fragmentation in MassiveStar Formation. *Science*, **303**, 1167–1169. 3, 5

Beuther, H. & Shepherd, D. (2005a). Precursors of UCHII Regions and the Evolution of Massive Outflows. In M. Kumar, M. Tafalla & P. Caselli, eds., *Cores to Clusters: Star Formation with Next Generation Telescopes*, 105–119. 15

Beuther, H. & Shepherd, D. (2005b). Precursors of UCHII Regions and the Evolution of Massive Outflows. In M.S.N. Kumar, M. Tafalla & P. Caselli, eds., *Cores to Clusters: Star Formation with Next Generation Telescopes*, 105–119. 16, 235, 240

Beuther, H., Schilke, P., Sridharan, T., Menten, K., Walmsley, C. & Wyrowski, F. (2002). Massive molecular outflows. *A&A*, **383**, 892–904. 12, 13, 14, 148, 149, 152

Beuther, H., Hunter, T.R., Zhang, Q., Sridharan, T.K., Zhao, J.H., Sollins, P., Ho, P.T.P., Ohashi, N., Su, Y.N., Lim, J. & Liu,

S.Y. (2004). Submillimeter Array Outflow/Disk Studies in the Massive Star-forming Region IRAS 18089-1732. *ApJL*, **616**, L23–L26. 15

Beuther, H., Churchwell, E.B., McKee, C.F. & Tan, J.C. (2007). The Formation of Massive Stars. *Protostars and Planets V*, 165–180. 4, 25

Blitz, L. (1993). Giant molecular clouds. In E.H. Levy & J.I. Lunine, eds., *Protostars and Planets III*, 125–161. 2, 3, 4

Bonnell, I.A., Bate, M.R., Clarke, C.J. & Pringle, J.E. (1997). Accretion and the stellar mass spectrum in small clusters. *MNRAS*, **285**, 201–208. 9

Bonnell, I.A., Bate, M.R. & Zinnecker, H. (1998). On the formation of massive stars. *MNRAS*, **298**, 93–102. 9, 11

Bontemps, S., Andre, P., Terebey, S. & Cabrit, S. (1996). Evolution of outflow activity around low-mass embedded young stellar objects. *A&A*, **311**, 858–872. 13, 14, 29, 71, 148, 149, 150, 151, 200

Breen, S.L., Ellingsen, S.P., Caswell, J.L. & Lewis, B.E. (2010). 12.2-GHz methanol masers towards 1.2-mm dust clumps: quantifying high-mass star formation evolutionary schemes. *MNRAS*, **401**, 2219–2244. 240

Bronfman, L., Alvarez, H., Cohen, R.S. & Thaddeus, P. (1989). A deep CO survey of molecular clouds in the southern Milky Way. *ApJS*, **71**, 481–548. 3

Buckle, J., Richer, J. & Davis, C. (2012). The structure of molecular gas associated with NGC 2264: wide-field ^{12}CO and H_2 imaging. *MNRAS*, **423**, 1127–1143. 87

Buckle, J.V., Hills, R.E., Smith, H., Dent, W.R.F., Bell, G., Curtis, E.I., Dace, R., Gibson, H., Graves, S.F., Leech, J., Richer, J.S., Williamson, R., Withington, S., Yassin, G., Bennett, R., Hastings, P., Laidlaw, I., Lightfoot, J.F., Burgess, T., Dewdney, P.E., Hovey, G., Willis, A.G., Redman, R., Wooff, B., Berry, D.S., Cavanagh, B., Davis, G.R., Dempsey, J., Friberg, P., Jenness, T., Kackley, R., Rees, N.P., Tilanus, R., Walther, C., Zwart, W., Klapwijk, T.M., Kroug, M. & Zijlstra, T. (2009). HARP/ACSIS: a submillimetre spectral imaging system on the James Clerk Maxwell Telescope. *MNRAS*, **399**, 1026–1043. 33, 34

Bunn, J.C., Hoare, M.G. & Drew, J.E. (1995). Observations of the IR recombination line emission from massive young stellar objects. *MNRAS*, **272**, 346–354. 132, 136, 153

Cabrit, S. & Bertout, C. (1992). CO line formation in bipolar flows. III - The energetics of molecular flows and ionized winds. *A&A*, **261**, 274–284. 13, 14, 30, 86, 147, 148, 149

Calcutt, H., Viti, S., Codella, C., Beltrán, M.T., Fontani, F. & Woods, P.M. (2014). A high-resolution study of complex organic molecules in hot cores. *MNRAS*, **443**, 3157–3173. 25

Carrasco-González, C., Rodríguez, L., Anglada, G., Martí, J., Torrelles, J. & Osorio, M. (2010). A Magnetized Jet from a Massive Protostar. *Science*, **330**, 1209–. 15, 21, 235

Caselli, P. & Myers, P.C. (1995). The Line Width–Size Relation in Massive Cloud Cores. *ApJ*, **446**, 665. 10

Caswell, J.L., Fuller, G.A., Green, J.A., Avison, A., Breen, S.L., Brooks, K.J., Burton, M.G., Chrysostomou, A., Cox, J., Diamond, P.J., Ellingsen, S.P., Gray, M.D., Hoare, M.G., Masheder, M.R.W., McClure-Griffiths, N.M., Pestalozzi, M.R., Phillips, C.J., Quinn, L., Thompson, M.A., Voronkov, M.A., Walsh, A.J., Ward-Thompson, D., Wong-McSweeney, D., Yates, J.A. & Cohen, R.J. (2010). The 6-GHz methanol multibeam maser catalogue - I. Galactic Centre region, longitudes 345°*to*6°. MNRAS, **404**, 1029 – −1060.

Cesaroni, R., Walmsley, C.M. & Churchwell, E. (1992). Hot ammonia toward ultracompact H II regions. *A&A*, **256**, 618–630. 4, 24

Cesaroni, R., Galli, D., Neri, R. & Walmsley, C.M. (2014). Imaging the disk around IRAS 20126+4104 at subarcsecond resolution. *A&A*, **566**, A73. 12, 25, 132

Cesaroni, R., Pestalozzi, M., Beltrán, M.T., Hoare, M.G., Molinari, S., Olmi, L., Smith, M.D., Stringfellow, G.S., Testi, L. & Thompson, M.A. (2015). Infrared emission of young HII regions: a Herschel/Hi-GAL study. *A&A*, **579**, A71. 26

Chambers, E.T., Jackson, J.M., Rathborne, J.M. & Simon, R. (2009). Star Formation Activity of Cores within Infrared Dark Clouds. *ApJS*, **181**, 360–390. 23

Choudhury, R., Schilke, P., Stéphan, G., Bergin, E., Möller, T., Schmiedeke, A. & Zernickel, A. (2015). Evolution of complex organic molecules in hot molecular cores. Synthetic spectra at (sub-)mm wavebands. *A&A*, **575**, A68. 25

Churchwell, E. (2002). Ultra-Compact HII Regions and Massive Star Formation. *ARA&A*, **40**, 27–62. 24, 26

Codella, C., Beltrán, M., Cesaroni, R., Moscadelli, L., Neri, R., Vasta, M. & Zhang, Q. (2013). SiO collimated outflows driven by high-mass YSOs in G24.78+0.08. *A&A*, **550**, A81. 17, 204

Codella, C., Cabrit, S., Gueth, F., Podio, L., Leurini, S., Bachiller, R., Gusdorf, A., Lefloch, B., Nisini, B., Tafalla, M. & Yvart, W. (2014). The ALMA view of the protostellar system HH212. The wind, the cavity, and the disk. *A&A*, **568**, L5. 17, 20, 31, 117, 118

Cooper, H.B. (2013). *Observational Studies of Regions of Massive Star Formation*. Ph.D. thesis, University of Leeds. 239

Csengeri, T., Bontemps, S., Schneider, N., Motte, F., Gueth, F. & Hora, J.L. (2011). Convergent Flows and Low-velocity Shocks in DR21(OH). *ApJL*, **740**, L5. 132

Cyganowski, C., Brogan, C., Hunter, T., Zhang, Q., Friesen, R., Indebetouw, R. & Chandler, C. (2012). The Protocluster G18.67+0.03: A Test Case for Class I CH_3OH Masers as Evolutionary Indicators for Massive Star Formation. *ApJL*, **760**, L20. 118, 120, 129

Cyganowski, C.J., Brogan, C.L., Hunter, T.R. & Churchwell, E. (2009). A Class I and Class II CH_3OH Maser Survey of EGOs from the GLIMPSE Survey. *ApJ*, **702**, 1615–1647. 136

Cyganowski, C.J., Brogan, C.L., Hunter, T.R., Churchwell, E. & Zhang, Q. (2011). Bipolar Molecular Outflows and Hot Cores in Glimpse Extended Green Objects (EGOs). *ApJ*, **729**, 124. 118, 120, 124, 133, 136, 141

Dame, T.M., Ungerechts, H., Cohen, R.S., de Geus, E.J., Grenier, I.A., May, J., Murphy, D.C., Nyman, L.A. & Thaddeus, P. (1987). A composite CO survey of the entire Milky Way. *ApJ*, **322**, 706–720. 3

Dame, T.M., Hartmann, D. & Thaddeus, P. (2001). The Milky Way in Molecular Clouds: A New Complete CO Survey. *ApJ*, **547**, 792–813. 3

Davies, B., Hoare, M.G., Lumsden, S.L., Hosokawa, T., Oudmaijer, R.D., Urquhart, J.S., Mottram, J.C. & Stead, J. (2011). The Red MSX Source survey: critical tests of accretion models for the formation of massive stars. *MNRAS*, **416**, 972–990. 72, 146

de Wit, W.J., Hoare, M.G., Fujiyoshi, T., Oudmaijer, R.D., Honda, M., Kataza, H., Miyata, T., Okamoto, Y.K., Onaka, T., Sako,

S. & Yamashita, T. (2009). Resolved 24.5 micron emission from massive young stellar objects. *A&A*, **494**, 157–178. 157, 195, 196

Di Francesco, J., Johnstone, D., Kirk, H., MacKenzie, T. & Ledwosinska, E. (2008). The SCUBA Legacy Catalogues: Submillimeter-Continuum Objects Detected by SCUBA. *ApJS*, **175**, 277–295. 52, 53, 90, 147, 191

Dobbs, C.L., Bonnell, I.A. & Clark, P.C. (2005). Centrally condensed turbulent cores: massive stars or fragmentation? *MNRAS*, **360**, 2–8. 10

Duarte-Cabral, A., Bontemps, S., Motte, F., Hennemann, M., Schneider, N. & André, P. (2013). CO outflows from high-mass Class 0 protostars in Cygnus-X. *A&A*, **558**, A125. 13, 14, 148, 149

Dunham, M.M., Crapsi, A., Evans, N.J., II, Bourke, T.L., Huard, T.L., Myers, P.C. & Kauffmann, J. (2008). Identifying the Low-Luminosity Population of Embedded Protostars in the c2d Observations of Clouds and Cores. *ApJS*, **179**, 249–282. 24

Dunham, M.M., Arce, H.G., Mardones, D., Lee, J.E., Matthews, B.C., Stutz, A.M. & Williams, J.P. (2014). Molecular Outflows Driven by Low-mass Protostars. I. Correcting for Underestimates When Measuring Outflow Masses and Dynamical Properties. *ApJ*, **783**, 29. 24, 56, 149, 151, 200

Edris, K.A., Fuller, G.A. & Cohen, R.J. (2007). A survey of OH masers towards high mass protostellar objects. *A&A*, **465**, 865–877. 159

Ellingsen, S.P., Voronkov, M.A., Cragg, D.M., Sobolev, A.M., Breen, S.L. & Godfrey, P.D. (2007). Investigating high-mass star formation through maser surveys. In J.M. Chapman & W.A. Baan, eds., *IAU Symposium*, vol. 242 of *IAU Symposium*, 213–217. 240

Fish, V.L., Muehlbrad, T.C., Pratap, P., Sjouwerman, L.O., Strelnitski, V., Pihlström, Y.M. & Bourke, T.L. (2011). First Interferometric Images of the 36 GHz Methanol Masers in the DR21 Complex. *ApJ*, **729**, 14. 118, 120

Flaccomio, E., Micela, G. & Sciortino, S. (2006). ACIS-I observations of NGC 2264. Membership and X-ray properties of PMS stars. *A&A*, **455**, 903–921. 135

Fontani, F., Zhang, Q., Caselli, P. & Bourke, T.L. (2009). Linking pre- and proto-stellar objects in the intermediate-/high-mass star forming region IRAS 05345+3157. *A&A*, **499**, 233–247. 118

Fontani, F., Cesaroni, R. & Furuya, R.S. (2010). Class I and Class II methanol masers in high-mass star-forming regions. *A&A*, **517**, A56. 159

Frank, A., Ray, T.P., Cabrit, S., Hartigan, P., Arce, H.G., Bacciotti, F., Bally, J., Benisty, M., Eislöffel, J., Güdel, M., Lebedev, S., Nisini, B. & Raga, A. (2014). Jets and Outflows from Star to Cloud: Observations Confront Theory. *Protostars and Planets VI*, 451–474. 12

Frerking, M.A., Langer, W.D. & Wilson, R.W. (1982). The relationship between carbon monoxide abundance and visual extinction in interstellar clouds. *ApJ*, **262**, 590–605. 76, 141

Fuller, G.A., Williams, S.J. & Sridharan, T.K. (2005). The circumstellar environment of high mass protostellar objects. III. Evidence of infall? *A&A*, **442**, 949–959. 32, 65, 79

Galván-Madrid, R., Zhang, Q., Keto, E., Ho, P., Zapata, L., Rodríguez, L., Pineda, J. & Vázquez-Semadeni, E. (2010). From the Convergence of Filaments to Disk-outflow Accretion: Massive Star Formation in W33A. *ApJ*, **725**, 17–28. 129

Gibb, A., Davis, C. & Moore, T. (2007). A survey of SiO 5-4 emission towards outflows from massive young stellar objects. *MNRAS*, **382**, 1213–1224. 17, 20, 31, 66

Gibb, A.G., Richer, J.S., Chandler, C.J. & Davis, C.J. (2004). A Survey of SiO 5-4 Emission toward Outflows from Low-Luminosity Protostellar Candidates. *ApJ*, **603**, 198–212. 17, 31, 80

Girart, J.M., Frau, P., Zhang, Q., Koch, P.M., Qiu, K., Tang, Y.W., Lai, S.P. & Ho, P.T.P. (2013). DR 21(OH): A Highly Fragmented, Magnetized, Turbulent Dense Core. *ApJ*, **772**, 69. 20, 80

Goddi, C., Moscadelli, L., Sanna, A., Cesaroni, R. & Minier, V. (2007). Associations of H_2O and CH_3OH masers at milli-arcsec angular resolution in two high-mass YSOs. *A&A*, **461**, 1027–1035. 158, 159, 187, 195

Goldsmith, P.F. & Langer, W.D. (1999). Population Diagram Analysis of Molecular Line Emission. *ApJ*, **517**, 209–225. 124

Gómez-Ruiz, A.I., Hirano, N., Leurini, S. & Liu, S.Y. (2013). The L 1157 protostellar outflow imaged with the Submillimeter Array. *A&A*, **558**, A94. 117

Gregersen, E.M., Evans, N.J., II, Zhou, S. & Choi, M. (1997). New Protostellar Collapse Candidates: An HCO^+ Survey of the Class 0 Sources. *ApJ*, **484**, 256–276. 32, 79

Grellmann, R., Ratzka, T., Kraus, S., Linz, H., Preibisch, T. & Weigelt, G. (2011). Mid-infrared interferometry of the massive young stellar object NGC 2264 IRS 1. *A&A*, **532**, A109. 132

Gueth, F. & Guilloteau, S. (1999). The jet-driven molecular outflow of HH 211. *A&A*, **343**, 571–584. 17, 19

Guillet, V., Jones, A.P. & Pineau Des Forêts, G. (2009). Shocks in dense clouds. II. Dust destruction and SiO formation in J shocks. *A&A*, **497**, 145–153. 18, 110

Gusdorf, A., Cabrit, S., Flower, D.R. & Pineau Des Forêts, G. (2008a). SiO line emission from C-type shock waves: interstellar jets and outflows. *A&A*, **482**, 809–829. 18, 110

Gusdorf, A., Pineau Des Forêts, G., Cabrit, S. & Flower, D.R. (2008b). SiO line emission from interstellar jets and outflows: silicon-

containing mantles and non-stationary shock waves. *A&A*, **490**, 695–706. 110

Haschick, A.D., Menten, K.M. & Baan, W.A. (1990). Detection of widespread strong methanol masers at 44 GHz. *ApJ*, **354**, 556–567. 121

Hatchell, J., Thompson, M.A., Millar, T.J. & MacDonald, G.H. (1998). A survey of molecular line emission towards ultracompact HII regions. *A&AS*, **133**, 29–49. 209

Henshaw, J.D., Caselli, P., Fontani, F., Jiménez-Serra, I., Tan, J.C. & Hernandez, A.K. (2013). Complex, quiescent kinematics in a highly filamentary infrared dark cloud. *MNRAS*, **428**, 3425–3442. 24

Herbst, E. & van Dishoeck, E.F. (2009). Complex Organic Interstellar Molecules. *ARA&A*, **47**, 427–480. 24

Hernández-Hernández, V., Zapata, L., Kurtz, S. & Garay, G. (2014). SMA Millimeter Observations of Hot Molecular Cores. *ApJ*, **786**, 38. 217, 231

Hirano, N., Liu, S.Y., Shang, H., Ho, P.T.P., Huang, H.C., Kuan, Y.J., McCaughrean, M.J. & Zhang, Q. (2006). SiO J = 5-4 in the HH 211 Protostellar Jet Imaged with the Submillimeter Array. *ApJL*, **636**, L141–L144. 17, 19

Hosokawa, T. & Omukai, K. (2009). Evolution of Massive Protostars with High Accretion Rates. *ApJ*, **691**, 823–846. 21

Hunter, T.R., Brogan, C.L., Cyganowski, C.J. & Young, K.H. (2014). Subarcsecond Imaging of the NGC 6334 I(N) Protocluster: Two Dozen Compact Sources and a Massive Disk Candidate. *ApJ*, **788**, 187. 118, 120

Ilee, J.D., Wheelwright, H.E., Oudmaijer, R.D., de Wit, W.J., Maud, L.T., Hoare, M.G., Lumsden, S.L., Moore, T.J.T., Urquhart, J.S. & Mottram, J.C. (2013). CO bandhead emission of massive young stellar objects: determining disc properties. *MNRAS*, **429**, 2960–2973. 12

Jiménez-Serra, I., Caselli, P., Tan, J.C., Hernandez, A.K., Fontani, F., Butler, M.J. & van Loo, S. (2010). Parsec-scale SiO emission in an infrared dark cloud. *MNRAS*, **406**, 187–196. 20

Johns-Krull, C.M. (2007). The Magnetic Fields of Classical T Tauri Stars. *ApJ*, **664**, 975–985. 21

Kahn, F.D. (1974). Cocoons around early-type stars. *A&A*, **37**, 149–162. 9

Kamezaki, T., Imura, K., Omodaka, T., Handa, T., Tsuboi, Y., Nagayama, T., Hirota, T., Sunada, K., Kobayashi, H., Chibueze, J.O., Kawai, E. & Nakano, M. (2014). Annual Parallax Determination toward a New X-Ray-emitting Class 0 Candidate with the Water Maser in the NGC 2264 Star-forming Region. *ApJS*, **211**, 18. 87, 135

Keto, E. (2007). The Formation of Massive Stars: Accretion, Disks, and the Development of Hypercompact H II Regions. *ApJ*, **666**, 976–981. 26

Kim, K.T. & Kurtz, S. (2006a). Occurrence Frequency of CO Outflows in Massive Protostellar Candidates. *ApJ*, **643**, 978–984. 14

Kim, K.T. & Kurtz, S.E. (2006b). Occurrence Frequency of CO Outflows in Massive Protostellar Candidates. *ApJ*, **643**, 978–984. 200

Klaassen, P., Testi, L. & Beuther, H. (2012). Looking for outflow and infall signatures in high-mass star-forming regions. *A&A*, **538**, A140. 31, 65, 71, 72, 73, 146

Klaassen, P.D., Plume, R., Ouyed, R., von Benda-Beckmann, A.M. & Di Francesco, J. (2006). The Possibly Remnant Massive Outflow in G5.89-0.39. I. Observations and Initial Magnetohydrodynamic Simulations. *ApJ*, **648**, 1079–1089. 17, 31

Klaassen, P.D., Johnston, K.G., Leurini, S. & Zapata, L.A. (2015). The SiO outflow from IRAS 17233-3606 at high resolution. *A&A*, **575**, A54. 150, 204, 236

Kraus, S., Hofmann, K.H., Menten, K.M., Schertl, D., Weigelt, G., Wyrowski, F., Meilland, A., Perraut, K., Petrov, R., Robbe-Dubois, S., Schilke, P. & Testi, L. (2010). A hot compact dust disk around a massive young stellar object. *Nature*, **466**, 339–342. 12

Krumholz, M.R., Klein, R.I., McKee, C.F., Offner, S.S.R. & Cunningham, A.J. (2009). The Formation of Massive Star Systems by Accretion. *Science*, **323**, 754–. 10

Kuiper, R., Yorke, H.W. & Turner, N.J. (2015). Protostellar Outflows and Radiative Feedback from Massive Stars. *ApJ*, **800**, 86. 21

Kurtz, S., Cesaroni, R., Churchwell, E., Hofner, P. & Walmsley, C.M. (2000). Hot Molecular Cores and the Earliest Phases of High-Mass Star Formation. *Protostars and Planets IV*, 299–326. 4, 24

Kurtz, S., Hofner, P. & Álvarez, C.V. (2004). A Catalog of CH_3OH 7_0-6_1 A^+ Maser Sources in Massive Star-forming Regions. *ApJS*, **155**, 149–165. 136

Kutner, M.L. & Ulich, B.L. (1981). Recommendations for calibration of millimeter-wavelength spectral line data. *ApJ*, **250**, 341–348. 34

Lada, C.J. & Lada, E.A. (2003). Embedded Clusters in Molecular Clouds. *ARA&A*, **41**, 57–115. 86

Larson, R.B. & Starrfield, S. (1971). On the formation of massive stars and the upper limit of stellar masses. *A&A*, **13**, 190–197. 9

Lee, C.F., Hasegawa, T.I., Hirano, N., Palau, A., Shang, H., Ho, P.T.P. & Zhang, Q. (2010). The Reflection-Symmetric Wiggle of the Young Protostellar Jet HH 211. *ApJ*, **713**, 731–737. 117

Leurini, S., Codella, C., Gusdorf, A., Zapata, L., Gómez-Ruiz, A., Testi, L. & Pillai, T. (2013). Evidence of a SiO collimated outflow from a massive YSO in IRAS 17233-3606. *A&A*, **554**, A35. 17

Leurini, S., Codella, C., López-Sepulcre, A., Gusdorf, A., Csengeri, T. & Anderl, S. (2014). SiO excitation from dense shocks in the

earliest stages of massive star formation. *A&A*, **570**, A49. 31, 71, 72, 110, 146

Longmore, S.N., Burton, M.G., Minier, V. & Walsh, A.J. (2006). Mid-infrared source multiplicity within hot molecular cores traced by methanol masers. *MNRAS*, **369**, 1196–1200. 195, 196

López-Sepulcre, A., Codella, C., Cesaroni, R., Marcelino, N. & Walmsley, C.M. (2009). Molecular outflows towards O-type young stellar objects. *A&A*, **499**, 811–825. 13, 148, 149

López-Sepulcre, A., Walmsley, C., Cesaroni, R., Codella, C., Schuller, F., Bronfman, L., Carey, S., Menten, K., Molinari, S. & Noriega-Crespo, A. (2011). SiO outflows in high-mass star forming regions: A potential chemical clock? *A&A*, **526**, L2. 17, 18, 20, 31, 71

Loren, R.B. & Mundy, L.G. (1984). The methyl cyanide hot and warm cores in Orion - Statistical equilibrium excitation models of a symmetric-top molecule. *ApJ*, **286**, 232–251. 121

Lu, X., Zhang, Q., Liu, H.B., Wang, J. & Gu, Q. (2014). Very Large Array Observations of Ammonia in High-mass Star Formation Regions. *ApJ*, **790**, 84. 40, 159, 160, 183, 194

Lumsden, S.L., Hoare, M.G., Urquhart, J.S., Oudmaijer, R.D., Davies, B., Mottram, J.C., Cooper, H.D.B. & Moore, T.J.T. (2013). The Red MSX Source Survey: The Massive Young Stellar Population of Our Galaxy. *ApJS*, **208**, 11. 12, 32, 203

Mardones, D., Myers, P.C., Tafalla, M., Wilner, D.J., Bachiller, R. & Garay, G. (1997). A Search for Infall Motions toward Nearby Young Stellar Objects. *ApJ*, **489**, 719–733. 62, 64

Martin-Pintado, J., Bachiller, R. & Fuente, A. (1992). SIO Emission as a Tracer of Shocked Gas in Molecular Outflows. *A&A*, **254**, 315. 18

Maud, L.T., Lumsden, S.L., Moore, T.J.T., Mottram, J.C., Urquhart, J.S. & Cicchini, A. (2015a). A distance-limited sample of massive star-forming cores from the RMS. *MNRAS*, **452**, 637–655. 47, 48, 56, 57

Maud, L.T., Moore, T.J.T., Lumsden, S.L., Mottram, J.C., Urquhart, J.S. & Hoare, M.G. (2015b). A distance limited sample of massive molecular outflows. *MNRASin press*. 12, 13, 14, 32, 33, 37, 45, 46, 58, 68, 69, 70, 76, 82, 83, 148, 149, 150, 151, 152, 156, 200

Maury, A., André, P. & Li, Z.Y. (2009). Probing the role of protostellar feedback in clustered star formation. Mapping outflows in the collapsing protocluster NGC 2264-C. *A&A*, **499**, 175–189. xix, 87, 141, 143, 144, 145, 147, 151

McCaughrean, M.J., Rayner, J.T. & Zinnecker, H. (1994). Discovery of a molecular hydrogen jet near IC 348. *ApJL*, **436**, L189–L192. 17, 19

McKee, C.F. & Tan, J.C. (2003). The Formation of Massive Stars from Turbulent Cores. *ApJ*, **585**, 850–871. 9, 10

Mikami, H., Umemoto, T., Yamamoto, S. & Saito, S. (1992). Detection of SiO emission in the L1157 dark cloud. *ApJL*, **392**, L87–L90. 18

Minier, V., Burton, M.G., Hill, T., Pestalozzi, M.R., Purcell, C.R., Garay, G., Walsh, A.J. & Longmore, S. (2005). Star-forming protoclusters associated with methanol masers. *A&A*, **429**, 945–960. 157

Molinari, S., Brand, J., Cesaroni, R. & Palla, F. (1996). A search for precursors of ultracompact HII regions in a sample of luminous IRAS sources. I. Association with ammonia cores. *A&A*, **308**, 573–587. 156

Molinari, S., Swinyard, B., Bally, J., Barlow, M., Bernard, J.P., Martin, P., Moore, T., Noriega-Crespo, A., Plume, R., Testi, L., Zavagno, A., Abergel, A., Ali, B., Anderson, L., André, P., Baluteau, J.P., Battersby, C., Beltrán, M.T., Benedettini, M., Billot, N., Blommaert, J., Bontemps, S., Boulanger, F., Brand, J., Brunt, C., Burton, M., Calzoletti, L., Carey, S., Caselli, P., Cesaroni, R., Cernicharo, J., Chakrabarti, S., Chrysostomou, A., Cohen, M., Compiegne, M., de Bernardis, P., de Gasperis, G., di Giorgio, A.M., Elia, D., Faustini, F., Flagey, N., Fukui, Y., Fuller, G.A., Ganga, K., Garcia-Lario, P., Glenn, J., Goldsmith, P.F., Griffin, M., Hoare, M., Huang, M., Ikhenaode, D., Joblin, C., Joncas, G., Juvela, M., Kirk, J.M., Lagache, G., Li, J.Z., Lim, T.L., Lord, S.D., Marengo, M., Marshall, D.J., Masi, S., Massi, F., Matsuura, M., Minier, V., Miville-Deschênes, M.A., Montier, L.A., Morgan, L., Motte, F., Mottram, J.C., Müller, T.G., Natoli, P., Neves, J., Olmi, L., Paladini, R., Paradis, D., Parsons,

H., Peretto, N., Pestalozzi, M., Pezzuto, S., Piacentini, F., Piazzo, L., Polychroni, D., Pomarès, M., Popescu, C.C., Reach, W.T., Ristorcelli, I., Robitaille, J.F., Robitaille, T., Rodón, J.A., Roy, A., Royer, P., Russeil, D., Saraceno, P., Sauvage, M., Schilke, P., Schisano, E., Schneider, N., Schuller, F., Schulz, B., Sibthorpe, B., Smith, H.A., Smith, M.D., Spinoglio, L., Stamatellos, D., Strafella, F., Stringfellow, G.S., Sturm, E., Taylor, R., Thompson, M.A., Traficante, A., Tuffs, R.J., Umana, G., Valenziano, L., Vavrek, R., Veneziani, M., Viti, S., Waelkens, C., Ward-Thompson, D., White, G., Wilcock, L.A., Wyrowski, F., Yorke, H.W. & Zhang, Q. (2010). Clouds, filaments, and protostars: The Herschel Hi-GAL Milky Way. *A&A*, **518**, L100. 4, 35, 241

Motte, F., Zavagno, A., Bontemps, S., Schneider, N., Hennemann, M., di Francesco, J., André, P., Saraceno, P., Griffin, M., Marston, A., Ward-Thompson, D., White, G., Minier, V., Men'shchikov, A., Hill, T., Abergel, A., Anderson, L.D., Aussel, H., Balog, Z., Baluteau, J.P., Bernard, J.P., Cox, P., Csengeri, T., Deharveng, L., Didelon, P., di Giorgio, A.M., Hargrave, P., Huang, M., Kirk, J., Leeks, S., Li, J.Z., Martin, P., Molinari, S., Nguyen-Luong, Q., Olofsson, G., Persi, P., Peretto, N., Pezzuto, S., Roussel, H., Russeil, D., Sadavoy, S., Sauvage, M., Sibthorpe, B., Spinoglio, L., Testi, L., Teyssier, D., Vavrek, R., Wilson, C.D. & Woodcraft, A. (2010). Initial highlights of the HOBYS key program, the Herschel imaging survey of OB young stellar objects. *A&A*,

518, L77. 35, 241

Müller, H.S.P., Schlöder, F., Stutzki, J. & Winnewisser, G. (2005). The Cologne Database for Molecular Spectroscopy, CDMS: a useful tool for astronomers and spectroscopists. *Journal of Molecular Structure*, **742**, 215–227. 101, 174

Myers, P.C. & Benson, P.J. (1983). Dense cores in dark clouds. II - NH3 observations and star formation. *ApJ*, **266**, 309–320. 3

Myers, P.C. & Fuller, G.A. (1992). Density structure and star formation in dense cores with thermal and nonthermal motions. *ApJ*, **396**, 631–642. 10

Myers, P.C., Mardones, D., Tafalla, M., Williams, J.P. & Wilner, D.J. (1996). A Simple Model of Spectral-Line Profiles from Contracting Clouds. *ApJL*, **465**, L133. 64

Nakano, M., Sugitani, K. & Morita, K. (2003). Dense Shell around a Young Intermediate-Mass Star: NGC 2264 IRS1. , **55**, 1–9. 136

Offner, S.S.R., Lee, E.J., Goodman, A.A. & Arce, H. (2011). Radiation-hydrodynamic Simulations of Protostellar Outflows: Synthetic Observations and Data Comparisons. *ApJ*, **743**, 91. 151

Ojha, D.K., Samal, M.R., Pandey, A.K., Bhatt, B.C., Ghosh, S.K., Sharma, S., Tamura, M., Mohan, V. & Zinchenko, I. (2011). Star Formation Activity in the Galactic H II Complex S255-S257. *ApJ*, **738**, 156. 203

Ossenkopf, V. & Henning, T. (1994). Dust opacities for protostellar cores. *A&A*, **291**, 943–959. 126

Palla, F., Brand, J., Comoretto, G., Felli, M. & Cesaroni, R. (1991). Water masers associated with dense molecular clouds and ultracompact H II regions. *A&A*, **246**, 249–263. 156, 159

Peretto, N., André, P. & Belloche, A. (2006). Probing the formation of intermediate- to high-mass stars in protoclusters. A detailed millimeter study of the NGC 2264 clumps. *A&A*, **445**, 979–998. 87, 91, 92, 96, 97, 130, 131, 132, 133, 134, 144, 237

Peretto, N., Hennebelle, P. & André, P. (2007). Probing the formation of intermediate- to high-mass stars in protoclusters. II. Comparison between millimeter interferometric observations of NGC 2264-C and SPH simulations of a collapsing clump. *A&A*, **464**, 983–994. 41, 80, 87, 91, 92, 93, 96, 97, 98, 109, 111, 130, 131, 134, 144

Peters, T., Klaassen, P.D., Mac Low, M.M., Schrön, M., Federrath, C., Smith, M.D. & Klessen, R.S. (2014). Collective Outflow from a Small Multiple Stellar System. *ApJ*, **788**, 14. 21

Pilbratt, G.L., Riedinger, J.R., Passvogel, T., Crone, G., Doyle, D., Gageur, U., Heras, A.M., Jewell, C., Metcalfe, L., Ott, S. & Schmidt, M. (2010). Herschel Space Observatory. An ESA facility for far-infrared and submillimetre astronomy. *A&A*, **518**, L1. 4, 35, 90

Pillai, T., Wyrowski, F., Carey, S.J. & Menten, K.M. (2006). Ammonia in infrared dark clouds. *A&A*, **450**, 569–583. 4, 23, 24

Pillai, T., Kauffmann, J., Wyrowski, F., Hatchell, J., Gibb, A.G. & Thompson, M.A. (2011). Probing the initial conditions of high-mass star formation. II. Fragmentation, stability, and chemistry towards high-mass star-forming regions G29.96-0.02 and G35.20-1.74. *A&A*, **530**, A118. 24

Pineau des Forêts, G. & Flower, D. (1997). Non thermal sputtering of grains and production of SiO in interstellar shocks. In E. van Dishoeck, ed., *IAU Symposium*, vol. 178 of *IAU Symposium*, 113–127. 18

Plambeck, R.L. & Menten, K.M. (1990). 95 GHz methanol masers near DR 21 and DR 21(OH). *ApJ*, **364**, 555–560. 136

Poglitsch, A., Waelkens, C., Geis, N., Feuchtgruber, H., Vandenbussche, B., Rodriguez, L., Krause, O. & Renotte, E. (2010). The Photodetector Array Camera and Spectrometer (PACS) on the Herschel Space Observatory. *A&A*, **518**, L2. 35, 90

Purcell, C.R., Balasubramanyam, R., Burton, M.G., Walsh, A.J., Minier, V., Hunt-Cunningham, M.R., Kedziora-Chudczer, L.L., Longmore, S.N., Hill, T., Bains, I., Barnes, P.J., Busfield, A.L., Calisse, P., Crighton, N.H.M., Curran, S.J., Davis, T.M., Dempsey, J.T., Derragopian, G., Fulton, B., Hidas, M.G., Hoare, M.G., Lee, J.K., Ladd, E.F., Lumsden, S.L., Moore, T.J.T., Murphy, M.T., Oudmaijer, R.D., Pracy, M.B., Rathborne, J., Robertson, S., Schultz, A.S.B., Shobbrook, J., Sparks, P.A., Storey, J. & Travouillion, T. (2006). A CH_3CN and HCO^+ survey towards southern

methanol masers associated with star formation. *MNRAS*, **367**, 553–576. 51, 209, 228

Qiu, K. & Zhang, Q. (2009). Discovery of Extremely High Velocity "Molecular Bullets" in the HH 80-81 High-Mass Star-Forming Region. *ApJL*, **702**, L66–L71. 118

Qiu, K., Zhang, Q., Wu, J. & Chen, H.R. (2009). Submillimeter Array Observations of the Molecular Outflow in High-Mass Star-Forming Region G240.31+0.07. *ApJ*, **696**, 66–74. 141

Ragan, S., Henning, T., Krause, O., Pitann, J., Beuther, H., Linz, H., Tackenberg, J., Balog, Z., Hennemann, M., Launhardt, R., Lippok, N., Nielbock, M., Schmiedeke, A., Schuller, F., Steinacker, J., Stutz, A. & Vasyunina, T. (2012). The Earliest Phases of Star Formation (EPoS): a Herschel key program. The precursors to high-mass stars and clusters. *A&A*, **547**, A49. 24

Rathborne, J.M., Jackson, J.M. & Simon, R. (2006). Infrared Dark Clouds: Precursors to Star Clusters. *ApJ*, **641**, 389–405. 23

Rathborne, J.M., Jackson, J.M., Chambers, E.T., Stojimirovic, I., Simon, R., Shipman, R. & Frieswijk, W. (2010). The Early Stages of Star Formation in Infrared Dark Clouds: Characterizing the Core Dust Properties. *ApJ*, **715**, 310–322. 23, 24

Rawlings, J.M.C., Taylor, S.D. & Williams, D.A. (2000). A source of extended HCO^+ emission in young stellar objects. *MNRAS*, **313**, 461–468. 32

Rawlings, J.M.C., Redman, M.P., Keto, E. & Williams, D.A. (2004). HCO^+ emission excess in bipolar outflows. *MNRAS*, **351**, 1054–1062. 32

Reipurth, B., Rodríguez, L.F., Anglada, G. & Bally, J. (2004). Radio Continuum Jets from Protostellar Objects. *ApJ*, **127**, 1736–1746. 124, 131, 132

Richer, J., Shepherd, D., Cabrit, S., Bachiller, R. & Churchwell, E. (2000). Molecular Outflows from Young Stellar Objects. *Protostars and Planets IV*, 867. 15, 86, 152

Rieke, G.H., Young, E.T., Engelbracht, C.W., Kelly, D.M., Low, F.J., Haller, E.E., Beeman, J.W. & Gordon, K.D. (2004). The Multiband Imaging Photometer for Spitzer (MIPS). *ApJS*, **154**, 25–29. 90

Rivera-Ingraham, A., Martin, P.G., Polychroni, D., Motte, F., Schneider, N., Bontemps, S., Hennemann, M., Men'shchikov, A., Nguyen Luong, Q., André, P., Arzoumanian, D., Bernard, J.P., Di Francesco, J., Elia, D., Fallscheer, C., Hill, T., Li, J.Z., Minier, V., Pezzuto, S., Roy, A., Rygl, K.L.J., Sadavoy, S.I., Spinoglio, L., White, G.J. & Wilson, C.D. (2013). Herschel Observations of the W3 GMC: Clues to the Formation of Clusters of High-mass Stars. *ApJ*, **766**, 85. 6

Robitaille, T.P., Whitney, B.A., Indebetouw, R. & Wood, K. (2007). Interpreting Spectral Energy Distributions from Young Stellar Objects. II. Fitting Observed SEDs Using a Large Grid of Precomputed Models. *ApJS*, **169**, 328–352. 147

Rosolowsky, E.W., Pineda, J.E., Kauffmann, J. & Goodman, A.A. (2008). Structural Analysis of Molecular Clouds: Dendrograms. *ApJ*, **679**, 1338–1351. 90

Rygl, K.L.J., Wyrowski, F., Schuller, F. & Menten, K.M. (2010). Initial phases of massive star formation in high infrared extinction clouds *. I. Physical parameters. *A&A*, **515**, A42. 24, 156, 157

Rygl, K.L.J., Wyrowski, F., Schuller, F. & Menten, K.M. (2013). Initial phases of massive star formation in high infrared extinction clouds. II. Infall and onset of star formation. *A&A*, **549**, A5. 32, 51, 79

Sakai, T., Sakai, N., Hirota, T. & Yamamoto, S. (2010). A Survey of Molecular Lines Toward Massive Clumps in Early Evolutionary Stages of High-mass Star Formation. *ApJ*, **714**, 1658–1671. 17, 20

Sanchez-Monge, A., Lopez-Sepulcre, A., Cesaroni, R., Walmsley, C., Codella, C., Beltran, M., Pestalozzi, M. & Molinari, S. (2013). Evolution and excitation conditions of outflows in high-mass star-forming regions. *ArXiv e-prints*. 17, 18, 20, 31, 71, 73, 74, 146

Santiago-García, J., Tafalla, M., Johnstone, D. & Bachiller, R. (2009). Shells, jets, and internal working surfaces in the molecular outflow from IRAS 04166+2706. *A&A*, **495**, 169–181. 114

Saruwatari, O., Sakai, N., Liu, S.Y., Su, Y.N., Sakai, T. & Yamamoto, S. (2011). Compact Molecular Outflow From NGC 2264 CMM3: A Candidate for Very Young High-mass Protostar. *ApJ*, **729**, 147. 88, 112, 129, 130, 137, 138, 140, 142

Sault, R.J., Teuben, P.J. & Wright, M.C.H. (1995). A Retrospective View of MIRIAD. In R.A. Shaw, H.E. Payne & J.J.E. Hayes, eds., *Astronomical Data Analysis Software and Systems IV*, vol. 77 of *Astronomical Society of the Pacific Conference Series*, 433. 89

Schilke, P., Walmsley, C.M., Pineau des Forets, G. & Flower, D.R. (1997). SiO production in interstellar shocks. *A&A*, **321**, 293–304. 18

Schilke, P., Pineau des Forêts, G., Walmsley, C.M. & Martín-Pintado, J. (2001). Observations of SiO towards photon dominated regions. *A&A*, **372**, 291–301. 20

Schreyer, K., Helmich, F., van Dishoeck, E. & Henning, T. (1997). A molecular line and infrared study of NGC 2264 IRS 1. *A&A*, **326**, 347–365. 132

Schreyer, K., Stecklum, B., Linz, H. & Henning, T. (2003). NGC 2264 IRS 1: The Central Engine and Its Cavity. *ApJ*, **599**, 335–341. 132, 136, 153

Schuller, F., Menten, K.M., Contreras, Y., Wyrowski, F., Schilke, P., Bronfman, L., Henning, T., Walmsley, C.M., Beuther, H., Bontemps, S., Cesaroni, R., Deharveng, L., Garay, G., Herpin, F., Lefloch, B., Linz, H., Mardones, D., Minier, V., Molinari, S., Motte, F., Nyman, L.Å., Reveret, V., Risacher, C., Russeil, D., Schneider, N., Testi, L., Troost, T., Vasyunina, T., Wienen, M., Zavagno, A., Kovacs, A., Kreysa, E., Siringo, G. &

Weiss, A. (2009). ATLASGAL - The APEX telescope large area survey of the galaxy at 870 μm. *A&A*, **504**, 415–427. 241

Scoville, N.Z., Solomon, P.M. & Penzias, A.A. (1975). The molecular cloud Sagittarius B2. *ApJ*, **201**, 352–365. 2

Scoville, N.Z., Sargent, A.I., Sanders, D.B., Claussen, M.J., Masson, C.R., Lo, K.Y. & Phillips, T.G. (1986). High-resolution mapping of molecular outflows in NGC 2071, W49, and NGC 7538. *ApJ*, **303**, 416–432. 17

Shepherd, D.S. & Churchwell, E. (1996). Bipolar Molecular Outflows in Massive Star Formation Regions. *ApJ*, **472**, 225. 14

Shu, F.H., Adams, F.C. & Lizano, S. (1987). Star formation in molecular clouds - Observation and theory. *ARA&A*, **25**, 23–81. 7, 8, 10

Simpson, J.P., Burton, M.G., Colgan, S.W.J., Cotera, A.S., Erickson, E.F., Hines, D.C. & Whitney, B.A. (2009). Hubble Space Telescope NICMOS Polarization Observations of Three Edge-on Massive Young Stellar Objects. *ApJ*, **700**, 1488–1501. 157, 185, 187, 188

Skrutskie, M.F., Cutri, R.M., Stiening, R., Weinberg, M.D., Schneider, S., Carpenter, J.M., Beichman, C., Capps, R., Chester, T. & Elias, J. (2006). The Two Micron All Sky Survey (2MASS). *ApJ*, **131**, 1163–1183. 90

Slysh, V.I. & Kalenskii, S.V. (2009). Structure of the class I methanol masers OMC-2 and NGC 2264. *Astronomy Reports*, **53**, 519–527. 121, 122, 136

Slysh, V.I., Kalenskiĭ, S.V. & Val'tts, I.E. (2002). Methanol Radio Emission at Millimeter Wavelengths: New Masers at 1.3 and 2.8 Millimeters. *Astronomy Reports*, **46**, 49–56. 118, 120

Smith, R.J., Shetty, R., Beuther, H., Klessen, R.S. & Bonnell, I.A. (2013). Line Profiles of Cores within Clusters. II. Signatures of Dynamical Collapse during High-mass Star Formation. *ApJ*, **771**, 24. 79, 83, 240

Snell, R.L., Loren, R.B. & Plambeck, R.L. (1980). Observations of CO in L1551 - Evidence for stellar wind driven shocks. *ApJL*, **239**, L17–L22. 17

Sunada, K., Nakazato, T., Ikeda, N., Hongo, S., Kitamura, Y. & Yang, J. (2007). Water Maser and Ammonia Survey toward IRAS Sources in the Galaxy I. H_2O Maser Data. , **59**, 1185–. 159

Tafalla, M., Santiago-García, J., Hacar, A. & Bachiller, R. (2010). A molecular survey of outflow gas: velocity-dependent shock chemistry and the peculiar composition of the EHV gas. *A&A*, **522**, A91. 17, 117

Tamura, M., Gatley, I., Joyce, R.R., Ueno, M., Suto, H. & Sekiguchi, M. (1991). Infrared polarization images of star-forming regions. I - The ubiquity of bipolar structure. *ApJ*, **378**, 611–627. 157

Tan, J.C., Kong, S., Butler, M.J., Caselli, P. & Fontani, F. (2013). The Dynamics of Massive Starless Cores with ALMA. *ApJ*, **779**, 96. 11

Tan, J.C., Beltrán, M.T., Caselli, P., Fontani, F., Fuente, A., Krumholz, M.R., McKee, C.F. & Stolte, A. (2014). Massive Star Formation. *Protostars and Planets VI*, 149–172. 235

Vaidya, B., Fendt, C., Beuther, H. & Porth, O. (2011). Jet Formation from Massive Young Stars: Magnetohydrodynamics versus Radiation Pressure. *ApJ*, **742**, 56. 15

van der Marel, N., Kristensen, L.E., Visser, R., Mottram, J.C., Yildiz, U.A. & van Dishoeck, E.F. (2013). Outflow forces of low-mass embedded objects in Ophiuchus: a quantitative comparison of analysis methods. *A&A*, **556**, A76. 13, 148, 149

Vasyunina, T., Linz, H., Henning, T., Zinchenko, I., Beuther, H. & Voronkov, M. (2011). Chemistry in infrared dark clouds. *A&A*, **527**, A88. 238

Viti, S., Collings, M.P., Dever, J.W., McCoustra, M.R.S. & Williams, D.A. (2004). Evaporation of ices near massive stars: models based on laboratory temperature programmed desorption data. *MNRAS*, **354**, 1141–1145. 25

Voronkov, M.A., Caswell, J.L., Britton, T.R., Green, J.A., Sobolev, A.M. & Ellingsen, S.P. (2010). High-velocity feature of the class I methanol maser in G309.38-0.13. *MNRAS*, **408**, 133–138. 136

Voronkov, M.A., Caswell, J.L., Ellingsen, S.P., Green, J.A. & Breen, S.L. (2014). Southern class I methanol masers at 36 and 44 GHz. *MNRAS*, **439**, 2584–2617. 136, 240

Wang, H., Yang, J., Wang, M. & Yan, J. (2002). Near infrared molecular hydrogen emission in the NGC 2264 IRS1 region. *A&A*, **389**, 1015–1019. 87

Wang, K., Zhang, Q., Testi, L., Tak, F.v.d., Wu, Y., Zhang, H., Pillai, T., Wyrowski, F., Carey, S., Ragan, S.E. & Henning, T. (2014). Hierarchical fragmentation and differential star formation in the Galactic 'Snake': infrared dark cloud G11.11-0.12. *MNRAS*, **439**, 3275–3293. 129

Wang, Y., Beuther, H., Bik, A., Vasyunina, T., Jiang, Z., Puga, E., Linz, H., Rodón, J.A., Henning, T. & Tamura, M. (2011). Different evolutionary stages in the massive star-forming region S255 complex. *A&A*, **527**, A32. 158, 159, 162, 168, 183, 187, 200

Wang, Y., Beuther, H., Zhang, Q., Bik, A., Rodón, J.A., Jiang, Z. & Fallscheer, C. (2012). Different Evolutionary Stages in the Massive Star-forming Region W3 Main Complex. *ApJ*, **754**, 87. 168

Ward-Thompson, D., Zylka, R., Mezger, P. & Sievers, A. (2000). Dust emission from star-forming regions. VI. The submillimetre YSO cluster in NGC 2264. *A&A*, **355**, 1122–1128. 87, 96, 126, 130, 131, 147

Whelan, E.T., Alcalá, J.M., Bacciotti, F., Nisini, B., Bonito, R., Antoniucci, S., Stelzer, B., Biazzo, K., D'Elia, V. & Ray, T.P. (2014). Accretion-ejection connection in the young brown dwarf candidate ISO-ChaI 217. *A&A*, **570**, A59. 14

Williams, J.P., Blitz, L. & McKee, C.F. (2000). The Structure and Evolution of Molecular Clouds: from Clumps to Cores to the IMF. *Protostars and Planets IV*, 97. 3, 4

Wood, D.O.S. & Churchwell, E. (1989). Massive stars embedded in molecular clouds - Their population and distribution in the galaxy. *ApJ*, **340**, 265–272. 156, 157

Wu, Y., Wei, Y., Zhao, M., Shi, Y., Yu, W., Qin, S. & Huang, M. (2004). A study of high velocity molecular outflows with an up-to-date sample. *A&A*, **426**, 503–515. 14, 15

Wu, Y.W., Sato, M., Reid, M.J., Moscadelli, L., Zhang, B., Xu, Y., Brunthaler, A., Menten, K.M., Dame, T.M. & Zheng, X.W. (2014). Trigonometric parallaxes of star-forming regions in the Sagittarius spiral arm. *A&A*, **566**, A17. 37, 48, 67

Xu, Y., Voronkov, M.A., Pandian, J.D., Li, J.J., Sobolev, A.M., Brunthaler, A., Ritter, B. & Menten, K.M. (2009). Absolute positions of 6.7-GHz methanol masers. *A&A*, **507**, 1117–1139. 158, 159, 195

Zhang, Q., Ho, P.T.P. & Ohashi, N. (1998). Dynamical Collapse in W51 Massive Cores: CS (3-2) and CH_3CN Observations. *ApJ*, **494**, 636–656. 121

Zhang, Q., Hunter, T.R., Brand, J., Sridharan, T.K., Cesaroni, R., Molinari, S., Wang, J. & Kramer, M. (2005). Search for CO Outflows toward a Sample of 69 High-Mass Protostellar Candidates. II. Outflow Properties. *ApJ*, **625**, 864–882. 12, 14, 15

Zhang, Q., Hunter, T.R., Beuther, H., Sridharan, T.K., Liu, S.Y., Su, Y.N., Chen, H.R. & Chen, Y. (2007). Multiple Jets from the High-Mass (Proto)stellar Cluster AFGL 5142. *ApJ*, **658**, 1152–1163. 129

Zhang, Y., Tan, J.C., De Buizer, J.M., Sandell, G., Beltran, M.T., Churchwell, E., McKee, C.F., Shuping, R., Staff, J.E., Telesco, C. & Whitney, B. (2013). A Massive Protostar Forming by Ordered Collapse of a Dense, Massive Core. *ApJ*, **767**, 58. 14

Zinchenko, I., Liu, S.Y., Su, Y.N., Kurtz, S., Ojha, D.K., Samal, M.R. & Ghosh, S.K. (2012). A Multi-wavelength High-resolution study of the S255 Star-forming Region: General Structure and Kinematics. *ApJ*, **755**, 177. 159, 162, 192, 196

Ziurys, L.M., Friberg, P. & Irvine, W.M. (1989). Interstellar SiO as a tracer of high-temperature chemistry. *ApJ*, **343**, 201–207. 18